ΔΙΔΑΚΤΟΡΙΚΗ ΔΙΑΤΡΙΒΗ ΤΟΥ

ΚΩΝΣΤΑΝΤΙΝΟΥ ΠΕΤΡΟΥ ΤΟΥ ΣΤΑΜΑΤΙΟΥ

ΔΙΠΛΩΜΑΤΟΥΧΟΥ ΗΛΕΚΤΡΟΛΟΓΟΥ ΜΗΧΑΝΙΚΟΥ ΤΟΥ ΤΜΗΜΑΤΟΣ ΗΛΕΚΤΡΟΛΟΓΩΝ ΜΗΧΑΝΙΚΩΝ ΚΑΙ ΤΕΧΝΟΛΟΓΙΑΣ ΥΠΟΛΟΓΙΣΤΩΝ ΤΟΥ ΠΑΝΕΠΙΣΤΗΜΙΟΥ ΠΑΤΡΩΝ

ΜΕ ΤΙΤΛΟ

ΜΕΛΕΤΗ ΑΛΓΟΡΙΘΜΩΝ ΨΗΦΙΑΚΗΣ ΕΠΕΞΕΡΓΑΣΙΑΣ ΣΗΜΑΤΟΣ ΓΙΑ ΟΜΟΔΥΝΟ ΔΕΚΤΗ QPSK ΣΕ ΟΠΤΙΚΑ ΣΥΣΤΗΜΑΤΑ ΜΕΓΑΛΩΝ ΑΠΟΣΤΑΣΕΩΝ ΥΨΗΛΗΣ ΦΑΣΜΑΤΙΚΗΣ ΑΠΟΔΟΣΗΣ

ΠΑΝΕΠΙΣΤΗΜΙΟ ΠΑΤΡΩΝ
ΤΜΗΜΑ ΗΛΕΚΤΡΟΛΟΓΩΝ ΜΗΧΑΝΙΚΩΝ

ΚΑΙ ΤΕΧΝΟΛΟΓΙΑΣ ΥΠΟΛΟΓΙΣΤΩΝ

ΑΡΙΘΜΟΣ ΔΙΑΤΡΙΒΗΣ: 246

ΠΑΤΡΑ

ΙΟΥΛΙΟΣ 2010

ii

ΠΙΣΤΟΠΟΙΗΣΗ

Πιστοποιείται ότι η παρούσα διδακτορική διατριβή με θέμα:

"Μελέτη Αλγορίθμων Ψηφιακής Επεξεργασίας Σήματος για Ομόδυνο Δέκτη QPSK σε Οπτικά Συστήματα Μεγάλων Αποστάσεων Υψηλής Φασματικής Απόδοσης "

του ΚΩΝΣΤΑΝΤΙΝΟΥ ΠΕΤΡΟΥ ΤΟΥ ΣΤΑΜΑΤΙΟΥ, Διπλωματούχου Ηλεκτρολόγου Μηχανικού & Τεχνολογίας Υπολογιστών παρουσιάστηκε δημοσίως στο Τμήμα Ηλεκτρολόγων Μηχανικών & Τεχνολογίας Υπολογιστών του Πανεπιστημίου Πατρών την 4η Ιουνίου 2010 και εξετάστηκε και εγκρίθηκε από την ακόλουθη Εξεταστική Επιτροπή:

Ιωάννης Ρούδας. Αναπλ. Καθηγητής Πολυτεχνικής Σχολής του Πανεπιστημίου Πατρών, Συντονιστής Συμβουλευτικής Επιτροπής

Κυριάκος Βλάχος, Επίκουρος Καθηγητής Πολυτεχνικής Σχολής του Πανεπιστημίου Πατρών, Μέλος Συμβουλευτικής Επιτροπής

Βασίλειος Στυλιανάκης, Λέκτορας Πολυτεχνικής Σχολής του Πανεπιστημίου Πατρών, Μέλος Συμβουλευτικής Επιτροπής

Δημήτριος-Αλέξανδρος Τουμπακάρης, Επίκουρος Καθηγητής Πολυτεχνικής Σχολής του Πανεπιστημίου Πατρών

Βασίλειος Παλιουράς, Επίκουρος Καθηγητής Πολυτεχνικής Σχολής του Πανεπιστημίου Πατρών

Βασίλειος Μακιός, Ομότιμος Καθηγητής Πολυτεχνικής Σχολής του Πανεπιστημίου Πατρών

Θωμάς Καμαλάκης, Λέκτορας Τμήματος Πληροφορικής και Τηλεματικής, Χαροκόπειου Πανεπιστημίου Αθηνών
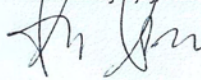
Πάτρα 4η Ιουνίου 2010

Ο ΣΥΝΤΟΝΙΣΤΗΣ

Ο ΠΡΟΕΔΡΟΣ ΤΟΥ ΤΜΗΜΑΤΟΣ

Ιωάννης Ρούδας, Αναπλ. *Καθηγητής*

Αντώνιος Τζες, *Καθηγητής*

iv

Σύμφωνα με απόφαση της υπ' αριθμόν 02 – 10/11/2010 Γενικής Συνέλευσης με Ειδική Σύνθεση του Τμήματος Ηλεκτρολόγων Μηχανικών και Τεχνολογίας Υπολογιστών, ως γλώσσα συγγραφής της διατριβής ορίζεται η αγγλική, με την υποχρέωση επισύναψης περίληψης της διατριβής στα ελληνικά, ίσης με περίπου το 30% αυτής.

Η διατριβή αυτή είναι αφιερωμένη στους γονείς μου, Πατρίτσια-Άνν Πέτρου και Σταμάτιο Πέτρου, οι οποίοι με στήριξαν κατά τη διάρκειά της με κάθε μέσο.

Ευχαριστίες

x

Πίνακας περιεχομένων/Table of contents

Κατάλογος δημοσιεύσεων/List of publications

International journals

[1] N. Mantzoukis, C. S. Petrou, A. Vgenis, I. Roudas, T. Kamalakis, and L. Raptis, "Comparison of electronic equalizers for coherent PDM QPSK systems based on outage probability", submitted to *IEEE J. Lightw. Technol.*.

[2] N. Mantzoukis, C. S. Petrou, A. Vgenis, T. Kamalakis, I. Roudas, and L. Raptis, "Outage probability due to PMD in coherent PDM QPSK systems with electronic equalization," *IEEE Photon. Technol. Lett.*, accepted for publication.

[3] I. Roudas, A. Vgenis, C. S. Petrou, D. Toumpakaris, J. Hurley, M. Sauer, J. Downie, Y. Mauro, and S. Raghavan, "Optimal polarization demultiplexing for coherent optical communications systems," *IEEE J. Lightw. Technol.*, vol. 28, no. 7, pp. 1121–1134, Apr. 2010.

[4] A. Vgenis, C. S. Petrou, C. Papadias, I. Roudas, and L. Raptis, "Non-singular constant modulus equalizer for PDM-QPSK coherent optical receivers," *IEEE Photon. Technol. Lett.*, vol. 22, no. 1, pp. 45–47, Jan. 2010.

[5] C. S. Petrou, A. Vgenis, I. Roudas, and L. Raptis, "Quadrature imbalance compensation for PDM QPSK coherent optical systems," *IEEE Photon. Technol. Lett.*, vol. 21, no. 24, pp. 1876–1888, Dec. 2009.

International conferences

[1] N. Mantzoukis, A. Vgenis, C. Petrou, I. Roudas, T. Kamalakis, and L. Raptis, "Design guidelines for electronic PMD equalizers used in coherent PDM QPSK system," accepted at *Eur. Conf. Optical Communication (ECOC)*, Milan, Italy, Sept. 2010.

[2] F. Karinou, K. Vlachos, I. Roudas, B. R. Hemenway, C. S. Petrou, and A. Vgenis, "Wavelength-space permutation switch with coherent PDM QPSK transmission for supercomputer optical interconnects," *Optical Fiber Communication Conference*, paper JWA62, San Diego, CA, Mar. 2010.

[3] I. Roudas, A. Vgenis, C. S. Petrou, Y. Mauro, S. Raghavan, and L. Raptis, "Constrained polarization for coherent optical receivers," *IEEE Lasers and Electro-Optics Society annual meeting (LEOS)*, paper WE2, Turkey, Antalya, Oct. 2009.

[4] C. S. Petrou, A. Vgenis, I. Roudas, and L. Raptis, "Quadrature imbalance compensation algorithms for coherent PDM QPSK systems," *IEEE Lasers and Electro-Optics Society annual meeting (LEOS)*, paper ThE3, Turkey, Antalya, Oct. 2009.

[5] N. Mantzoukis, C. Petrou, A. Vgenis, I. Roudas, and T. Kamalakis, "Electronic equalization of polarization mode dispersion in coherent POL-MUX QPSK systems", *European Conference on Optical Communications (ECOC)*, paper P4.15, Austria, Vienna, Sep. 2009.

[6] C. S. Petrou, A. Vgenis, A. Kiourti, I. Roudas, J. Hurley, M. Sauer, J. Downie, Y. Mauro, and S. Raghavan, "Impact of Transmitter and Receiver Imperfections on the Performance of Coherent Optical QPSK Communication Systems," *IEEE Lasers and Electro-Optics Society annual meeting (LEOS)*, paper TuFF3, Newport Beach, CA, Nov. 2008.

[7] A. Vgenis, C. S. Petrou, I. Roudas, I. Chochliouros, G. Agapiou, and T. Doukoglou, "Adaptive electronic equalization for non-ideal optical coherent receivers," *6th Int. Symp. Commun. Syst. Networks and Digital Signal Process. (CSNDSP)*, Graz, Austria, Jul. 2008, pp. 349–353.

[8] C. S. Petrou, I. Roudas, and L. Raptis, "Impact of transmitter and receiver imperfections on the performance of coherent optical QPSK communication systems," *paper CThJJ1, Conference on Lasers and Electro-Optics (CLEO)*, paper CThJJ1, San Jose, Ca., USA, May 2008.

Κατάλογος συντομογραφιών/List of acronyms

ADC(s)	Analog-to-Digital Converter(s)
AFC	Automatic Frequency Control
AGC	Automatic Gain Control
ASE	Amplified Spontaneous Emission
ASIC	Application Specific Integrated Circuit
ASK	Amplitude-Shift Keying
Baud	Symbols per second
bit(s)	Binary digit(s)
BPD	Balanced Photodetector
Bps	Bit(s) per second
BPSK	Binary Phase-Shift Keying
CD	Chromatic Dispersion
CW	Continuous Wave
DD	Direct Detection
DFB lasers	Distributed Feed-Back lasers
DSF	Dispersion Shifted Fiber
DSO	Digital Storage Oscilloscope
DSP	Digital Signal Processing
DPLL	Digital Phase Locked Loop
DPSK	Differential Phase Shift Keying
ECL	External Cavity Laser
EDFA	Erbium Doped Fiber Amplifier
FFE	Feedforward Equalizer
FPGA(s)	Field Programmable Gate Array(s)
FSK	Frequency Shift Keying
I	In-phase
IF	Intermediate Frequency

i.i.d.	Independent Identically Distributed
IM	Intensity Modulation
ISI	Inter-Symbol Interference
LPF	Low-pass Filter
LO	Local Oscillator
LOSPR	LO-to-signal power ratio
MLSE	Maximum Likelihood Sequence Estimator
MZM	Mach-Zehnder Modulator
NRZ	Non-return to Zero
OOK	On-Off Keying
OPLL	Optical Phase-Locked Loop
OSNR	Optical Signal to Noise Ratio
PAM	Pulse-Amplitude Modulation
PBC	Polarization Beam Combiner
PBS	Polarization Beam Splitter
PC	Polarization Controller
pdf	Probability Density Function
PDM	Polarization Division Multiplexing (Multiplexed)
PMD	Polarization Mode Dispersion
POLCOMB	Polarization Combiner
POLDMUX	Polarization Demultiplexer
PPG	Pulse Pattern Generator
PRBS(s)	Pseudo Random Binary Sequence(s)
PRQS(s)	Pseudo Random Quaternary Sequence(s)
PSD	Power Spectral Density
PSK	Phase-Shift Keying
Q	Quadrature-phase
QAM	Quadrature Amplitude Modulation
QM	Quadrature Modulator
QPSK	Quadrature Phase-Shift Keying

RF	Radio Frequency
ROADM	Reconfigurable Optical Add-drop Multiplexer
SOP	State of Polarization
SP	Single Polarization
SSMF	Standard Single Mode Fiber
TE	Transverse Electric
VOA	Variable Optical Attenuator
WDM	Wavelength Division Multiplexing

ΜΕΡΟΣ Α

ΠΕΡΙΛΗΨΗ ΔΙΑΤΡΙΒΗΣ ΣΤΑ ΕΛΛΗΝΙΚΑ

I. Εισαγωγή

Τα επίγεια συστήματα οπτικών τηλεπικοινωνιών μπορούν να υποστηρίξουν ταχύτητες μετάδοσης αρκετών Tb/s, σε αποστάσεις χιλιάδων χιλιομέτρων. Το γεγονός αυτό, τα καθιστά κατάλληλα για τηλεπικοινωνιακά δίκτυα κορμού. Οι πάροχοι τηλεπικοινωνιακών υπηρεσιών επιδιώκουν ολοένα και περισσότερο τη χρήση οπτικών συστημάτων για να καλύψουν τη διαρκώς αυξανόμενη ζήτηση σε όγκο δεδομένων και εύρος ζώνης, ενώ παράλληλα αναζητούν τρόπους για να καλύψουν την ανάγκη για μείωση του κόστους μετάδοσης ανά μεταδιδόμενο bit [1].

Στα κλασσικά οπτικά τηλεπικοινωνιακά συστήματα, τα οποία χρησιμοποιούν δυαδική διαμόρφωση πλάτους (On-Off-Keying – OOK), μείωση του κόστους ανά μεταδιδόμενο bit επιτυγχάνεται με χρήση πολυπλεξίας στο μήκος κύματος (wavelength division multiplexing - WDM). Σύμφωνα με τη τεχνική αυτή, ακριβοί οπτικοί πόροι μοιράζονται ανάμεσα σε πολλά τηλεπικοινωνιακά κανάλια, κάθε ένα από τα οποία διαδίδεται σε διαφορετικό μήκος κύματος. Η αύξηση της χωρητικότητας ενός συστήματος επιτυγχάνεται μέσω της αύξησης του ρυθμού σηματοδοσίας ανά κανάλι και της ταυτόχρονης συμπίεσης περισσότερων καναλιών σε περισσότερα μήκη κύματος, σε δεδομένο εύρος ζώνης.

Οι προηγούμενες τεχνικές προσκρούουν στις δυνατότητες των ηλεκτρονικών πόρων, οι οποίοι έχουν περιορισμένο εύρος ζώνης συγκριτικά με τους οπτικούς, και περιορισμένες δυνατότητες ως προς την αύξηση του ρυθμού σηματοδοσίας. Ένας τρόπος για να παρακαμφθεί ο περιορισμός των δυνατοτήτων των ηλεκτρονικών πόρων είναι να χρησιμοποιηθούν τεχνικές που να εκμεταλλεύονται καλύτερα το εύρος ζώνης ενός οπτικού καναλιού, όπως για παράδειγμα οι πολυεπίπεδες διαμορφώσεις M-ary QAM (quadrature amplitude modulation – QAM) ή M–ary PSK (M–ary phase shift keying – PSK). Χρησιμοποιώντας πολυεπίπεδες διαμορφώσεις, μεταδίδονται με δεδομένο ρυθμό συμβόλων, πολλαπλάσια δυαδικά ψηφία. Πιο συγκεκριμένα, οι τετραδικές διαμορφώσεις φάσης (quadrature PSK– QPSK) με σύμφωνη φώραση (coherent detection) έχουν τραβήξει τη προσοχή της βιομηχανίας οπτικών τηλεπικοινωνιακών συστημάτων προσφάτως, λόγω μιας σειράς πλεονεκτημάτων που προσφέρουν.

Η διαμόρφωση QPSK κωδικοποιεί κάθε έναν από τους τέσσερεις συνδυασμούς δυο δυαδικών ψηφίων σε μια από τέσσερεις διακριτές τιμές φάσης ενός φορέα. Η τιμή της φάσης ονομάζεται σύμβολο φάσης. Με τον τρόπο αυτό, ένα σύμβολο φάσης μεταφέρει ανά μονάδα χρόνου την ίδια πληροφορία με δυο δυαδικά σύμβολα. Συνεπώς, ένα σύστημα QPSK μεταφέρει τη διπλάσια πληροφορία σε σχέση με ένα σύστημα δυαδικής διαμόρφωσης πλάτους στο ίδιο εύρος ζώνης, ή την ίδια πληροφορία στο μισό εύρος ζώνης.

Οι διαμορφώσεις φάσης απαιτούν πολύπλοκους δέκτες, ευαίσθητους στη φάση του διαμορφωμένου σήματος, σε αντίθεση με τις διαμορφώσεις πλάτους όπου απλά ανιχνεύεται το πλάτος του διαμορφωμένου σήματος. Οι περισσότεροι δέκτες που είναι κατάλληλοι για αποδιαμόρφωση σημάτων διαμορφωμένων κατά φάση, εντάσσονται σε δυο κατηγορίες, τους σύμφωνους δέκτες, στους οποίους το λαμβανόμενο σήμα αναμιγνύεται με το σήμα ενός τοπικού ταλαντωτή, και τους διαφορικούς δέκτες, στους οποίους το λαμβανόμενο σήμα αναμιγνύεται με μια καθυστερημένη έκδοση του εαυτού του. Οι σύμφωνοι δέκτες προσφέρουν την καλύτερη δυνατή ευαισθησία, πράγμα που σημαίνει ότι απαιτούν τον μικρότερο δυνατό οπτικό λόγο σήματος προς θόρυβο (optical signal to noise ratio – OSNR) για δεδομένη πιθανότητα σφάλματος [2], [7], [9]. Μια ειδική κατηγορία σύμφωνων δεκτών, οι δέκτες διαφοροποίησης της φάσης, παράγουν στην έξοδό τους δυο ορθογώνιες συνιστώσες του σήματος που λαμβάνουν. Τα δυο αυτά ορθογώνια σήματα περικλείουν ολόκληρη την πληροφορία της μιγαδικής περιβάλλουσας του οπτικού ηλεκτρικού πεδίου το μέτρο και η φάση, και τη μεταφέρουν σε ηλεκτρικό σήμα, το οποίο μπορεί να υποστεί επεξεργασία με ηλεκτρονικά στοιχεία, να δειγματοληπτηθεί, και να επεξεργαστεί με αλγόριθμους ψηφιακής επεξεργασίας σήματος.

Το ηλεκτρικό πεδίο του οπτικού σήματος αναπαρίσταται με δυο ορθογώνιες πολώσεις, κάθε μια από τις οποίες μπορεί να διαμορφωθεί ανεξάρτητα από την άλλη. Διαμορφώνοντας κάθε πόλωση, επιτυγχάνεται πολυπλεξία κατά πόλωση (polarization division multiplexing) και σε συνδυασμό με τη διαμόρφωση QPSK, η τεχνική αυτή τετραπλασιάζει την πληροφορία που αποστέλλεται σε σχέση με ένα σύστημα δυαδικής διαμόρφωσης πλάτους ιδίου εύρους ζώνης. Στην πλευρά του δέκτη,

απαιτούνται δυο δέκτες διαφοροποίησης της φάσης, ένας για κάθε μια από τις ορθογώνιες πολώσεις, ώστε να ανακτηθεί ολόκληρη η πληροφορία από τη μιγαδική περιβάλλουσα του οπτικού ηλεκτρικού πεδίου σε ηλεκτρικό σήμα.

Ανάλογα τις μη ιδανικότητες και τα φαινόμενα διάδοσης που υπάρχουν σε μια οπτική ζεύξη, διαφοροποιούνται οι αλγόριθμοι ψηφιακής επεξεργασίας σήματος που πρέπει να χρησιμοποιηθούν. Όταν χρησιμοποιείται πολυπλεξία κατά πόλωση, απαιτείται αποπολυπλέκτης πόλωσης για να διαχωριστούν τα δυο σήματα, διότι οι συνήθεις οπτικές ίνες στρέφουν την κατάσταση πόλωσης στην έξοδό τους και μάλιστα με τυχαίο και χρονικά μεταβαλλόμενο τρόπο. Έτσι, τα δυο σήματα φτάνουν πολυπλεγμένα με τυχαίο τρόπο στον δέκτη. Εκτός από τον αποπολυπλέκτη, απαιτείται μια σειρά από αλγορίθμους οι οποίοι να εκτιμούν και να αναιρούν μη ιδανικότητες. Πιο συγκεκριμένα, οι σημαντικότερες μη ιδανικότητες είναι ο θόρυβος φάσης των laser, ιδιαίτερα επιβλαβής για τις διαμορφώσεις φάσης, η διαφορετική συχνότητα των laser πομπού και τοπικού ταλαντωτή (ενδιάμεση συχνότητα), η διασυμβολική παρεμβολή εξαιτίας φίλτρων ή φαινομένων διάδοσης (π.χ. διασπορά τρόπων πόλωσης, polarization mode dispersion – PMD) και η ανισοσταθμία ορθογωνιότητας στους δέκτες διαφοροποίησης της φάσης, λόγω μη ιδανικής κατασκευής.

Οι σύμφωνοι δέκτες διαφοροποίησης της φάσης και της πόλωσης, αποτέλεσαν ερευνητικό αντικείμενο στις οπτικές τηλεπικοινωνίες τη δεκαετία του 1980 [12]–[20]. Ωστόσο, η έλευση της ίνας με προσμίξεις ερβίου (erbium doped fiber amplifier – EDFA), έκανε εφικτό το στόχο της επίτευξης υψηλής ευαισθησίας δέκτη, με συστήματα διαμόρφωσης πλάτους, χωρίς να χρειάζεται αναβάθμιση σε συστήματα με σύμφωνους δέκτες, τα οποία ήταν ακριβότερα και πιο πολύπλοκα. Οι σύμφωνοι δέκτες διαφοροποίησης της φάσης και της πόλωσης επανήλθαν στο προσκήνιο στα μέσα της δεκαετίας του 2000, λόγω της έλευσης μιας νέας τεχνολογίας, τη δειγματοληψία και ψηφιακή επεξεργασία σήματος σε ρυθμούς δεκάδων GHz [39]–[43].

Προσφάτως, ένας μεγάλος αριθμός πειραμάτων έχει επιβεβαιώσει με τον πιο ισχυρό τρόπο την ανωτερότητα της χρήσης QPSK με πολυπλεξία κατά πόλωση και ψηφιακούς σύμφωνους δέκτες σε σχέση με τη δυαδική διαμόρφωση πλάτους [44]–[110] (σε χρονολογική σειρά για ευκολία).

Σκοπός της διατριβής αυτής είναι να υλοποιήσει αλγορίθμους για χρήση σε συστήματα PDM QPSK με σύμφωνους δέκτες διαφοροποίησης της φάσης και της πόλωσης, και ψηφιακή επεξεργασία των φωτορευμάτων. Υλοποιήθηκε ένας μεγάλος αριθμός αλγορίθμων και η απόδοσή τους μελετήθηκε, αναλύθηκε και συγκρίθηκε, τόσο σε περιβάλλον εξομοίωσης, όσο και με πειραματικά δεδομένα.

Η εκτεταμένη περίληψη της διατριβής είναι οργανωμένη ως εξής: Στην Ενότητα II, περιγράφονται τα βασικά οπτικά δομικά στοιχεία που μοντελοποιήθηκαν, τα οποία επιτρέπουν τη διαμόρφωση φάσης και τη λήψη οπτικών σημάτων διαμορφωμένων κατά φάση. Στην Ενότητα III, περιγράφονται οι αλγόριθμοι οι οποίοι υλοποιήθηκαν στα πλαίσια της διατριβής αυτής. Στην Ενότητα IV παρατίθενται δεδομένα εξομοίωσης που περιγράφουν τη λειτουργία των παραπάνω αλγορίθμων σε διάφορα πρακτικά σενάρια. Τέλος, στην Ενότητα V, αναλύονται κάποια πειραματικά δεδομένα με τη χρήση των παραπάνω αλγορίθμων.

II. Οπτικά συστήματα τετραδικής διαμόρφωσης φάσης με πολυπλεξία μήκους κύματος

Στην ενότητα αυτή, περιγράφουμε τα δομικά οπτικά στοιχεία που μοντελοποιήθηκαν για να χρησιμοποιηθούν στα πλαίσια αυτής της διατριβής, και τα οποία χρησιμοποιούνται σε οπτικά συστήματα PDM QPSK. Τα μοντέλα που περιγράφονται υλοποιήθηκαν σε προγραμματιστικό περιβάλλον MATLAB και ενσωματώθηκαν στο πακέτο εξομοίωσης VPI Transmission Maker, μέσω συνεξομοίωσης [113].

1. Ο οπτικός πομπός QPSK

Ένας οπτικός πομπός QPSK αποτελείται από ένα μονότροπο ημιαγωγικό laser, το οποίο ιδανικά παράγει ένα ημιτονοειδές ηλεκτρικό πεδίο σταθερής συχνότητας (φορέας), έναν διαμορφωτή ορθογωνιότητας (quadrature modulator – QM), και ηλεκτρικά κυκλώματα για την οδήγηση του διαμορφωτή. Το δομικό διάγραμμα του οπτικού πομπού φαίνεται στο Σχ. 1. Το φως από το laser διαχωρίζεται σε δυο ίσες συνιστώσες και κάθε μια από αυτές διαμορφώνεται κατά δυαδική διαμόρφωση φάσης (binary phase shift keying – BPSK) σε κάθε έναν από τους κλάδους του διαμορφωτή ορθογωνιότητας. Κάθε κλάδος του διαμορφωτή αποτελείται από έναν διαμορφωτή Mach-Zehnder (Mach-Zehnder Modulator – MZM). Μια διαφορά φάσης π/2 που δημιουργείται μεταξύ των δυο κλάδων του τετραγωνικού διαμορφωτή δημιουργεί δυο σήματα BPSK με διαφορά φάσης π/2, τα οποία, αν επανασυνδεθούν, δημιουργούν ένα σήμα διαμορφωμένο κατά QPSK. Το διαμορφωμένο σήμα γράφεται ως

$$\hat{s}(t) = \sum_{k=0}^{\infty} \left(a_{1,k} + j a_{2,k} \right) g\left(t - kT_S \right) e^{j2\pi f_c t} = \sum_{k=0}^{\infty} a_{1,k} g\left(t - kT_S \right) e^{j2\pi f_c t} + \sum_{k=0}^{\infty} a_{2,k} g\left(t - kT_S \right) e^{j2\pi f_c t + j\pi/2} \quad (1)$$

όπου τα $a_{1,k}$, $a_{2,k}$, ανήκουν σε ένα αλφάβητο $\{a_n\}=\{-1,1\}$, $n=0,1$, δηλαδή καθένα τους αντιστοιχεί σε διαμόρφωση BPSK.

Επισημαίνεται ότι ο διαμορφωτής ορθογωνιότητας είναι κατασκευασμένος από ηλεκτρο-οπτικό υλικό (στη συγκεκριμένη περίπτωση LiNbO₃), το οποίο είναι διπλοθλαστικό, οπότε απαιτείται ένας ελεγκτής πόλωσης στην είσοδο του διαμορφωτή, ώστε να ρυθμίζεται η κατάσταση πόλωσης του οπτικού πεδίου στην έξοδο του laser και να ευθυγραμμίζεται με την κύρια κατάσταση πόλωσης χαμηλής εξασθένησης του διαμορφωτή.
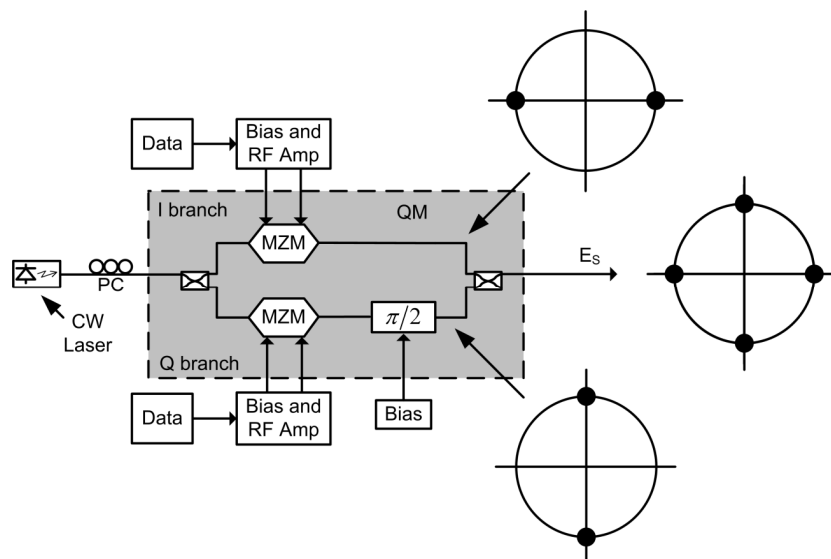
Σχ. 1 Δομικό διάγραμμα οπτικού πομπού QPSK.

Ιδανικά, τα μονότροπα ημιαγωγικά laser είναι μονοχρωματικές πηγές πολωμένου φωτός, με γωνιακή συχνότητα $\omega=2\pi f_c t$ και φέρουσα συχνότητα f_c. Τα πρακτικά laser παρ' όλα αυτά, παρουσιάζουν διακυμάνσεις στη στιγμιαία συχνότητα και την κατάσταση πόλωσης. Στο σύνολο της διατριβής, θεωρούμε ότι η πόλωση στην έξοδο των laser είναι σταθερή και πως είναι γραμμική κατά τον άξονα των x. Επιπλέον, χρησιμοποιούμε κανονικοποιημένα διανύσματα Jones [114], τα οποία συμβολίζουμε χρησιμοποιώντας την αναπαράσταση Dirac ($|e\rangle$) [115]. Η μιγαδική περιβάλλουσα του διανύσματος του ηλεκτρικού πεδίου του οπτικού κύματος με μέση ισχύ P γράφεται

$$\tilde{\mathbf{E}}(t) = \sqrt{2P}e^{j\phi_n(t)}|e\rangle \tag{2}$$

όπου

$$\phi_n(t) = \int_{-\infty}^{t} \dot{\phi}(t')dt' \tag{3}$$

είναι ο χρονικά μεταβαλλόμενος θόρυβος φάσης. Ο θόρυβος φάσης είναι μια τυχαία διαδικασία Wiener-Lévy [25], [116]. Η στιγμιαία απόκλιση συχνότητας $\dot{\phi}(t)$ μοντελοποιείται ως Γκαουσιανή τυχαία μεταβλητή με μηδενική μέση τιμή και διακύμανση $2\pi\Delta\nu\delta(0)$, όπου $\Delta\nu$ είναι το φασματικό εύρος γραμμής του laser και $\delta(t)$ η συνάρτηση δέλτα του Dirac.

Για τη μαθηματική αναπαράσταση της κατάστασης πόλωσης, χρησιμοποιούνται κανονικοποιημένα διανύσματα Jones [114]. Τα μιγαδικά διανύσματα Jones 2×1 ισοδυναμούν με πραγματικά διανύσματα 3×1 (διανύσματα Stokes) μέσω ενός ισομορφισμού. Στον χώρο Stokes η κατάσταση πόλωσης αναπαρίσταται ως σημείο πάνω σε μια σφαίρα μοναδιαίας ακτίνας, τη σφαίρα Poincaré [114]. Το αζιμούθιο και η ελλειπτικότητα της κατάστασης πόλωσης, α και ε, αντιστοίχως, χρησιμοποιούνται για να ορίσουν το κανονικοποιημένο διάνυσμα Jones ως [114]

$$|e\rangle = \begin{bmatrix} \cos a \ \cos\varepsilon - j\sin a \ \sin\varepsilon \\ \sin a \ \cos\varepsilon + j\cos a \ \sin\varepsilon \end{bmatrix}, \tag{4}$$

Η έκφραση για το διαμορφωμένο κατά QPSK σήμα στην έξοδο ενός τετραγωνικού διαμορφωτή έχει τη μορφή

$$\hat{\mathbf{E}}_S(t) = \frac{1}{2}\left\{\sum_{k=0}^{\infty} d_k \sin\left[\frac{\pi}{2}g(t-kT_S)\right]\right\}\hat{\mathbf{E}}_{in}(t) \tag{5}$$

όπου $\hat{\mathbf{E}}_S(t)$ είναι το ηλεκτρικό πεδίο του διαμορφωμένου σήματος, $\hat{\mathbf{E}}_{in}(t)$ είναι το ηλεκτρικό πεδίο του οπτικού κύματος στην είσοδο του διαμορφωτή, d_k είναι το μιγαδικό σύμβολο διαμόρφωσης για την k–στή περίοδο, και $g(t)$ η συνάρτηση σχήματος του παλμού που διαμορφώνει το οπτικό σήμα.

Για να πραγματοποιηθεί πολυπλεξία κατά πόλωση απαιτούνται δυο διαμορφωτές ορθογωνιότητας, καθένας εκ των οποίων διαμορφώνει κατά QPSK μια από τις δυο ορθογώνιες συνιστώσες του ηλεκτρικού πεδίου του οπτικού σήματος. Το σήμα στην έξοδο του laser χωρίζεται στις ορθογώνιες συνιστώσες του, χρησιμοποιώντας ένα διαχωριστή πόλωσης (polarization beam splitter – PBS). Ένας ελεγκτής πόλωσης (polarization controller – PC) ευθυγραμμίζει την κατάσταση πόλωσης του κάθε σήματος στην έξοδο του κάθε διαχωριστή πόλωσης με τους κύριους άξονες του κάθε τετραγωνικού διαμορφωτή, και πραγματοποιείται διαμόρφωση QPSK σε κάθε συνιστώσα. Μετά τη διαμόρφωση, το κάθε σήμα περνάει από έναν ελεγκτή πόλωσης, ο οποίος μετατρέπει τα δυο σήματα ξανά σε ορθογώνια και κατόπιν τα σήματα επανασυνδέονται με έναν συνδυαστή πολώσεων (polarization beam combiner – PBC) ώστε να σχηματίσουν ένα σήμα QPSK με πολυπλεξία πόλωσης. Το σχηματικό διάγραμμα του διαμορφωτή πολύπλεξης κατά πόλωση φαίνεται στο Σχ. 2. Θεωρώντας για λόγους απλότητας ότι ο διαχωριστής πόλωσης εμφανίζει στην έξοδό του τις καταστάσεις πόλωσης $|x\rangle$ και $|y\rangle$ άξονα αναφοράς, η έκφραση για το διαμορφωμένο σήμα QPSK με πολυπλεξία κατά πόλωση είναι

$$\hat{\mathbf{E}}_S(t) = \frac{1}{2}\left\{\sum_{k=0}^{\infty} d_{k,x}\sin\left[\frac{\pi}{2}g(t-kT_S)\right]\right\}\hat{E}_{In}(t)\langle x\,|\,e\rangle|x\rangle + \frac{1}{2}\left\{\sum_{k=0}^{\infty} d_{k,y}\sin\left[\frac{\pi}{2}g(t-kT_S)\right]\right\}\hat{E}_{In}(t)\langle y\,|\,e\rangle|y\rangle \qquad (6)$$

όπου $d_{k,x}$ και $d_{k,y}$ είναι τα μιγαδικά σύμβολα που διαμορφώνουν καθεμία από τις δυο πολώσεις.
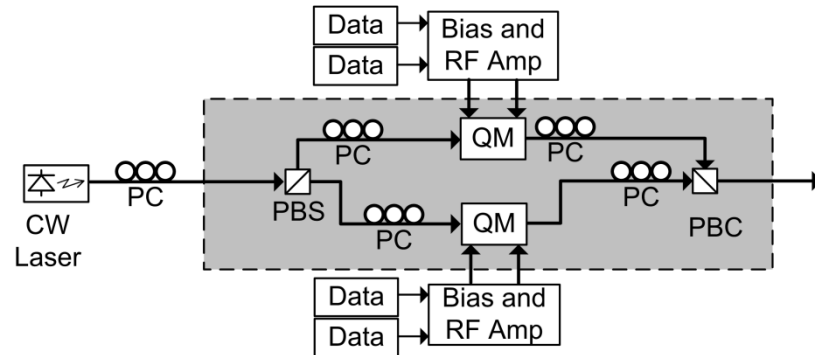
Σχ. 2 Δομικό διάγραμμα διαμορφωτή QPSK πολυπλεξίας κατά πόλωση

2. Ο οπτικός δέκτης διαφοροποίησης φάσης

Στα πλαίσια αυτής της διατριβής, για τη λήψη σημάτων διαμορφωμένων κατά QPSK, μελετήθηκαν οι σύμφωνοι δέκτες διαφοροποίησης φάσης [25]–[27]. Οι σύμφωνοι δέκτες μεταφέρουν τη φασματική πυκνότητα ισχύος του οπτικού διαμορφωμένου σήματος, από τη συχνότητα του φορέα (τυπικά κοντά στα 193.1 THz), στη βασική ζώνη ή κοντά στη βασική ζώνη, όπου, μέσω φωτοδιόδων, μετατρέπεται το οπτικό σήμα σε ηλεκτρική κυματομορφή. Το ηλεκτρικό σήμα φέρει όλη τη πληροφορία για το πλάτος και τη φάση του διαμορφωμένου φορέα. Η λειτουργία όλων των υπόλοιπων δομικών μονάδων του δέκτη είναι να εξάγουν εκτιμήσεις για την πληροφορία που εστάλη στον πομπό. Το ηλεκτρικό πεδίο που φτάνει στον δέκτη μπορεί να αναπαρασταθεί ως

$$\hat{\mathbf{E}}_S = \sqrt{2P_S} \exp\left[j\left(2\pi f_S t + \phi_{n,S} + \phi_k\right)\right]|e_S\rangle \tag{7}$$

ενώ το ηλεκτρικό πεδίο του τοπικού ταλαντωτή ως

$$\hat{\mathbf{E}}_{LO} = \sqrt{2P_{LO}} \exp\left[j\left(2\pi f_{LO} t + \phi_{n,LO}\right)\right]|e_{LO}\rangle \tag{8}$$

όπου P_S, P_{LO} είναι οι μέσες ισχείς, f_S, f_{LO} είναι οι συχνότητες εκπομπής, $\phi_{n,S}$, $\phi_{n,LO}$ οι θόρυβοι φάσης των δυο laser, αντίστοιχα, και $|e_S\rangle$, $|e_{LO}\rangle$ τα κανονικοποιημένα διανύσματα Jones των δυο οπτικών κυμάτων. Στην παραπάνω σχέση, φ_k είναι η φάση διαμόρφωσης για την k-στή χρονική στιγμή. Στη παρακάτω ανάλυση θεωρούμε για λόγους απλότητας, ότι, οι καταστάσεις πόλωσης των δυο σημάτων είναι ίδιες και σταθερές. Ορίζουμε την ενδιάμεση συχνότητα ως $f_{IF} = f_S - f_{LO}$, και τη διαφορά των θορύβων φάσης ως $\Delta\phi_n = \phi_{n,S} - \phi_{n,LO}$. Σκοπός του δέκτη είναι να εξάγει τη διαμόρφωση φάσης από το σήμα. Ανάλογα την τιμή της ενδιάμεσης συχνότητας σε σχέση το ρυθμό σηματοδοσίας, οι δέκτες κατηγοριοποιούνται σε ομόδυνους ($f_{IF} = 0$), ετερόδυνους ($f_{IF} \geq R_S$) και ενδόδυνους ($f_{IF} < R_S$) [10].

Οι σύμφωνοι δέκτες διαφοροποίησης φάσης αποτελούνται από δυο δομικά στοιχεία, το οπτικό υβρίδιο 90º, το οποίο είναι υπεύθυνο να δημιουργήσει δυο ή περισσότερους κατάλληλους γραμμικούς συνδυασμούς του ληφθέντος ηλεκτρικού πεδίου και του ηλεκτρικού πεδίου του τοπικού ταλαντωτή, και τις ισοσταθμισμένες φωτοδιόδους, οι οποίες μετατρέπουν το ηλεκτρικό πεδίο σε ηλεκτρικό ρεύμα. Οι σύμφωνοι δέκτες διαφοροποίησης φάσης στοχεύουν στο να δημιουργήσουν δυο ορθογώνια σήματα τα οποία να περιέχουν τη πληροφορία της φάσης του ηλεκτρικού πεδίου, ώστε για καμία χρονική στιγμή να μη χάνεται η πληροφορία της φάσης του ληφθέντος σήματος.

Τα οπτικά υβρίδια 90º είναι παθητικές διατάξεις και υπάρχει ένας αριθμός διαφορετικών πρακτικών υλοποιήσεων [122]. Η πιο κοινή υλοποίηση είναι το οπτικό υβρίδιο 90º δυο εισόδων – τεσσάρων εξόδων (2×4 90° optical hybrid) το οποίο αποτελείται από τέσσερεις κατευθυντικούς συζεύκτες, οι οποίοι διασπούν και αναμιγνύουν τα οπτικά σήματα, και δυο ολισθητές φάσης, οι οποίοι μεταβάλουν διαφορικά τη φάση των δυο σημάτων. Υβρίδια αυτής της λογικής κατασκευάζονται ως ολοκληρωμένα κυκλώματα από LiNbO₃ [117],[123], [124].

Το γενικό δομικό διάγραμμα ενός δέκτη διαφοροποίησης φάσης, φαίνεται στο Σχ. 3α. Το Σχ. 3β δείχνει το δομικό διάγραμμα ενός δέκτη διαφοροποίησης φάσης με ολοκληρωμένο οπτικό υβρίδιο 90º, το οποίο ακολουθείται από δυο ισοσταθμισμένες διαφορικές φωτοδιόδους. Καθένας από τους κατευθυντικούς συζεύκτες στην είσοδο διαχωρίζει το αντίστοιχο σήμα σε δυο όμοιες συνιστώσες. Μια από τις συνιστώσες κάθε σήματος αναμιγνύεται με το άλλο σήμα στους κατευθυντικούς συζεύκτες εξόδου, ενώ η άλλη συνιστώσα υφίσταται μια ολίσθηση φάσης από τους ολισθητές φάσης. Για ιδανική λειτουργία, η διαφορική ολίσθηση φάσης μεταξύ των συνιστωσών είναι 90º. Για ιδανική λειτουργία, και θεωρώντας ίδιες καταστάσεις πόλωσης για το ληφθέν σήμα και το σήμα του τοπικού ταλαντωτή, στις τέσσερεις εξόδους του υβριδίου λαμβάνουμε τους εξής γραμμικούς συνδυασμούς: $\hat{E}_S - \hat{E}_{LO}$, $j\hat{E}_S + j\hat{E}_{LO}$, $j\hat{E}_S + \hat{E}_{LO}$ και $-\hat{E}_S + j\hat{E}_{LO}$ από πάνω προς τα κάτω, αντιστοίχως. Στην έξοδο των φωτοδιόδων, οι ορθογώνιες συνιστώσες είναι

$$i_I = R\sqrt{P_s P_{lo}}\cos\left(2\pi f_{IF}t + \Delta\phi_n + \varphi_k\right)$$

$$i_Q = R\sqrt{P_s P_{lo}}\sin\left(2\pi f_{IF}t + \Delta\phi_n + \varphi_k\right)$$

$$(9)$$

όπου R είναι η αποκρισιμότητα των φωτοδιόδων, η οποία είναι ίδια για όλες τις φωτοδιόδους. Παρατηρούμε ότι ιδανικά, τα φωτορεύματα δεν έχουν κανέναν όρο συνεχούς ρεύματος.

Ένας άλλος τύπος οπτικού υβριδίου 90°, ο οποίος χρησιμοποιείται κυρίως σε εργαστήρια διότι κατασκευάζεται από διακριτά στοιχεία, είναι το οπτικό υβρίδιο 90° δυο εισόδων – δυο εξόδων (2×2 90° optical hybrid) [125]. Αποτελείται από έναν κατευθυντικό συζεύκτη, τέσσερις ελεγκτές πόλωσης, και δυο πολωτές. Το Σχ. 3γ δείχνει το δομικό διάγραμμα ενός τέτοιου δέκτη διαφοροποίησης φάσης, ο οποίος ακολουθείται από δυο απλές φωτοδιόδους. Οι ελεγκτές πόλωσης στην είσοδο του υβριδίου μεταβάλλουν την κατάσταση πόλωσης των δυο σημάτων, σε γραμμική 45° και κυκλική, για το σήμα εισόδου και τοπικό ταλαντωτή, αντίστοιχα. Οι δυο ελεγκτές πόλωσης στην έξοδο του κατευθυντικού συζεύκτη μεταβάλλουν την κατάσταση πόλωσης του αναμεμειγμένου οπτικού σήματος, ώστε η επιθυμητή συνιστώσα να περάσει από τους πολωτές (ο οποίοι έχουν κύριους άξονες ευθυγραμμισμένους με τις καταστάσεις πόλωσης $|x\rangle$ και $|y\rangle$). Στις δυο εξόδους του υβριδίου παίρνουμε τους εξής γραμμικούς συνδυασμούς: $\hat{E}_S + j\hat{E}_{LO}$ και $\hat{E}_S + \hat{E}_{LO}$ από πάνω προς τα κάτω, αντίστοιχα. Στην έξοδο των φωτοδιόδων, οι συνιστώσες ορθογωνιότητας είναι

$$i_I = \frac{R}{4}\left\{P_S + P_{LO} + 2\sqrt{P_S P_{LO}}\cos\left(2\pi f_{IF}t + \Delta\phi_n + \varphi_k\right)\right\}$$

$$i_Q = \frac{R}{4}\left\{P_S + P_{LO} + 2\sqrt{P_S P_{LO}}\sin\left(2\pi f_{IF}t + \Delta\phi_n + \varphi_k\right)\right\}$$

$$(10)$$

όπου R είναι η αποκρισιμότητα των φωτοδιόδων, ίδια για όλες τις φωτοδιόδους. Παρατηρούμε ότι ιδανικά, τα φωτορεύματα δεν έχουν κανέναν όρο συνεχούς ρεύματος.
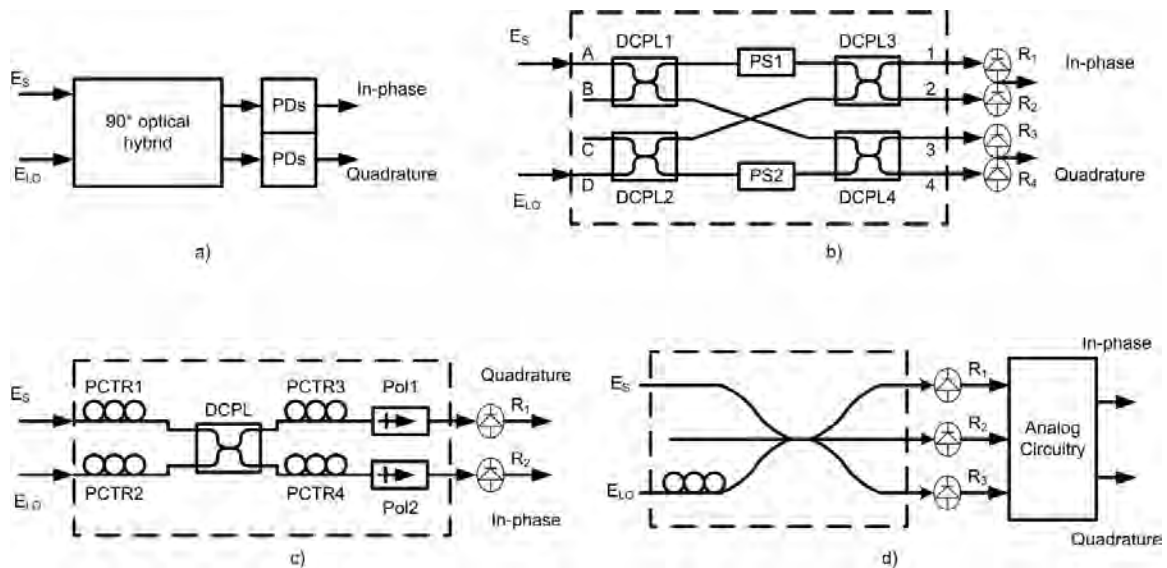
Σχ. 3 (α) Γενικό δομικό διάγραμμα ενός δέκτη διαφοροποίησης φάσης, (β) Δομικό διάγραμμα δέκτη διαφοροποίησης φάσης με ολοκληρωμένο οπτικό υβρίδιο 90°, (γ) Δομικό διάγραμμα δέκτη διαφοροποίησης φάσης με οπτικό υβρίδιο 90° διακριτών στοιχείων, (δ) Δομικό διάγραμμα δέκτη διαφοροποίησης φάσης με οπτικό υβρίδιο 90° κατευθυντικού συζεύκτη πολλαπλών εισόδων.

Ανεξάρτητα από το είδος του οπτικού υβριδίου 90° που χρησιμοποιείται και τον αντίστοιχο αριθμό των φωτοδιόδων, παράγονται δυο ορθογώνια φωτορεύματα, η σε φάση (I) και σε ορθογωνιότητα (Q) συνιστώσα, των οποίων η πιο γενική μορφή γραφής είναι

9

$$i_I(t) = I_I + I_{ip} \cos\left(2\pi f_{IF}t + \Delta\phi_n + \varphi_k + \varepsilon\right)$$
$$i_Q(t) = I_Q + I_{qp} \sin\left(2\pi f_{IF}t + \Delta\phi_n + \varphi_k - \delta\right)$$

$$(11)$$

όπου I_I, I_Q είναι οι συνιστώσες συνεχούς ρεύματος, I_{ip}, I_{qp} είναι τα πλάτη των δυο συνιστωσών ορθογωνιότητας και ε, δ είναι οι αποκλίσεις φάσης. Για ιδανική λειτουργία, τα δυο φωτορεύματα πρέπει να έχουν ίδια πλάτη, και να είναι ορθογώνια, δηλαδή, $I_{ip} = I_{qp} = I$, και $\varepsilon = \delta = 0°$. Επιπλέον, οι DC συνιστώσες του ρεύματος πρέπει να είναι σταθερές, κάτι που επιτυγχάνεται όταν το σήμα του τοπικού ταλαντωτή έχει περίπου 20 dB μεγαλύτερη ισχύ από το λαμβανόμενο σήμα [44], [68]. Τα ιδανικά φωτορεύματα της (96) μπορούν να αναπαρασταθούν ως ένα μιγαδικό ηλεκτρικό σήμα $\tilde{i}(t) = i_I(t) + ji_Q(t)$, το οποίο γράφεται

$$\tilde{i}(t) = I \exp\left(2\pi f_{IF}t + \Delta\phi_n + \varphi_k\right).$$

$$(12)$$

3. Ο οπτικός δέκτης διαφοροποίησης φάσης και πόλωσης

Όλοι οι δέκτες διαφοροποίησης φάσης που περιγράφηκαν στην προηγούμενη ενότητα παράγουν φωτορεύματα τα οποία εξαρτώνται από την κατάσταση πόλωσης του ηλεκτρικού πεδίου. Απαιτούν συγκεκριμένες καταστάσεις πόλωσης τόσο για το ληφθέν σήμα, όσο και για το σήμα του τοπικού ταλαντωτή, ώστε τα φωτορεύματα να είναι μη μηδενικά και δη ορθογώνια. Αυτό εισάγει την ανάγκη για συνεχόμενο έλεγχο των καταστάσεων πόλωσης ή για χρήση δεκτών διαφοροποίησης πόλωσης [23], [24]. Οι δέκτες διαφοροποίησης πόλωσης επιτυγχάνουν απόδοση ανεξάρτητη της πόλωσης, λαμβάνοντας το οπτικό ηλεκτρικό πεδίο από τις δυο ορθογώνιες πολώσεις ξεχωριστά, και συνδυάζοντάς το σε ένα ηλεκτρικό σήμα ανεξάρτητο από τη ληφθείσα κατάσταση πόλωσης. Οι δέκτες διαφοροποίησης πόλωσης είναι απαραίτητοι για λήψη σημάτων διαμορφωμένων κατά QPSK με πολυπλεξία πόλωσης, διότι υπάρχει διαφορετική πληροφορία σε κάθε μια από τις ορθογώνιες πολώσης. Απαιτείται ένας αλγόριθμος ηλεκτρονικής αποπολύπλεξης της πόλωσης για να ανακτηθούν τα δεδομένα που διαμόρφωσαν κάθε πόλωση.

Το δομικό διάγραμμα ενός σύμφωνου δέκτη διαφοροποίησης φάσης και της πόλωσης φαίνεται στο Σχ. 4. Το σήμα του τοπικού ταλαντωτή, με γραμμική πόλωση 45° για να διαμοιράζεται η ισχύς του εξίσου στις δυο πολώσεις, και το ληφθέν σήμα, με αυθαίρετη κατάσταση πόλωσης, διαχωρίζονται σε ένα διαχωριστή πόλωσης. Κάθε μια από τις ορθογώνιες καταστάσεις πόλωσης των σημάτων αναμειγνύονται σε έναν από τους δυο δέκτες διαφοροποίησης φάσης. Ανεξάρτητα από το είδος του δέκτη διαφοροποίησης φάσης, τα φωτορεύματα θα είναι, ιδανικά, ορθογώνια, και θα υπάρχει η συνιστώσα σε φάση και σε ορθογωνιότητα, για κάθε μια από τις δυο ληφθείσες ορθογώνιες πολώσεις.
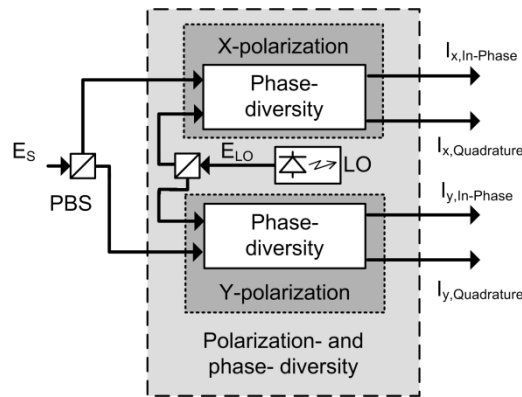
Σχ. 4 Δομικό διάγραμμα ενός σύμφωνου δέκτη διαφοροποίησης φάσης και της πόλωσης.

4. Εκφράσεις για τα φωτορεύματα σε νωτεπίνωτη συνδεσμολογία

Στα συστήματα QPSK χωρίς πολυπλεξία κατά πόλωση, η αναλυτική μορφή του σήματος στον πομπό (5) μπορεί να ξαναγραφτεί σε μια πιο απλουστευμένη μορφή, αγνοώντας το σχήμα του παλμού και την παλμοσειρά, ως

$$\hat{\mathbf{E}}_S = \sqrt{2P_S}\, e^{j(2\pi f_c t + \phi_{n,S})} e^{j\varphi_k} \left| e_S \right\rangle = \sqrt{2P_S}\, e^{j(2\pi f_c t + \phi_{n,S})} e^{j\varphi_k} \begin{pmatrix} \sqrt{1-r} \\ \sqrt{r}\,e^{j\eta} \end{pmatrix} \tag{13}$$

όπου έχουμε χρησιμοποιήσει μια εναλλακτική μορφή για να εκφράσουμε τα μοναδιαία διανύσματα Jones, η οποία περιέχει τον λόγο των ισχύων των οπτικών σημάτων στις δυο πολώσεις, r, και τη διαφορά φάσης η μεταξύ των ηλεκτρικών πεδίων των δυο πολώσεων [114]. Το αναλυτικό σήμα του τοπικού ταλαντωτή, πολωμένο με γραμμική πόλωση 45°, γράφεται ως

$$\hat{\mathbf{E}}_{LO} = \sqrt{2P_{LO}}\, e^{j(2\pi f_{LO} t + \phi_{n,LO})} \frac{1}{\sqrt{2}} \begin{pmatrix} 1 \\ 1 \end{pmatrix} \tag{14}$$

Ένα μικρό τμήμα οπτικής ίνας, όπως για παράδειγμα ένα οπτικό καλώδιο σε νωτεπίνωτη (back-to-back) συνδεσμολογία, μοντελοποιείται ως ένας μοναδιαίος πίνακας Jones 2×2 [115]

$$\mathbf{J} = \begin{pmatrix} J_{11} & J_{12} \\ J_{21} & J_{22} \end{pmatrix} \tag{15}$$

για τον οποίο ισχύει $J_{21} = -J_{12}^*$ and $J_{22} = J_{11}^*$. Ο πίνακας (15) αντιστοιχεί σε μια στροφή στη σφαίρα Poincaré, και μπορεί να εκφραστεί συναρτήσει μιας γωνίας αζιμούθιου και μιας γωνίας ελλειπτικότητας, $α, ε$, αντίστοιχα [114] (οι οποίες δεν έχουν σχέση με τις γωνίες αζιμούθιου και ελλειπτικότητας των καταστάσεων πόλωσης των laser), ως

$$\mathbf{J}(a,e) = \begin{bmatrix} \cos\alpha\cos\varepsilon - j\sin\alpha\sin\varepsilon & -\sin\alpha\cos\varepsilon + j\cos\alpha\sin\varepsilon \\ \sin\alpha\cos\varepsilon + j\cos\alpha\sin\varepsilon & \cos\alpha\cos\varepsilon + j\sin\alpha\sin\varepsilon \end{bmatrix} \tag{16}$$

Κάνοντας την υπόθεση ότι οι δέκτες διαφοροποίησης φάσης είναι ιδανικοί και δεν παράγουν συνιστώσες συνεχούς ρεύματος, τα μιγαδικά φωτορεύματα στην έξοδο των δεκτών, για την x και y πόλωση αναφοράς, είναι

$$\tilde{i}_X = I\left(\sqrt{1-r}\,J_{11} + \sqrt{r}\,J_{12}\,e^{j\eta}\right) e^{j(2\pi f_{IF} t + \Delta\phi_n + \varphi_k)}$$

$$\tilde{i}_Y = I\left(\sqrt{1-r}\,J_{21} + \sqrt{r}\,J_{22}\,e^{j\eta}\right) e^{j(2\pi f_{IF} t + \Delta\phi_n + \varphi_k)} \tag{17}$$

Λόγω των ιδιοτήτων του πίνακα (15), τα δυο φωτορεύματα δεν θα μηδενιστούν ταυτόχρονα σε καμία περίπτωση. Έτσι, η λήψη είναι ανεξάρτητη της κατάστασης πόλωσης.

Στην περίπτωση σημάτων QPSK με πολυπλεξία κατά πόλωση, η αναλυτική μορφή του ληφθέντος σήματος μπορεί να γραφτεί, όπως και πριν, ως

$$\hat{\mathbf{E}}_S = \sqrt{2P_S}\, e^{j(2\pi f_S t + \phi_{n,S})} \begin{pmatrix} \sqrt{1-r}\,e^{j\varphi_{X,k}} \\ \sqrt{r}\,e^{j\eta}\,e^{j\varphi_{Y,k}} \end{pmatrix} \tag{18}$$

Κάνοντας την υπόθεση ότι οι δέκτες διαφοροποίησης φάσης είναι ιδανικοί, και δεν παράγουν συνιστώσες συνεχούς ρεύματος, τα μιγαδικά φωτορεύματα στην έξοδο των δεκτών, για την x και y πόλωση αναφοράς, είναι

$$\tilde{i}_X = I\left(\sqrt{1-r}\,J_{11}\,e^{j\phi_{X,k}} + \sqrt{r}\,J_{12}\,e^{j\eta}\,e^{j\phi_{X,k}}\right) e^{j(2\pi f_{IF} t + \Delta\phi_n)}$$

$$\tilde{i}_Y = I\left(\sqrt{1-r}\,J_{21}\,e^{j\phi_{X,k}} + \sqrt{r}\,J_{22}\,\varepsilon^{j\eta}\,e^{j\phi_{X,k}}\right) e^{j(2\pi f_{IF} t + \Delta\phi_n)} \tag{19}$$

Σε αντίθεση με την περίπτωση χωρίς πολυπλεξία κατά πόλωση, διαφορετική πληροφορία βρίσκεται σε κάθε μια από τις πολώσεις. Μια οπτική ίνα που εισάγει μια απλή στροφή πόλωσης, προκαλεί αλληλοπαρεμβολή της πληροφορίας των πολώσεων στα δυο μιγαδικά φωτορεύματα και ο μοναδικός τρόπος επανάκτησης ολόκληρης της πληροφορίας που εστάλη στον πομπό, είναι να υπάρχουν ταυτόχρονα και τα δυο φωτορεύματα τα οποία πρέπει να αποπολυπλεχθούν.

Σε οποιαδήποτε από τις δυο περιπτώσεις, μια σειρά αλγορίθμων δειγματοληπτούν και επεξεργάζονται τα φωτορεύματα, όπως περιγράφεται στην Ενότητα III.

5. Υπό μελέτη σύστημα

Στις προηγούμενες ενότητες περιγράψαμε όλα τα οπτικά δομικά στοιχεία που χρησιμοποιούνται στα οπτικά συστήματα QPSK με πολυπλεξία κατά πόλωση. Στην ενότητα αυτή, περιγράφουμε το σύστημα που υλοποιήθηκε και μελετήθηκε στα πλαίσια αυτής της διατριβής. Το δομικό διάγραμμα του συστήματος φαίνεται στο Σχ. 5.
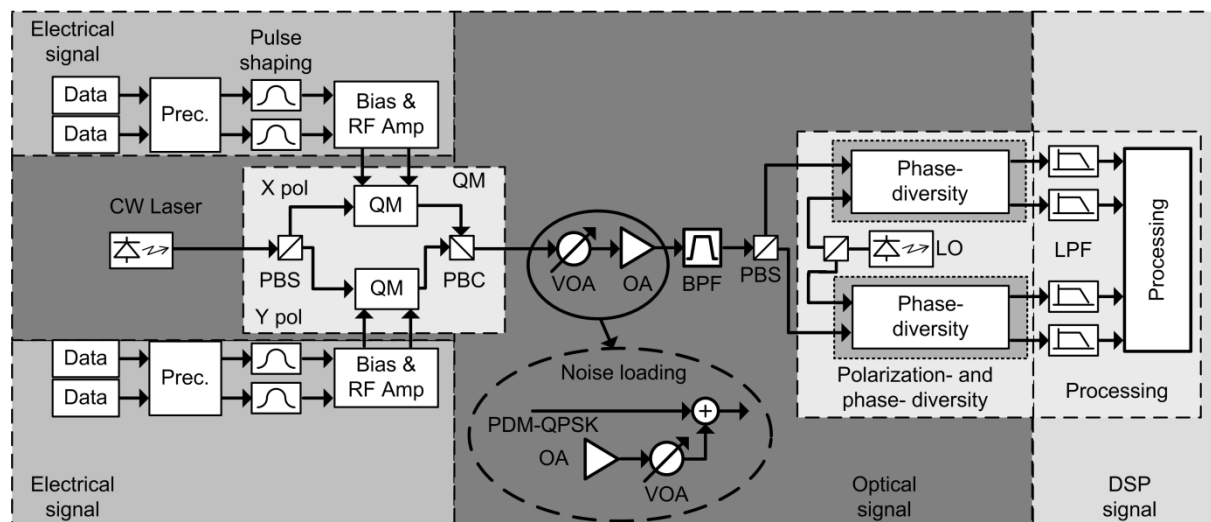
Σχ. 5 Δομικό διάγραμμα του οπτικού συστήματος διαμόρφωσης QPSK με πολυπλεξία κατά πόλωση με σύμφωνο δέκτη διαφοροποίησης φάσης και της πόλωσης.

Το φως ενός laser, πολωμένου με γραμμική πόλωση 45°, διαχωρίζεται σε έναν ιδανικό διαχωριστή πόλωσης, του οποίου οι κύριοι άξονες είναι προσανατολισμένοι πάνω στη γραμμική κατά x και γραμμική κατά y πόλωση. Κάθε πόλωση διαμορφώνεται κατά QPSK με ανεξάρτητα δεδομένα, σε έναν ιδανικό διαμορφωτή ορθογωνιότητας, του οποίου η λειτουργία είναι ανεξάρτητη της πόλωσης. Οι διαμορφωμένες πολώσεις εισέρχονται σε έναν συνδυαστή πολώσεων και επανενώνονται σε ένα σήμα QPSK πολυπλεγμένο κατά πόλωση. Σε κάθε τετραγωνικό διαμορφωτή εισέρχονται δυο ακολουθίες δυαδικών ψηφίων με ρυθμό σηματοδοσίας R_b η καθεμία. Το πολυπλεγμένο κατά πόλωση σήμα QPSK έχει ρυθμό συμβόλων $R_S=R_b$. Το σήμα εξασθενεί και κατόπιν ενισχύεται ξανά σε έναν ενισχυτή με προσμίξεις ερβίου, ο οποίος παράγει θόρυβο αυθόρμητης ενισχυμένης εκπομπής (amplified spontaneous emission noise – ASE noise). Κατά αυτόν το τρόπο, ρυθμίζεται ο οπτικός λόγος σήματος προς θόρυβο (optical signal to noise ratio – OSNR). Τέλος, το σήμα εισέρχεται σε ένα σύμφωνο δέκτη διαφοροποίησης φάσης και της πόλωσης. Χρησιμοποιούνται δυο πανομοιότυπα οπτικά υβρίδια 90° 2×4. Τα τέσσερα φωτορεύματα διέρχονται από χαμηλοδιαβατά φίλτρα Bessel 4^{ης} τάξης, των οποίων το εύρος ζώνης αλλάζει κατά περίσταση.

Μια σειρά αλγορίθμων ψηφιακής επεξεργασίας σήματος δειγματοληπτούν και επεξεργάζονται τα φωτορεύματα. Μετά από την επεξεργασία, το είδος της οποίας εξαρτάται από τα φαινόμενα που ελήφθησαν υπ' όψιν, γίνεται εκτίμηση του απεσταλμένου μιγαδικού συμβόλου και μετράται ο αριθμός σφαλμάτων των δυαδικών ψηφίων.

III.   Αλγόριθμοι ψηφιακής επεξεργασίας

Τα φωτορεύματα στην έξοδο ενός σύμφωνου δέκτη διαφοροποίησης φάσης και της πόλωσης περιέχουν ολόκληρη τη πληροφορία της μιγαδικής περιβάλλουσας και των δυο πολώσεων του ηλεκτρικού πεδίου του οπτικού σήματος. Με δειγματοληψία, η πληροφορία αυτή μετατρέπεται σε ψηφιακό σήμα, το οποίο μπορεί να υποστεί οποιουδήποτε είδους επεξεργασία. Μια πλειάδα από πρόσφατα άρθρα περιγράφουν τα πλεονεκτήματα των ψηφιακών σύμφωνων δεκτών [11], [44], [129]–[137]. Όλα τα πειράματα που πραγματοποιήθηκαν πρόσφατα χρησιμοποίησαν ψηφιακή επεξεργασία σήματος για να επεξεργαστούν τα πειραματικά δεδομένα [44]–[110].

1. Αρχιτεκτονική ψηφιακού σύμφωνου δέκτη

Το Σχ. 6 απεικονίζει τις δυο διαφορετικές τοπολογίες ψηφιακού δέκτη που χρησιμοποιήθηκαν στα πλαίσια της διατριβής. Τα τέσσερα φωτορεύματα από τις εξόδους των δυο δεκτών διαφοροποίησης φάσης φιλτράρονται για να περιοριστεί ο θόρυβος και κατόπιν δειγματοληπτούνται. Δειγματοληψία πραγματοποιείται με συχνότητα f_s ίδια ή πολλαπλάσια του ρυθμού συμβόλων R_s, δηλαδή, $f_s=mR_s$, με πιο συνήθη τιμή $m=2$ (δειγματοληψία με δύο δείγματα ανά σύμβολο).

Τα δείγματα τροφοδοτούνται στο κύκλωμα ψηφιακής επεξεργασίας όπου περνάνε από μια σειρά αλγορίθμων επεξεργασίας, ανάλογα τα φαινόμενα που επηρέασαν το σήμα. Στο τέλος της επεξεργασίας, απαιτείται τα δείγματα να αντιστοιχούν σε ένα δείγμα ανά σύμβολο, ώστε να γίνει εκτίμηση του μιγαδικού συμβόλου, και να μετρηθεί ο ρυθμός σφαλμάτων. Έτσι, όταν χρησιμοποιούνται δυο δείγματα ανά σύμβολο, απαιτείται επαναδειγματοληψία σε κάποιο σημείο του κυκλώματος. Η διαφορά μεταξύ των δυο δεκτών στο Σχ. 6, είναι η σειρά με την οποία πραγματοποιείται η διαφορική αποκωδικοποίηση και η απόφαση για το μιγαδικό σύμβολο. Στον δέκτη του Σχ. 6α, η διαφορική αποκωδικοποίηση πραγματοποιείται πριν από το κύκλωμα μιγαδικής απόφασης, γεγονός που καθιστά τον δέκτη αυτόν έναν διαφορικό δέκτη. Ο δέκτης αυτός έχει καλή απόδοση όταν οι αστερισμοί που παράγονται είναι στραμμένοι διότι τους επαναφέρει σε μορφή ώστε να χρησιμοποιηθούν σταθερά κατώφλια απόφασης στο κύκλωμα μιγαδικών αποφάσεων. Παρ' όλα αυτά, έχει μια ποινή περίπου 3 dB, σε ιδανικές συνθήκες, σε σχέση με τον σύγχρονο δέκτη του Σχ. 6β. Στον δέκτη του Σχ. 6β, η διαφορική αποκωδικοποίηση πραγματοποιείται μετά το κύκλωμα μιγαδικών αποφάσεων. Ο δέκτης αυτός έχει την ίδια απόδοση με τον ιδανικό σύμφωνο δέκτη, αλλά σε περιπτώσεις όπου ο αστερισμός είναι στραμμένος, έχει ποινή απόδοσης, ή απαιτεί μεταβαλλόμενα κατώφλια απόφασης.

Θεωρώντας ότι η δειγματοληψία γίνεται με τον ρυθμό συμβόλων, τα φωτορεύματα, για σύστημα QPSK, γράφονται ως (19)

$$\tilde{i}_{X,Y}[n] = IA_{X,Y}[n]e^{j\phi_k[n]}e^{j(2\pi f_{IF}nT_S+\Delta\phi_n[n])} + p_{X,Y}[n] \qquad (20)$$

ενώ για σύστημα QPSK με πολυπλεξία κατά πόλωση, γράφονται ως (104)

$$\tilde{i}_{X,Y}[n] = I\left\{a_{X,Y}[n]e^{j\phi_{X,k}[n]}+b_{X,Y}[n]e^{j\phi_{Y,k}[n]}\right\}e^{j(2\pi f_{IF}nT_S+\Delta\phi_n[n])} + p_{X,Y}[n] \qquad (21)$$

όπου οι δείκτες X, Y αναφέρονται στους δέκτες διαφοροποίησης πόλωσης που αντιστοιχούν στην X και Y πόλωση αντίστοιχα, n είναι ο αριθμός του δείγματος, $I = R\sqrt{P_S P_{LO}/2}$ είναι μια ποσότητα κανονικοποίησης λόγω της οπτικής ισχύος, A, a, b είναι μιγαδικοί συντελεστές οι οποίοι εξαρτώνται από τη ληφθείσα κατάσταση πόλωσης, και $p[n]$ είναι μια μιγαδική ακολουθία Γκαουσιανού προσθετικού θορύβου, με διασπορά σ_p^2. Ο θόρυβος φάσης των laser $\Delta\phi_n[n]$ είναι μια τυχαία μεταβλητή τυχαίας κίνησης [140],

$$\Delta\phi_n[n] = \Delta\phi_n[n-1] + w[n] \qquad (22)$$

15

όπου $w[n]$ είναι μια πραγματική ακολουθία Γκαουσιανού θορύβου με διασπορά σ_w^2, με $\sigma_w^2 = 2\pi\Delta v/R_S$ και όπου Δv είναι το συνδυασμένο εύρος ζώνης των laser πομπού και τοπικού ταλαντωτή [140]. Η ενδιάμεση συχνότητα f_{IF} σε πραγματικά συστήματα μεταβάλλεται επειδή οι συχνότητες των laser μεταβάλλονται, αλλά είναι σχετικά σταθερή στον χρόνο σε σχέση με άλλα χρονικά μεταβαλλόμενα φαινόμενα, και συνεπώς για τις εξομοιώσεις θεωρείται σταθερά.
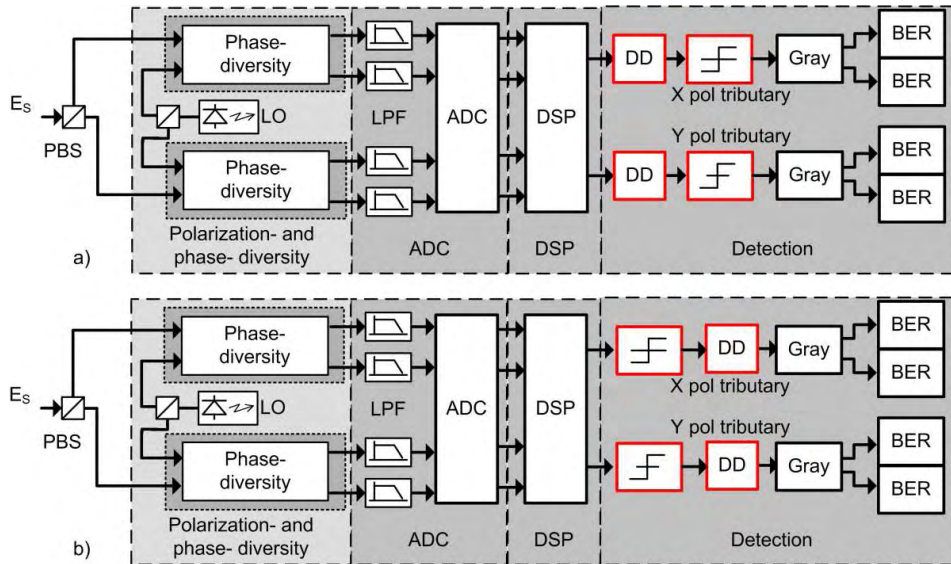
Σχ. 6 Δομικό διάγραμμα ψηφιακού σύμφωνου δέκτη διαφοροποίησης φάσης και της πόλωσης. α) Διαφορικός δέκτης, β) Σύγχρονος δέκτης.

2. Αποπολύπλεξη πολώσεων

Ανεξάρτητα από το αν χρησιμοποιείται πολυπλεξία κατά πόλωση ή όχι, η ληφθείσα κατάσταση πόλωσης επηρεάζει σημαντικά το μέτρο και τη φάση των ληφθέντων φωτορευμάτων και των ψηφιακών δειγμάτων, όπως φαίνεται στις (20) και (21). Για να είναι η απόδοση του συστήματος ανεξάρτητη της πόλωσης, απαιτείται αποπολύπλεξη των πολώσεων. Στην ενότητα αυτή θα περιγράψουμε τους βασικούς αλγόριθμους αποπολύπλεξης της πόλωσης που χρησιμοποιήθηκαν στα πλαίσια αυτής της διατριβής.

Οι στροφές πόλωσης που προκαλούνται από την οπτική ίνα μπορούν να μοντελοποιηθούν με τη χρήση πινάκων, όπου το ηλεκρικό πεδίο στην είσοδο της ίνας πολλαπλασιάζεται από τον πίνακα που αντιστοιχεί στην ίνα, για να δώσει το ηλεκτρικό πεδίο στην έξοδο της ίνας. Η αναλυτική μορφή του οπτικού πεδίου στην έξοδο $\hat{\mathbf{E}}_R$ δίνεται από τη σχέση πινάκων

$$\hat{\mathbf{E}}_R = \mathbf{J}\hat{\mathbf{E}}_S \tag{23}$$

όπου ο πίνακας $\mathbf{J}$ δίνεται από την (15) ή (16) και το $\hat{\mathbf{E}}_S$ δίνεται από την (13) ή (18). Η αποπολύπλεξη πολώσεων ισοδυναμεί με την εκτίμηση του μιγαδικού ανάστροφου συζυγούς πίνακα στροφής της οπτικής ίνας, δηλαδή,

$$\mathbf{W} = \mathbf{J}^{\dagger} \tag{24}$$

Το διάνυσμα των ληφθέντων μιγαδικών δειγμάτων $\tilde{\mathbf{I}}[n] = \begin{bmatrix} \tilde{i}_X[n] & \tilde{i}_Y[n] \end{bmatrix}^T$ μετατρέπεται σε ένα διάνυσμα μιγαδικών δειγμάτων $\tilde{\mathbf{Z}}[n] = \begin{bmatrix} \tilde{z}_X[n] & \tilde{z}_Y[n] \end{bmatrix}^T$ χρησιμοποιώντας την

$$\tilde{\mathbf{Z}}[n] = \hat{\mathbf{W}}[n]\tilde{\mathbf{I}}[n] \tag{25}$$

όπου $\hat{\mathbf{W}}[n]$ είναι μια εκτίμηση της (24) για τη χρονική στιγμή *n*.

Μια σειρά από μεθόδους έχουν προταθεί για την αποπολύπλεξη των πολώσεων [111], [148]–[156]. Στα πλαίσια αυτής της διατριβής, επικεντρωθήκαμε σε τρεις από αυτές, μια μέθοδο οδηγούμενη από απόφαση [111], μια μέθοδο η οποία θέτει περιορισμούς στις αποδεκτές τιμές των στοιχείων του πίνακα $\hat{\mathbf{W}}[n]$ σύμφωνα με την αναλυτική του μορφή, η οποία χρησιμοποιεί το κριτήριο CMA [156], και μια μέθοδο η οποία δε θέτει κανέναν περιορισμό στις αποδεκτές τιμές των στοιχείων του πίνακα $\hat{\mathbf{W}}[n]$, η οποία πάλι στηρίζεται στο κριτήριο CMA [153].

i. Αποπολύπλεξη πολώσεων οδηγούμενη από απόφαση [111]

Η μέθοδος οδηγούμενη από απόφαση προσπαθεί να εκτιμήσει το γινόμενο $\mathbf{Q}=\mathbf{W}\mathbf{J}$, το οποίο ιδανικά θα έπρεπε να δίνει $\mathbf{Q}=\mathbf{I}$, όπου $\mathbf{I}$ είναι ο 2×2 μοναδιαίος πίνακας. Χρησιμοποιεί την αναδρομική σχέση

$$\hat{\mathbf{W}}[n+1] = \mathbf{Q}^{-1}[n]\hat{\mathbf{W}}[n] \tag{26}$$

Για μικρά σήματα, ο αντίστροφος πίνακας μπορεί να προσεγγιστεί από τη σχέση

$$\mathbf{Q}^{-1}[n] = (\mathbf{I} - (\mathbf{I} - \mathbf{Q}[n]))^{-1} = (\mathbf{I} + (\mathbf{I} - \mathbf{Q}[n])) \tag{27}$$

οπότε

$$\hat{\mathbf{W}}[n+1] = (\mathbf{I} + \mu(\mathbf{I} - \mathbf{Q}[n]))\hat{\mathbf{W}}[n] \tag{28}$$

όπου *μ* είναι το βήμα του αλγορίθμου. Ο πίνακας $\mathbf{Q}$ υπολογίζεται από τις μιγαδικές εκτιμήσεις των συμβόλων, υποθέτοντας ότι αυτές είναι σωστές εκτιμήσεις, ως ακολούθως

$$\mathbf{Q}[n] = \frac{1}{2}\tilde{\mathbf{Z}}[n]\hat{\mathbf{Z}}^T[n] \tag{29}$$

όπου $\hat{\mathbf{Z}}[n]$ είναι το διάνυσμα με της μιγαδικές εκτιμήσεις των ληφθέντων συμβόλων $\tilde{\mathbf{Z}}[n]$, εάν έχουν αφαιρεθεί όλες οι υπόλοιπες παραμορφώσεις και θόρυβοι.

ii.   Αποπολύπλεξη με χρήση CMA

Ο αλγόριθμος CMA [144] πραγματοποιεί απλή αποπολύπλεξη όταν χρησιμοποιεί ένα μιγαδικό βάρος στα φίλτρα του. Τα μιγαδικά βάρη δύναται να πάρουν οποιαδήποτε τιμή. Η εξίσωση ανανέωσης των βαρών γράφεται [143]

$$\hat{\mathbf{W}}[n+1] = \hat{\mathbf{W}}[n] + \mu \begin{bmatrix} \tilde{i}_X^*[n] \\ \tilde{i}_Y^*[n] \end{bmatrix} \begin{bmatrix} \tilde{z}_X[n]\left\{1 - \left|\tilde{z}_X[n]\right|^2\right\} & \tilde{z}_Y[n]\left\{1 - \left|\tilde{z}_Y[n]\right|^2\right\} \end{bmatrix} \tag{30}$$

όπου μ είναι το βήμα του αλγορίθμου.

iii.   Αποπολύπλεξη με χρήση CMA με περιορισμούς [156]

Εάν ληφθεί υπόψη η αναλυτική μορφή του πίνακα στροφής (16), τότε ο ανάστροφος μπορεί να γραφτεί συναρτήσει δυο πραγματικών συντελεστών και έτσι μειώνεται ο αριθμός των μεταβλητών που πρέπει να υπολογιστούν, από τέσσερεις μιγαδικές ποσότητες, σε δυο πραγματικές. Ο αντίστροφος πίνακας της οπτικής ίνας γράφεται

$$\mathbf{W}(\alpha,\varepsilon) = \begin{bmatrix} \cos\alpha\cos\varepsilon - j\sin\alpha\sin\varepsilon & \sin\alpha\cos\varepsilon - j\cos\alpha\sin\varepsilon \\ -\sin\alpha\cos\varepsilon - j\cos\alpha\sin\varepsilon & \cos\alpha\cos\varepsilon + j\sin\alpha\sin\varepsilon \end{bmatrix} \tag{31}$$

Οι εκτιμήσεις $\hat{\alpha}$ και $\hat{\varepsilon}$ του αζιμούθιου και της ελλειπτικότητας α και ε, αντίστοιχα, υπολογίζονται ως

$$\mathbf{D}[n+1] = \mathbf{D}[n] - \mu\nabla\xi[n] \tag{32}$$

όπου $\mathbf{D}[n]$ είναι το διάνυσμα των εκτιμήσεων των παραμέτρων $\mathbf{D}[n] = \begin{bmatrix} \hat{\alpha}[n] & \hat{\varepsilon}[n] \end{bmatrix}^T$, μ είναι το βήμα του αλγορίθμου, και η παράγωγος $\nabla\xi(n)$ ορίζεται ως το διάνυσμα

$$\nabla\xi[n] = \begin{bmatrix} \dfrac{\partial\xi[n]}{\partial\alpha} & \dfrac{\partial\xi[n]}{\partial\varepsilon} \end{bmatrix}^T \tag{33}$$

Στις παραπάνω, $\xi[n]$ είναι η στιγμιαία συνάρτηση κόστους, η οποία για τον αποπολυπλέκτη CMA δίνεται από τη σχέση

$$\xi = \left(\left|z_1[n]\right|^2 - R_2^{(1)}\right)^2 + \left(\left|z_2[n]\right|^2 - R_2^{(2)}\right)^2 \tag{34}$$

3. Θόρυβος φάσης των laser

Ο θόρυβος φάσης είναι μια αναπόφευκτη μορφή θορύβου στις οπτικές τηλεπικοινωνίες, λόγω της χρήσης των laser. Μάλιστα, σε συστήματα μικρών αποστάσεων ή όταν χρησιμοποιούνται φθηνά εμπορικά laser, ο θόρυβος φάσης μπορεί να είναι η μεγαλύτερη μορφή θορύβου. Το Σχ. 7 δείχνει την εξέλιξη της φάσης ενός μονότροπου ημιαγωγικού laser για χρονική περίοδο 3.5 μs για τρία διαφορετικά laser, με εύρος φασματικής γραμμής στα 3 dB ίσο με , 500 kHz, 5 MHz, και 50 MHz, αντιστοίχως.
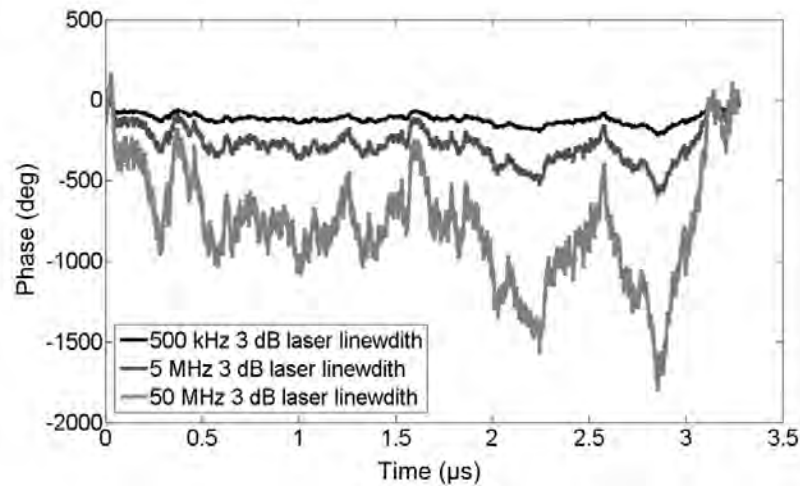
Σχ. 7 Μεταβολή της φάσης ενός μονότροπου ημιαγωγικού laser συναρτήσει του χρόνου για διάφορες τιμές εύρους γραμμής.

Στις σύμφωνες οπτικές τηλεπικοινωνίες, σημασία έχει ο λόγος του εύρους ζώνης με τον ρυθμό συμβόλων $\Delta v/R_S$, ή αλλιώς το γινόμενο του εύρους ζώνης με την περίοδο συμβόλου $\Delta v T_S$. Ο θόρυβος φάσης προκαλεί μια τυχαία δεξιόστροφη ή αριστερόστροφη στροφή του μιγαδικού δείγματος ανά δείγμα, με συνέπεια, αν ο θόρυβος φάσης είναι μεγάλος, το μιγαδικό δείγμα να βγει από το σωστό τεταρτημόριο και να προκληθεί σφάλμα. Το Σχ. 8 δείχνει την ποινή OSNR σε σχέση με το ιδανικό QPSK σύστημα με σύμφωνο δέκτη για πιθανότητα σφάλματος BER = 10^{-3} συναρτήσει του γινομένου $\Delta v T_S$, για τους δυο δέκτες του Σχ. 6. Το πρώτο πράγμα που παρατηρεί κανείς, είναι ότι διαφορικός δέκτης έχει μια ποινή περίπου 1.9 dB απουσία θορύβου φάσης Μπορεί επίσης να υποστηρίξει γινόμενα $\Delta v T_S$ ως και 3×10^{-3} με ποινή μικρότερη του 3 dB (που αντιστοιχεί σε laser με εύρος φασματικής γραμμής στα 3 dB ίσο με 30 MHz στα 10 GBd). Ο σύγχρονος δέκτης, αν και έχει το πλεονέκτημα στην λειτουργία με μηδενικό θόρυβο φάσης, μπορεί να αντέξει γινόμενα $\Delta v T_S$ της τάξης των 1.5×10^{-6} (τα οποία αντιστοιχούν σε laser με εύρος φασματικής γραμμής στα 3 dB ίσο με 10 kHz στα 10 GBd).

Ένας μεγάλος αριθμός αλγορίθμων εκτίμησης και διόρθωσης του θορύβου φάσης έχει αναπτυχθεί για τις οπτικές τηλεπικοινωνίες με ψηφιακούς σύμφωνους δέκτες. Σε όλες τις μεθόδους, η πληροφορία του μιγαδικού συμβόλου διαμόρφωσης πρέπει πρώτα να αφαιρεθεί και κατόπιν να εφαρμοστεί μια μέθοδος περιορισμού ή εκτίμησης του θορύβου φάσης. Τα μιγαδικά σύμβολα διαμόρφωσης αφαιρούνται είτε με ανατροφοδότηση της απόφασης [140], είτε υψώνοντας τα μιγαδικά δείγματα στην τετάρτη [158]. Η πρώτη μέθοδος έχει χρησιμοποιηθεί στις [160]–[163], ενώ η δεύτερη στις [111], [140], [157], [164], [165].

Η έκφραση για το μιγαδικό δείγμα απουσία ενδιάμεσης συχνότητας, στην έξοδο του αποπολυπλέκτη, δίνεται ιδανικά από την έκφραση

$$\tilde{i}_{X,Y}[n] = I e^{j\phi_{k,X,Y}[n]} e^{j\Delta\phi_n} + p_{X,Y}[n] \tag{35}$$

19
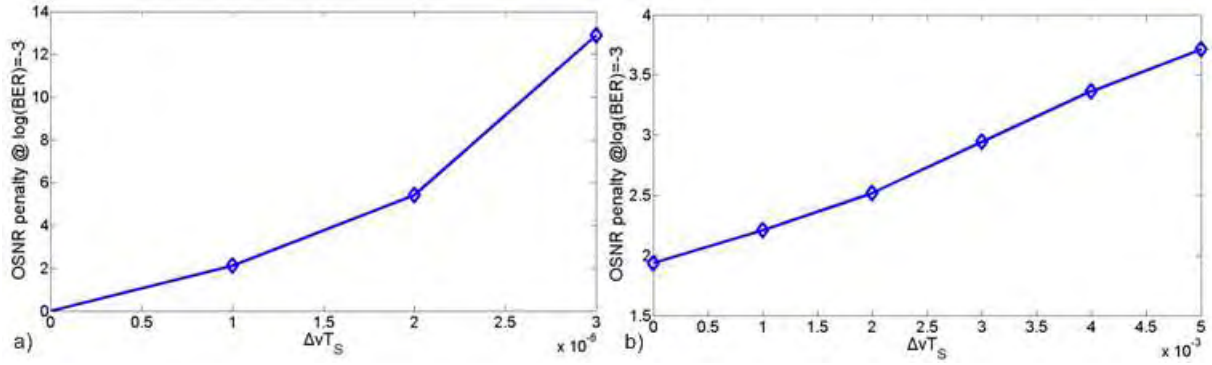
Σχ. 8 Ποινή OSNR σε σχέση με τον ιδανικό σύμφωνο δέκτη QPSK συναρτήσει του γινομένου $\Delta v T_S$. α) διαφορικός δέκτης, β) Σύγχρονος δέκτης.

i.   Εκτίμηση του θορύβου φάσης με ανατροφοδότηση απόφαση

Οι αλγόριθμοι με ανατροφοδότηση από απόφαση λαμβάνουν αποφάσεις για το ποιο σύμβολο εστάλη, και θεωρώντας ότι η απόφαση είναι σωστή, αφαιρούν το σύμβολο από το ληφθέν δείγμα. Το αποτέλεσμα είναι μια ποσότητα η οποία οφείλεται μονάχα στον θόρυβο φάσης και αποτελεί εκτίμηση αυτού. Υπάρχουν δυο παρόμοιοι αλγόριθμοι, οι οποίοι φαίνονται στο Σχ. 9. Η κύρια διαφορά έγκειται στην αλληλουχία των πράξεων και όχι στην ουσία των αλγόριθμων.

Ο πρώτος αλγόριθμος (Σχ. 9α [160], [162]) ξεκινά από το μιγαδικό δείγμα (35), και αφαιρεί από αυτό μια εκτίμηση του θορύβου φάσης, η οποία προήλθε από την αμέσως προηγούμενη χρονική στιγμή. Το αποτέλεσμα είναι ένα μιγαδικό δείγμα

$$\hat{d}[n] = e^{j\phi_k[n]}e^{j\left(\Delta\phi_n[n] - \Delta\hat{\phi}_n[n-1]\right)} + p_1[n] \tag{36}$$

όπου $p_1[n]$ είναι διαφορετικός θόρυβος από τον $p[n]$ αλλά με την ίδια διασπορά σ_p^2. Το δείγμα $\hat{d}[n] = \exp\left(j\hat{\phi}_k[n]\right)$ είναι μια εκτίμηση του μιγαδικού συμβόλου $d[n] = \exp\left(j\phi_k[n]\right)$. Η εκτίμηση αυτή περνάει από το μιγαδικό κύκλωμα αποφάσεων και προκύπτει η εκτίμηση $\widehat{d}[n]$. Θεωρώντας ότι η εκτίμηση $\widehat{d}[n]$ είναι ορθή, πραγματοποιείται η πράξη

$$\hat{d}[n]\widehat{d}^*[n] = e^{j\left(\hat{\phi}_k[n] - \bar{\phi}_k[n]\right)}e^{j\left(\Delta\phi_n[n] - \Delta\hat{\phi}_n[n]\right)} + p_2[n] \tag{37}$$

της οποίας το αποτέλεσμα εξαρτάται μόνο από τον θόρυβο φάσης και χρησιμοποιείται για να γίνει η εκτίμηση του θορύβου φάσης ως εξής

$$\Delta\hat{\phi}_n[n] = \mu\arg\left\{\hat{d}[n]\widehat{d}^*[n]\right\} \tag{38}$$

η οποία θα χρησιμοποιηθεί στο νέο εισερχόμενο δείγμα, όπου μ είναι το βήμα του αλγορίθμου ($0\le\mu\le1$) (αλγόριθμος Crivelli [160]).

Ο δεύτερος αλγόριθμος (Σχ. 9β [140], [161]) ξεκινά ξανά από το μιγαδικό δείγμα (133), και αφαιρεί από αυτό μια εκτίμηση του θορύβου φάσης, η οποία προήλθε από την προηγούμενη χρονική στιγμή. Η βασική διαφορά με πριν είναι ότι η έξοδος του μιγαδικού κυκλώματος απόφασης αφαιρείται από το εισερχόμενο δείγμα και όχι από την εκτίμηση του μιγαδικού συμβόλου δηλαδή

$$\tilde{i}[n]\widehat{d}^*[n] = e^{j\left(\phi_k[n] - \bar{\phi}_k[n]\right)}e^{j\Delta\phi_n[n-1]} + p_3[n] \tag{39}$$

όπου $p_3[n]$ είναι διαφορετικός θόρυβος από τον $p[n]$ αλλά με την ίδια διασπορά σ_p^2. Θεωρώντας ότι η εκτίμηση $\widehat{d}[n]$ είναι ορθή, η εκτίμηση του θορύβου φάσης είναι

20

$$\Delta\hat{\phi}_n[n] = \arg\left\{\tilde{i}[n]\widehat{d}^*[n]\right\} \tag{40}$$

(αλγόριθμος Taylor [140]). Μια εναλλακτική προσέγγιση είναι να πραγματοποιηθεί ταυτόχρονο φιλτράρισμα των δειγμάτων στην (40) ώστε να μειωθεί η επίδραση του προσθετικού θορύβου, δηλαδή

$$\Delta\hat{\phi}_n[n] = \arg\left\{\sum^N \tilde{i}[n]\widehat{d}^*[n]\right\} \tag{41}$$

(αλγόριθμος Savory [161]). Ο αλγόριθμος του Savory εκφυλίζεται στον αλγόριθμο του Taylor για N=1.
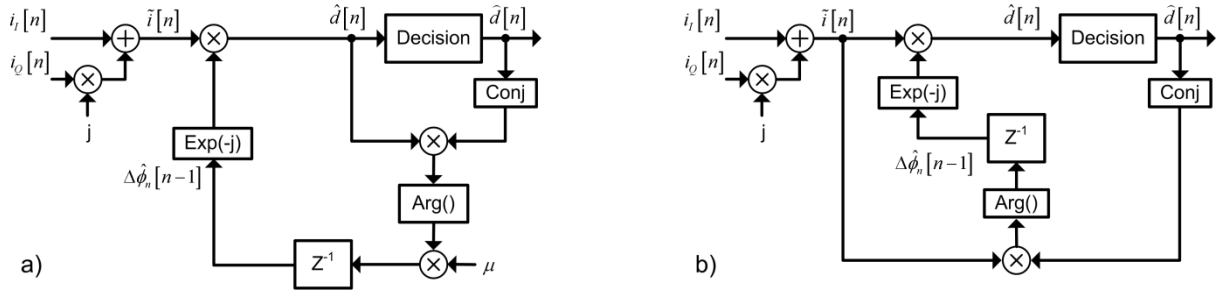
Σχ. 9 Δομικό διάγραμμα αλγορίθμων ανατροφοδότησης από απόφαση για την αφαίρεση του θορύβου φάσης. α) Αλγόριθμος Crivelli [160], β) Αλγόριθμος Taylor [140].

ii.   Εκτίμηση του θορύβου φάσης με ύψωση στην τετάρτη

Οι αλγόριθμοι που βασίζονται στην ύψωση στην τετάρτη για την αφαίρεση της φάσης διαμόρφωσης, εκμεταλλεύονται το χαρακτηριστικό γνώρισμα της διαμόρφωσης QPSK, ότι οι φάσεις διαμόρφωσης είναι πολλαπλάσιες του π/4. Συνεπώς, όταν τα μιγαδικά σύμβολα υψωθούν στην τετάρτη, η φάση διαμόρφωσης γίνεται πολλαπλάσια του π και εξαφανίζεται. Εάν τα μιγαδικά δείγματα της (35) υψωθούν στην τετάρτη, η εκτίμηση του θορύβου φάσης $\Delta\phi_n[n]$ είναι

$$\Delta\hat{\phi}_n[n] = \frac{1}{4}\arg\left\{\tilde{i}^4[n]\right\} = \Delta\phi_n[n] + m[n] \tag{42}$$

όπου m[n] είναι θόρυβος. Εάν χρησιμοποιηθούν διαδοχικά δείγματα στον χρόνο, η φάση χρειάζεται αναδίπλωση (unwrapping).

Η πρώτη μέθοδος που υλοποιήθηκε είναι μια μέθοδος φιλτραρίσματος των αναδιπλωμένων φάσεων σε ένα FIR φίλτρο [140], [157], [164], [165]. Το δομικό διάγραμμα αυτής της μεθόδου φαίνεται στο Σχ. 10. Τα εισερχόμενα δείγματα υψώνονται στην τετάρτη και το όρισμα αναδιπλώνεται. Η ακολουθία των αναδιπλωμένων φάσεων περνάει από το FIR φίλτρο

$$\Delta\hat{\phi}_{n,filt}^{unwrap}[n] = \Delta\hat{\phi}_n^{unwrap}[n] \otimes w[n] \tag{43}$$

όπου $\otimes$ αντιστοιχεί σε συνέλιξη, και w[n] είναι η κρουστική απόκριση του φίλτρου. Τα φιλτραρισμένα δείγματα φάσης αφαιρούνται από τα εισερχόμενα δείγματα, αφαιρώντας την εκτίμηση του θορύβου φάσης.
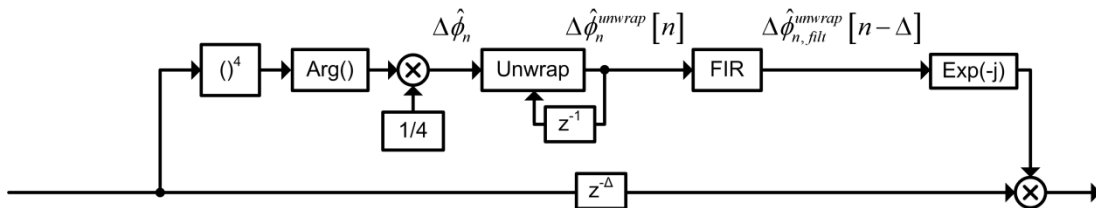
Σχ. 10 Δομικό διάγραμμα κυκλώματος αφαίρεσης του θορύβου φάσης με χρήση FIR φίλτρου.

Η βέλτιστη εκτίμηση του θορύβου φάσης $\Delta\hat{\phi}_n[n]$ επιτυγχάνεται όταν χρησιμοποιείται φίλτρο Wiener [157], [140]. Η κρουστική απόκριση είναι

$$w[n] = A\left(a^n u[-n-1] + b^n u[n]\right) \tag{44}$$

όπου $u[n]$ είναι η βηματική συνάρτηση και A, a, b είναι συντελεστές που προκύπτουν από τις σχέσεις

$$
\begin{aligned}
A &= \frac{r}{a-b} \\
a &= \frac{1}{2}\left(2 + r + \sqrt{r}\sqrt{r+4}\right) \\
b &= \frac{1}{2}\left(2 + r - \sqrt{r}\sqrt{r+4}\right) \\
r &= \frac{\sigma_w^2}{\sigma_m^2}
\end{aligned}
\tag{45}
$$

και σ_m^2 είναι η διασπορά του θορύβου $m[n]$. Εξαιτίας των πολύπλοκων στατιστικών του θορύβου για το μεγάλο εύρος τιμών OSNR και γινομένου $\Delta v T_S$, στις εξομοιώσεις, ο λόγος r επιλέγεται εμπειρικά και κατά περίπτωση. Στη δημοσίευση [164] προτάθηκε μια προσέγγιση του φίλτρου Wiener με συντελεστές οι οποίοι αντιστοιχούν σε δυαδικούς αριθμούς. Στη [111] προτάθηκε μια προσέγγιση του φίλτρου Wiener με συντελεστές οι οποίοι έχουν ίδιο πλάτος (τετραγωνικό φίλτρο).
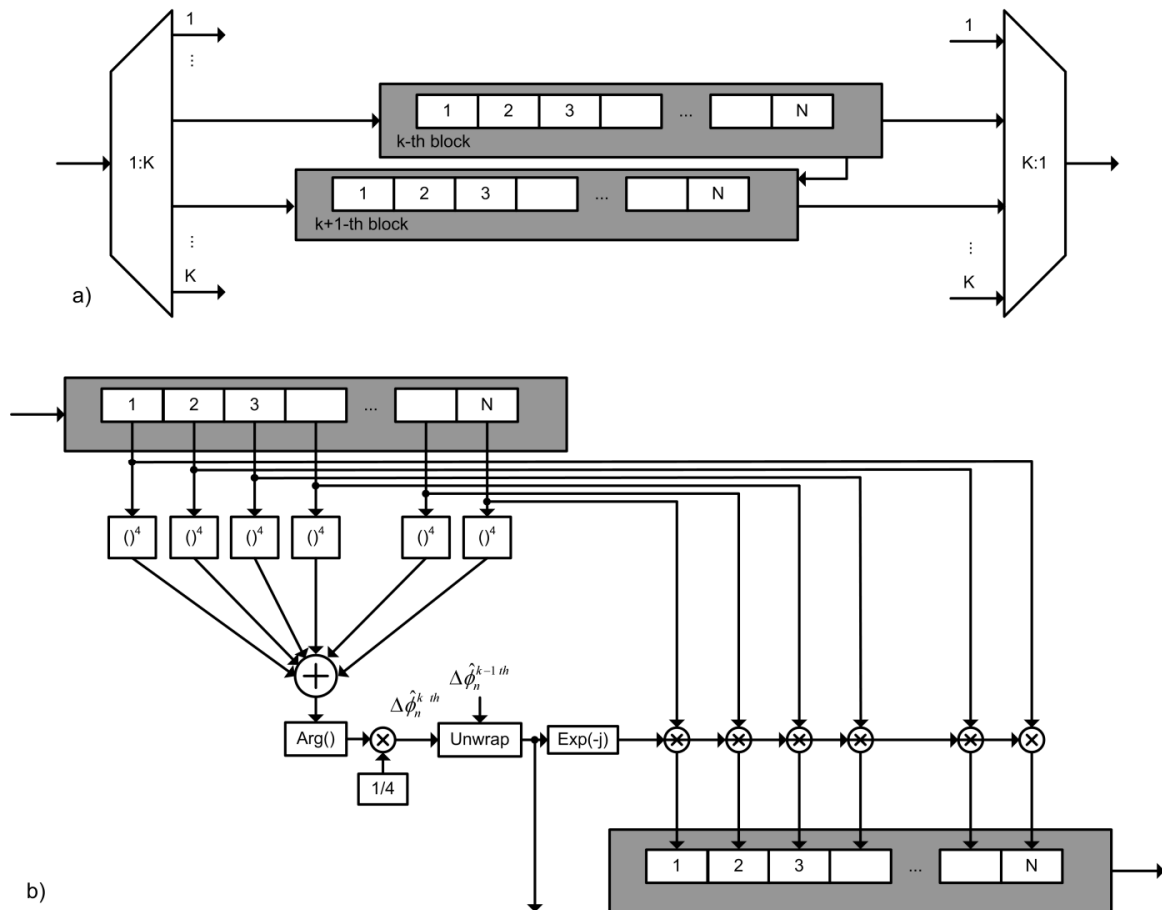
Σχ. 11 Δομικό διάγραμμα αλγορίθμου block-phase.

Μια εναλλακτική προσέγγιση για την εκτίμηση του θορύβου φάσης, είναι να εκτιμηθεί ο θόρυβος φάσης σε συστάδα N δειγμάτων, σύμφωνα με τη σχέση

$$\Delta\hat{\phi}_n^{k-th} = \frac{1}{4}\arg\left\{\sum_{n=(k-1)N+1}^{kN}\tilde{i}^4[n]\right\} \tag{46}$$

για το *k*-στό block. Η μέθοδος αυτή απαιτεί αναδίπλωση μεταξύ των εκτιμήσεων διαδοχικών συστάδων και συνεπώς είναι απλούστερη. Το δομικό διάγραμμα του αλγορίθμου αυτού φαίνεται στο Σχ. 11 (αλγόριθμος block-phase). Τα συγκριτικά αποτελέσματα των αλγορίθμων δίνονται στην Ενότητα IV.

4. Ενδιάμεση συχνότητα

Οι δέκτες διαφοροποίησης φάσης είναι ορθογώνιοι δέκτες, δηλαδή παράγουν στην έξοδο τις δυο ορθογώνιες συνιστώσες ανάλογες του σήματος στην είσοδο. Μαθηματικά, είναι ισοδύναμοι με το να πολλαπλασιαστεί το εισερχόμενο σήμα με ένα φάσορα, του οποίου η συχνότητα είναι αυτή του τοπικού ταλαντωτή. Σε περίπτωση που η ενδιάμεση συχνότητα είναι μηδενική, το μιγαδικό σήμα στην έξοδο του δέκτη περιέχει μόνο όρους θορύβου και παραμόρφωσης. Εάν η ενδιάμεση συχνότητα είναι μη μηδενική, τότε το μιγαδικό σήμα περιστρέφεται στο μιγαδικό επίπεδο δεξιόστροφα ή αριστερόστροφα, με σταθερό ρυθμό, ο οποίος εξαρτάται από την τιμή της ενδιάμεσης συχνότητας. Παρουσία ενδιάμεσης συχνότητας αργά ή γρήγορα τα μιγαδικά δείγματα θα βγουν από το σωστό τεταρτημόριο και θα προκληθεί σφάλμα.

Στις σύμφωνες οπτικές τηλεπικοινωνίες, σημασία έχει ο λόγος της ενδιάμεσης συχνότητας με τον ρυθμό συμβόλων f_{IF}/R_S, ή το γινόμενο της ενδιάμεσης συχνότητας με τον ρυθμό συμβόλων $f_{IF}T_S$. Το Σχ. 12 δείχνει την ποινή OSNR σε σχέση με το ιδανικό QPSK σύστημα με σύμφωνο δέκτη σε πιθανότητα σφάλματος BER = 10^{-3} συναρτήσει του γινομένου $f_{IF}T_S$, για τους δυο δέκτες του Σχ. 6. Ο διαφορικός δέκτης ανέχεται γινόμενα $f_{IF}T_S$ της τάξης του 0.02 με ποινή μικρότερη των 3 dB (που αντιστοιχεί σε ενδιάμεση συχνότητα 200 MHz στα 10 GBd). Ο σύγχρονος δέκτης παρουσιάζει ποινή 3 dB σε ένα εξαιρετικά μικρό γινόμενο $f_{IF}T_S$, της τάξης του 0.8×10^{-6} (που αντιστοιχεί σε ενδιάμεση συχνότητα 8 kHz στα 10 GBd).
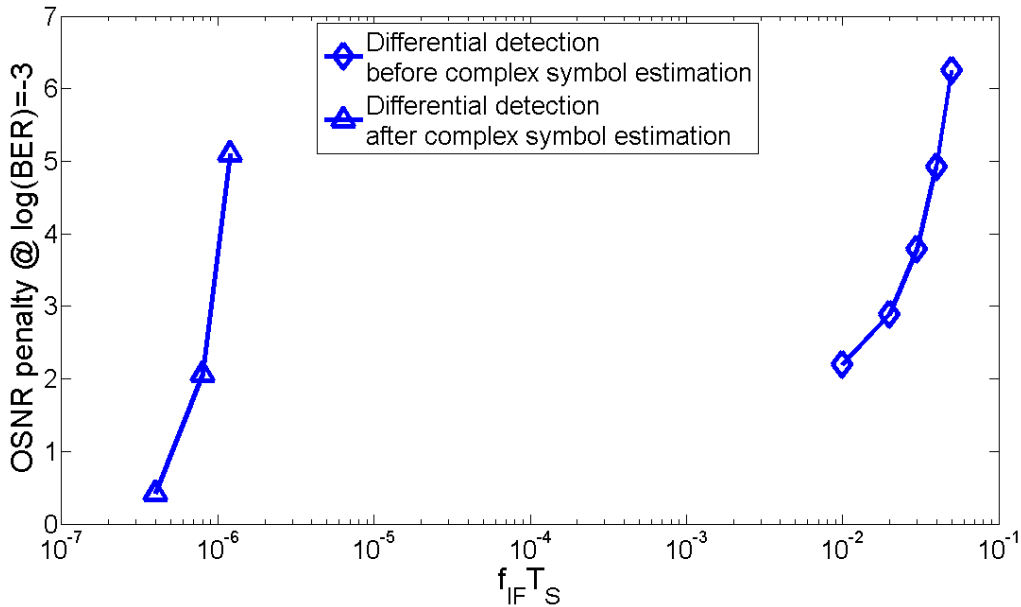
Σχ. 12 Ποινή OSNR σε σχέση με τον ιδανικό σύμφωνο δέκτη QPSK συναρτήσει του γινομένου $f_{IF}T_S$ για τον ψηφιακό σύγχρονο δέκτη (αριστερά), και για τον ψηφιακό διαφορικό δέκτη (δεξιά).

Ανάλογα με την τιμή του γινομένου $f_{IF}T_S$, τα οπτικά συστήματα κατατάσσονται σε τρεις κατηγορίες: i) ομόδυνα ($f_{IF}=0$) ii) ετερόδυνα ($f_{IF}\geq R_S$), και iii) ενδόδυνα ($0<f_{IF}<R_S$). Στην περίπτωση των ετερόδυνων συστημάτων, η ενδιάμεση συχνότητα πρέπει να αφαιρεθεί πριν από οποιαδήποτε λειτουργία του

δέκτη [171]. Τα πρακτικά σύμφωνα οπτικά συστήματα αναμένεται να έχουν κάποιον μηχανισμό ελέγχου της ενδιάμεσης συχνότητας ώστε να ισχύει $f_{IF} \cong 0$ οπότε θα υπάρχει μόνο μια μικρή εναπομείνασα ενδιάμεση συχνότητα εξαιτίας μη ιδανικής εκτίμησης, οπότε θα κατατάσσονται στην ενδόδυνη κατηγορία [172], [173]. Για τους ενδόδυνους δέκτες, η εκτίμηση της εναπομείνασας ενδιάμεσης συχνότητας μπορεί να μεταφερθεί μέσα στον ψηφιακό δέκτη και μπορεί να γίνει και με εμπρόσθια τροφοδότηση. Υπάρχει μια μεγάλη γκάμα αλγορίθμων για την εκτίμηση της ενδιάμεσης συχνότητας, δανεισμένη από τις κλασσικές ψηφιακές επικοινωνίες [171], [174]. Προσφάτως, νέοι αλγόριθμοι έχουν προταθεί, ειδικά για τις ανάγκες των οπτικών τηλεπικοινωνιών [175]–[179].

Στα πλαίσια αυτής της διατριβής υλοποιήθηκαν τρεις αλγόριθμοι εκτίμησης και αφαίρεσης της ενδιάμεσης συχνότητας ο αλγόριθμος phase increment [171], [175], και οι αλγόριθμοι Tretter και Kay [174].

Η έκφραση για το μιγαδικό δείγμα απουσία ενδιάμεσης συχνότητας στην έξοδο του αποπολυπλέκτη, ιδανικά, δίνεται από την έκφραση

$$\tilde{i}_{X,Y}\left[n\right] = Ie^{j\phi_{k,X,Y}\left[n\right]}e^{j\Delta\phi_n + j2\pi f_{IF}nT_S} + p_{X,Y}\left[n\right] \tag{47}$$

i. Αλγόριθμος Phase Increment

Ο αλγόριθμος phase increment βασίζεται στο γεγονός ότι η διαφορά φάσης μεταξύ δυο διαδοχικών δειγμάτων της (47), εάν αφαιρεθεί η φάση διαμόρφωσης, είναι μια σταθερά η οποία εξαρτάται από την ενδιάμεση συχνότητα. Ο θόρυβος φάσης δημιουργεί μια αβεβαιότητα για την πραγματική τιμή αυτής της σταθεράς. Παρ' όλα αυτά, ο θόρυβος φάσης έχει μηδενική μέση τιμή, οπότε εάν υπολογιστεί η διαφορά φάσης μεταξύ διαδοχικών δειγμάτων, για έναν μεγάλο αριθμό δειγμάτων, τότε μπορεί να υπολογιστεί η ενδιάμεση συχνότητα ορθά. Αρχικά, δείγματα διαδοχικών χρονικών στιγμών πολλαπλασιάζονται το ένα με το μιγαδικό συζυγές του άλλου, και το αποτέλεσμα υψώνεται στην τετάρτη για να αφαιρεθεί η φάση διαμόρφωσης

$$\frac{1}{4}\arg\left\{\left(\tilde{i}\left[n\right]\tilde{i}^*\left[n-1\right]\right)^4\right\} \cong 2\pi f_{IF}T_S + \Delta\phi_n\left[n\right] - \Delta\phi_n\left[n-1\right] \tag{48}$$

Προσθέτοντας τις διαφορές φάσης σε ένα μεγάλο μπλοκ L συμβόλων, λαμβάνεται απευθείας η εκτίμηση της ενδιάμεσης συχνότητας

$$\hat{f}_{IF} \cong \frac{1}{2\pi T_S}\frac{1}{4}\arg\left\{\sum_{n=0}^{L-1}\left(\tilde{i}\left[n\right]\tilde{i}^*\left[n-1\right]\right)^4\right\} \tag{49}$$

Όσο μεγαλύτερο το μπλοκ, τόσο καλύτερη η εκτίμηση. Το Σχ. 13 δείχνει το δομικό διάγραμμα του αλγορίθμου.
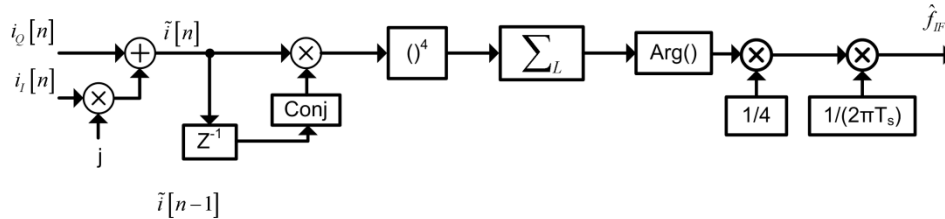
Σχ. 13 Δομικό διάγραμμα του αλγορίθμου phase increment για την εκτίμηση της ενδιάμεσης συχνότητας.

ii. Αλγόριθμοι Tretter και Kay

Οι αλγόριθμοι εκτίμησης της ενδιάμεσης συχνότητας που προτάθηκαν από τους Tretter και Kay είναι εκτιμητές ελαχίστων τετραγώνων [174]. Η ουσία των αλγορίθμων είναι να ακολουθούν την διαρκώς αυξανόμενη (ή μειούμενη) τροχιά της (αναδιπλωμένης) φάσης συναρτήσει του χρόνου, και να εκτιμήσουν την κλίση της καμπύλης, η οποία συνδέεται άμεσα με την ενδιάμεση συχνότητα. Εάν αφαιρεθεί η φάση διαμόρφωσης από το μιγαδικό δείγμα εισόδου με ύψωση στην τετάρτη, λαμβάνουμε

$$\frac{1}{4}\arg\left\{\tilde{i}^4[n]\right\} \cong 2\pi f_{IF}nT_S + \Delta\phi_n[n] \tag{50}$$

Τότε η (αναδιπλωμένη) φάση που προκύπτει μεγαλώνει ή μικραίνει μονοτονικά ως μια ευθεία γραμμή με θορυβώδη δείγματα, λόγω του θορύβου φάσης. Η φάση που προκύπτει από διαδοχικά δείγματα της (50) πρέπει να αναδιπλωθεί. Για να επιτευχθεί η εκτίμηση ελαχίστων τετραγώνων σε ένα μπλοκ δεδομένων μεγέθους L, χρησιμοποιούνται διορθωτικοί συντελεστές. Για τον αλγόριθμο του Tretter, η εκτίμηση και της απόκλισης ενδιάμεσης συχνότητας δίνεται από τη σχέση

$$\hat{f}_{IF} = \frac{1}{2\pi T_S}\frac{1}{4}\sum_{n=0}^{L-1} w_n^{(T)} \arg^{unwrap}\left\{\tilde{i}^4[n]\right\} \tag{51}$$

όπου χρησιμοποιήσαμε τους συντελεστές

$$w_k^{(T)} = \frac{6(2k-L+1)}{L(L^2-1)}, 0 \le k \le L-1 \tag{52}$$

Ο αλγόριθμος του Kay είναι μαθηματικά ισοδύναμος με τον αλγόριθμο του Tretter [174], αλλά αποφεύγει την αναδίπλωση της φάσης, οπότε είναι και απλούστερος. Για τον αλγόριθμο του Kay, η εκτίμηση της απόκλισης ενδιάμεσης συχνότητας δίνεται από τη σχέση

$$\hat{f}_{IF} = \frac{1}{2\pi T_S}\frac{1}{4}\sum_{n=0}^{L-1} w_n^{(T)} \arg\left\{\left(\tilde{i}[n]\tilde{i}^*[n-1]\right)^4\right\} \tag{53}$$

όπου χρησιμοποιήσαμε τους συντελεστές

$$w_k^{(T)} = \frac{6k(L-k)}{L(L^2-1)}, 0 \le k \le L-1 \tag{54}$$

Η αφαίρεση της ενδιάμεσης συχνότητας πραγματοποιείται με πολλαπλασιασμό των μιγαδικών δειγμάτων με ένα φάσορα του οποίου η περιστροφή ακολουθεί την αντίθετη φορά κίνησης από αυτή που επιβάλει η ενδιάμεση συχνότητα, και του οποίου η φάση μεταβάλλεται με τον ίδιο ρυθμό

$$i = e^{-i2\pi f_{IF}nT_S} \tag{55}$$

Μετά την αφαίρεση της ενδιάμεσης συχνότητας τα μιγαδικά δείγματα έχουν την εξής μορφή

$$\tilde{i}_{X,Y}[n] = Ie^{j\phi_{k,X,Y}[n]}e^{j\Delta\phi_n + j2\pi f_d nT_S} + c_{X,Y}[n] \tag{56}$$

όπου $f_d = f_{IF} - \hat{f}_{IF}$ είναι η υπολειπόμενη ενδιάμεση συχνότητα και $c[n]$ είναι προσθετικός θόρυβος.

5. Ανισοσταθμία ορθογωνιότητας

Η γενική μορφή των φωτορευμάτων στην έξοδο του δέκτη διαφοροποίησης φάσης δίνεται από τη σχέση (11). Γενικά τα φωτορεύματα έχουν διαφορετικό πλάτος ($I_{ip} \neq I_{qp}$) και δεν έχουν τη σωστή φάση ($\varepsilon \neq \delta \neq 0°$). Αυτές οι αποκλίσεις από την ιδανική περίπτωση, ονομάζονται ανισοσταθμία πλάτους και φάσης, αντίστοιχα και το φαινόμενο ονομάζεται ανισοσταθμία ορθογωνιότητας (quadrature imbalance – QI ή I/Q mismatch) [169], [170], [180].

Η ανισοσταθμία ορθογωνιότητας αλλάζει τη μορφή των μιγαδικών δειγμάτων, προσθέτοντας έναν ανεπιθύμητο όρο, ο οποίος επηρεάζει και τη λειτουργία όλων των υπόλοιπων αλγορίθμων του ψηφιακού δέκτη. Λαμβάνοντας υπ' όψιν τις μη ιδανικές μορφές των φωτορευμάτων σε μια απλοϊκή μορφή, γράφουμε

$$i_I(t) = I_I + I_{ip} \cos\left[\varphi(t) + \varepsilon\right]$$
$$i_Q(t) = I_Q + I_{qp} \sin\left[\varphi(t) - \delta\right] \tag{57}$$

όπου $\varphi(t)$ είναι ο κοινός όρος φάσης που εμπεριέχει τη φάση λόγω διαμόρφωσης, την ενδιάμεση συχνότητα και το θόρυβο φάσης. Από τις παραπάνω, προκύπτει το εξής μιγαδικό φωτόρευμα

$$\tilde{i}(t) = \left(I_I + jI_Q\right) + I_{ip}\left[K_1 e^{j\varphi(t)} + K_2 e^{-j\varphi(t)}\right] \tag{58}$$

όπου

$$K_1 = \frac{1}{2}e^{j\varepsilon}\left[1 + \left(I_{qp}/I_{ip}\right)e^{-j(\varepsilon+\delta)}\right]$$
$$K_2 = \frac{1}{2}e^{-j\varepsilon}\left[1 - \left(I_{qp}/I_{ip}\right)e^{j(\varepsilon+\delta)}\right] \tag{59}$$

Το Σχ. 14 παρουσιάζει τυπικά διαγράμματα οφθαλμού και τους αντίστοιχους αστερισμούς για τα φωτορεύματα στην έξοδο ενός μη ιδανικού δέκτη διαφοροποίησης φάσης, απουσία θορύβου και ενδιάμεσης συχνότητας, στην ιδανική περίπτωση (Σχ. 14α), παρουσία ανισοσταθμίας πλάτους (Σχ. 14β), και παρουσία ανισοσταθμίας φάσης (Σχ. 14γ).

Παρουσία ενδιάμεσης συχνότητας, οι αστερισμοί περιστρέφονται και σχηματίζουν ελλείψεις. Ειδικά για συστήματα με πολυπλεξία κατά πόλωση, οι αστερισμοί αποτελούνται από μέχρι τέσσερις ομόκεντρες ελλείψεις, όπως φαίνεται στο Σχ. 15.

Η ανισοσταθμία ορθογωνιότητας επηρεάζει την απόδοση του συστήματος εάν δεν ισοσταθμιστεί με κάποιον τρόπο. Στα πλαίσια της διατριβής, έγινε ενδελεχής μελέτη της επίδρασης διαφόρων μορφών ανισοσταθμίας στην απόδοση συστημάτων QPSK χωρίς πολυπλεξία πόλωσης. Χρησιμοποιήθηκε το μοντέλο ενός οπτικού υβριδίου 90° 2×4 και αναλύθηκε η επίπτωση των μη ιδανικών παραμέτρων του στην πιθανότητα σφάλματος του συστήματος, βάση μιας ημιαναλυτικής μεθόδου υπολογισμού της πιθανότητας σφάλματος. Μελετήθηκε η ανισοσταθμία φάσης που προκαλείται από τους μη ιδανικούς ολισθητές φάσης, των οποίων οι φάσεις ολίσθησης είναι ιδανικά $\varepsilon=0$ και $90°+\delta=90°$, σε συνδυασμό με μη ιδανικούς κατευθυντικούς συζεύκτες στην είσοδο και στην έξοδο του οπτικού υβριδίου, των οποίων οι συντελεστές σύζευξης είναι α_1, α_2, α_3, και α_4 (ιδανικά έχουν τιμή 0.5), και σε συνδυασμό με ανόμοιες αποκρισιμότητες στις φωτοδιόδους R_1, R_2, R_3, and R_4. Το Σχ. 16 δείχνει την ποινή OSNR για πιθανότητα σφάλματος $P_e=10^{-9}$ για διάφορους συνδυασμούς. Όπως φαίνεται από την (59), η ανισοσταθμία φάσης εξαρτάται από το άθροισμα των αποκλίσεων φάσης $\theta = \varepsilon+\delta$. Έτσι, για κάθε τιμή ανισοσταθμίας φάσης που φαίνεται στο σχήμα χρησιμοποιήθηκαν , είκοσι συνδυασμοί γωνιών ε και δ. Για να περιγραφεί η μη ιδανικότητα των αποκρισιμοτήτων των φωτοδιόδων, χρησιμοποιήθηκε ο λόγος των αποκρισιμοτήτων των φωτοδιόδων.

Από το Σχ. 16 φαίνεται ότι η ποινή είναι μεγαλύτερη από 3 dB για ένα μεγάλο αριθμό περιπτώσεων και ακόμα και για μικρές αποκλίσεις από το ιδανικό. Η ανισοσταθμία φάσης είναι η πιο σημαντική μη ιδανικότητα. Από την ανάλυση της επίδρασης των κατευθυντικών συζευκτών, φαίνεται ότι η απόδοση

του συστήματος εξαρτάται περισσότερο από τους κατευθυντικούς συζεύκτες στην έξοδο του υβριδίου, παρά στην είσοδο.
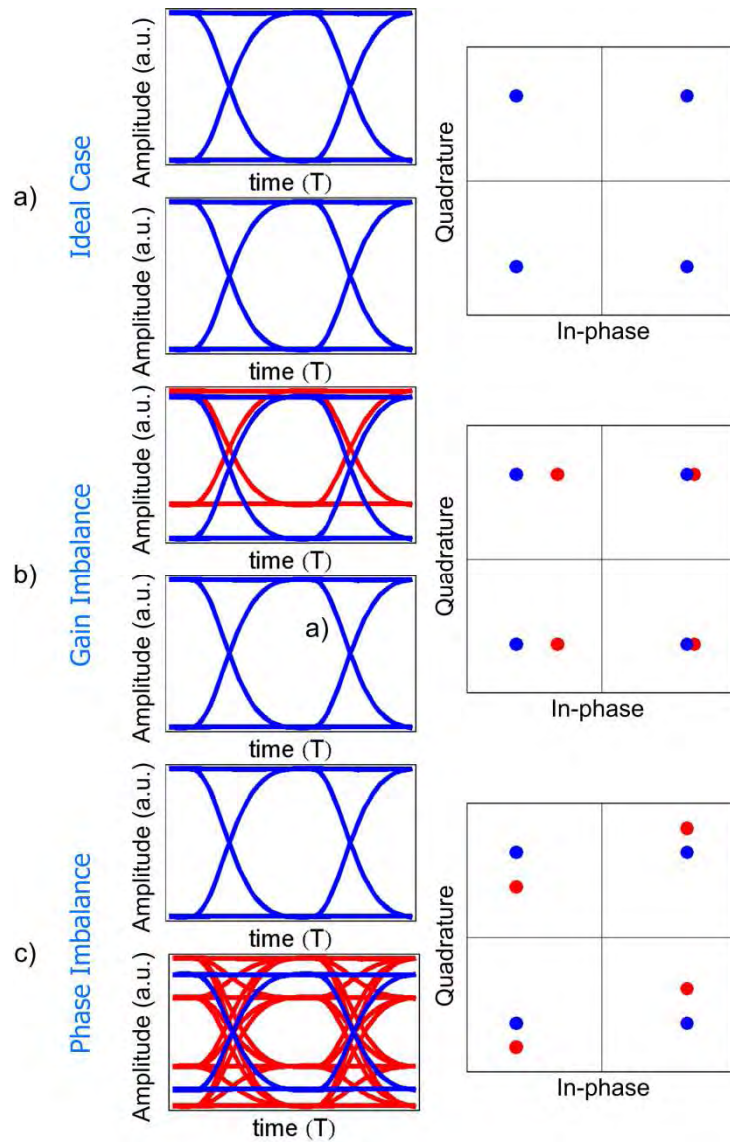
Σχ. 14 Διαγράμματα οφθαλμού και αστερισμοί για διάφορους τύπους ανισοσταθμίας ορθογωνιότητας. α) Ιδανικό σύστημα, β) Ανισοσταθμία πλάτους (I_{ip}=-0.4 I_{qp}), γ) Ανισοσταθμία φάσης (δ=20°, ε=0°).
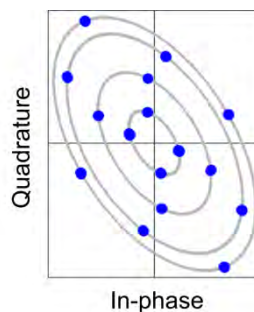
Σχ. 15 Αστερισμός σημείων στην έξοδο ενός μη ιδανικού δέκτη διαφοροποίησης φάσης, στην περίπτωση ενός συστήματος QPSK με πολυπλεξία κατά πόλωση, παρουσία ανισοσταθμίας πλάτους (I_{ip}=-0.2 I_{qp}), ανισοσταθμία φάσης (δ=30°, ε=0°) και παρουσία ενδιάμεσης συχνότητας.
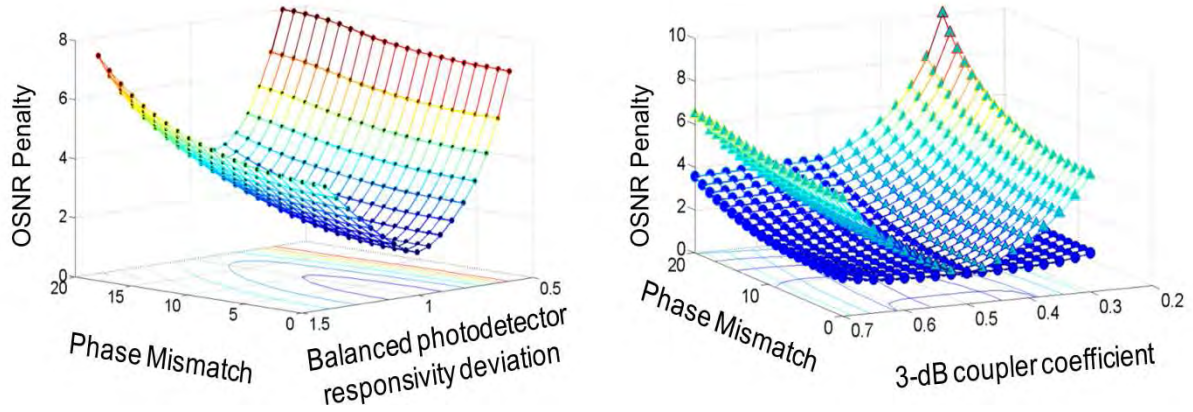
Σχ. 16 Ποινή OSNR για πιθανότητα σφάλματος $P_e=10^{-9}$ για διάφορους συνδυασμούς των παραμέτρων του υβριδίου. (α) Συνδυασμός ανισοσταθμίας φάσης και μη ιδανικών φωτοδιόδων, (β) Συνδυασμός ανισοσταθμίας φάσης και μη ιδανικών κατευθυντικών συζευκτών (Κυκλίσκοι: κατευθυντικοί συζεύκτες εισόδου, τρίγωνα: κατευθυντικοί συζεύκτες εξόδου).

Αρκετοί αλγόριθμοι εκτίμησης και διόρθωσης της ανισοσταθμίας αναπτύχθηκαν ειδικά για τις ανάγκες των οπτικών τηλεπικοινωνιών με ψηφιακούς σύμφωνους δέκτες. Ο πρώτος εξ αυτών βασίστηκε στο χαρακτηριστικό ελλειπτικό σχήμα του αστερισμού και προτάθηκε στην [129], ενώ χρησιμοποιήθηκε για την ανάλυση πειραματικών δεδομένων στη δημοσίευση [181], και αναλύθηκε διεξοδικότερα στην [182]. Στη δημοσίευση [183], προτάθηκε μια μέθοδος ορθογωνιοποίησης τύπου Gram-Schmidt [141]. Μια απλούστερη μέθοδος προτάθηκε στην [184]. Τέλος, στις δημοσιεύσεις [185], [186], προτάθηκε ένας προσαρμοστικός αλγόριθμος βασιζόμενος στο κριτήριο CMA.

i. Εκτίμηση ελλειπτικού αστερισμού

Η (57) ξαναγράφεται σε διακριτό χρόνο ως

$$i_I[n] = I_I + I_{ip}\cos\big(\omega[n]\big)$$
$$i_Q[n] = I_Q + I_{qp}\sin\big(\omega[n] + \theta\big)$$

(60)

όπου $\omega[n]=\varphi[n]+\varepsilon$ και $\theta = \varepsilon+\delta$. Το ζεύγος των παραμετρικών εξισώσεων της (60), αντιστοιχεί σε μια έλλειψη εάν αναπαρασταθεί στο μιγαδικό επίπεδο [187]. Το ίδιο ισχύει και στην περίπτωση σημάτων πολυπλεγμένων κατά πόλωση, μόνο που προκύπτουν πολλές ομόκεντρες ελλείψεις.

Η ανισοσταθμία πλάτους και φάσης σχετίζονται με τις παραμέτρους της έλλειψης. Πιο συγκεκριμένα, το κέντρο της έλλειψης σχετίζεται με τις συνεχείς συνιστώσες των φωτορευμάτων, τα μέγιστα της έλλειψης σχετίζονται με την ανισοσταθμία πλάτους (η οποία για ευκολία εκφράζεται και ως $\lambda=I_{ip}/I_{qp}$), και η γωνία στροφής της έλλειψης σχετίζεται με την ανισοσταθμία φάσης θ. Εκτιμώντας τις παραμέτρους της έλλειψης, προκύπτουν εκτιμήσεις για τις παραμέτρους ανισοσταθμίας των φωτορευμάτων I_I, I_Q, λ και θ [188]–[191].

Έχοντας αποκτήσει τις εκτιμήσεις των παραμέτρων της ανισοσταθμίας, η ανισοσταθμία μπορεί να αναιρεθεί χρησιμοποιώντας μια μέθοδο ορθογωνιοποίησης που μετατρέπει μια έλλειψη σε κύκλο [192]. Ξεκινώντας από το διάνυσμα δειγμάτων στην έξοδο του οπτικού υβριδίου, $\mathbf{I}[n]=\begin{bmatrix} i_I[n] & i_Q[n] \end{bmatrix}^T$, αρχικά αφαιρούνται οι DC συνιστώσες, οπότε προκύπτει ένα νέο διάνυσμα, το $\mathbf{I}_{DC-free}[n]$, ως

$$\mathbf{I}_{DC-free}[n] = \begin{bmatrix} i_I[n] - \hat{I}_I \\ i_Q[n] - \hat{I}_Q \end{bmatrix}$$

(61)

Κατόπιν, το διάνυσμα αυτό υφίσταται μια επεξεργασία από (πολλαπλασιάζεται με έναν πίνακα ορθογωνιοποίησης)

28

$$\mathbf{I}_Q\left[n\right]=\begin{pmatrix} E & 0 \\ P & 1 \end{pmatrix}\cdot\mathbf{I}_{DC-free}\left[n\right] \tag{62}$$

όπου

$$E=\hat{\lambda}^{-1}\cos\left(\hat{\theta}\right)$$
$$P=-\hat{\lambda}^{-1}\sin\left(\hat{\theta}\right) \tag{63}$$

ii. Προσαρμοστικός αλγόριθμος CMA με περιορισμούς

Εάν αφαιρεθούν οι συνεχείς συνιστώσες από τα φωτορεύματα στην (57), για παράδειγμα με χρήση κάποιου πυκνωτή, η (57) δύναται να επαναδιατυπωθεί σε μορφή πίνακα ως,

$$\mathbf{I}=\mathbf{M}\mathbf{I}_{\mathbf{Q}} \tag{64}$$

όπου $\mathbf{I}=\begin{bmatrix} i_I\left(t\right) & i_Q\left(t\right) \end{bmatrix}^T$ είναι το διάνυσμα των ληφθέντων φωτορευμάτων, $\mathbf{I}_{\mathbf{Q}}=\begin{bmatrix} \cos\varphi\left(t\right) & \sin\varphi\left(t\right) \end{bmatrix}^T$ είναι το επιθυμητό διάνυσμα με τα ορθογώνια φωτορεύματα και $\mathbf{M}$ είναι ένας πραγματικός πίνακας 2×2 ο οποίος περιγράφει την επίδραση της ανισοσταθμίας, και ο οποίος είναι

$$\mathbf{M}=\begin{pmatrix} I_{ip}\cos\varepsilon & -I_{ip}\sin\varepsilon \\ -I_{qp}\sin\delta & I_{qp}\cos\delta \end{pmatrix} \tag{65}$$

Συνεπώς, η επίδραση της ανισοσταθμίας ορθογωνιότητας θα αναιρεθεί, εάν βρεθεί μια εκτίμηση του αντίστροφου πίνακα $\hat{\mathbf{M}}^{-1}$, του οποίου η αναλυτική μορφή είναι

$$\mathbf{M}^{-1}=\sec\theta\begin{pmatrix} I_{ip}^{-1}\cos\delta & I_{qp}^{-1}\sin\varepsilon \\ I_{ip}^{-1}\sin\delta & I_{qp}^{-1}\cos\varepsilon \end{pmatrix} \tag{66}$$

Αγνοώντας τον πολλαπλασιαστικό συντελεστή $\sec(\theta)$, ορίζουμε τον πίνακα εξίσωσης ως

$$\mathbf{W}\left(I_{ip},I_{qp},\varepsilon,\delta\right)=\begin{pmatrix} I_{ip}^{-1}\cos\delta & I_{qp}^{-1}\sin\varepsilon \\ I_{ip}^{-1}\sin\delta & I_{qp}^{-1}\cos\varepsilon \end{pmatrix} \tag{67}$$

Το κριτήριο CMA χρησιμοποιείται για να εκτιμηθούν οι παράμετροι I_{ip}, I_{qp}, ε, δ, ελαχιστοποιώντας τη στιγμιαία συνάρτηση κόστους $\xi\left[n\right]=e^2\left[n\right]$, όπου $e\left[n\right]=\hat{\mathbf{I}}_{\mathbf{Q}}^{\mathbf{T}}\left[n\right]\cdot\hat{\mathbf{I}}_{\mathbf{Q}}\left[n\right]-R$ είναι το σφάλμα, R η ισχύς σήματος και θορύβου, και $\hat{\mathbf{I}}_{\mathbf{Q}}\left[n\right]$ είναι η εκτίμηση του επιθυμητού διανύσματος, που προκύπτει ως

$$\hat{\mathbf{I}}_{\mathbf{Q}}\left[n\right]=\mathbf{W}\left(\hat{I}_{ip}\left[n\right],\hat{I}_{qp}\left[n\right],\hat{\varepsilon}\left[n\right],\hat{\delta}\left[n\right]\right)\mathbf{I}\left[n\right] \tag{68}$$

Για να προκύψουν οι εκτιμήσεις $\hat{I}_{ip}\left[n\right],\hat{I}_{qp}\left[n\right],\hat{\varepsilon}\left[n\right],\hat{\delta}\left[n\right]$, ορίζουμε ένα διάνυσμα παραμέτρων $\mathbf{Z}\left[n\right]=\begin{bmatrix} \hat{I}_{ip}\left[n\right] & \hat{I}_{qp}\left[n\right] & \hat{\varepsilon}\left[n\right] & \hat{\delta}\left[n\right] \end{bmatrix}^T$, του οποίου οι τιμές ανανεώνονται χρησιμοποιώντας την σχέση

$$\mathbf{Z}\left[n+1\right]=\mathbf{Z}\left[n\right]-\mu\nabla\xi\left[n\right] \tag{69}$$

όπου

$$\nabla\xi\left[n\right]=\begin{bmatrix} \dfrac{\partial\xi\left[n\right]}{\partial I_{ip}} & \dfrac{\partial\xi\left[n\right]}{\partial I_{qp}} & \dfrac{\partial\xi\left[n\right]}{\partial\varepsilon} & \dfrac{\partial\xi\left[n\right]}{\partial\delta} \end{bmatrix}^T \tag{70}$$

και μ είναι το βήμα. Οι ανεξάρτητες μεταβλητές του συστήματος μπορούν να περιοριστούν χρησιμοποιώντας απλουστεύσεις, όπως για παράδειγμα θέτοντας ε ή $\delta=0°$, ή χρησιμοποιώντας λ αντί για δυο παραμέτρους I_{ip} και I_{qp}. Παρ' όλα αυτά, οι απλουστεύσεις οδηγούν σε ελαφρώς χειρότερες εκτιμήσεις.

iii. Ορθογωνιοποίηση Gram-Schmidt

Στη δημοσίευση [183], χρησιμοποιείται μια μέθοδος διόρθωσης της ανισοσταθμίας η οποία αντιμετωπίζει το πρόβλημα με πίνακες, όπως και ο προσαρμοστικός αλγόριθμος που περιγράφηκε στην προηγούμενη ενότητα. Η διαφορά έγκειται στη μέθοδο εκτίμησης των παραμέτρων του πίνακα. Η συνιστώσα του φωτορεύματος σε φάση κανονικοποιείται αρχικά σε μοναδιαία ισχύ, σχηματίζοντας ένα νέο διάνυσμα φωτορευμάτων

$$\mathbf{I}^{(0)}[n] = \begin{bmatrix} i_I[n]/\sqrt{P_I} \\ i_Q[n] \end{bmatrix} \tag{71}$$

όπου $P_I = E\{i_I^2[n]\}$. Η προβολή της κανονικοποιημένος συνιστώσας σε-φάση αφαιρείται από την ορθογώνια συνιστώσα, πολλαπλασιάζοντας την (71) με τον πίνακα

$$\mathbf{W} = \begin{bmatrix} 1 & 0 \\ -\rho/\sqrt{P_I} & 1 \end{bmatrix} \tag{72}$$

πράξη η οποία δίνει ένα νέο διάνυσμα

$$\mathbf{I}^{(1)}[n] = \begin{bmatrix} i_I[n]/\sqrt{P_I} \\ i_Q[n] - i_I[n]/P_I \end{bmatrix} = \begin{bmatrix} i_I'[n] \\ i_Q'[n] \end{bmatrix} \tag{73}$$

Στις παραπάνω σχέσεις, $\rho = E\{i_I[n]i_Q[n]\}$ είναι η σταθερά ετεροσυσχέτισης. Τέλος, η ορθογώνια συνιστώσα $i_Q'[n]$ κανονικοποιείται σε μοναδιαία ισχύ, και το επιθυμητό διάνυσμα ορθογώνιων φωτορευμάτων γράφεται ως

$$\mathbf{I}_Q[n] = \begin{bmatrix} i_I'[n] \\ i_Q'[n]/\sqrt{P_{Q'}} \end{bmatrix} \tag{74}$$

όπου $P_{Q'} = E\{i_Q'^2[n]\}$.

IV.   Ανάλυση του συστήματος μέσω προσομοίωσης

Σε αυτήν την ενότητα αναλύουμε σε βάθος διάφορες πτυχές των οπτικών συστημάτων QPSK με σύμφωνη φώραση και πολυπλεξία κατά πόλωση.

1. Απόδοση αλγορίθμων αποπολύπλεξης της πόλωσης παρουσία θορύβου αυθόρμητης εκπομπής

Στην ενότητα αυτή, συγκρίνουμε την απόδοση των αλγορίθμων αποπολύπλεξης της πόλωσης. Σε όλες τις εξομοιώσεις, ο ρυθμός συμβόλων είναι 10 GBd και ο θόρυβος μετράται σε εύρος ζώνης 0.125 R_S.

Το Σχ. 17α απεικονίζει ένα τυπικό διάγραμμα οφθαλμού στην έξοδο του δέκτη διαφοροποίησης φάσης για ένα σύστημα QPSK χωρίς πολυπλεξία κατά πόλωση, με 13 dB OSNR. Το Σχ. 17β απεικονίζει τον αντίστοιχο αστερισμό. Ο προσθετικός θόρυβος αυξάνει το μέγεθος των σημείων του αστερισμού, μετατρέποντάς τα σε δίσκους. Εάν η διακύμανση του θορύβου είναι μεγάλη, κάποιο θορυβώδες σημείο θα περάσει το κατώφλι και θα προκαλέσει σφάλμα.
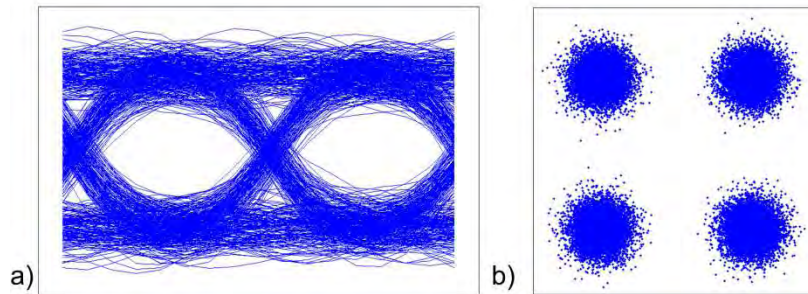
Σχ. 17 Διάγραμμα οφθαλμού και ο αντίστοιχος αστερισμός για τα ληφθέντα φωτορεύματα στην έξοδο του δέκτη διαφοροποίησης φάσης, παρουσία αποκλειστικά θορύβου αυθόρμητης εκπομπής.

Το Σχ. 18 δείχνει τον μετρημένο ρυθμό σφαλμάτων συναρτήσει του λόγου σήματος προς θόρυβο ανά δυαδικό ψηφίο για τα δυο συστήματα που μελετήθηκαν στα πλαίσια του διδακτορικού, το διαφορικό δέκτη και το σύγχρονο δέκτη. Το ηλεκτρικό φίλτρο που χρησιμοποιήθηκε είναι ένα $4^{ης}$ τάξης Bessel με εύρος ζώνης 0.5 R_S. Ο διαφορικός δέκτης έχει μια ποινή περίπου 1.9 dB. Η ποινή των περίπου 1 dB μεταξύ του ιδανικού συστήματος και του ιδανικού σύμφωνου δέκτη οφείλεται στη χρήση πρακτικών μοντέλων οπτικών διατάξεων κατά την προσομοίωση.

Το Σχ. 19 απεικονίζει το απαιτούμενο OSNR για ρυθμό σφαλμάτων BER 10^{-3} συναρτήσει του εύρους ζώνης του ηλεκτρικού πεδίου, εκπεφρασμένου ως κλάσμα του ρυθμού συμβόλων, για ένα σύστημα QPSK με πολυπλεξία κατά πόλωση. Εντύπωση προκαλεί το γεγονός ότι για τόσο υψηλό BER, το ιδανικό εύρος ζώνης του ηλεκτρικού φίλτρου είναι περίπου 0.5 R_S.
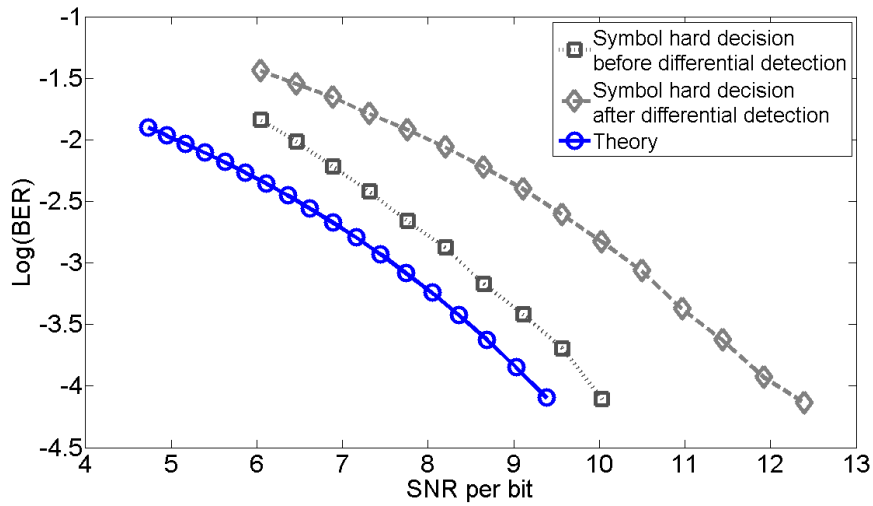
Σχ. 18 Μετρημένος ρυθμός σφαλμάτων συναρτήσει του λόγου σήματος προς θόρυβο ανά bit για προσθετικό θόρυβο, και για τους δυο δέκτες που χρησιμοποιήθηκαν (Σύγχρονος δέκτης και διαφορικός δεκτής). Για σύγκριση, παρατίθεται η θεωρητική απόδοση ιδανικού QPSK συστήματος με ιδανικό σύμφωνο δέκτη.
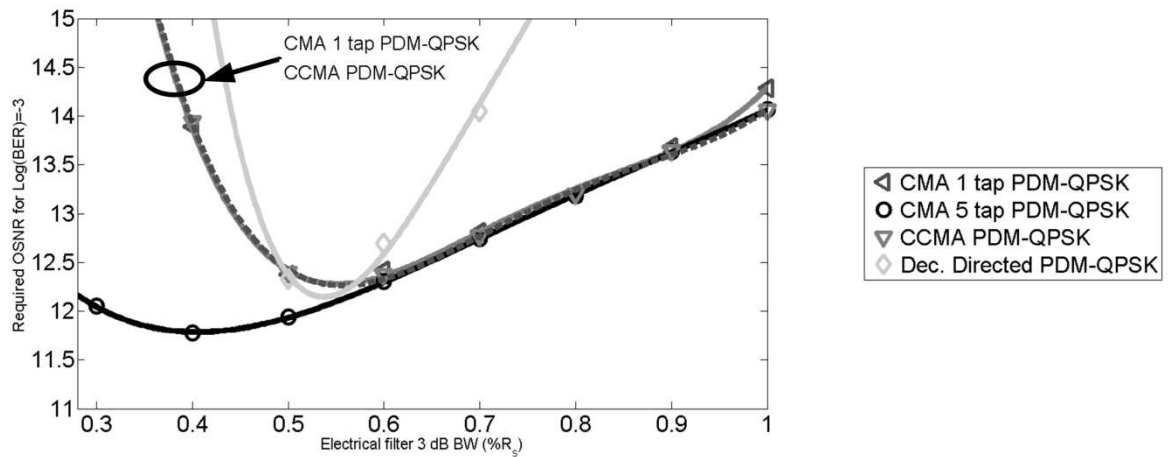
Σχ. 19 Απαιτούμενο OSNR για επίτευξη ρυθμού σφαλμάτων BER= 10^{-3} συναρτήσει του εύρους ζώνης του ηλεκτρικού φίλτρου για σύστημα QPSK με πολυπλεξία κατά πόλωση.

2. Απόδοση αλγορίθμων αποπολύπλεξης της πόλωσης παρουσία θορύβου αυθόρμητης εκπομπής και χρονικά μεταβαλλόμενης πόλωσης

Στην ενότητα αυτή, μελετάμε την απόδοση των διάφορων αλγορίθμων αποπολύπλεξης της πόλωσης παρουσία χρονικά μεταβαλλόμενης κατάστασης πόλωσης για ένα σύστημα QPSK με πολυπλεξία κατά πόλωση. Το κίνητρο πίσω από αυτή τη μελέτη είναι ότι πρόσφατα, προτάθηκε η χρήση QPSK με πολυπλεξία κατά πόλωση σε οπτικούς διακόπτες, όπου η κατάσταση πόλωσης αλλάζει γρήγορα, λόγω της διακοπτικής λειτουργίας των διατάξεων αυτών [193].

Χρησιμοποιήθηκε το μοντέλο της ίνας (16) μόνο που το αζιμούθιο $α$ και η ελλειπτικότητα $ε$ θεωρούνται χρονικά μεταβαλλόμενες. Δυο μοντέλα χρονικής μεταβλητότητας χρησιμοποιήθηκαν. Το πρώτο μοντέλο θεωρεί ότι η κατάσταση πόλωσης αλλάζει με βηματικό τρόπο, όπως θα συνέβαινε σε περίπτωση που αλλάζει κατάσταση ο διακόπτης. Με το μοντέλο αυτό έγινε προσπάθεια να συγκριθούν οι αλγόριθμοι με βάση την ταχύτητα σύγκλισης. Το σύστημα ξεκινάει από μια αρχική κατάσταση πόλωσης ($α$, $ε$=0) οπότε και ο αποπολυπλέκτης συγκλίνει σε μια μόνιμη κατάσταση λειτουργίας. Τότε, το αζιμούθιο $α$ και η ελλειπτικότητα $ε$ αλλάζουν με βηματικό και τυχαίο τρόπο, και ο ρυθμός σφαλμάτων υπολογίζεται από αυτή τη χρονική στιγμή και εντεύθεν. Το δεύτερο μοντέλο θεωρεί ότι η κατάσταση της πόλωσης αλλάζει συνεχώς με τυχαίο τρόπο. Με το μοντέλο αυτό έγινε προσπάθεια να συγκριθούν οι αλγόριθμοι σε περιβάλλον έντονων διαταραχών. Το σύστημα ξεκινάει από μια αρχική κατάσταση πόλωσης ($α$, $ε$=0) και κάθε χρονική στιγμή (κβάντο χρόνου στην προσομοίωση) προστίθεται μια μικρή γωνία με τυχαίο τρόπο, δηλαδή $α_{k+1}=α_k+δα$, και $ε_{k+1}=ε_k+δε$. Οι τυχαίες μεταβλητές $δα$, $δε$ ανήκουν στην κανονική κατανομή. Το Σχ. 20 απεικονίζει δυο παραδείγματα της κατάστασης πόλωσης για τα δυο μοντέλα. Στο Το Σχ. 20α απεικονίζονται 100 διαφορετικές τυχαίες βηματικές αλλαγές της πόλωσης, ενώ στο Σχ. 20β απεικονίζεται μια τυχαία διαδρομή για την περίπτωση χρονικά μεταβαλλόμενης κατάστασης πόλωσης.

Το Σχ. 21 απεικονίζει τον μετρημένο ρυθμό σφαλμάτων συναρτήσει του OSNR για ένα σύστημα με βηματικές αλλαγές στην κατάσταση πόλωσης. Χρησιμοποιήθηκε το βέλτιστο εύρος ζώνης ηλεκτρικού φίλτρου, ήτοι 0.5 R_S. Κάθε σημείο στην καμπύλη προκύπτει από τον μέσο ρυθμό σφαλμάτων μετά από 100 τυχαίες βηματικές αλλαγές της κατάστασης πόλωσης. Παρατηρούμε ότι όσο μεγαλώνει το OSNR, επέρχεται ένας κορεσμός στον ρυθμό σφαλμάτων, διότι ο ρυθμός σφαλμάτων εξαρτάται περισσότερο από τα σφάλματα κατά τη μετάβαση και σύγκλιση των αλγορίθμων περισσότερο από τον θόρυβο. Παρ' όλα αυτά ο αλγόριθμος με κριτήριο CMA με περιορισμούς έχει κορεσμό σε ρυθμό σφαλμάτων μιας τάξης μεγέθους μικρότερο από ότι οι άλλοι αλγόριθμοι, λόγω γρηγορότερης σύγκλισης.

Το Σχ. 22 απεικονίζει το απαιτούμενο OSNR για επίτευξη ρυθμού σφαλμάτων BER= 10^{-3} συναρτήσει της ταχύτητας αλλαγής της χρονικά μεταβαλλόμενης κατάστασης πόλωσης, για τους διαφόρους αλγορίθμους. Κάθε αλγόριθμος παρουσιάζει ένα κατώφλι πάνω από το οποίο δεν μπορεί να αντεπεξέλθει στις γρήγορες αλλαγές. Ξανά, ο αλγόριθμος με κριτήριο CMA με περιορισμούς έχει πολύ καλύτερη απόδοση. Κάθε σημείο στην καμπύλη προκύπτει από το μέσο απαιτούμενο OSNR για 100 τυχαίες μεταβολές.
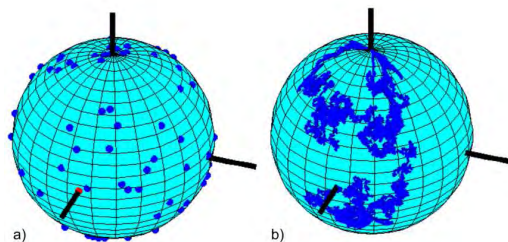
Σχ. 20 Τροχιά της κατάστασης πόλωσης πάνω σε μια σφαίρα Poincaré για δυο διαφορετικά χρονικά μεταβαλλόμενα μοντέλα. α) Βηματική αλλαγή της κατάστασης πόλωσης, κόκκινη κουκίδα: αρχική κατάσταση πόλωσης, μπλε κουκίδες: κατάσταση πόλωσης μετά από βηματική αλλαγή, β) Συνεχόμενος τυχαίος βηματισμός της κατάστασης πόλωσης.
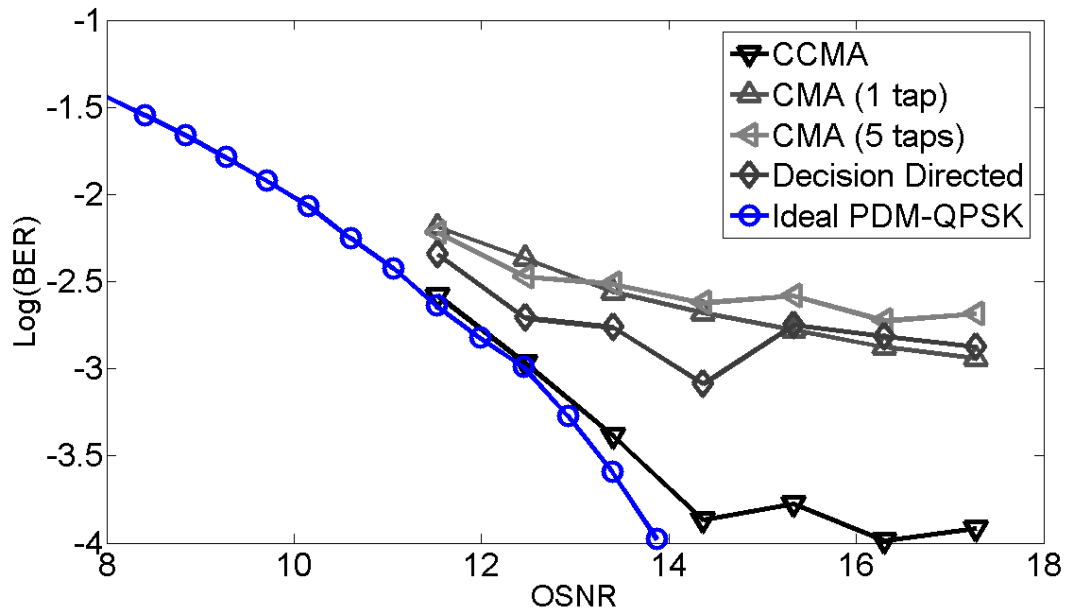
Σχ. 21 Μετρημένος ρυθμός σφαλμάτων συναρτήσει του OSNR για ένα σύστημα με βηματικές αλλαγές στην κατάσταση πόλωσης.
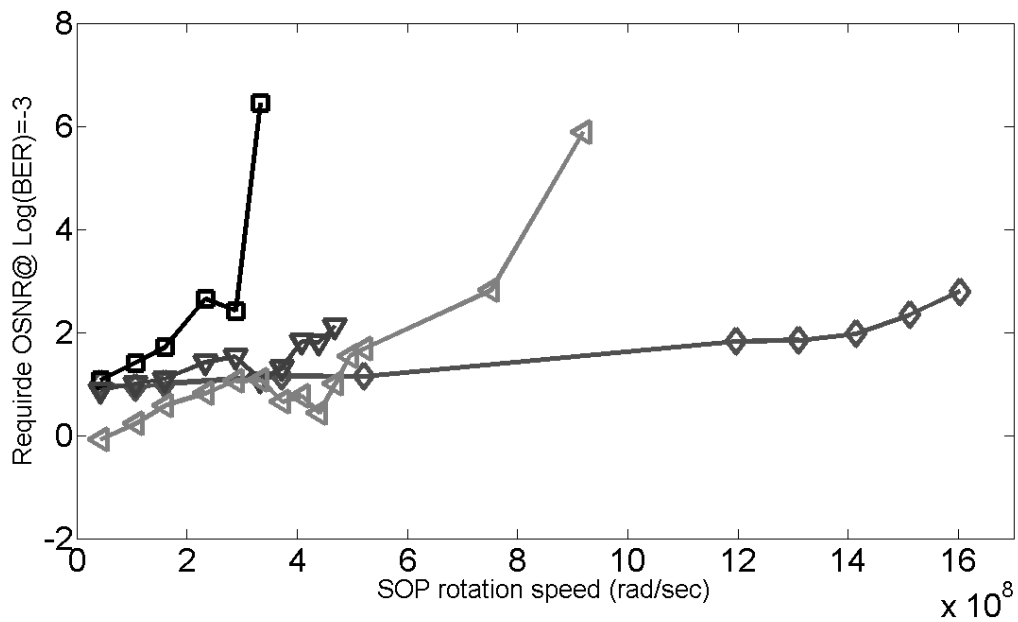
Σχ. 22 Απαιτούμενο OSNR για επίτευξη ρυθμού σφαλμάτων BER= 10^{-3} συναρτήσει της ταχύτητας αλλαγής της χρονικά μεταβαλλόμενης κατάστασης πόλωσης.

3. Αλγόριθμοι εκτίμησης και διόρθωσης του θορύβου φάσης

Στην ενότητα αυτή συγκρίνουμε του αλγορίθμους εκτίμησης και διόρθωσης του θορύβου φάσης. Η μελέτη πραγματοποιήθηκε σε σύστημα QPSK χωρίς πολυπλεξία κατά πόλωση, παρουσία θορύβου αυθόρμητης εκπομπής και θορύβου φάσης.

Το Σχ. 23 απεικονίζει την ποινή OSNR για ρυθμό σφαλμάτων 10^{-3} συναρτήσει του γινομένου $\Delta\nu T_S$ για διάφορες περιπτώσεις χρήσης για διάφορους αλγορίθμους ανατροφοδότησης της απόφασης. Το Σχ. 23α αντιστοιχεί στον σύγχρονο δέκτη, ενώ το Σχ. 23β αντιστοιχεί στον διαφορικό δέκτη. Παρατηρούμε ότι οι αλγόριθμοι ανατροφοδότησης της απόφασης δεν βελτιώνουν την απόδοση των συστημάτων με διαφορικό δέκτη, ενώ καθιστούν τους σύγχρονους δέκτες ελαφρά καλύτερους από τους διαφορικούς δέκτες, μόνο για μικρές τιμές του θορύβου φάσης.
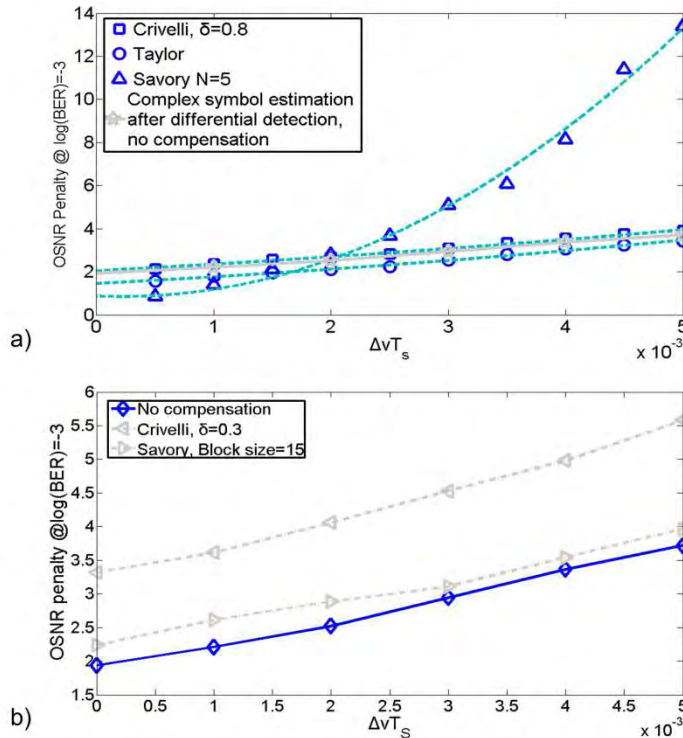
Σχ. 23 Ποινή OSNR για ρυθμό σφαλμάτων 10^{-3} συναρτήσει του γινομένου $\Delta\nu T_S$ για διάφορους αλγορίθμους ανατροφοδότησης της απόφασης. α) Σύγχρονος δέκτης, β) Διαφορικός δέκτης.

Το Σχ. 24 απεικονίζει την ποινή OSNR για ρυθμό σφαλμάτων 10^{-3} συναρτήσει του γινομένου $\Delta\nu T_S$ για διάφορες περιπτώσεις χρήσης του φίλτρου Wiener. Το Σχ. 24α αντιστοιχεί στον σύγχρονο δέκτη, ενώ το Σχ. 24β αντιστοιχεί στον διαφορικό δέκτη. Παρατηρούμε ότι το φίλτρο Wiener επιτυγχάνει πολύ καλή απόδοση για τους σύγχρονους δέκτες, κάνοντάς τους καλύτερους από τους διαφορικούς δέκτες, στο σύνολο των γινομένων $\Delta\nu T_S$ που μελετήθηκαν, ενώ σε κάποιες περιπτώσεις, βελτιώνει λίγο και την απόδοση των διαφορικών δεκτών. Αντίστοιχα, το Σχ. 25 απεικονίζει με την ίδια σειρά, την απόδοση των αλγορίθμων για τους δυο δέκτες, όταν χρησιμοποιείται προσέγγιση του φίλτρου Wiener. Τέλος, στο Σχ. 26 απεικονίζεται με την ίδια σειρά η απόδοση των αλγορίθμων για τους δυο δέκτες, όταν χρησιμοποιείται ο block-phase αλγόριθμος. Είναι προφανές ότι οι αλγόριθμος block-phase δεν προσφέρει τίποτα στον διαφορικό δέκτη, ενώ βελτιώνει αισθητά την απόδοση του σύγχρονου δέκτη ειδικά σε μικρά γινόμενα $\Delta\nu T_S$. Το Σχ. 27 συγκρίνει τις καλύτερες αποδόσεις των αλγορίθμων και πιστοποιεί ότι η λύση του φίλτρου τύπου Wiener και οι προσεγγίσεις του προσφέρουν την καλύτερη απόδοση.
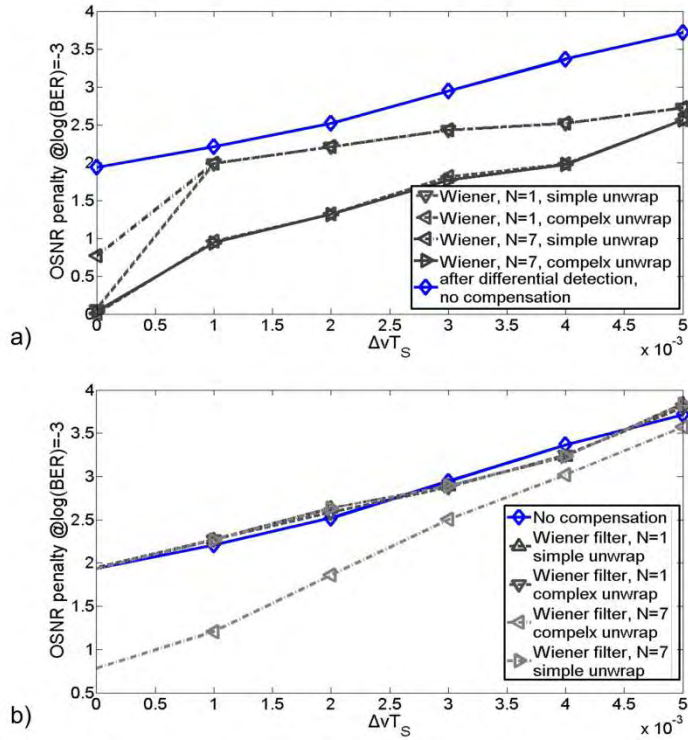
Σχ. 24 Ποινή OSNR για ρυθμό σφαλμάτων 10^{-3} συναρτήσει του γινομένου $\varDelta v T_S$ για διάφορες περιπτώσεις χρήσης του φίλτρου Wiener. α) Σύγχρονος δέκτης, β) Διαφορικός δέκτης.
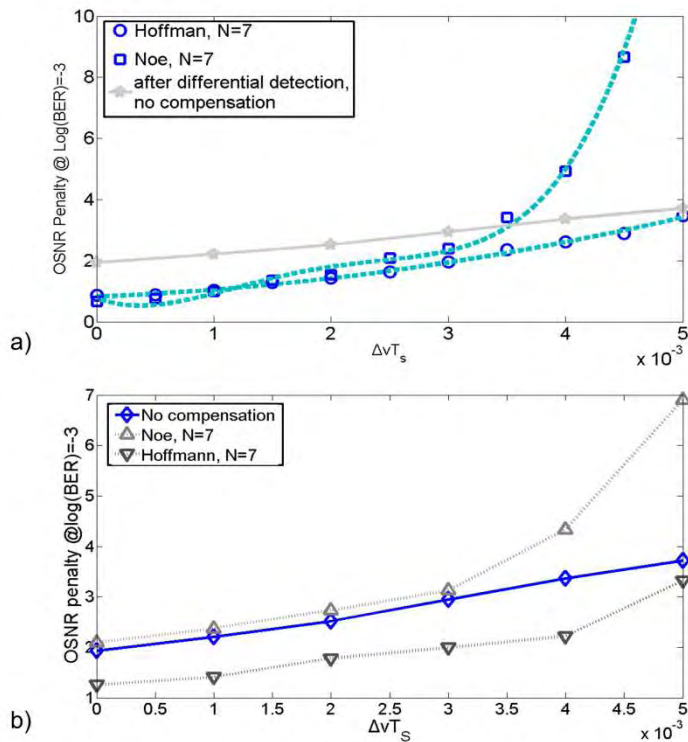
Σχ. 25 Ποινή OSNR για ρυθμό σφαλμάτων 10^{-3} συναρτήσει του γινομένου $\varDelta v T_S$ για διάφορες περιπτώσεις χρήσης του προσεγγίσεων του φίλτρου Wiener. α) Σύγχρονος δέκτης, β) Διαφορικός δέκτης.
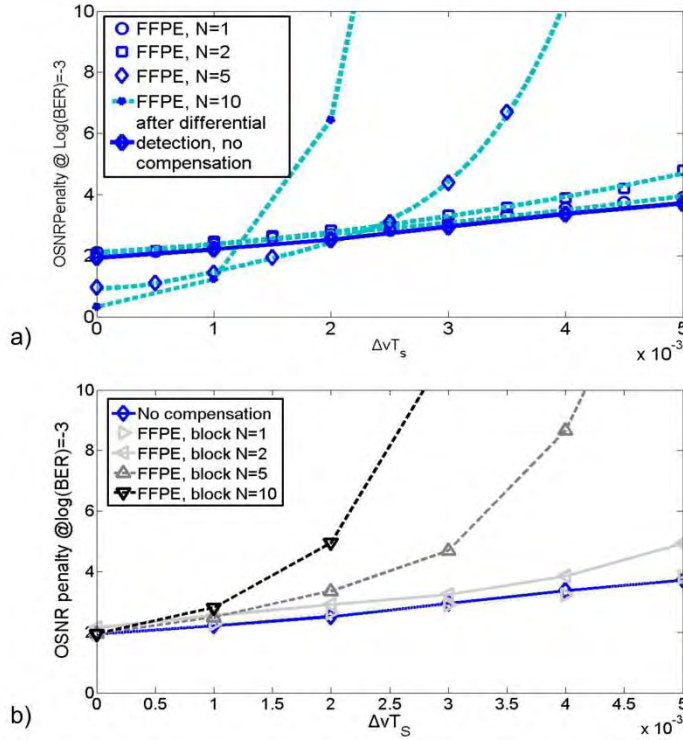
Σχ. 26 Ποινή OSNR για ρυθμό σφαλμάτων 10^{-3} συναρτήσει του γινομένου $\Delta\nu T_S$ για διάφορες περιπτώσεις χρήσης του αλγορίθμου block-phase. α) Σύγχρονος δέκτης, β) Διαφορικός δέκτης.
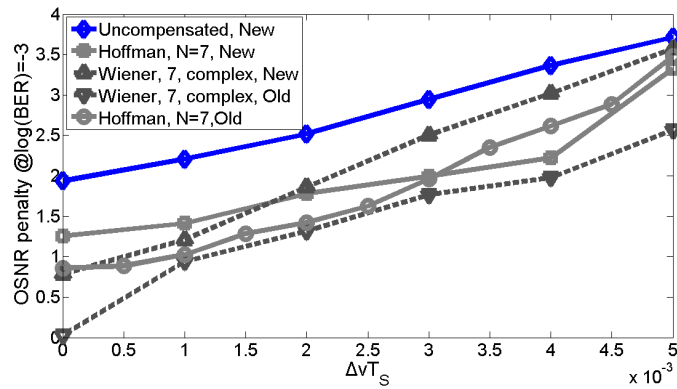
Σχ. 27 Σύγκριση των καλύτερων αλγορίθμων εκτίμησης και διόρθωσης του θορύβου φάσης.

4. Αλγόριθμοι εκτίμησης και διόρθωσης της ενδιάμεσης συχνότητας

Στην ενότητα αυτή συγκρίνουμε του αλγορίθμους εκτίμησης και διόρθωσης της ενδιάμεσης συχνότητας. Η μελέτη πραγματοποιήθηκε σε σύστημα QPSK χωρίς πολυπλεξία κατά πόλωση, παρουσία θορύβου αυθόρμητης εκπομπής και θορύβου φάσης. Μελετήθηκε η απόκλιση της συχνότητας που εκτιμάται από τους αλγορίθμους από την πραγματική ενδιάμεση συχνότητα που εισάγεται.

Το Σχ. 28 απεικονίζει το σφάλμα στην εκτίμηση της ενδιάμεσης συχνότητας που παρουσιάζουν οι τρεις αλγόριθμοι, για τρία διαφορετικά γινόμενα $\Delta v T_S$, και πιο συγκεκριμένα, για $\Delta v T_S = 0$, $\Delta v T_S = 5 \times 10^{-5}$ (500 kHz laser για 10 GBd), και $\Delta v T_S = 2 \times 10^{-3}$ (20 MHz laser για 10 GBd), για τον αλγόριθμο phase increment (Σχ. 28a), τον αλγόριθμο του Tretter (Σχ. 28b), και τον αλγόριθμο του Kay (Σχ. 28c). Φαίνεται ξεκάθαρα ότι ο θόρυβος φάσης δεν επηρεάζει τη λειτουργία κανενός αλγορίθμου Σημειώνεται παρ' όλα αυτά ότι η εκτίμηση έγινε πάνω σε όλα τα μιγαδικά σύμβολα της εξομοίωσης, ήτοι 32768 σύμβολα.
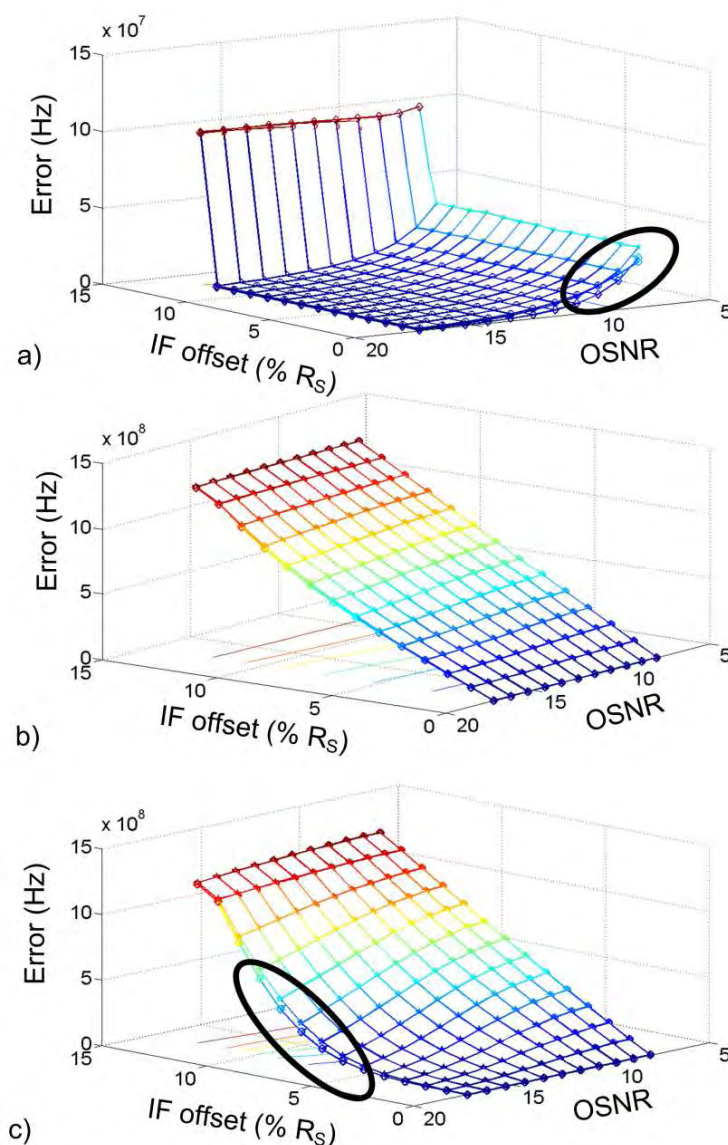
Σχ. 28 Σφάλμα εκτίμησης για τους τρεις αλγορίθμους. α) Αλγόριθμος phase increment, β) Αλγόριθμος Tretter, γ) Αλγόριθμος Kay. Το σφάλμα μετρήθηκε για τρεις διαφορετικές περιπτώσεις του γινομένου $\Delta v T_S$: $\Delta v T_S = 0$, $\Delta v T_S = 5 \times 10^{-5}$, and $\Delta v T_S = 2 \times 10^{-3}$.

Το Σχ. 29 συγκρίνει τους τρεις αλγορίθμους στο ίδιο γράφημα, ώστε να είναι εμφανής η διαφορά στην απόδοση. Ο αλγόριθμος phase increment έχει μακράν το μικρότερο σφάλμα εκτίμησης.
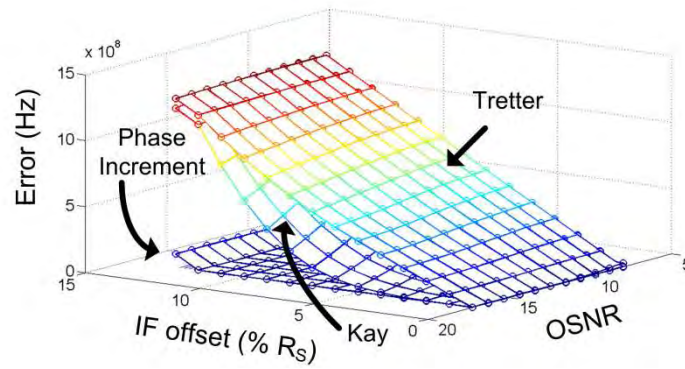
Σχ. 29 Σύγκριση του σφάλματος εκτίμησης για τους τρεις αλγορίθμους, για τη περίπτωση γινομένου $\Delta\nu T_S = 2\times10^{-3}$.

5. Αλγόριθμοι εκτίμησης και διόρθωσης της ανισοσταθμίας ορθογωνιότητας

Στην ενότητα αυτή συγκρίνουμε του αλγορίθμους εκτίμησης και διόρθωσης της ανισοσταθμίας. Η μελέτη πραγματοποιήθηκε σε σύστημα QPSK με πολυπλεξία κατά πόλωση, παρουσία θορύβου αυθόρμητης εκπομπής, θορύβου φάσης και ενδιάμεσης συχνότητας. Η ενδιάμεση συχνότητα επελέγη να είναι 500 MHz, η οποία, όπως προέκυψε από τα πειράματα, είναι τυπική τιμή. Ο θόρυβος φάσης των laser, επελέγη να είναι 5 MHz, τυπική τιμή για DFB laser. Για την διόρθωση του θορύβου φάσης, χρησιμοποιήθηκε ο block-phase αλγόριθμος με μέγεθος συστάδας Ν=10, ενώ για την διόρθωση της ενδιάμεσης συχνότητας, ο αλγόριθμος phase increment, με εκτίμηση σε ολόκληρο το παράθυρο της εξομοίωσης. Για την μελέτη των αλγορίθμων διόρθωσης της ανισοσταθμίας, χρησιμοποιήθηκαν ακραίες τιμές για να διαπιστωθεί το εύρος λειτουργίας των αλγορίθμων. Χρησιμοποιήθηκε $\varepsilon=0°$, $\delta=\pm30°$, κατευθυντικοί συζεύκτες με τιμή συντελεστή +30% από τη κανονική τιμή, και φωτοδίοδοι με λόγο αποκρισιμοτήτων ίσο με +20%.

Τα Σχ. 30 και Σχ. 31 απεικονίζουν τον μετρημένο ρυθμό σφαλμάτων συναρτήσει του OSNR για ένα σύστημα QPSK με πολυπλεξία κατά πόλωση και με ανισοσταθμία ορθογωνιότητας όπως περιγράφηκε στην προηγούμενη παράγραφο, και για δειγματοληψία στον ρυθμό συμβόλων και με ρυθμό διπλάσιο από το ρυθμό συμβόλων, αντίστοιχα. Ενδιαφέρον παρουσιάζει το γεγονός ότι εξισωτές για διόρθωση της αλληλοπαρεμβολής συμβόλων δεν καταφέρνουν να διορθώσουν την ανισοσταθμία ορθογωνιότητας. Όλοι οι υπόλοιποι αλγόριθμοι έχουν παραπλήσια συμπεριφορά, εκτός από τον προσαρμοστικό αλγόριθμο CMA με περιορισμούς όταν χρησιμοποιούνται λιγότερες από τέσσερεις μεταβλητές. Πρέπει επίσης να σημειωθεί ότι ο αλγόριθμος εκτίμησης της έλλειψης δεν μπορεί να εφαρμοστεί στην περίπτωση όπου χρησιμοποιείται δειγματοληψία με ρυθμό διπλάσιο από τον ρυθμό συμβόλων, διότι ο αστερισμός παύει να είναι ελλειπτικός.
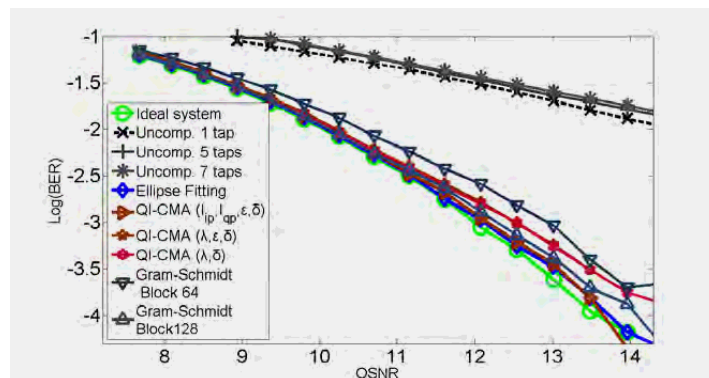
Σχ. 30 Μετρημένος ρυθμός σφαλμάτων συναρτήσει του OSNR για ένα σύστημα QPSK με πολυπλεξία κατά πόλωση και με ανισοσταθμία ορθογωνιότητας. Η δειγματοληψία γίνεται με τον ρυθμό συμβόλων.
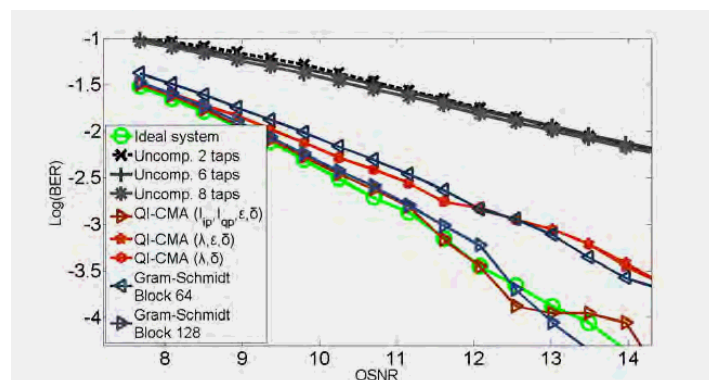
Σχ. 31 Μετρημένος ρυθμός σφαλμάτων συναρτήσει του OSNR για ένα σύστημα QPSK με πολυπλεξία κατά πόλωση και με ανισοσταθμία ορθογωνιότητας. Η δειγματοληψία γίνεται με ρυθμό διπλάσιο του ρυθμού των συμβόλων.

V. Ανάλυση πειραματικών δεδομένων

Σε αυτή την ενότητα παρουσιάζουμε την πειραματική διάταξη και την ανάλυση επιλεγμένων πειραματικών δεδομένων με χρήση των αλγορίθμων που υλοποιήθηκαν στα πλαίσια αυτής της διατριβής.

1. Πειραματική διάταξη

Η βασική πειραματική διάταξη για ένα οπτικό σύστημα QPSK χωρίς πολυπλεξία κατά πόλωση με σύμφωνο δέκτη διαφοροποίησης φάσης και της πόλωσης φαίνεται στο Σχ. 32. Το φως από την έξοδο ενός laser διαμορφώνεται κατά QPSK σε έναν οπτικό τετραγωνικό διαμορφωτή από LiNbO$_3$ (Photline MPZ-LN). Ο διαμορφωτής ορθογωνιότητας οδηγείται από διπολικές κυματομορφές μη επιστροφής στο μηδέν με περίοδο 2^7-1. Χρησιμοποιήθηκαν ρυθμοί σηματοδοσίας 0.1–10.7 Gbps.

Το διαμορφωμένο κατά φάση οπτικό σήμα μεταδίδεται μέσω οπτικών ινών διάφορων τύπων, και διάφορων μηκών και λαμβάνεται σε έναν σύμφωνο δέκτη διαφοροποίησης φάσης και της πόλωσης. Ένας από τους δυο δέκτες διαφοροποίησης φάσης αποτελείται από ένα οπτικό υβρίδιο 2×2 κατασκευασμένο από διακριτά στοιχεία, ενώ ο άλλος δέκτης διαφοροποίησης φάσης αποτελείται από ένα ολοκληρωμένο οπτικό υβρίδιο 2×4 (CeLight CL-QOH-90). Η συχνότητα του laser που χρησιμοποιήθηκε ως τοπικός ταλαντωτής συγχρονίστηκε χειροκίνητα με τη συχνότητα του πομπού, με τη χρήση ενός αναλυτή φάσματος.
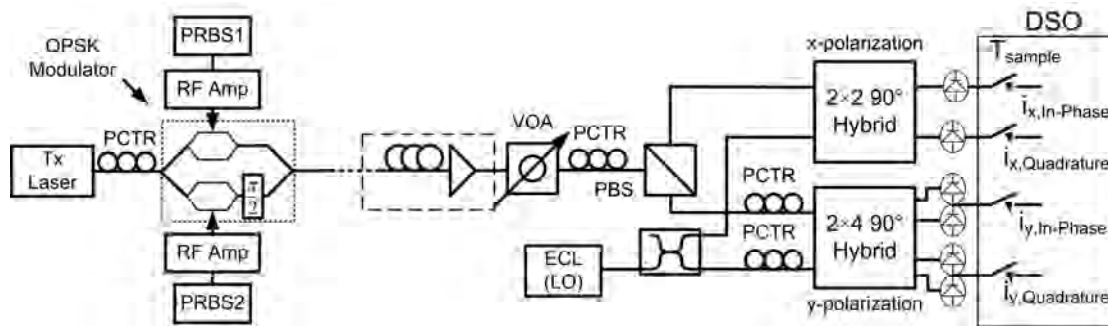
Σχ. 32 Πειραματική διάταξη ενός συστήματος QPSK χωρίς πολυπλεξία κατά πόλωση με σύμφωνο δέκτη διαφοροποίησης φάσης και της πόλωσης.

Κάθε ένα από τα τέσσερα φωτορεύματα υπέστη δειγματοληψία σε έναν ψηφιακό παλμογράφο (Agilent Infiniium 80804B), όπου και αποθηκεύτηκαν για ανάλυση με προσωπικό υπολογιστή. Η δυνατότητα δειγματοληψίας του παλμογράφου ήταν 20 GSamples per second, ενώ κάθε μέτρηση διήρκεσε 51.25 μs. Για να πραγματοποιηθεί πολυπλεξία κατά πόλωση, χρησιμοποιήθηκε η διάταξη που φαίνεται στο Σχ. 33. Το διαμορφωμένο σήμα στην έξοδο του τετραγωνικού διαμορφωτή διασπάται σε δυο ίσες συνιστώσες οι οποίες υπόκεινται σε μια διαφορική καθυστέρηση. Με τη χρήση ελεγκτών πόλωσης, τα δυο σήματα επανασυνδέονται έχοντας ορθογώνιες πολώσεις.
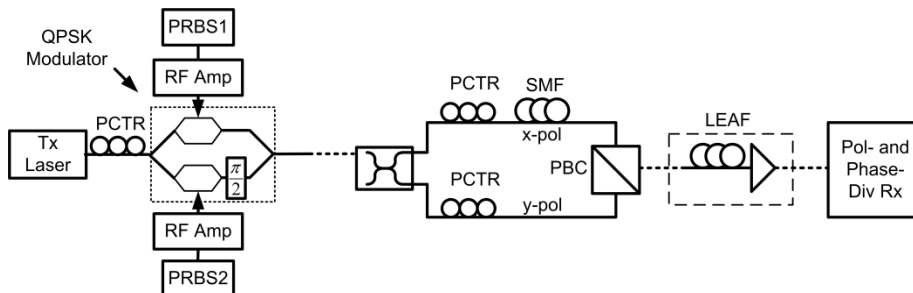
Σχ. 33 Πειραματική διάταξη για την πολυπλεξία κατά πόλωση ενός σήματος QPSK.

2. Ανάλυση πειραματικών δεδομένων ρυθμού συμβόλων 1 GBd

Στην ενότητα αυτή αναλύονται διεξοδικά τα πειραματικά δεδομένα από ένα πείραμα 1 GBd σήματος διαμορφωμένου κατά QPSK με πολυπλεξία κατά πόλωση, τα οποία διαδόθηκαν σε 100 km οπτικής ίνα τύπου LEAF. Η αλληλουχία των αλγορίθμων που χρησιμοποιήθηκαν φαίνεται στο Σχ. 34.
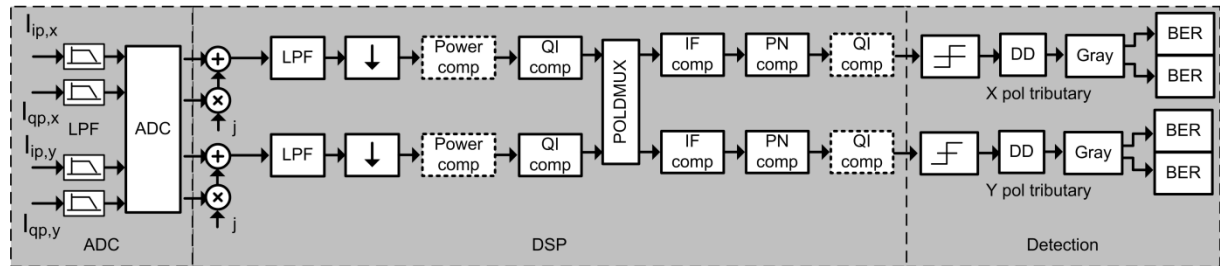
Σχ. 34 Αλληλουχία αλγορίθμων ψηφιακής επεξεργασίας σήματος για την ανάλυση πειραματικών δεδομένων 1 GBd QPSK με πολυπλεξία κατά πόλωση, μέσα από 100 km οπτικής ίνας τύπου LEAF.

Τα τέσσερα φωτορεύματα από την έξοδο του δέκτη διαφοροποίησης φάσης και της πόλωσης δειγματοληπτώνται και αποθηκεύονται στον ψηφιακό παλμογράφο, ο οποίος δρα ταυτόχρονα ως ένα χαμηλοδιαβατό φίλτρο με εύρος ζώνης περίπου 4 GHz. Τα φωτορεύματα δειγματοληπτώνται με ρυθμό 20 GHz, ο οποίος για σήμα 1 GBd αντιστοιχεί σε 20 δείγματα ανά σύμβολο. Η μέτρηση αντιστοιχεί σε περίπου 50000 σύμβολα. Η συχνότητα του τοπικού ταλαντωτή, η οποία ελέγχεται χειροκίνητα, φέρνει στην ενδιάμεση συχνότητα μεταξύ 100 και 500 MHz. Αυτό κατατάσσει το συγκεκριμένο πείραμα στην κατηγορία των ενδόδυνων πειραμάτων και συνεπώς, η ενδιάμεση συχνότητα μπορεί να αφαιρεθεί με χρήση κάποιου από τους αλγορίθμους που μελετήθηκαν στα πλαίσια αυτής της διατριβής [171].

Μετά την ανάκτηση των δεδομένων από τον ψηφιακό παλμογράφο, ακολουθεί ακόμα ένα στάδιο φιλτραρίσματος με μικρότερο εύρος ζώνης. Ακολουθεί επαναδειγματοληψία από 20 σε ένα ή δυο δείγματα ανά σύμβολο, ανάλογα τους αλγορίθμους που θα χρησιμοποιηθούν. Ακολουθεί συγχρονισμός των τεσσάρων ακολουθιών και μετά εφαρμόζονται οι επιθυμητοί αλγόριθμοι.

Το Σχ. 35 απεικονίζει του αστερισμούς που αντιστοιχούν στην Χ και Υ πόλωση, μετά από τον συγχρονισμό των ακολουθιών. Φαίνεται καθαρά η ελλειπτική μορφή των αστερισμών η οποία παραπέμπει σε ανισοσταθμία ορθογωνιότητας. Συνεπώς, ο πρώτος αλγόριθμος που εφαρμόζεται είναι ένας από τους αλγορίθμους εκτίμησης και διόρθωσης της ανισοσταθμίας. Σε όλες τις περιπτώσεις εφαρμόζουμε την ορθογωνιοποίηση Gram-Schmidt επειδή είναι η απλούστερη μέθοδος.

Δοκιμάζουμε στα δεδομένα διάφορους αλγορίθμους αποπολύπλεξης των πολώσεων. Για να προκύψουν οι τελικοί αστερισμοί, χρησιμοποιείται ο αλγόριθμος phase increment για την εκτίμηση και διόρθωση της ενδιάμεσης συχνότητας και ο αλγόριθμος block phase για την διόρθωση του θορύβου φάσης, με μέγεθος συστάδας N=14. Στο Σχ. 36α απεικονίζεται ο τελικός αστερισμός όταν χρησιμοποιηθεί ο αλγόριθμος CMA με 13 βάρη (ο αποπολυπλέκτης λειτουργεί ως εξισωτής). Για να προκύψει ο αστερισμός αυτός, εισήχθη σκόπιμα μια διαφορική καθυστέρηση ίση με τρία σύμβολα σε σχέση με την ιδανική, μεταξύ των δυο εισόδων του αποπολυπλέκτη. Αυτό έγινε διότι αλλιώς ο αποπολυπλέκτης CMA συγκλίνει στην ίδια ακολουθία στις δυο εξόδους [196], [197], όπως φαίνεται στο Σχ. 37, όπου χρησιμοποιήθηκε η ορθή διαφορική καθυστέρηση. Οι αστερισμοί είναι πανομοιότυποι, με διαφορά μια στροφή 90°. Ο λόγος για τον οποίο συμβαίνει αυτό είναι ότι μια από τις δυο απεσταλθείσες πολώσεις έχει μεγαλύτερη ισχύ από την άλλη, και σε αυτή τη πόλωση συγκλίνουν και οι δυο έξοδοι του αποπολυπλέκτη. Το φαινόμενο αυτό λέγεται ανισοσταθμία πόλωσης και οφείλεται στην μέθοδο δημιουργίας του πολυπλεγμένου κατά πόλωση σήματος στον πομπό.

Υπάρχουν δυο τρόποι να αποφευχθεί το πρόβλημα αυτό στην έξοδο του αποπολυπλέκτη. Ο ένας είναι να χρησιμοποιηθεί ο αλγόριθμος CMA με περιορισμούς για την αποπολύπλεξη. Ο άλλος είναι να χρησιμοποιηθεί ο αλγόριθμος multi-user CMA (MU-CMA) [197].
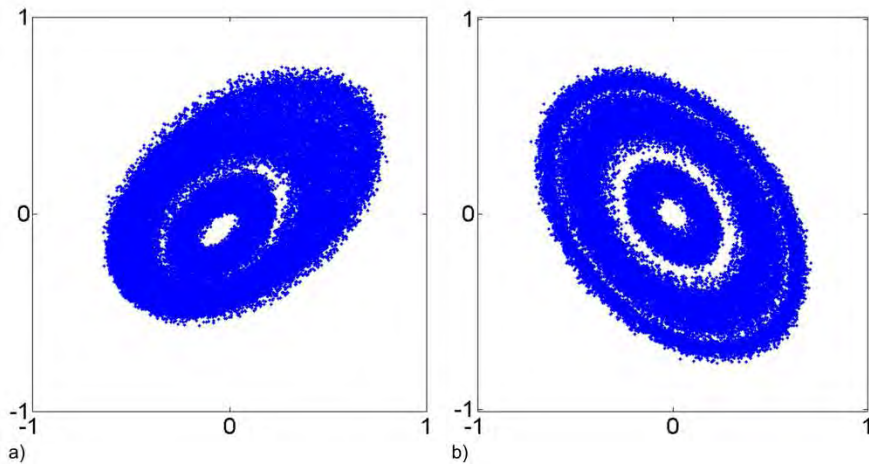
Σχ. 35 Ληφθέντες αστερισμοί για την Χ και Υ πόλωση.
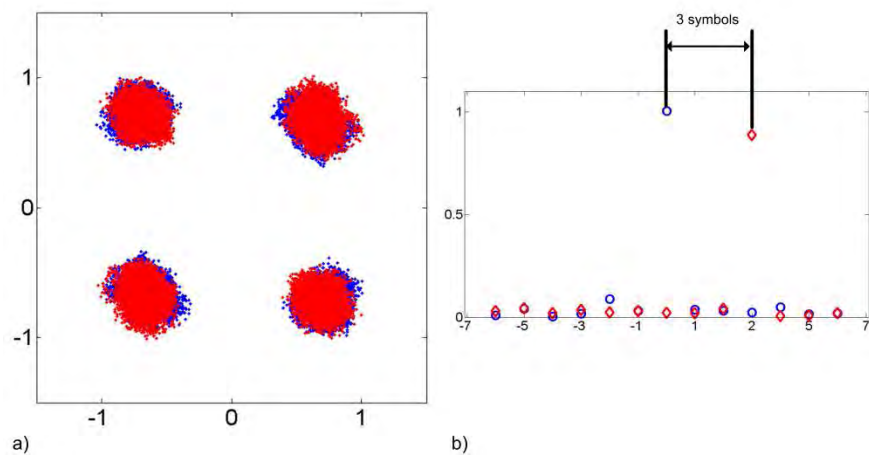
Σχ. 36 α) Τελικός αστερισμός με χρήση του αλγορίθμου CMA για την αποπολύπλεξη. β) Το μέτρο των βαρών του εξισωτή μετά τη σύγκλιση, όταν επιτηδευμένα έχει εισαχθεί μια διαφορική καθυστέρηση τριών συμβόλων μεταξύ των ακολουθιών της Χ και Υ πόλωσης.
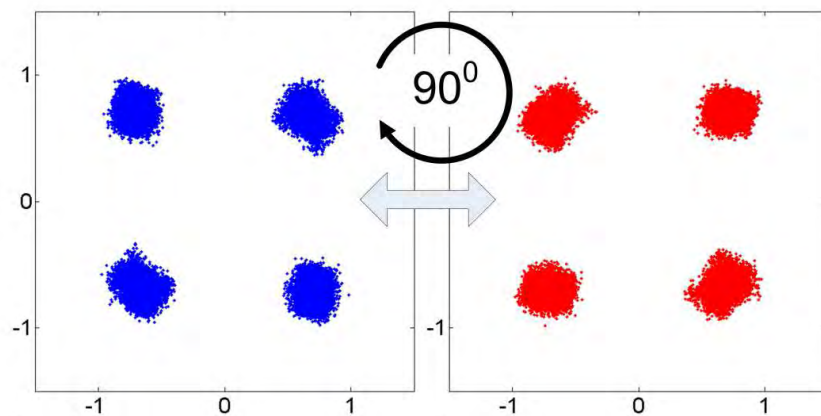
Σχ. 37 Τελικοί αστερισμοί όταν χρησιμοποιείται ο αλγόριθμος CMA για την αποπολύπλεξη των σημάτων και χρησιμοποιούνται οι ορθές διαφορικές καθυστερήσεις μεταξύ των ακολουθιών στην είσοδο.

Ο επόμενος αλγόριθμος που δοκιμάστηκε ήταν ο αλγόριθμος CMA με περιορισμούς. Το Σχ. 38 αντιστοιχεί σε αστερισμούς που προέκυψαν από διάφορους συνδυασμούς παραμέτρων και αλγορίθμων. Το Σχ. 38α αντιστοιχεί στην περίπτωση όπου χρησιμοποιήθηκε διόρθωση της ανισοσταθμίας ορθογωνιότητας πριν τον αποπολυπλέκτη, και διόρθωση της ανισοσταθμίας πόλωσης μετά από την διόρθωση της ενδιάμεσης συχνότητας [195] (η διόρθωση ανισοσταθμίας πόλωσης έγινε με τον αλγόριθμο ορθογωνιοποίησης Gram-Schmidt). Για τον αποπολυπλέκτη CMA με περιορισμούς, χρησιμοποιήθηκαν οι αναμενόμενες τιμές για QPSK, δηλαδή $R_2^{(1)} = R_2^{(2)} = 1$. Παρ' όλα αυτά το αποτέλεσμα δεν είναι το επιθυμητό. Δοκιμάζοντας διάφορες τιμές, βρέθηκε ότι οι βέλτιστες τιμές είναι οι $R_2^{(1)} = 2R_2^{(2)} = 2$, με τις οποίες προκύπτει ο αστερισμός του Σχ. 38β όπου οι αστερισμοί των δυο πολώσεων εμφανίζονται ως όφειλαν. Οι άνισες τιμές των παραμέτρων αντικατοπτρίζουν ακριβώς την άνιση ισχύ που έχουν οι δυο πολώσεις καθώς αποστέλλονται στον πομπό. Στο Σχ. 38γ, επιβεβαιώνεται ο ισχυρισμός αυτός, διότι αφαιρώντας τη διόρθωση της ανισοσταθμίας ορθογωνιότητας του πομπού, οι δυο αστερισμοί προκύπτουν με διαφορετικό πλάτος. Το Σχ. 38δ αντιστοιχεί στην περίπτωση όπου δεν χρησιμοποιείται διόρθωση της ανισοσταθμίας ορθογωνιότητας πριν τον αποπολυπλέκτη. Φαίνεται ότι η ανισοσταθμία ορθογωνιότητας δεν παίζει τόσο καίριο ρόλο σε αυτή τη περίπτωση, μιας και ο αστερισμός είναι ανοιχτός.
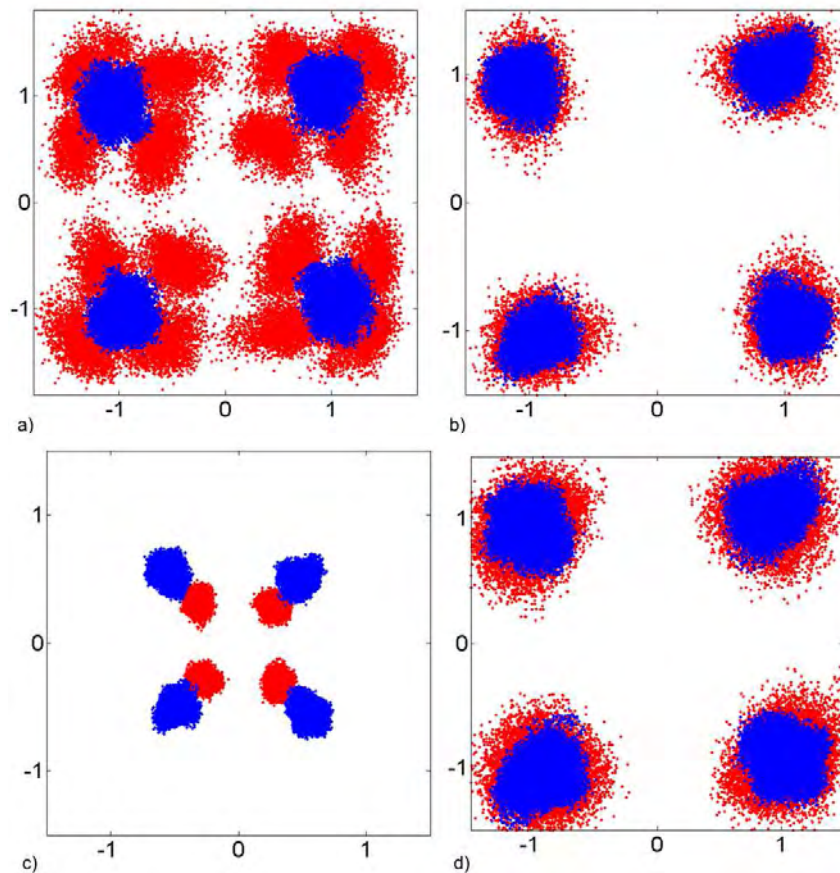
Σχ. 38 Τελικοί αστερισμοί όταν χρησιμοποιείται ο αλγόριθμος CMA με περιορισμούς. α) Λάθος παράμετροι στην ανανέωση των βαρών ($R^{(1)} = R^{(2)} = 1$), β) Σωστές παράμετροι στην ανανέωση των βαρών ($R^{(1)} = 2R^{(2)} = 2$), και εξίσωση της ανισοσταθμίας πόλωσης του πομπού, c) Σωστές παράμετροι στην ανανέωση των βαρών ($R^{(1)} = 2R^{(2)} = 2$), χωρίς εξίσωση της ανισοσταθμίας πόλωσης του πομπού d) Σωστές παράμετροι στην ανανέωση των βαρών ($R^{(1)} = 2R^{(2)} = 2$), με εξίσωση της ανισοσταθμίας πόλωσης του πομπού αλλά χωρίς εξίσωση της ανισοσταθμίας ορθογωνιότητας.

Τέλος, δοκιμάζουμε την χρήση του αλγορίθμου MU-CMA. [197]. Το Σχ. 39 απεικονίζει τους τελικούς αστερισμούς για διάφορους συνδυασμούς παραμέτρων. Το Σχ. 39α αντιστοιχεί στην περίπτωση όπου χρησιμοποιείται διόρθωση της ανισοσταθμίας ορθογωνιότητας και πόλωσης ενώ για τον MU-CMA χρησιμοποιούνται φίλτρα με τέσσερα βάρη και δ_{max}=2. Διαπιστώθηκε ότι ο αλγόριθμος MU-CMA είναι πολύ ευαίσθητος στις τιμές των παραμέτρων. Για παράδειγμα, στο Σχ. 39β φαίνεται ο τελικός αστερισμός εάν χρησιμοποιηθούν φίλτρα με επτά βάρη και δ_{max}=8. Κοιτώντας το Σχ. 39γ, όπου δεν έχει χρησιμοποιηθεί το κύκλωμα διόρθωσης της ανισοσταθμίας πόλωσης, είναι εύκολο να διαπιστώσουμε ότι η ανισοσταθμία πόλωσης δεν παίζει τόσο σημαντικό ρόλο στην περίπτωση που χρησιμοποιείται ο MU-CMA. Αντιθέτως, κοιτώντας το Σχ. 39δ, όπου δεν έχει χρησιμοποιηθεί ούτε ο αλγόριθμος εκτίμησης της ανισοσταθμίας ορθογωνιότητας, διαπιστώνουμε ότι η ανισοσταθμία ορθογωνιότητας είναι πιο σημαντική.
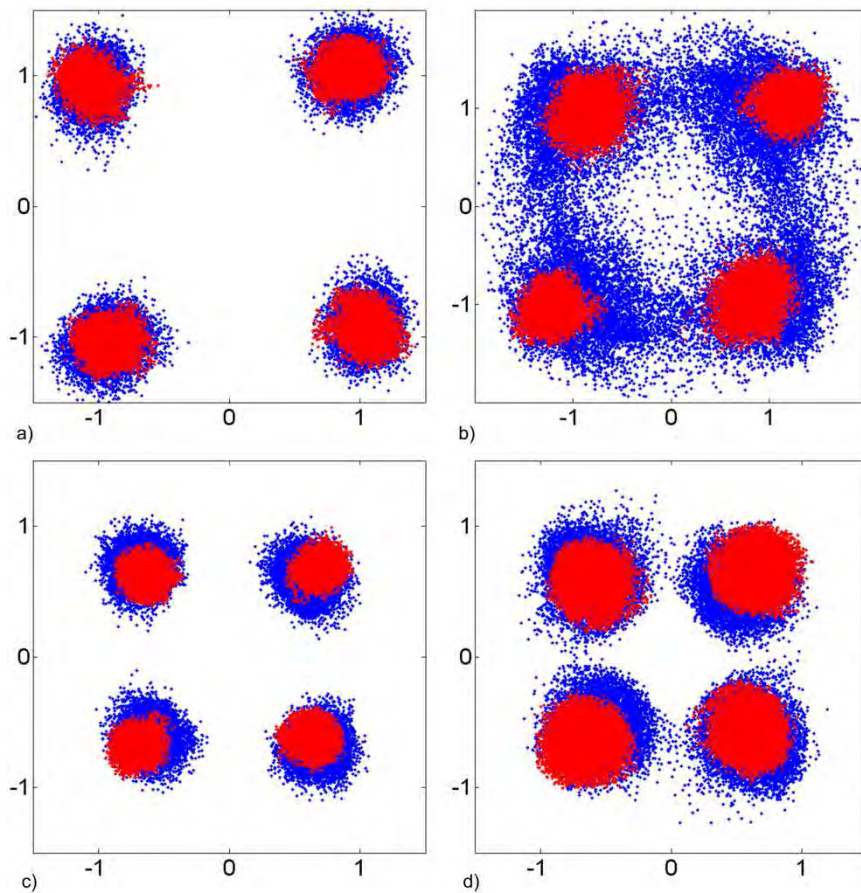
Σχ. 39 Τελικοί αστερισμοί με αποπολύπλεξη χρησιμοποιώντας τον αλγόριθμο MU-CMA. α) MUCMA με φίλτρα τεσσάρων βαρών και δ_{max}=2, b) MUCMA με φίλτρα επτά βαρών και δ_{max}=8 and M=10, and transmitter QI compensation using the GSOP, c) MUCMA με φίλτρα τεσσάρων βαρών και δ_{max}=2 χωρίς την διόρθωση της ανισοσταθμίας πόλωσης, d) MUCMA με φίλτρα τεσσάρων βαρών και δ_{max}=2, χωρίς την διόρθωση της ανισοσταθμίας πόλωσης ή ορθογωνιότητας.

VI.   Συμπεράσματα

Ο σκοπός αυτής της διατριβής ήταν να μοντελοποιήσει από άκρη σε άκρη ένα οπτικό σύστημα τετραδικής διαμόρφωσης φάσης με πολυπλεξία κατά πόλωση, με σύμφωνους ψηφιακούς δέκτες διαφοροποίησης φάσης και πόλωσης και τη μελέτη της απόδοσης του συστήματος σε πραγματικές συνθήκες λειτουργίας. Για τον σκοπό αυτό υλοποιήθηκε ένας μεγάλος αριθμός αλγορίθμων ψηφιακής επεξεργασίας, η απόδοση των οποίων μελετήθηκε τόσο με προσομοίωση, όσο και χρησιμοποιώντας πραγματικά πειραματικά δεδομένα.

Αρχικά, έγινε εξομοίωση του συστήματος σε νωτεπίνωτη συνδεσμολογία, με χρήση εμπορικού πακέτου προσομοίωσης [113]. Αναπτύχθηκαν μοντέλα εξομοίωσης για τις βασικές δομικές μονάδες των σύμφωνων συστημάτων QPSK με πολυπλεξία πόλωσης, ήτοι, ο διαμορφωτής ορθογωνιότητας, και ο σύμφωνος δέκτης διαφοροποίησης φάσης και της πόλωσης. Αναπτύχθηκαν κάποιοι βασικοί αλγόριθμοι ψηφιακής επεξεργασίας σήματος για την αφαίρεση της ενδιάμεσης συχνότητας και την αφαίρεση του θορύβου φάσης, οι οποίοι χρησιμοποιήθηκαν για την ανάλυση κάποιων πειραματικών δεδομένων με χαμηλούς ρυθμούς συμβόλων, ήτοι 0.1 GBd και 1 GBd.

Στα πλαίσια των αναλύσεων των πειραματικών δεδομένων, προέκυψε ότι μια σειρά από μη ιδανικότητες στον πομπό και στον δέκτη επηρεάζουν αρκετά την απόδοση του συστήματος και η ανισοσταθμία ορθογωνιότητας αναγνωρίστηκε ως ο κυριότερος παράγοντας, γεγονός το οποίο οδήγησε και στις πρώτες δημοσιεύσεις [182], [202]. Υλοποιήθηκε ένας μεγάλος αριθμός αλγορίθμων εκτίμησης και διόρθωσης της ανισοσταθμίας, ένας εκ των οποίων προτάθηκε από την ομάδα, και η απόδοσή τους μελετήθηκε και συγκρίθηκε, τόσο σε επίπεδο προσομοίωσης όσο και σε πειραματικά δεδομένα [185], [186].

Αφού περατώθηκε η μελέτη των βασικών λειτουργιών του ψηφιακού δέκτη και διαπιστώθηκαν οι βασικές μη ιδανικότητες, ήτοι η ανισοσταθμία ορθογωνιότητας, η ενδιάμεση συχνότητα και ο θόρυβος φάσης, το ενδιαφέρον επικεντρώθηκε στα φαινόμενα διάδοσης. Μελετήθηκε η σταθερή και χρονικά μεταβαλλόμενη στροφή φάσης λόγω της οπτικής ίνας και υλοποιήθηκαν και συγκρίθηκαν αρκετοί αλγόριθμοι αποπολύπλεξης της πόλωσης, οι οποίοι υιοθετήθηκαν από την [143]. Οι αλγόριθμοι αυτοί χρησιμοποιήθηκαν επιτυχώς σε πειραματικά δεδομένα [156]. Κατά τη διαδικασία εφαρμογής τους στα πειραματικά δεδομένα, διαπιστώθηκε ότι στα συστήματα με πολυπλεξία κατά πόλωση, δύναται η έξοδος του αποπολυπλέκτη να συγκλίνει λανθασμένα στην ίδια ακολουθία στις δυο εξόδους του. Αυτό το φαινόμενο αντιμετωπίστηκε επιτυχώς με δυο αλγορίθμους που προτάθηκαν από την ομάδα μας [156], [197]. Ο δεύτερος, χρησιμοποιήθηκε επιτυχώς και σε πειραματικά δεδομένα [203].

Ταυτοχρόνως, τα αποτελέσματα και η τεχνογνωσία που προέκυψε από αυτή τη διατριβή, χρησιμοποιήθηκε σε άλλες μελέτες από άτομα της ίδιας ομάδας. Υλοποιήθηκε ένα σύστημα μελέτης διασποράς τρόπων πόλωσης όλων των τάξεων με χρήση πολυκανονικής μεθόδου Monte Carlo [204], ενώ παράλληλα οι αλγόριθμοι χρησιμοποιήθηκαν για την ανάλυση πειραματικών αποτελεσμάτων με χρήση QPSK σε οπτικούς διακόπτες [193].

Σε όλο το φάσμα της διατριβής έγινε σαφές ότι τα συστήματα QPSK με πολυπλεξία κατά πόλωση και ψηφιακούς σύμφωνους δέκτες μπορούν να αντιμετωπίσουν επιτυχώς έναν μεγάλο αριθμό από πρακτικά προβλήματα που συναντώνται στις οπτικές τηλεπικοινωνίες. Πιο συγκεκριμένα, μπορούν να χρησιμοποιηθούν ηλεκτρονικοί αποπολυπλέκτες για να αντιμετωπίσουν τυχαίες, χρονικά μεταβαλλόμενες στροφές φάσης που πηγάζουν από την χρήση οπτικών ινών. Ο εγγενής θόρυβος φάσης των laser αντιμετωπίζεται επιτυχώς σε βαθμό που μπορούν να χρησιμοποιηθούν και laser χαμηλής ποιότητας με θόρυβο φάσης εύρους ζώνης 50 MHz σε συστήματα 10 GBd, με ποινή

μικρότερη από 3 dB. Η αναπόφευκτη ενδιάμεση συχνότητα, λόγω μη ευθυγράμμισης της συχνότητας laser πομπού και δέκτη αντιμετωπίζεται εύκολα μέχρι του ποσοστού 0.125 επί του ρυθμού συμβόλων. Τέλος, η ανισοσταθμία ορθογωνιότητας, φαινόμενο έντονο λόγω των οπτικών δομικών στοιχείων στο δέκτη, αντιμετωπίζεται επιτυχώς αφήνοντας μηδαμινή ποινή.

Όλες αυτές οι ανοχές σε μη ιδανικότητες και φυσικά φαινόμενα, καθιστούν τα συστήματα QPSK με πολυπλεξία κατά πόλωση και ψηφιακό σύμφωνο δέκτη διαφοροποίησης φάσης και της πόλωσης, τους κύριους υποψήφιους για τη νέα γενιά οπτικών συστημάτων με ρυθμό σηματοδοσίας 40 Gb/s ή 100 Gb/s, ενώ έχουν προκύψει ήδη τα πρώτα εμπορικά προϊόντα.

ΜΕΡΟΣ Β
ΔΙΑΤΡΙΒΗ ΣΤΑ ΑΓΓΛΙΚΑ

I. Abstract

Today's information society relies to an unprecedented extent on broadband communications solutions, with applications such as high-speed Internet access, mobile voice and data services, multimedia broadcast systems, and high-capacity data networking for grid computing and remote storage. In order to most cost-effectively meet the widely differing bandwidth demands of various communication applications, several communication technologies are being used, each with their very own characteristics and advantages.

Optical communications systems can support Tb/s capacities over many thousand kilometers, which makes them the ideal technology base for high-capacity wireline networking. Optical communications systems vendors have steadily pursued an increase in system reach and aggregate wavelength division multiplexing (WDM) transport capacity, in order to fulfill the steadily growing volume and bandwidth demand of data services and the desire to meet this demand by simultaneously reducing the cost per transported information bit [1].

In WDM systems, this cost reduction is achieved by sharing optical components among many channels. For optical components with limited bandwidth, this means packing WDM channels as close together as possible, while increasing the per-channel information data rate as much as possible. The increase of per-channel information data stumbles upon electrical equipment bandwidth limitations. One way to circumvent this limitation is to use multilevel modulation formats, such as M-ary phase-shift keying (PSK), or quadrature amplitude modulation (QAM). Multilevel modulation formats can also trade off noise resilience, fiber propagation characteristics, and resilience to narrowband optical filtering due to multiple passes through reconfigurable optical add-drop multiplexers (ROADMs) [1].

The scope of this dissertation is to investigate the merits and implications of using multilevel modulation formats in optical communications systems. Following the trend in academia and industry, special focus is placed on quadrature phase-shift keying (QPSK), and specifically on polarization division multiplexed (PDM) QPSK. A special kind of receiver is investigated thoroughly, the digital coherent receiver, the equivalent of the coherent quadrature demodulator in classical communications nomenclature. A large number of digital signal processing (DSP) algorithms are implemented, some of them novel, and their performance is examined, analyzed, and compared in a number of practical system scenarios. The impact of transmitter / receiver imperfections and a number of optical fiber impairments on system performance is studied. Experimental results taken from proof-of-concept experiments are also analyzed.

The dissertation is organized as follows: In Section II, key concepts of digital modulation formats are presented. The abstract model of the QPSK digital modulator and demodulator is presented. In Section III, a detailed survey of the field is presented. Key terminology is introduced, along with a historical overview of coherent optical communications, from the early days of coherent detection to the most recent hero experiments. In Section IV, the key components enabling QPSK modulation and demodulation in optical communications are analyzed. In Section V, all the DSP algorithms developed and implemented in the context of this dissertation are analyzed, in parallel with the physical phenomena they are designed to mitigate. Section VI contains simulation results that highlight the performance bounds of the algorithms described in Section V, and attempts to answer fundamental questions as to the performance limits of coherent PDM-QPSK optical communications systems. Finally, Section VII contains key experimental results, highlighting the performance of the algorithms described in Section V, on real data. Section VIII presents the major findings and conclusions of this work and recommends future research work.

II.   Multilevel modulation formats

1.   Digital communications system [2]

Most generally, a communications system aims at transmitting information from a source to one or more destinations across a channel. In a *digital* communications system, the information transmitted is of discrete nature, i.e., the information symbols belong to a finite alphabet. A digital communications system has the generic block diagram depicted in Fig. 1. At the transmitter, a discrete information source generates a message, to be conveyed to the receiver. This message is formed by the concatenation of characters belonging to a finite element alphabet, which, in the majority of cases, are encoded into binary digits (bits), i.e., 0s and 1s. The source encoder reduces the redundancy in the message, in order to represent it with as few characters as possible, and generates an information sequence which is in bit form. The channel encoder purposefully introduces some redundancy in the binary information sequence, in a controlled manner, in order to help the receiver overcome the effects of noise, distortion and interference encountered upon transmission of the signals through the channel. The modulator serves as the interface to the communication channel and its primary function is to map the binary information sequence into signal waveforms.

At the receiver end, the exact inverse procedure is performed in the opposite order compared to the transmitter. The demodulator processes the channel-corrupted received waveforms and reduces them to a binary information sequence, which represents an estimate of the transmitted sequence, at the input of the modulator. The channel decoder attempts to reconstruct the original information sequence from knowledge of the redundancy contained in the received sequence. Finally, the source decoder attempts to reconstruct the original message.
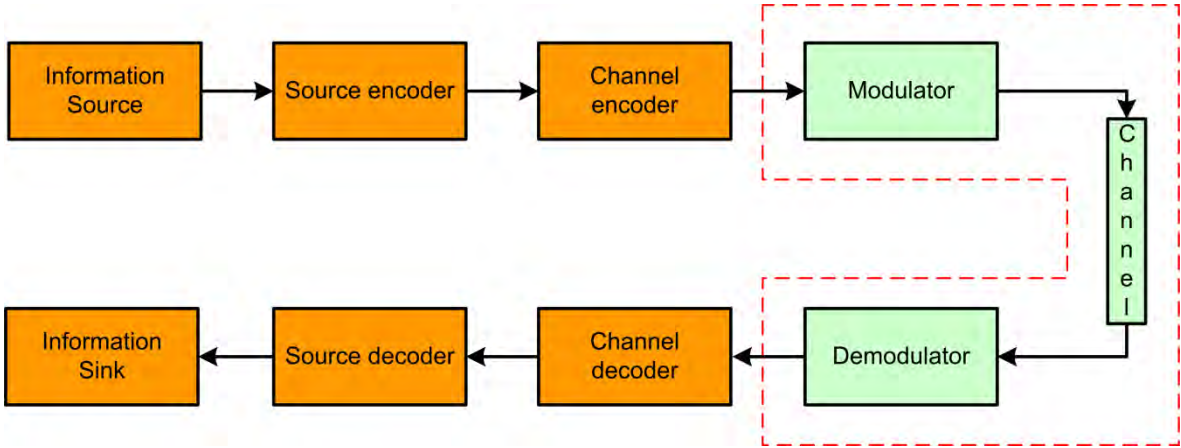
Fig. 1 Generic block diagram of a digital communications system [2].

2. Digital modulation formats

In any communications system, the modulator serves as the interface to the channel and produces a continuous-time signal with characteristics suitable for transmission. Continuous-time signal waveforms can be written as a linear combination of orthonormal waveforms. In digital communications systems, the modulator input is a bit sequence generated at a uniform rate by the channel encoder, and the output, is a set of deterministic, finite energy waveforms, which may differ in either amplitude, phase or frequency, or some combination of two or more of these attributes [2]. The orthonormal functions used to expand the waveforms are the sine and cosine functions, and thus the signal space is two-dimensional. Thus, waveforms can be represented as a set of points on a two-dimensional diagram, the signal space diagram [2]. Equivalently, the points can also be represented by complex in general quantities, the modulation symbols. In the remainder of this section, we clarify the notion of complex modulation symbols and use the signal-space diagram to graphically represent the various digital modulation formats.

We assume that bits are produced from the channel encoder at a uniform rate of R_b bits per second (bps) and are of duration $T_b=1/R_b$ seconds. The bit sequence at the input of the modulator is b_n, n denoting the n–th bit period, each b_n belonging to an alphabet $\{b_i\}=\{0,1\}$, $i=0,1$, of size two. It is transformed into a new sequence, the symbol sequence c_k, k denoting the k-th symbol period, each c_k belonging to an alphabet $\{c_n\}$, $n=0,1,…,M$-1 of size $M=2^m$. This is done by taking m consecutive bits and mapping each of the possible 2^m combinations to one of the elements of $\{c_n\}$, n=0,1,…,M-1. If $M=2$, we refer to the subsequent modulation processes as binary modulation, whereas if $M>2$ as M-ary modulation. The symbol period is $T_S=mT_b$ and the rate of symbol generation (symbol rate) is $R_S=1/T_S$ symbols per second (Baud).

Depending on the symbol alphabet used, a variety of digital modulation formats are defined. Fig. 2 depicts the signal space diagrams corresponding to the complex symbols $\{c_n\}$, $n=0,1,…,M$-1, for a number of modulation formats [1]. Fig. 2a corresponds to the simple case where $\{c_n\}=\{0, A\}$, a binary modulation format better known as on-off keying (OOK) or amplitude-shift keying (ASK). Fig. 2b corresponds to the general case where $\{c_n\}=(2n+1-M)d$, $n=0,1,…,M$-1 (in Fig. 2b, $M=4$), $2d$ being the distance between adjacent symbol amplitudes, a modulation format known as M-ary pulse-amplitude modulation (M-PAM). Fig. 2c corresponds to the case where $\{c_n\}=\{-A, A\}$, which can either be viewed as a 2-PAM modulation format, or as binary phase-shift keying (BPSK). (Despite the similarity between the signal space diagrams of 2-PAM and BPSK, these modulation formats are totally different in implementation.) Fig. 2d corresponds to the case where $\{c_n\}=\exp(j2\pi n/M+j\varphi)$ $n=0,1,…,M$-1 (in Fig. 2d, $M=4$, $\varphi=0$), a modulation format known as M-ary phase shift-keying (M-PSK). Angle φ is a rotation angle determining the exact position of the complex symbols on the complex plane. Fig. 2e and Fig. 2f correspond to the most general case, where the complex symbol $\{c_n\}$ has both amplitude and phase, formats known as quadrature amplitude modulation (QAM) modulation formats.

There is not a unique mapping from the 2^m combinations of m bits to the M symbols of $\{c_n\}$, $n=0,1,…,M$-1, but a number of ways to perform the one-to-one mapping. The preferred assignment is one in which adjacent symbols differ by one bit. This mapping is called (binary-reflected) *Gray encoding* [2]. It is better suited to the detection of the signal, because the most likely symbol errors caused by noise will result in a single bit error. This is due to the fact that most likely symbol errors, involve erroneous selection of an *adjacent* symbol to the transmitted symbol. Gray encoding is performed by converting the m bits at the input, to their decimal equivalent n_b, and then calculating the Gray coded equivalent decimal n_g. From n_g, the mapping to $\{c_n\}$, $n=0,1,…,M$-1 is performed simply by using $n=n_g$, i.e., the Gray-coded equivalent decimal is the index to the symbol alphabet element. In all cases depicted in Fig. 2, Gray encoding has been used to map the incoming bits to complex symbol values and they are shown on the corresponding symbol values.

---

[1] Strictly speaking, a signal space diagram should ideally be scaled to the energy of the modulation signal waveform. For simplicity, this is not taken into account. Rather, the points on the signal space diagram are scaled according to the amplitude of the corresponding complex symbol.

The signal space diagrams of *M*-ary PSK are invariant to phase rotations, which are multiples *2π/M*. Consequently, at the receiver, even in the absence of any distortion or noise source, there is a phase ambiguity between the received phases, due to the unknown phase shift inflicted by transmission through the channel [3]. To address this phenomenon, memory is introduced into the symbols to be transmitted, by assigning symbols to *phase differences* rather than absolute phases. Therefore, an additional step is introduced in phase modulation, called *differential encoding*. Assuming that, initially, the symbol alphabet is {*c_n*} = exp(*j2πn/M*) *n=0,1,...,M*-1, differential encoding is performed by the recursion

$$d_k = c_k d_{k-1} \tag{75}$$

producing a new symbol alphabet {*d_n*} = exp(*j2πn/M+jφ*) *n=0,1,...,M*-1. An initial condition $d_{-1} = e^{j\varphi}$ is needed for time instant *k=0*, and its choice affects the signal space diagram shape. If no differential encoding is performed, d_k simply equals c_k.
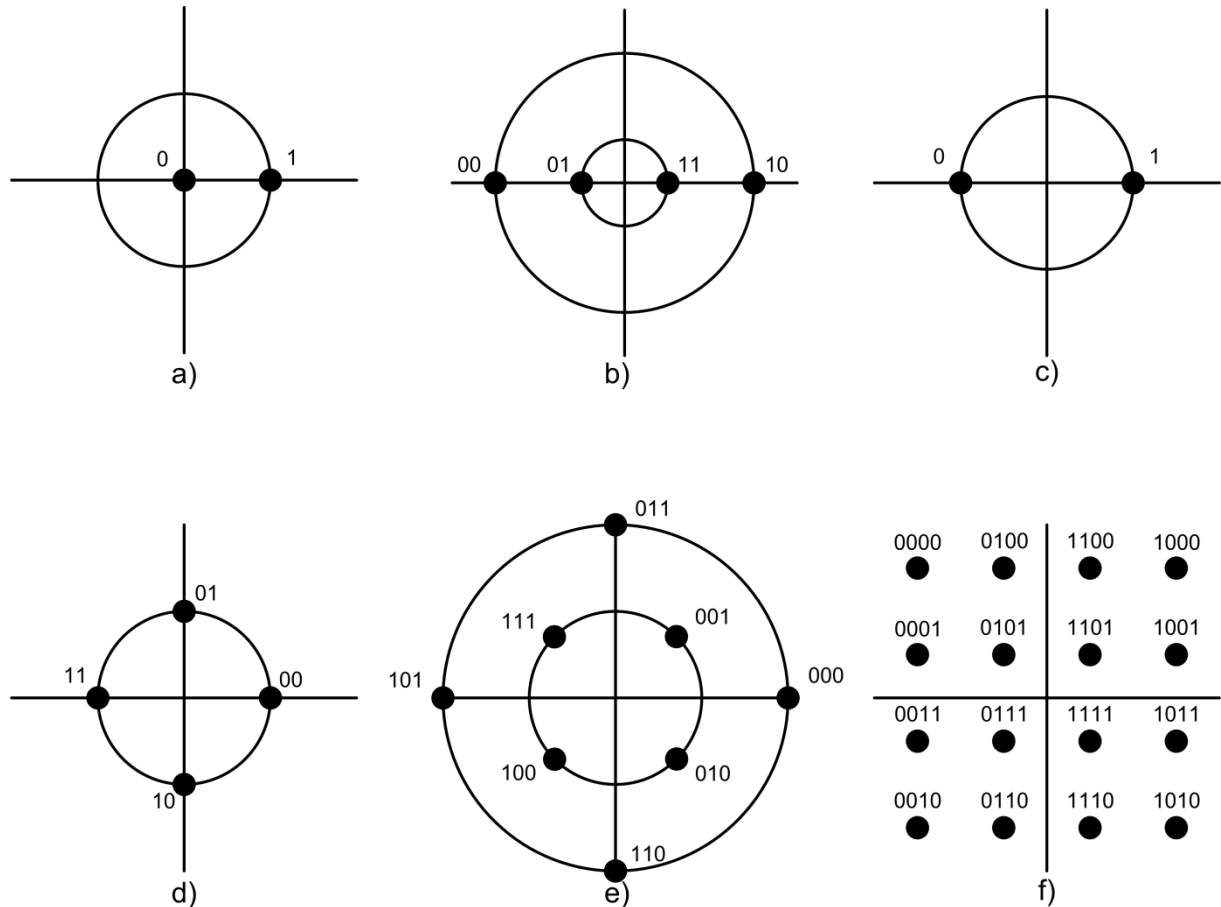
Fig. 2 Signal space diagrams for various digital modulation formats. (a) On-off keying (OOK), (b) M-ary pulse-amplitude modulation (M-PAM); M=4, (c) 2-PAM or binary phase-shift keying (BPSK), (d) M-ary phase-shift keying (M-PSK); M=4, (e) Quadrature amplitude modulation (QAM); 2-PAM, 4-PSK, (f) Quadrature amplitude modulation (QAM); star 16 QAM. Gray encoding is assumed in the mapping procedure for all cases.

The resulting symbol sequence d_k is then transformed into a continuous signal by shaping a basic pulse *g(t)*, a process known as baseband pulse modulation, or line coding [4]. The result is a pulse train of infinite duration

$$\tilde{s}(t) = \sum_{k=0}^{\infty} d_k g(t - kT_S) \tag{76}$$

where $\tilde{s}(t)$ is the low-pass equivalent signal, or complex envelope of a real signal $s(t)$ (Appendix A). It should be stressed that the duration of $g(t)$ need not be limited to a symbol period, nor even be of finite duration. Nevertheless, in much of the literature $g(t)$ is taken as a rectangular pulse of amplitude A and duration T_S.

The pulse train can further modulate a sinusoidal carrier, producing a modulated bandpass signal, which, in analytic form, is written as

$$\hat{s}(t) = \sum_{k=0}^{\infty} d_k g(t - kT_S) e^{j2\pi f_c t} \tag{77}$$

where f_c is the carrier frequency, and $\hat{s}(t)$ is the analytic signal representation of a real signal $s(t)$ (Appendix A).

Fig. 3 shows an example of the detailed modulation procedure for the case of 4-PSK, also known as Quadrature PSK or QPSK, which will play the central role in this dissertation. Inset Table 1 depicts the Gray coded decimals corresponding to the input bit pairs, inset Table 2 depicts the complex modulation symbols after differential encoding for each input Gray coded decimal, and Fig. 3b shows the final signal space diagram with the corresponding input bits next to the differentially encoded symbols. In this example we have used $d_{-1} = e^{j\pi/4} = 1 + j$.
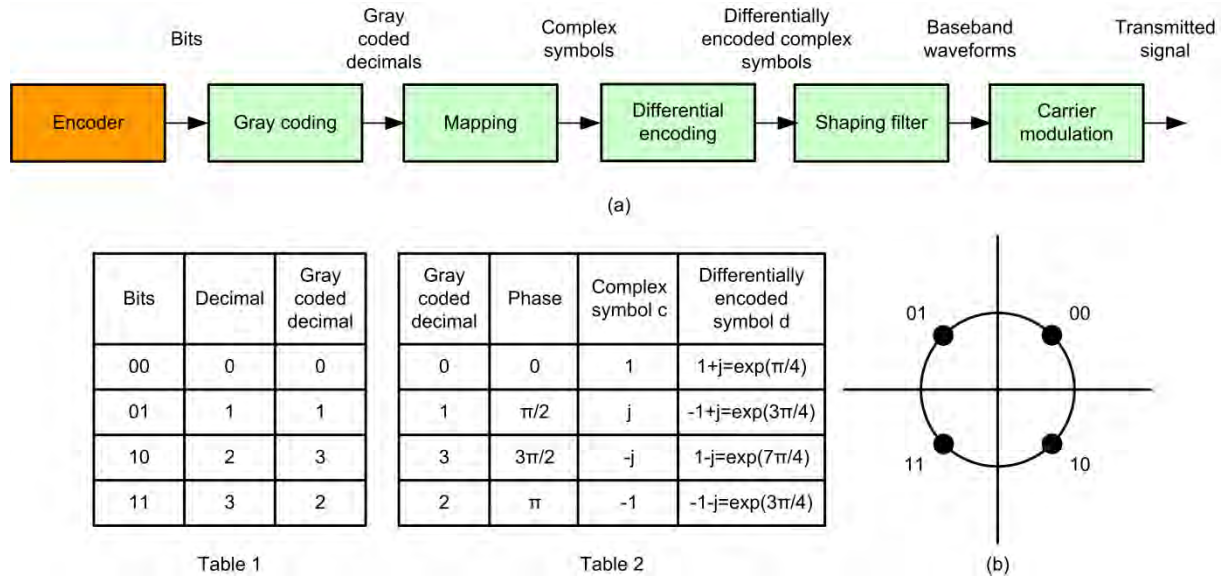
Fig. 3 Block diagram of an ideal QPSK modulator.

Demodulation is the complementary, or, inverse operation of modulation, and is performed at the receiver. However, the demodulation method is not unique, in the sense that, given a specific modulated signal, it may be possible to demodulate the signal using more than one receiver implementations. Nevertheless, nearly all demodulators may be put into one of two classes: *coherent* demodulators, which use a locally generated carrier signal for demodulation, and *non-coherent* demodulators, which do not require a local carrier [4].

The ideal demodulator corresponding to the ideal modulator (77) is of the coherent type. In order to remove the carrier, the signal is multiplied by a complex sinusoid $\hat{m}(t)$ whose frequency is the negative frequency of the carrier, i.e.,

$$\hat{m}(t) = e^{-j2\pi f_c t} \tag{78}$$

This multiplication results in a baseband signal which ideally equals (76). In order to obtain the complex symbol sequence $\{d_k\}$, some sort of processing should be performed, which normally, is just filtering and sampling. Filtering aims at minimizing the effect of noise and interference at the receiver.

Since the scope of this section is to provide general concepts of the demodulation and detection process, no detailed analysis of filtering will be given. Assuming sampling at instances $t=kT_S$, and also that $g(0)=1$, we acquire the transmitted complex symbol sequence $\{d_k\}$. In the event of differential encoding at the modulator, differential decoding should be performed, i.e.,

$$c_k = d_k d_{k-1}^*$$ (79)

where * denotes complex conjugation. The same initial condition used for d_{-1} at the transmitter should be used for c_{-1}. If no differential encoding was performed, c_k simply equals d_k.

Subsequently, de-mapping is performed and the decimal n_k corresponding to each complex symbol c_k is found. This is a Gray coded decimal and $n_k=n_{g,k}$. Following the inverse mapping used at the modulator, i. e., Gray decoding, the equivalent decimal $n_{b,k}$ is found. Finally, the binary digit of length m corresponding to $n_{b,k}$ is re-created and the transmitted bit sequence is formed. This demodulation process is depicted in Fig. 4, again for the case of QPSK.
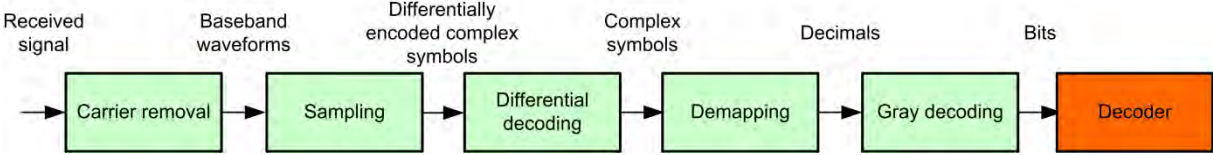
Fig. 4 Block diagram of an ideal QPSK demodulator

3. The practical QPSK quadrature modulator

For modulation formats such as *M*-PSK or QAM, a more practical modulation procedure can be used. Two orthogonal carriers are modulated independently by two real symbol sequences $\alpha_{1,k}$, $\alpha_{2,k}$ rather than a single (differentially encoded) complex symbol sequence d_k. The two orthogonal carriers are then transmitted simultaneously over the channel. This is better understood if we re-write (77) using real/imaginary representation of the complex symbol sequence, i. e., $d_k = \alpha_{1,k} + j\alpha_{2,k}$

$$\hat{s}(t) = \sum_{k=0}^{\infty} \left(a_{1,k} + ja_{2,k} \right) g\left(t - kT_S \right) e^{j2\pi f_c t} = \sum_{k=0}^{\infty} a_{1,k} g\left(t - kT_S \right) e^{j2\pi f_c t} + \sum_{k=0}^{\infty} a_{2,k} g\left(t - kT_S \right) e^{j2\pi f_c t + j\pi/2} \quad (80)$$

Each of the real symbol sequences $\alpha_{1,k}$, $\alpha_{2,k}$, whose elements belong to an alphabet $\{a_n\}$, $n=0,1,\ldots,M/2-1$ of size *M/2* separately modulate the in-phase (I) and quadrature (Q) carriers, indirectly producing a complex symbol sequence d_k. Such a modulator is consequently called an I/Q modulator, or quadrature modulator (QM). Depending on the modulation format, the alphabet $\{a_n\}$, $n=0,1,\ldots,M/2-1$ has to be chosen accordingly. For example, QPSK is implemented by using $\{a_n\}=\{-1,1\}$, $n=0,1$. A drawback of this type of modulator is that Gray encoding and differential encoding are not straightforward to perform, and need a specialized circuit, the *precoder*.

Due to the central role of QPSK in this thesis, we will describe in detail the precoder for the I/Q modulator, specifically for this modulation format. Two bit sequences $b_{1,k}$, $b_{2,k}$ whose elements belong to an alphabet $\{b_i\}=\{0,1\}$, $i=0,1$, each generated at a bit rate equal to R_b bps, are fed into a two-input/two-output sequential-logic circuit, the precoder, in which differential encoding and Gray encoding are performed. The outputs of the precoder, $e_{1,k}$, $e_{2,k}$, are also bit sequences, whose elements belong to an alphabet $\{e_i\}=\{0,1\}$, $i=0,1$, and are given by Boolean expressions (Appendix A)

$$e_{1,k} = \overline{b}_{1,k}\overline{b}_{2,k}e_{1,k-1} + \overline{b}_{1,k}b_{2,k}\overline{e}_{2,k-1} + b_{1,k}b_{2,k}\overline{e}_{1,k-1} + b_{1,k}\overline{b}_{2,k}e_{2,k-1}$$
$$e_{2,k} = \overline{b}_{1,k}\overline{b}_{2,k}e_{2,k-1} + \overline{b}_{1,k}b_{2,k}e_{1,k-1} + b_{1,k}b_{2,k}\overline{e}_{2,k-1} + b_{1,k}\overline{b}_{2,k}\overline{e}_{1,k-1}$$

$$(81)$$

where $e_{1,-1}$, $e_{2,-1}$ can be either 0 or 1 and - denotes the Boolean NOT function. The outputs $e_{1,k}$, $e_{2,k}$, of the precoder are mapped into symbol sequences $\alpha_{1,k}$, $\alpha_{2,k}$, respectively, using the mapping

$$e_k = 0 \rightarrow a_k = -1$$
$$e_k = 1 \rightarrow a_k = 1$$

$$(82)$$

It is thus easy to verify that the complex symbol sequence d_k belongs to the alphabet $\{d_n\}=\{1+j,-1+j,-1-j,1-j\}$, $n=\{0,1,2,3\}$. The complex symbol sequence can also be associated to a phase sequence φ_k with phases belonging to an alphabet $\{\varphi_n\}=\{\pi/4, 3\pi/4, 5\pi/4, 7\pi/4\}$, n=0, 1, 2, 3. The mapping between the symbol sequences $\alpha_{1,k}$, $\alpha_{2,k}$, and phase sequence φ_k is

$$\{a_{1,k}, a_{2,k}\} = \{1,1\} \rightarrow \varphi_k = \pi/4$$
$$\{a_{1,k}, a_{2,k}\} = \{-1,1\} \rightarrow \varphi_k = 3\pi/4$$
$$\{a_{1,k}, a_{2,k}\} = \{-1,-1\} \rightarrow \varphi_k = 5\pi/4$$
$$\{a_{1,k}, a_{2,k}\} = \{1,-1\} \rightarrow \varphi_k = 7\pi/4$$

$$(83)$$

Symbol sequences $\alpha_{1,k}$, $\alpha_{2,k}$ are separately pulse shaped and are used to modulate the two orthogonal carriers. The symbol rate R_S is equal to the bit rate R_b of the initial bit sequences. The block diagram of the I/Q modulator for QPSK is shown in Fig. 5.

The I/Q demodulator, performing the inverse functionality of the I/Q modulator described by (80), is depicted in Fig. 6. The incoming signal is split into its two orthogonal components and each component is separately demodulated to baseband, by using appropriate sinusoidal carriers $\hat{m}_1(t) = e^{-j2\pi f_c t}$ and $\hat{m}_2(t) = e^{-(j2\pi f_c t + j\pi/2)}$, respectively. Practical circuits may first demodulate the incoming signal using a single carrier, and then generate the two orthogonal components. The topic of exact receiver architecture to be used in the context of this dissertation will be revisited in Section IV.2

The resulting baseband signals are filtered and sampled, producing two real symbol sequences, $\alpha_{1,k}$, and $\alpha_{2,k}$, which are then combined into a complex symbol sequence $c_k = a_{1,k} + ja_{2,k}$. Differential decoding and Gray decoding are then performed on the complex symbol sequence c_k, as described in the previous section. After Gray decoding, a single bit sequence is produced, which, in the case of QPSK, has a bit rate twice the symbol rate. The two transmitted bit sequences are produced from this sequence through de-interleaving, using a one-to-two de-interleaver, the outputs of which produce bit sequences $b_{1,k}$ and $b_{2,k}$.
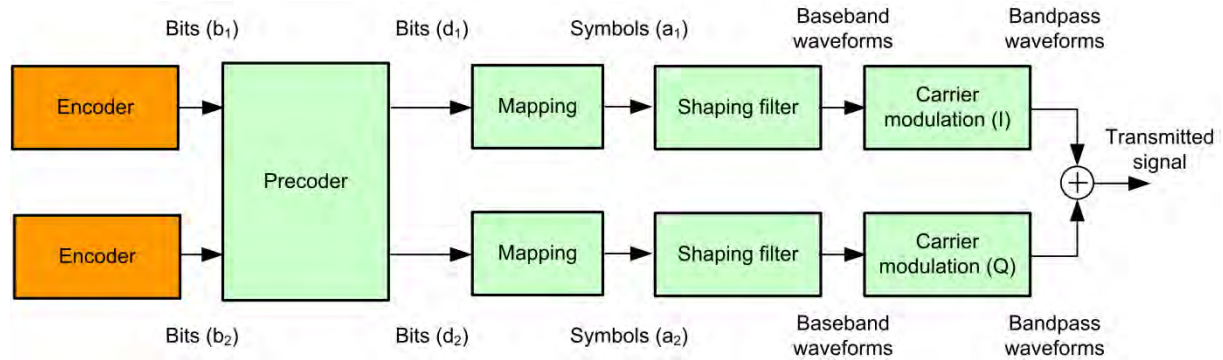
Fig. 5 Block diagram of the I/Q QPSK modulator.
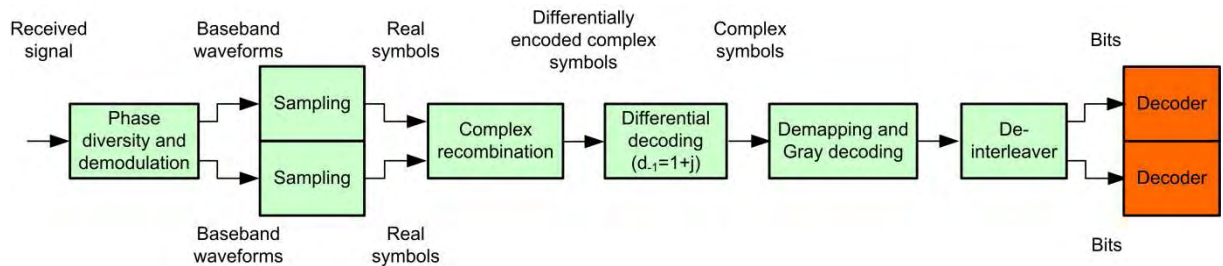
Fig. 6 Block diagram of an I/Q QPSK demodulator.

58

4. Simulation of QPSK systems

Simulation of digital communications systems using binary modulation formats involves the generation of binary sequences which are the input to the modulator. These binary sequences should be random, but, for simulation, it is more practical to produce *pseudo*-random sequences. Pseudo-random binary sequences (PRBSs) are deterministic and periodic but have an autocorrelation function that resembles the autocorrelation function of a random binary sequence [5]. Such sequences can be produced by linear feedback shift registers. The initial contents of the register and its feedback logic determine the successive contents of the shift register and therefore its output. An m-state shift register can produce a maximum of 2^m distinct states. The sequence of states and the output sequence are periodic with a period of at most 2^m. However, if a linear shift register contains all zeros at any time, it might be stuck in that state forever, so the maximum period cannot actually exceed 2^m-1 states. Designing the pseudo-random number generator using primitive polynomials produces maximal length sequences, i.e., sequences with period 2^m-1, in which all possible m-bit combinations appear exactly once in the period, except for the pattern of m zeros [4],[5].

PRBSs which produce maximal length sequences are especially useful in the simulation of intersymbol interference. In order to simulate the effects of intersymbol interference between m bits, the system has to be driven with a binary sequence that has all possible combinations of m bits, where m is the memory length of the channel. Using a PRBS generator, which produces maximal length sequences with periodicity 2^m-1, guarantees that all but one m-bit combinations will occur in the minimum amount of simulation time. In order to produce the all-zero m-bit combination, an extra 0 digit is added to the output at the part of the sequence where there are m-1 zeros. A sequence of length 2^m containing all possible patterns of m bits within a period 2^m exactly once is called a de Bruijn sequence [4],[5].

Simulation of digital communication systems using M-ary modulation formats involves the generation of M-ary waveforms. Pseudo-random M-ary sequences belonging to an alphabet $\{n\}=\{0,1,\ldots,M\text{-}1\}$ can also be generated using a feedback sift register, in much the same way as for the binary case [5]. The same holds for the generation of maximal length sequences using primitive polynomials. QPSK systems should use pseudo-random quaternary sequence (PRQS) generators in order to produce pseudo-random phase sequences. The PRQS generator produces integers from an alphabet $\{n\}=\{0,1,2,3\}$, which are assigned to complex, differentially and Gray encoded, symbols (Appendix B). Maximal length quaternary sequences contain all phase combinations of length m, except for the one corresponding to all-zeros, within a period 4^m-1. De Bruijn sequences contain all phase combinations of length m including the one corresponding to all-zeros within a period 4^m. Although it is feasible to construct a pseudo-random number generator to produce maximal quaternary sequences, this technique does not cover the study of practical QPSK transmitters (e.g., Fig. 5), in which two binary sequences are used at the input. In order to circumvent this problem in this dissertation, we have used two methods.

The first method is to produce a de Bruijn sequence of length 4^m using a software package suitable for numerical calculations (e.g., Mathematica), other than that used for system simulation. The de Bruijn sequence of length 4^m corresponds to the integers $\{n\}=\{0,1,2,3\}$. The latter are used to form a complex symbol sequence. The bit sequences at the input of the precoder, which will produce this sequence in the channel, are calculated by differentially and Gray decoding the index sequence n_k, into sequence n_b, and finding bit sequences $b_{1,k}$, $b_{2,k}$, by (Appendix B, (188)). These sequences are then fed at the input of the precoder. Using this method, de Bruijn sequences of length 4^3, 4^4, 4^5, 4^6, and 4^6 were generated. It should be stressed that, using this method, the two bit sequences $b_{1,k}$, $b_{2,k}$, though pseudo-random, i.e., periodic, with a period 4^m, do not contain all possible bit combinations of length or $2m$. A demonstration of the use of these systems is presented in Fig. 7. The eye closure penalty, expressed as -10$\log_{10}$(eye opening/ideal eye opening), is plotted for a 10 GBd PDM QPSK system using no chromatic dispersion compensation, for various de Bruijn sequence lengths. A fiber with 16 ps/km/nm dispersion parameter is used. The receiver electrical filter is a 4th-order Bessel filter with a 3-dB bandwidth equal to 3R_S, in order to minimize the effect of filter-induced inter-symbol interference (ISI). Though the penalty when using 4^5 and 4^7 de Bruijn sequences is the same, using 4^3 de Bruijn sequences produces a significantly smaller penalty for fiber lengths larger than 40 km, and is therefore

unreliable. Eye diagrams for the 4^5 case are shown in the inset of the figure for illustrational purposes. This method of producing de Bruijn symbol sequences is especially useful in semi-analytical techniques for the estimation of the error probability of a system (Appendix C).
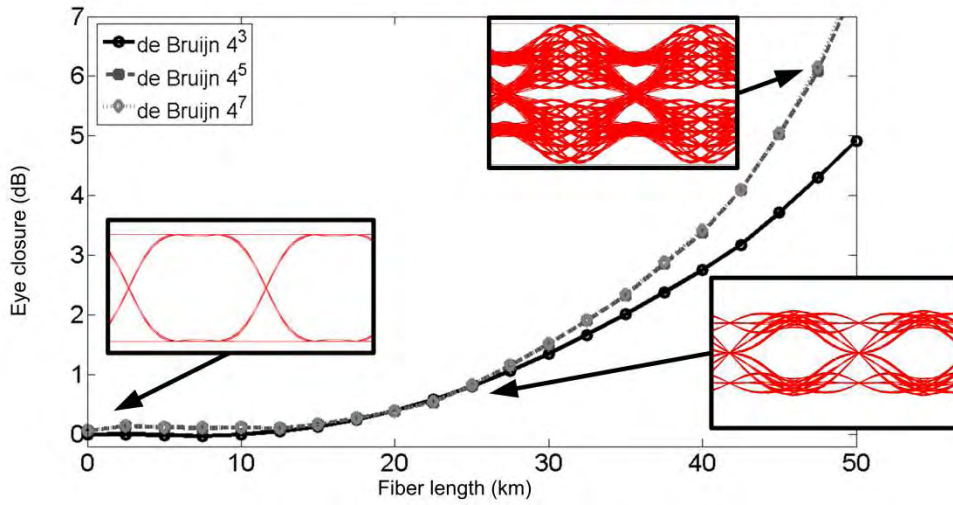
Fig. 7 Eye closure penalty vs fiber length for a 10 GBd PDM PSK system with no chromatic dispersion compensation, using de Bruijn complex symbol sequences. The fiber has D=16 ps/km/nm and the receiver electrical filter bandwidth is $3R_S$, in order to minimize the effect of filter-induced ISI.

The second method to produce all possible quaternary sequences of length up to m, is to use PRBS sequences at the precoder inputs. It has been shown that, in a DQPSK system which uses a transmitter with a precoder for differential encoding (but not Gray encoding), using binary de Bruijn sequences of length 2^{2m} at each precoder input, produces quaternary de Bruijn sequences of length 4^m [5], [6]. The two precoder inputs use the same binary de Bruijn sequence, with a specific relative cyclic shift imposed between the two. The appropriate cyclic shift in this case is $\pm m$ symbols. However, this method does not produce similar results when the precoder performing differential and Gray encoding is used. Applying two identical, circularly shifted binary de Bruijn sequences of length 2^{2m} at the precoder input, never produces more than 80% of the combinations of a de Bruijn sequence of length 4^m, whatever the cyclic shift. This point is illustrated in Fig. 8, for binary de Bruijn sequences of length 2^6 (Fig. 8a), 2^8 (Fig. 8b) and 2^{10} (Fig. 8c). It was found that, using binary maximal length sequences of length $2^{2(m+1)}$-1 does produce all quaternary combinations of length m in a sequence with period 4^{m+1}. This however, is not a de Bruijn sequence, which would contain all combinations of length m in a sequence of period 4^m. This method is not suitable for semi-analytical techniques, but can be used in other simulations, since it is much faster.
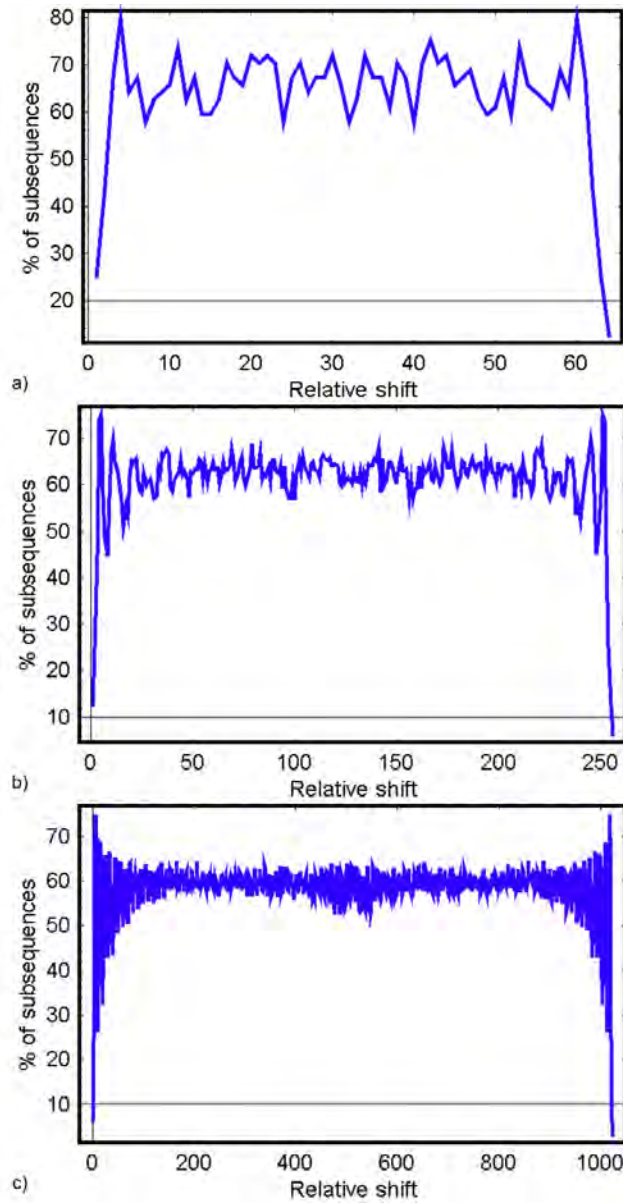
Fig. 8 (a) Percentage of all 3-phase combinations in a periodic sequence of length 4^3 produced by applying a 2^6 binary de Bruijn sequence and all possible cyclic shifts at the inputs of the precoder; (b) Percentage of all 4-phase combinations in a periodic sequence of length 4^4 produced by applying a 2^8 binary de Bruijn sequence and all possible cyclic shifts at the inputs of the precoder; (c) Percentage of all 5-phase combinations in a periodic sequence of length 4^5 produced by applying a 2^{10} binary de Bruijn sequence and all possible cyclic shifts at the inputs of the precoder;

61

III.   Literature survey of coherent optical communications

In this section, we present a detailed literature survey on past and current research aspects of using the PSK modulation format in optical communications, and focus on the coherent polarization- and phase-diversity receiver. After introducing some terminology, we start from the early research conducted in the field of coherent lightwave systems, dating back to the 1980s. We then present a short overview of the usage of digital signal processing (DSP) at the receiver side, since the progress in this field is what has driven current research in coherent polarization- and phase-diversity receivers. Finally, we review all recent experiments in the field of coherent optical communications using PSK.

Optical communications using PSK encode digital information on the phase of the optical carrier. QPSK exhibits the best theoretical receiver sensitivity among all two and four level modulation formats (9 photons/bit at the shot-noise limit), while offering a theoretical spectral efficiency of 2 b/s/Hz [7]. It encodes 2 bits per modulation symbol, thus halving the symbol rate R_S compared to the bit rate R_b. Employing PDM can further increase the theoretical spectral efficiency to 4 b/s/Hz, encoding 4 bits per modulation symbol, while reducing R_S to a quarter of the overall bit rate. PDM-QPSK can, thus, enable transmission of 40 Gbps data with a 10 GBd symbol rate. This alleviates the need for upgrading system components' bandwidth to 40 GHz, increases tolerances to propagation effects (Chromatic Dispersion - CD and Polarization Mode Dispersion - PMD), and offers resilience to non-linearities.

Two different detection techniques can be employed for optical QPSK. The first, coherent detection, is based on mixing the received signal with the light of a laser situated at the receiver end, which plays the role of a local oscillator (LO). The power spectral density (PSD) of the received signal is downconverted to a frequency equal to the difference between the frequencies of the transmitter and local oscillator laser. The second, interferometric or direct detection, uses a delay interferometer to detect the relative phase difference between two consecutive symbols. At this point, we should point out some abuse of terminology regarding the term *coherent*. In the radio communications literature the term coherent is used to refer to detection techniques in which the absolute phase of the incoming signal is tracked by the receiver. Many of the techniques which have come to be labeled coherent in optical communications are explicitly incoherent in the radio communications literature.

Coherent detection of QPSK is preferred to direct detection because it has the lowest achievable sensitivity (9 photons/bit at the shot noise limit), it exhibits high spectral selectivity and transfers the electric field complex envelope information to the electrical domain, enabling perfect electronic equalization of linear transmission impairments (i.e. CD, PMD) [8]. QPSK and coherent detection can be combined with PDM to achieve a theoretical spectral efficiency of 4 b/s/Hz without any penalty in sensitivity.

Coherent detection can be classified depending on the relative value of the frequencies of the two lasers. The difference between the transmitter carrier frequency f_S and the LO frequency f_{LO} is the *intermediate frequency* (IF) offset, $f_{IF} = f_S f_{LO}$. If $f_{IF} = 0$, the received signal PSD is downconverted directly to baseband. This is the case of *homodyne* coherent detection. If $f_{IF} \geq R_S$, then the received PSD is transferred to the microwave region and an extra downconversion performed in the electrical domain is needed. This is the case of *heterodyne* coherent detection. If $f_{IF} < R_S$, then the received PSD is transferred around baseband and an extra downconversion must be performed in the electrical domain. This is the case of *intradyne* coherent detection [10]. Each of these coherent detection methods have their advantages and disadvantages.

The best sensitivity for optical QPSK modulation is achieved using homodyne receivers (9 photons/bit at the shot noise limit). However, homodyne detection needs a mechanism for locking the phase of the local oscillator to the phase of the received signal, which is traditionally performed using an optical phase-locked loop (OPLL). This technique imposes extremely stringent requirements on the spectral linewidths of the lasers [9]. On the other hand, heterodyne detection needs only frequency locking, but has a 3-dB receiver sensitivity penalty (18 photons/bit at the shot noise limit) and needs wideband electronic equipment in the microwave region.

A compromising solution is the *phase-diversity* receiver, which is a homodyne technique but doesn't necessarily need phase locking. Using a device named a 90° *optical hybrid* at the front end of the receiver produces different trigonometric functions of the complex envelope of the optical field, and produces an analogue version of it at the electrical domain, using photodiodes. Subsequently the electrical signal is digitized by analog-to-digital converters (ADCs) and the electrical field complex envelope is reconstructed in a digital signal processor. The phase information is manipulated using digital signal processing (DSP) algorithms. Digital phase estimation techniques have been developed, alleviating the need for the two lasers to be frequency-, or phase-locked. When using free running lasers, detection is inevitably intradyne [10]. Again, some abuse of terminology exists. The diversity technique, well-known in radio links, describes the transmission over two or more different transmission paths (e.g., antenna diversity). Usually these paths are chosen in order to obtain statistically independent signals in each receiver branch. However, in optical phase-diversity receivers, the transmitted signal (lightwave) is split not until the receiver end. As the signals in the two receiver branches are only different trigonometric functions of the same argument they are not statistically independent.

Polarization-independent operation can be achieved using a polarization-diversity receiver, implemented by doubling the receiver complexity, and performing phase-diversity on the two orthogonal polarizations composing the received optical signal. PDM can then be implemented with no extra cost in receiver complexity, assuming polarization-diversity is used, and with no additional sensitivity penalty.

Since polarization- and phase-diversity coherent intradyne QPSK receivers need DSP algorithms for feedforward phase recovery, high-speed sampling and processing is needed. Integration of DSP circuits is normally not an issue and thus, a number of other DSP functions can be implemented, apart from phase recovery. A practical 10 GBd system will need two fold sampling per symbol (sampling at the Nyquist rate) for using efficient DSP algorithms. Unfortunately, commercially available technology does not yet support sampling and ADC at these rates. Despite this, commercially available Digital Storage Oscilloscopes (DSOs) can sample at frequencies as high as 50 GHz and have been used in a multitude of experiments, demonstrating all the aforementioned properties of QPSK and PDM-QPSK, at bit rates as high as 100 Gbps. Only recently, has an application specific integrated circuit (ASIC) been manufactured by Nortel, which performs PDM-QPSK real time reception at a line rate of 40 Gbps (10 GBd) [11].

Coherent systems attracted considerable attention in the 1980s. They were initially considered as a means to increase receiver sensitivity compared to conventional intensity modulation direct detection (IM/DD) systems, and in this way extend unrepeated system transmission reach. They were also seen as a means to permit tighter packing of signals in frequency, due to increased receiver selectivity, owing to the ability to use narrowband electrical filters rather than wideband optical filters. In this context, initially, the performance of various modulation formats with coherent demodulation was investigated and compared, amongst them: ASK, PSK, differential PSK (DPSK), and frequency shift keying (FSK), using both homodyne and heterodyne demodulation. Many excellent reviews exist for the research performed at this period, e.g. [12]–[16], and references therein, and many text books were written at the same period, e.g., [17]–[20].

Practical limitations hindered the achievement of theoretically predicted sensitivities; however, remarkable improvements were made in receiver sensitivity compared to conventional IM/DD systems. Limitations included large laser phase noise, polarization wandering due to fiber movement, restrictions in attainable bandwidth of electronic devices, especially for large bit rates, the low output power of the LO, and a spectral noise peak of semiconductor lasers at some gigahertz, affecting large bit rate experiments. Homodyne detection, which resides on phase-locking, imposed extremely stringent constraints on laser phase noise, because it used an OPLL, which is extremely sensitive to random phase changes. Heterodyne detection, relaxes the constraints on laser phase noise, because it resides on, simpler to achieve, frequency locking [21], [22]. However, it requires complex electronic circuitry with a bandwidth at least twice the bit rate, which was a tough technical constraint at that time, especially for large bit rates. Polarization wandering can, in principle, be combated with a number of ways [23], amongst them polarization-diversity receivers [24].

Due to the problems in realizing homodyne and heterodyne demodulation, phase-diversity was introduced as a neat solution, since it requires frequency-locking, like heterodyne techniques, bit rate electronic circuitry bandwidth, like homodyne techniques, and can easily be combined with polarization-diversity, thus offering polarization-independent system operation [25]–[27]. The first experiment demonstrating polarization- and phase-diversity demodulation of DPSK was conducted as early as 1987 [28], [29], and then for larger bit-rates in 1989 [30], [31]. Naturally, experimental investigation of QPSK followed, and a coherent homodyne phase-diversity experiment was successfully demonstrated in 1990 [32], while others followed [10], [33], [34]. The use of digital signal processing, after detection, to implement a digital phase locked loop (DPLL) for phase tracking, was proposed in [10]. The use of feed-forward phase recovery, suitable for distributed feed-back (DFB) lasers, was implemented in [34].

The concept of a receiver employing linear digital filters and powerful DSP for compensation of transmission effects, also has its roots in the 1990s [36], but was not tested experimentally at that time. The first experimental testing of such a circuit was demonstrated in 2003, where a multi-tap feedforward equalizer (FFE) in a parallel implementation, with 2.5 GHz sampling and symbol-spaced taps, was used to equalize ISI, in a 10 Gbps IM/DD system [37]. Later, a DSO was used to sample a 10 Gbps IM/DD and DPSK demodulated signal, at 20 GHz (fractionally-spaced sampling at 2 samples per symbol) and the resulting samples were processed offline using a maximum likelihood sequence estimator (MLSE), for ISI compensation [38]. The first real-time implementation of an MLSE was implemented in a 10.7 Gbps IM/DD system, in which sampling at 25 GHz was performed [39]. Subsequent technological progress in the field of multi-gigabit sampling and high-speed DSP [40]–[43] have lead to the announcement of the ASIC manufactured by Nortel [11].

Recent record holding experiments, using coherent detection [44]–[110], enlisted in chronological order, indicate at all levels, the superiority of PDM-QPSK systems using coherent intradyne receivers followed by DSP, compared to any other modulation format of inferior or similar complexity.

Coherent experiments can be classified into two main categories: those with off-line signal processing [44]–[55], [58]–[60], [66]–[69], [71], [73]–[76],[78]–[81], [83]–[86], [88]–[93], [95]–[109], and those with real-time signal processing [11],[56], [57], [61]–[63], [70], [72], [76], [77], [82], [87], [94]. The former use a DSO to store a burst of samples (approx. 1–2 million samples) and signal processing is performed off-line. The latter use ADCs and field programmable gate arrays (FPGAs) [56], [57], [61]–[63], [70], [72], [76], [77], [82], or specially designed ADCs and ASICs, using a 90 nm CMOS technology [11], [87], [94]. Another classification of experiments is whether they use DFB lasers with 3-dB laser linewidths larger than 1 MHz, [56]–[59], [61], [62], [64], [70], [72], [74], [76], [77], [82], [85], [86], [90]–[93], [100], [104], [106], or external cavity lasers (ECL) with 3-dB laser linewidths smaller than 200 kHz [44]–[52], [53]–[55], [60], [63], [69], [71], [73], [75], [78], [81], [83], [84], [87]–[89], [94]–[99], [101], [102], [103], [105], [107]–[110] though it has been recently shown that laser phase noise should not be the limiting factor in system performance [111], [112], and, thus, commercially available DFB lasers will eventually be used, in order to keep the system cost low. Finally, experiments can be classified as to whether they use RZ pulse shaping [59], [68], [79], [84], [85], [88], [90], [92], [98], [101], [102], [110], or not.

The first proof-of-concept experiment, demonstrating the feasibility of coherent phase-diversity PSK and digital signal processing, was performed with BPSK and off-line signal processing [44]. A proof-of-concept experiment for digital equalization of chromatic dispersion followed [45], also employing BPSK. The first coherent QPSK experiment performed was at the low symbol rate of 1.6 GBd [46]. The first 10 GBd coherent QPSK experiment was performed over 210 km of dispersion shifted fiber (DSF) [47], [48], while the same experimental setup was used to demonstrate the first WDM PDM QPSK experiment, transmitting three channels with 10 GBd per channel, over 200 km of DSF, on a 16 GHz grid [49]. Electronic dispersion compensation of CD was used in a 10 GBd QPSK experiment for the first time, to compensate the dispersion caused by 200 km of standard single mode fiber (SSMF) [51]. Meanwhile, the possibility of real-time signal processing using FPGAs, for QPSK and PDM QPSK systems was investigated, using 400 MBd and 800 MBd QPSK signals over 63 km of SSMF [56], [57], 2.2 GBd QPSK and 2.5 GBd signals back-to-back [63], [76] 700 MBd PDM QPSK signals over 120 km SSMF [70], [72].

The possibility of using PDM QPSK for the transmission of 100 Gbps signals was investigated by transmitting 10 channels of 25 GBd PDM QPSK signals on a 50 GHz grid over 2375 km SSMF [68]. A multitude of 100 Gbps experiments have followed [79], [85], [86], [88], [90]–[93], [97]–[99], [101], [102], [104], [106], [107], [109], [110]. Higher order modulation formats with coherent detection have also been investigated. Experiments using 10 GBd 8-PSK over 200 km SSMF [52], 20 MBd 128 QAM over 525 km DSF (using OPLL) [55], 1 GBd 64 QAM over 150 km DSF (using OPLL) [69], 12.5 GBd 16 QAM back-to-back [75], 1 GBd 128 QAM over 150 km DSF (using OPLL) [81],[83], 10 GBd 8-PSK over 2800 km SSMF [84], 19 GBd PDM-8-PSK over 640 km SMF [85], [92], 10 GBd 16 QAM over 100 km SSMF[89], [95], 10 GBd PDM 16 QAM back-to-back [96], 20 GBd 64 QAM back-to-back [103], 20 channel 100 GBd 16 QAM over 1022 km [107], 20 GBd 16 QAM over 1022 km [108], 100 GBd 32 QAM over 200 km [109], 8 channel 114 GBd 8 QAM over 800 km [110] were implemented.

Table 1 summarizes record capacities, distances and spectral efficiencies obtained by using coherent QPSK and PDM QPSK.

Table 1 Overview of recent record coherent PSK transmission experiments. Bold characters denote record characteristics or combinations of record characteristics.

Ref.	Format	Baud rate	Channels	Channel Spacing	Spectral efficiency	Distance	Distance capacity product
[49]	PDM QPSK	10 GBd	3	**16 GHz**	2.5 b/s/Hz	200 km	0.024 Tbps.km
[64]	PDM QPSK	10 GBd	–	–	–	**6400 km**	–
[85]	PDM 8-PSK	19 GBd	8	25 GHz	**4.2 b/s/Hz**	640 km	0.58 Pbps.km
[86]	PDM QPSK	25 GBd	**164**	50 GHz	2 b/s/Hz	2550 km	41.8 Pbps.km
[104]	PDM QPSK	25 GBd	155	50 GHz	2 b/s/Hz	**7200 km**	**112 Pbps.km**
[105]	PDM QPSK	**56 GBd**				2500 km	

IV.   Optical PDM QPSK communications systems

This section is devoted to describing a practical coherent PDM-QPSK optical communications system. All necessary optical components are described and modeled. The models described are implemented in MATLAB and incorporated in a commercially available simulation environment, VPI TransmissionMaker [113].

1.   The optical QPSK transmitter

An optical single polarization (SP) QPSK transmitter is composed of a continuous wave (CW) laser, an optical QM, and appropriate driving circuitry. The block diagram of an optical QPSK transmitter is shown in Fig. 9. The light from the CW laser is equally split, and each part BPSK modulated, in each of the two branches of the QM. Each branch of the QM is composed of a Mach-Zehnder modulator (MZM). A $\pi/2$ phase-shift difference between the two branches creates two orthogonal phase modulated carriers, which are combined at the output of the modulator, creating a QPSK modulated signal ideally represented by (80). Because the optical QM is constructed of LiNbO$_3$, a birefringent material, a polarization controller (PC) is used to adjust the laser optical field state of polarization (SOP) with the principle axes of the modulator.
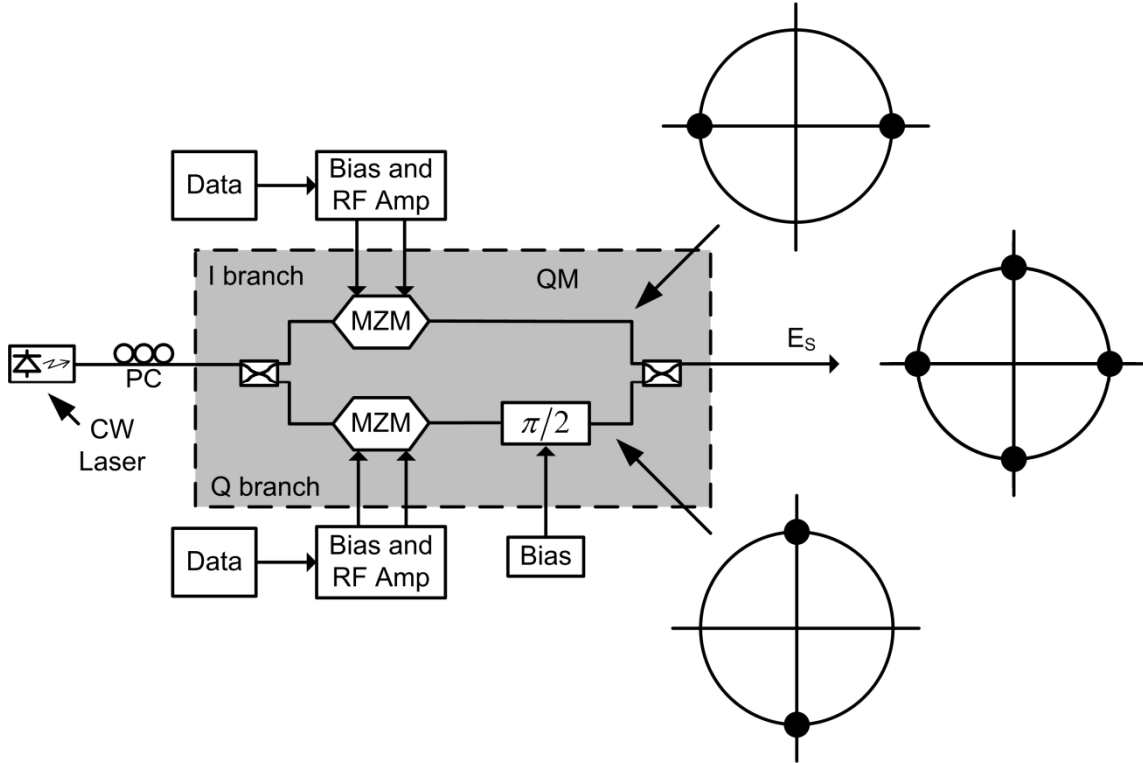
Fig. 9 Schematic diagram of an optical SP-QPSK transmitter. The light from a CW laser is equally split and BPSK modulated in each branch of a QM. A $\pi/2$ phase-shift difference between the two branches creates two orthogonal phase modulated carriers which are combined at the output of the modulator, creating the QPSK modulated signal.

The CW laser is, ideally, a monochromatic source of polarized light of angular frequency $\omega=2\pi f_c t$ and emission frequency f_c. Any practical laser will have variations in the instantaneous emission frequency and SOP. We assume constant linear polarization along a reference SOP, whose normalized Jones vector [114] is denoted as $|e\rangle$ [115], where we have used the Dirac notation for representing 2×1 vectors [115]. The complex envelope of the vector electric field with average power P can thus be written as

$$\tilde{\mathbf{E}}(t) = \sqrt{2P}e^{j\phi_n(t)}|e\rangle \tag{84}$$

where

$$\phi_n(t) = \int_{-\infty}^{t} \dot{\phi}(t')dt' \tag{85}$$

is the time dependent laser phase noise. The instantaneous angular frequency offset $\dot{\phi}(t)$ is modeled as a Gaussian random process with zero mean and variance $2\pi\Delta v\delta(0)$, where Δv is the 3-dB laser linewidth. The phase noise is a Wiener-Lévy random walk process [25], [116].

For the mathematical representation of SOPs, normalized Jones vectors are used. In Stokes space they are depicted as points on a Poincaré sphere with unit radius [114]. The azimuth and ellipticity of the polarization ellipse, α and ε, respectively, are used to calculate the coordinates of normalized Jones vectors, as

$$|e\rangle = \begin{bmatrix} \cos a \, \cos \varepsilon - j\sin a \, \sin \varepsilon \\ \sin a \, \cos \varepsilon + j\cos a \, \sin \varepsilon \end{bmatrix}, \tag{86}$$

which leads to a right-circular Stokes space according to the coordinate convention of [115].

State-of-the-art optical QMs are integrated devices, constructed on x-cut [117], or z-cut [118], y-propagation LiNbO$_3$ crystal substrates, using Titanium in-diffused technology, supporting single-mode transverse electric (TE) propagation. A Mach-Zehnder structure, comprised of two 3-dB Y-junctions, one at its input and one at its output, contains in each of its branches a nested, push-pull, electro-optic MZM. Each of the nested MZMs produce a BPSK modulated waveform. One of the nested MZMs is followed by a $\pi/2$ phase shifter, which serves as a rotator for the BPSK signal space diagram, thus producing four distinct phases after recombining the electrical fields at the output of the modulator. LiNbO$_3$ devices are highly birefringent and so a PC is used at the input of the QM, in order to match the transmitted SOP with the principle axes of the device.

In order to produce a BPSK waveform using a MZM, the bias voltage circuit should bias the MZM at a transmission null and the radio frequency (RF) circuit should produce a peak-to-peak voltage swing equal to $2V_\pi$, V_π being the half-wave voltage of the substrate electro-optic material [119], [120]. This biasing and RF drive voltage configuration transits the MZM between two consecutive transmission maxima, which produce electrical fields with a π phase difference. The RF drive voltage is usually the appropriately scaled output of a binary data source, which produces bits at a rate of R_b. The shape of the RF drive voltage pulse $g(t)$ determines the transition trajectory and speed, and affects the output pulse shape, as shown in Fig. 10, for BPSK modulation. The two binary data sources at the input of the QM have an aggregate bit rate of $2R_b$ which results in a symbol rate at the output of the modulator equal to $R_S = R_b$.

The expression for the QPSK modulated electrical field analytic signal $\hat{\mathbf{E}}_S(t)$ at the output of an ideal, polarization-independent QM, with respect to the input electrical field $\hat{\mathbf{E}}_{in}(t)$ is (Appendix D)

$$\hat{\mathbf{E}}_S(t) = \frac{1}{2}\left\{\sum_{k=0}^{\infty} d_k \sin\left[\frac{\pi}{2}g(t-kT_S)\right]\right\}\hat{\mathbf{E}}_{in}(t) \tag{87}$$

where d_k is the complex modulation symbol, k denotes the k–th symbol period and $g(t)$ is the pulse shape at the output of the RF circuit, assumed to be the same for both branches. Propagation losses in LiNbO$_3$ waveguides are not taken into account. The QM incurs at least a 3 dB insertion loss due to its principle of operation.

The modulation procedure described in (87) corresponds to SP-QPSK modulation. PDM-QPSK modulation is performed by QPSK modulating two orthogonal SOPs using two QMs, and combining the two SP-QPSK signals after modulation. The electrical field from a CW laser source is split into two orthogonal polarization components using a polarization beam splitter (PBS). A PC is used to align each of the SOPs with the principle axes of each QM. Each of the polarization components are

independently QPSK modulated. After modulation, a PC is used to transform each of the two polarization components back to being orthogonal once again. The QPSK modulated signals are combined using a polarization beam combiner (PBC) to form a PDM-QPSK modulated signal. The schematic diagram of the PDM-QPSK transmitter is shown in Fig. 11. We can assume, for simplicity, that the PBS produces polarized signals along the $|x\rangle$ and $|y\rangle$ reference axes. The expression for the output electrical field is then formulated as

$$\hat{\mathbf{E}}_S(t) = \frac{1}{2}\left\{\sum_{k=0}^{\infty} d_{k,x} \sin\left[\frac{\pi}{2}g(t-kT_S)\right]\right\}\hat{E}_{In}(t)\langle x\,|\,e\rangle|x\rangle + \frac{1}{2}\left\{\sum_{k=0}^{\infty} d_{k,y} \sin\left[\frac{\pi}{2}g(t-kT_S)\right]\right\}\hat{E}_{In}(t)\langle y\,|\,e\rangle|y\rangle \quad (88)$$

where $d_{k,x}$ and $d_{k,y}$ are two independent complex modulation symbols for polarization tributaries x and y, respectively.
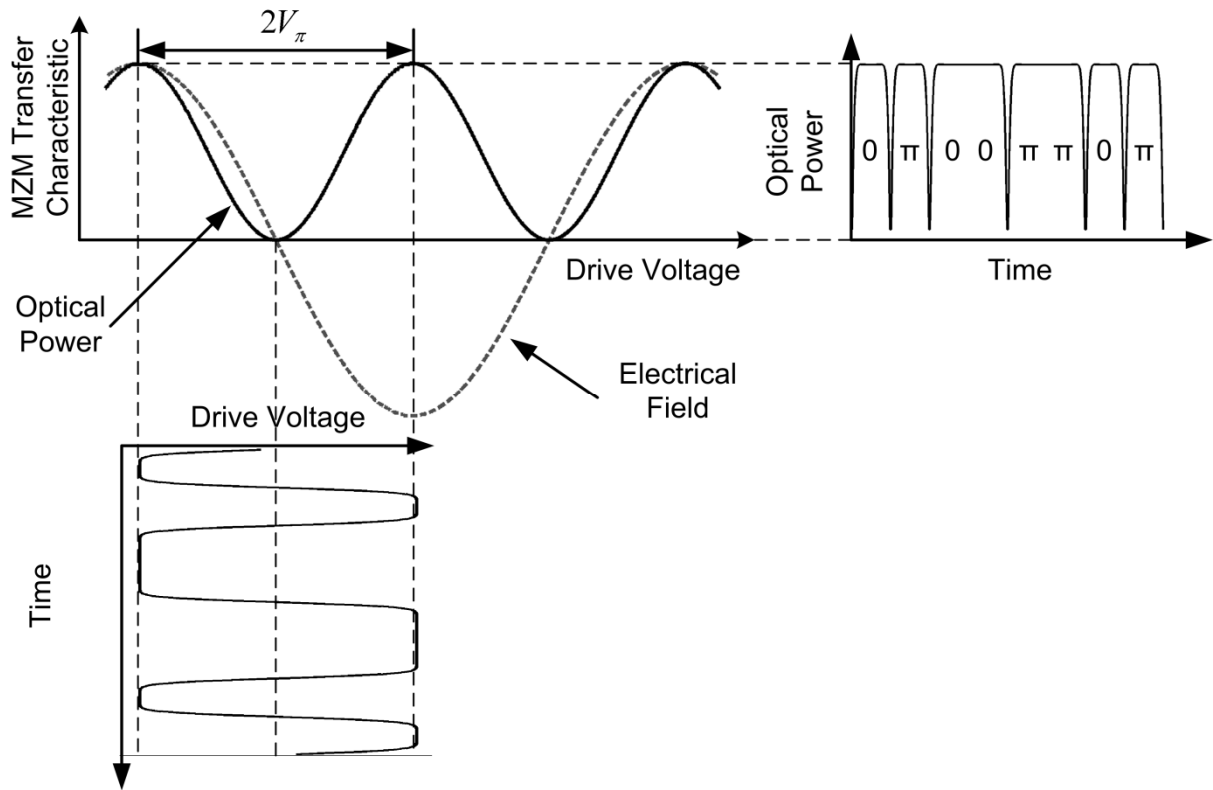
Fig. 10 Mach-Zehnder modulator transmission characteristic, with examples of the bias and RF voltages used for BPSK modulation and the corresponding output optical power (Adapted from [121]).
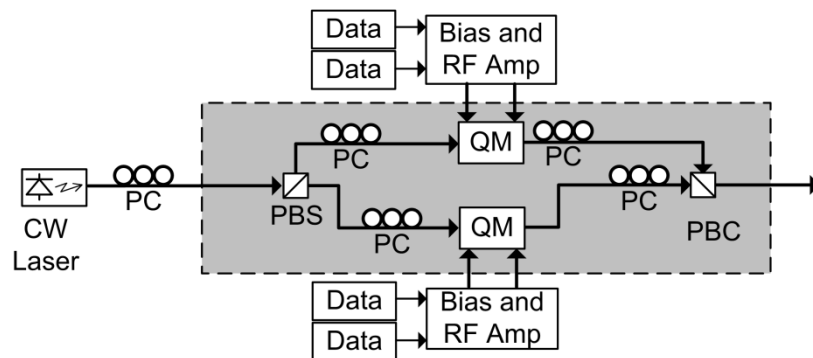
Fig. 11 Schematic diagram of an optical PDM QPSK-transmitter.

2. The optical coherent phase-diversity receiver

In the context of this thesis, we study an optical coherent polarization- and phase-diversity receiver. Such receivers were first investigated in [25]–[27].

An optical coherent receiver downconverts the optical PSD of the modulated optical signal to baseband, or the microwave region, transforming it into an electrical signal for further processing. The electrical signal is simply the measured interference between a modulated signal and a CW laser playing the role of the LO. The electrical signal conveys all phase and amplitude information of the modulated optical signal. The function of the rest of the receiver is to retrieve the modulation symbols from the coherent beating term. Depending on the relative frequency difference between the modulated and LO optical signal compared to the symbol rate, receivers can be categorized as homodyne, heterodyne and intradyne (Section III).

The aforementioned concept of an optical coherent receiver is illustrated in Fig. 12, where the simplest of all coherent receivers is shown. A lossless, semi-transparent mirror is used to produce the linear superposition between the received and CW signal, followed by a single photodetector. Assume that the received analytic signal is

$$\hat{\mathbf{E}}_S = \sqrt{2P_S} \exp\left[j\left(2\pi f_S t + \phi_{n,S} + \phi_k\right)\right] |e_S\rangle \tag{89}$$

and the LO analytic signal is

$$\hat{\mathbf{E}}_{LO} = \sqrt{2P_{LO}} \exp\left[j\left(2\pi f_{LO} t + \phi_{n,LO}\right)\right] |e_{LO}\rangle \tag{90}$$

where P_S, P_{LO} are the average optical powers, f_S, f_{LO} are the carrier frequencies, $\phi_{n,S}$, $\phi_{n,LO}$ are the laser phase noises, and, $|e_S\rangle$, $|e_{LO}\rangle$ are the normalized Jones vectors, for the modulated and LO signals, respectively. φ_k is the modulation phase corresponding to the k-th symbol interval. We further assume that the SOPs are identical and constant, and thus drop vector notation. The resulting superposition of electrical fields yields

$$\hat{E}_r(t) = \frac{1}{\sqrt{2}}\left(\hat{E}_S(t) + j\hat{E}_{LO}(t)\right) \tag{91}$$

The received light illuminates a single photodiode with responsivity R. The photocurrent is given by

$$i(t) = \frac{1}{2}R\left\langle \hat{E}_r(t)\hat{E}_r^\dagger(t)\right\rangle \tag{92}$$

where the angle brackets denote time averaging over an interval proportional to the response time of the photodiode and † denotes complex conjugation. Substituting (89), (90) into (92) yields

$$i(t) = \underbrace{R\left[P_S + P_{LO}\right]}_{\substack{\text{direct-detection} \\ \text{term}}} + \underbrace{R\sqrt{P_S P_{LO}}\cos(2\pi f_{IF} t + \Delta\phi_n + \varphi_k)}_{\substack{\text{coherent-detection} \\ \text{term}}} \tag{93}$$

The resulting photocurrent bears the modulation phase φ_k, the IF offset $f_{IF} = f_S$-f_{LO}, and the laser phase noise difference $\Delta\phi_n = \phi_{n,S} - \phi_{n,LO}$. The modulation phase has to be extracted by the rest of the receiver circuitry.

A profound setback of this simple receiver is evident from (93). If the argument of the coherent-detection term becomes $\pi/2$, all modulation information is lost. Phase-diversity receivers on the other hand produce two coherent-detection terms, which are in quadrature, i.e., a sine and cosine term, ensuring that no information is lost, irrespective of the phase argument. This is achieved by producing two or more linear superpositions of the input optical fields in a device called an optical 90° hybrid, which is followed by an appropriate number of photodiodes.

Optical 90° hybrids are multiport optical devices [122]. A number of different hybrid types exist. The most common optical hybrid type is a 2×4 90° optical hybrid composed of four directional couplers, which split and re-mix the two input signals, and two phase shifters, which introduce appropriate phase shifts between the signal components. An integrated form of this hybrid has been proposed [123], constructed [117], and used [124], amongst others. A bulk component hybrid following the same principle of operation has also been implemented and used [44].
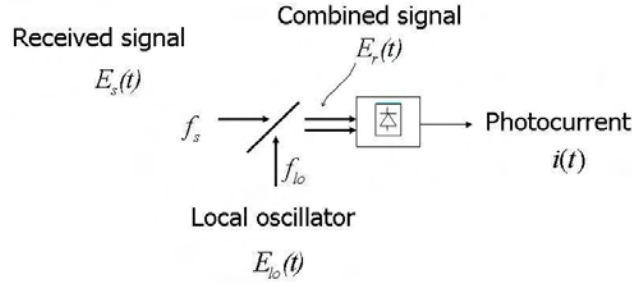
Fig. 12 Schematic diagram of the simplest form of an optical coherent receiver.

The generic block diagram of a phase-diversity receiver, producing the two quadrature coherent-detection photocurrents, is shown in Fig. 13a. Fig. 13b shows the block diagram of the phase-diversity receiver utilizing the aforementioned 2×4 90° optical hybrid, followed by two balanced photodetectors (BPDs). Each of the input directional couplers split the optical signals at their inputs into two equal components. These signals are then intermixed at the output directional couplers, after being shifted relative to each other by the phase shifters. For ideal operation, the upper phase shifter does not shift the optical signal (i.e., phase shift 0°), and the lower phase shifter shifts the optical signal by 90°. Assuming identical SOPs for the two input signals and dropping the polarization notation, the signals impingent to the four photodetectors are proportional to $\hat{E}_S - \hat{E}_{LO}$, $j\hat{E}_S + j\hat{E}_{LO}$, $j\hat{E}_S + \hat{E}_{LO}$ and $-\hat{E}_S + j\hat{E}_{LO}$ from top to bottom, respectively. The in-phase and quadrature photocurrents at the output of the phase-diversity receiver are ideally (Appendix E)

$$i_I = R\sqrt{P_s P_{lo}} \cos\left(2\pi f_{IF} t + \Delta\phi_n + \varphi_k\right)$$
$$i_Q = R\sqrt{P_s P_{lo}} \sin\left(2\pi f_{IF} t + \Delta\phi_n + \varphi_k\right)$$

(94)

where R is the responsivity of the photodetectors. Perfect balanced detection eliminates common mode terms and suppresses DC.

Another optical hybrid type, used mainly in laboratories, due to its simplicity in construction, is a 2×2 90° optical hybrid constructed of bulk optical components [125]. It is composed of a directional coupler, four polarization controllers and two fiber polarizers. Fig. 13c shows the block diagram of the phase-diversity receiver utilizing this hybrid, followed by two single-ended photodetectors. The two input polarization controllers change the state of polarization of the input signals to linear 45° and circular, respectively. The two output polarization controllers change the principle axes of the polarizers in order to select the linear-x and linear-y polarization components of the optical signals at the output of the 3-dB coupler, respectively. The signals impingent on the photodiodes, are proportional to $\hat{E}_S + j\hat{E}_{LO}$ (quadrature), and $\hat{E}_S + \hat{E}_{LO}$ (in-phase), top to bottom, respectively. Single-ended detection is used. The analytical expressions for the photocurrents are (Appendix F)

$$i_I = \frac{R}{4}\left\{P_S + P_{LO} + 2\sqrt{P_S P_{LO}} \cos\left(2\pi f_{IF} t + \Delta\phi_n + \varphi_k\right)\right\}$$
$$i_Q = \frac{R}{4}\left\{P_S + P_{LO} + 2\sqrt{P_S P_{LO}} \sin\left(2\pi f_{IF} t + \Delta\phi_n + \varphi_k\right)\right\}$$

(95)

where R is the responsivity of the photodetectors. Single-ended detection introduces DC terms.

70

A third way to produce quadrature photocurrents is to use a 3×3 coupler, followed by single-ended photodetectors [111], [126]. Fig. 13d shows the block diagram of the phase-diversity receiver utilizing this hybrid, followed by three single-ended photodetectors. An asymmetric coupler produces three photocurrents, of which two are orthogonal, all containing DC terms [127]. DC terms can, theoretically, be suppressed by using an analog electrical circuit [128]. A symmetric coupler can only produce orthogonal photocurrents using an analog electrical circuit to produce linear combinations of the 3 output photocurrents [82].
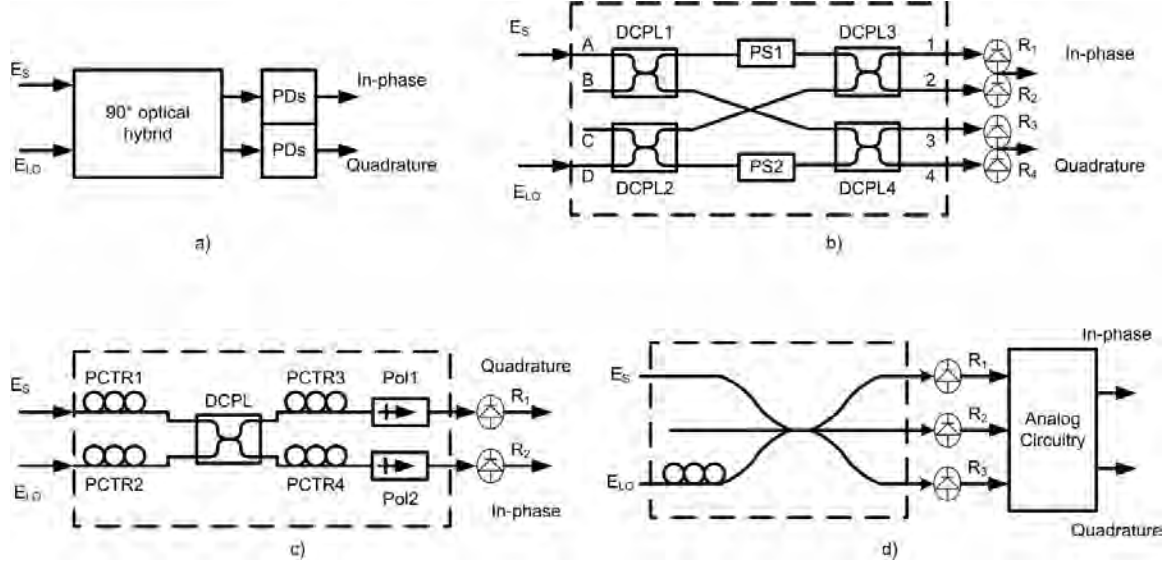
Fig. 13 (a) General block diagram of a phase-diversity receiver, (b) Block diagram of an integrated phase-diversity receiver, (c) Block diagram of a bulk component phase-diversity receiver, (d) Block diagram of a multiport coupler based phase-diversity receiver; (Abbreviations: E_S: received electrical field, E_{LO}, local oscillator electrical field, PD: Photodetectors, In-phase: In-phase (I) photocurrent, Quadrature: Quadrature (Q) photocurrent, PCTR: Polarization controller, DCPL: Directional coupler, Pol.: Fiber linear polarizer, PS: Phase shifter, R: Responsivity).

Regardless of the hybrid type and the number of photodetectors used at the output of the phase-diversity receiver, the analysis in Appendix D and Appendix E shows that two photocurrents are produced, the in-phase, and quadrature components, and their general form is

$$
\begin{aligned}
i_I(t) &= I_I + I_{ip}\cos\left(2\pi f_{IF}t + \Delta\phi_n + \varphi_k + \varepsilon\right) \\
i_Q(t) &= I_Q + I_{qp}\sin\left(2\pi f_{IF}t + \Delta\phi_n + \varphi_k - \delta\right)
\end{aligned}
\tag{96}
$$

where I_I, I_Q are the DC components, I_{ip}, I_{qp} are the amplitudes of the in-phase and quadrature photocurrents, and ε, δ, are phase deviations from the ideal. For ideal operation, the two photocurrents should be of equal amplitude, and orthogonal, i.e., $I_{ip} = I_{qp} = I$, and $\varepsilon = \delta = 0°$. Also, the DC component must be constant in time. The ideal photocurrents (96) can most conveniently be represented by a single complex electrical signal $\tilde{i}(t) = i_I(t) + ji_Q(t)$, which can be written as

$$
\tilde{i}(t) = I\exp\left(2\pi f_{IF}t + \Delta\phi_n + \varphi_k\right).
\tag{97}
$$

3. The optical coherent polarization- and phase-diversity receiver

All phase-diversity receivers described in the previous section have polarization dependent performance. They require specific SOPs for the received and LO signal in order to produce the two orthogonal photocurrents. This introduces the requirement for constant polarization control, or for the use of polarization-diversity receivers [23], [24]. Polarization-diversity receivers achieve SOP-independent performance, by retrieving the information from both orthogonal polarizations comprising the incoming signal, and combine it into a polarization-independent signal. Polarization-diversity is essential for un-interrupted transmission of SP-QPSK signals where polarization drifting can cause zero received power in one of the phase-diversity receivers and maximum power in the other, and vice-versa. In this case a polarization combiner (POLCOMB) algorithm is used. Polarization-diversity is *imperative* for demodulation of PDM signals since polarization demultiplexing requires the complex envelope of both the received orthogonal polarizations. In this case, a polarization demultiplexer (POLDMUX) algorithm is used.

The block diagram of a phase- and polarization-diversity coherent receiver is shown in Fig. 14. The incoming signal is split into two orthogonal polarizations in a PBS. The light of the local oscillator, ideally linearly polarized at 45°, is equally split by a PBS. Each of the incoming signal polarization tributaries are mixed with the light of the LO in a phase-diversity receiver. Regardless of the optical hybrid type, the photocurrents produced at the output of each phase-diversity receiver correspond to the in-phase and quadrature components of the electric field of the input polarization tributary.
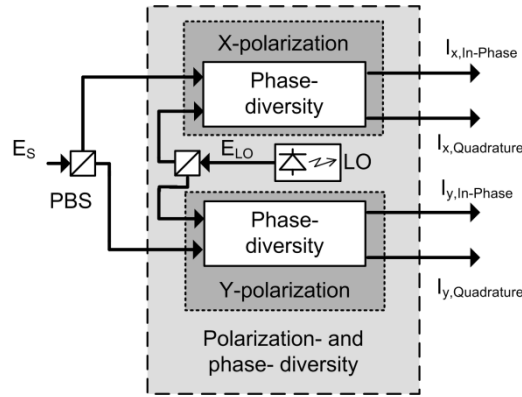
Fig. 14 Block diagram of a phase- and polarization-diversity coherent receiver; (Abbreviations: E_S: Received electrical field; PBS: Polarization beam splitter; E_{LO}: Local oscillator electrical field; $I_{X, In-phase}$: In-phase photocurrent for the X polarization optical hybrid; $I_{X, Quadrature}$: Quadrature photocurrent for the X polarization optical hybrid; $I_{Y, In-phase}$: In-phase photocurrent for the Y polarization optical hybrid; $I_{Y, Quadrature}$: Quadrature photocurrent for the Y polarization optical hybrid).

4. Photocurrent expressions for back-to-back operation

In SP-QPSK systems, the analytic signal at the transmitter (87) can be written in simplified form, omitting the pulse shape, and pulse train term, as

$$\hat{\mathbf{E}}_S = \sqrt{2P_S}\, e^{j\left(2\pi f_c t + \phi_{n,S}\right)} e^{j\varphi_k} \left| e_S \right\rangle = \sqrt{2P_S}\, e^{j\left(2\pi f_c t + \phi_{n,S}\right)} e^{j\varphi_k} \begin{pmatrix} \sqrt{1-r} \\ \sqrt{r}\, e^{j\eta} \end{pmatrix} \tag{98}$$

where we have used an alternative form for expressing the normalized Jones vector, utilizing the power splitting term r between the two polarization components, and the phase difference η between the two polarization components [114]. The analytic signal of the electric field of the local oscillator, linearly polarized at 45°, is similarly written as

$$\hat{\mathbf{E}}_{LO} = \sqrt{2P_{LO}}\, e^{j\left(2\pi f_{LO} t + \phi_{n,LO}\right)} \frac{1}{\sqrt{2}} \begin{pmatrix} 1 \\ 1 \end{pmatrix} \tag{99}$$

A small section of optical fiber (as in back-to-back operation), can be modeled as a 2×2 unitary Jones matrix with complex elements [115]

$$\mathbf{J} = \begin{pmatrix} J_{11} & J_{12} \\ J_{21} & J_{22} \end{pmatrix} \tag{100}$$

which should satisfy the Caley-Klein form [115], i.e., $J_{21} = -J_{12}^*$ and $J_{22} = J_{11}^*$. This matrix corresponds to a rotation on the Poincaré sphere, expressed by an azimuth and an ellipticity α, ε, not to be confused with the azimuth and ellipticity of the SOP of the lasers. Matrix (100) can thus be expressed in a different parametric form as a function of two variables [114], as

$$\mathbf{J}(a,e) = \begin{bmatrix} \cos\alpha\cos\varepsilon - j\sin\alpha\sin\varepsilon & -\sin\alpha\cos\varepsilon + j\cos\alpha\sin\varepsilon \\ \sin\alpha\cos\varepsilon + j\cos\alpha\sin\varepsilon & \cos\alpha\cos\varepsilon + j\sin\alpha\sin\varepsilon \end{bmatrix} \tag{101}$$

Assuming that both phase-diversity receivers are ideal and produce no DC components, the complex photocurrents at the two phase-diversity receivers, corresponding to the x and y reference polarization components of the received signal, are

$$\tilde{i}_X = I\left(\sqrt{1-r}\,J_{11} + \sqrt{r}\,J_{12}e^{j\eta}\right) e^{j\left(2\pi f_{IF} t + \Delta\phi_n + \varphi_k\right)}$$

$$\tilde{i}_Y = I\left(\sqrt{1-r}\,J_{21} + \sqrt{r}\,J_{22}e^{j\eta}\right) e^{j\left(2\pi f_{IF} t + \Delta\phi_n + \varphi_k\right)} \tag{102}$$

Following from the unitary nature of the Jones matrix and the Jones vector, the photocurrents will never be zero simultaneously. Polarization-diversity for SP-QPSK systems thus offer the benefit of continuous reception, although not in the same branch necessarily. Appropriately combining $\tilde{i}_X$ and $\tilde{i}_Y$ into a single complex photocurrent, produces polarization-insensitive reception (Section V. 4).

In PDM-QPSK systems, the analytic signal at the transmitter (88) can be written in simplified form, omitting the pulse shape, and pulse train term, as

$$\hat{\mathbf{E}}_S = \sqrt{2P_S}\, e^{j\left(2\pi f_S t + \phi_{n,S}\right)} \begin{pmatrix} \sqrt{1-r}\, e^{j\varphi_{X,k}} \\ \sqrt{r}\, e^{j\eta} e^{j\varphi_{Y,k}} \end{pmatrix} \tag{103}$$

Assuming that both phase-diversity receivers are ideal and produce no DC components, the complex photocurrents at the two phase-diversity receivers, corresponding to the x and y reference polarization components of the received signal, are

$$\tilde{i}_X = I\left(\sqrt{1-r}\,J_{11}e^{j\phi_{X,k}} + \sqrt{r}\,J_{12}e^{j\eta} e^{j\phi_{X,k}}\right) e^{j\left(2\pi f_{IF} t + \Delta\phi_n\right)}$$

$$\tilde{i}_Y = I\left(\sqrt{1-r}\,J_{21}e^{j\phi_{X,k}} + \sqrt{r}\,J_{22}\varepsilon^{j\eta} e^{j\phi_{X,k}}\right) e^{j\left(2\pi f_{IF} t + \Delta\phi_n\right)} \tag{104}$$

Unlike the single polarization case, in polarization multiplexed systems, transmitted information is in both of the received complex photocurrents. A simple polarization rotation caused by the fiber causes intra-polarization interference between the received photocurrents and polarization–diversity is the only way of retrieving all the transmitted information. Polarization demultiplexing is needed to retrieve the transmitted data (Section V. 4).

The photocurrents are then sampled, and processed by DSP, as will be described in Section V.

5. Coherent optical PDM-QPSK system simulation

In the previous sections, we described all the optical components used in a coherent optical PDM-QPSK system. We now describe the simulation model of the PDM-QPSK system used in the context of this thesis. Its block diagram is shown in Fig. 15. We have incorporated a gray-scale color coding to emphasize the different signal types used in the simulation, i.e., electrical signals, optical signals and sampled signals for DSP.
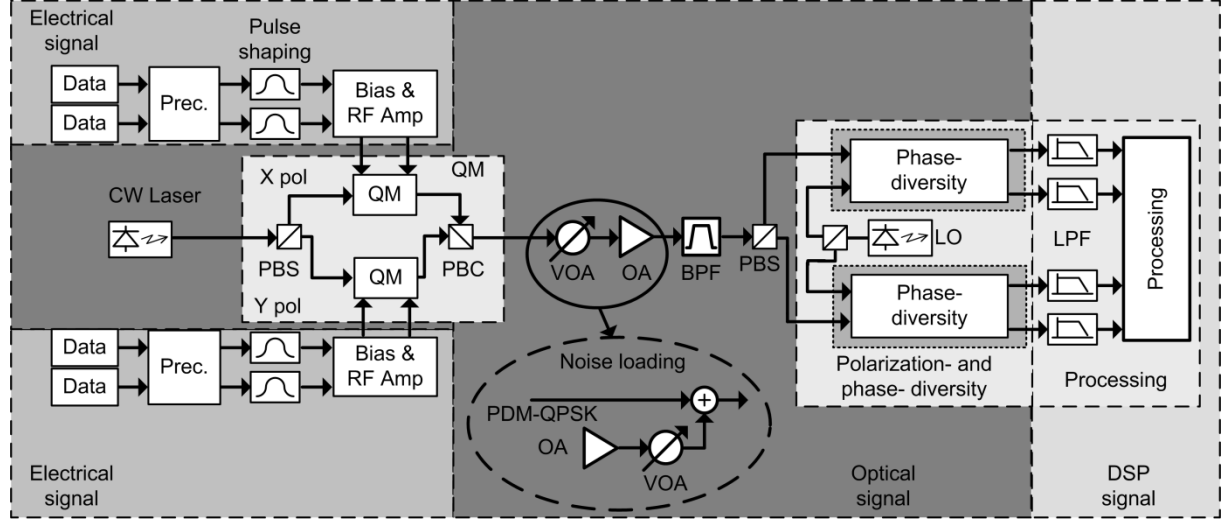
Fig. 15 Block diagram of the optical coherent polarization- and phase-diversity PDM-QPSK system used in the context of this thesis; (Abbreviations: Prec: Precoder, Bias & RF Amp.: Biasing circuit and RF amplifier, PBS: Polarization bam splitter, PBC: Polarization beam combiner, QM: Quadrature modulator, VOA: Variable controlled attenuator, OA: Optical amplifier, BPF, (optical) band-pass-filter, LO: Local oscillator, LPF: Low-pass filter).

The light from a laser diode, linearly polarized at 45°, is split in an ideal PBS with principle axes along the x- and y-polarizations. Each polarization tributary is QPSK modulated in a polarization-independent QM. The QPSK modulated signals are combined in a PBC whose principle axes are aligned with those of the PBS, forming a PDM-QPSK signal. For the modulation of each polarization tributary, two information bit sequences from two independent PRBSs, generated at a rate R_b each, are fed into the precoder. The bit sequences at the output of the precoder are pulse shaped by a 4th-order Gaussian filter with a 0.8 R_b 3-dB bandwidth and then used to drive the QM. The signal at the output of the PDM-QPSK transmitter, having a symbol rate $R_S=R_b$, is attenuated and then amplified by an erbium doped fiber amplifier (EDFA). The later generates amplified spontaneous emission (ASE) noise. The combination of the optical attenuator and the EDFA is used to control the optical signal to noise ratio (OSNR) in order to emulate noise loading (inset)[2] (for details on OSNR measurement see Appendix M). Afterwards, the signal is detected in a polarization- and phase-diversity coherent receiver. A 2×4 90° optical hybrid is used, followed by two balanced photodetectors. Each photocurrent is filtered by a 4th-order Bessel low-pass filter (LPF) with 3-dB bandwidth that is subject to optimization. The photocurrents are then sampled, and processed by DSP algorithms. After a number of DSP algorithms, depending on the simulated phenomena, complex symbol estimation for each polarization tributary is performed and estimates of the transmitted bit sequences are produced.

---

[2] Noise loading is somewhat different from the sequence of components used for measuring the OSNR, but for ideal optical amplifiers with constant gain it is the same. Noise loading involves the use of an amplifier with no input signal and therefore the noise power can be controlled independently from the signal power, whereas in real amplifier models, the noise power depends on the gain of the amplifier

V. Model of the digital coherent receiver and DSP algorithms

Coherent phase- and polarization- diversity receivers have been considered in the context of optical communications, since the 1980's [12]–[20]. However, the advent of the EDFA alleviated the need for the increased sensitivity offered by coherent detection, and hindered the deployment of such systems, due to their cost and complexity. Coherent phase- and polarization- diversity receivers have been revisited recently, due to the advent of another important technological breakthrough, that of multi-gigabit sampling and high-speed DSP [39]–[43].

The photocurrents at the output of a coherent phase-diversity receiver contain the full information of the complex envelope of the modulated optical signal, i.e., its amplitude and phase (Section IV.2, eq. (97)). Sampling the photocurrents transfers this information to the digital domain, and thus demodulation can be performed by DSP. The four outputs of a polarization- and phase-diversity coherent receiver should ideally be sampled at the Nyquist rate. The digitized photocurrents can be used to reconstruct the optical field of both polarizations in the digital domain. A digital coherent receiver is highly advantageous because adaptive DSP algorithms can be used to compensate for time-varying transmission impairments in a very hardware-efficient manner. Digitized signals can be delayed, split and amplified without degradation in signal quality. A multitude of recent papers describe the merits of digital coherent receivers [11], [44], [129]–[137]. All experiments have used DSP to analyze experimental results, either off-line or in real time [44]–[110].

1. Digital coherent receiver architecture

Fig. 16 shows two instances of a typical digital coherent phase- and polarization-diversity receiver used in the optical communications literature. The four photocurrents at the output of the polarization- and phase-diversity receiver are first filtered to remove additive noise. ASE noise and shot-noise are the dominant noise sources in transmission systems using optical amplifiers, whereas receiver thermal noise is negligible [138]. The filtered photocurrents are subsequently sampled in an ADC. Sampling is performed at a sampling rate f_s, which, in general, is an integer multiple of the symbol rate R_s, i.e., $f_s=mR_s$. The two most common cases, and the only ones used in the context of this thesis, are $m=1$ (symbol-spaced sampling) and $m=2$ (fractionally-spaced sampling at twice the symbol rate). Other sampling rates have also been investigated [139]. It is assumed that when symbol-spaced sampling is employed, it is performed at the center of the received pulse, whereas for fractionally-spaced sampling the optimal sampling instant is evaluated for each case separately.

The samples are fed into a DSP unit, where they are processed, using different algorithms to remove transmission impairments and imperfections. When fractionally-spaced sampling is performed, a resampling operation must take place at some stage of the DSP, in order to produce one sample per symbol, which is needed at the end of the processing chain for symbol detection. Once downsampling to one sample per symbol has been performed, the estimates of the transmitted bit sequences can be found and the BER can be counted. Each complex sample corresponds to an estimate of a transmitted complex symbol. From the symbol estimate, estimates of the transmitted bit sequences are produced by a complex symbol detector, using two different configurations. In the first, corresponding to Fig. 16a, differential decoding is performed upon soft estimates[3] of the transmitted complex symbol, followed by hard decision[4] and finally Gray decoding. This is in effect a differential receiver, since the soft decisions are noisy. In the second, corresponding to Fig. 16b, complex symbol hard decision is first performed, followed by differential decoding upon the hard decision estimates, and finally Gray

---

[3] In the context of this thesis, we use the term *soft estimate* to denote the numerical value of a complex symbol expressed in machine-sized floating point accuracy.

[4] In the context of this thesis, we use the term *hard decision* to denote the complex symbol thresholding (slicing) operation performed on soft estimates of a signal and *hard decision estimates* to denote the numerical value at the output of the thresholding circuit. For QPSK, thresholding is performed separately for the I and Q components and the threshold value is zero. The output of the thresholding circuit is ±1, unless stated otherwise.

decoding. This is called the synchronous receiver. The differences in performance between the two receiver architectures will become apparent in subsequent sections (Section VI.1).
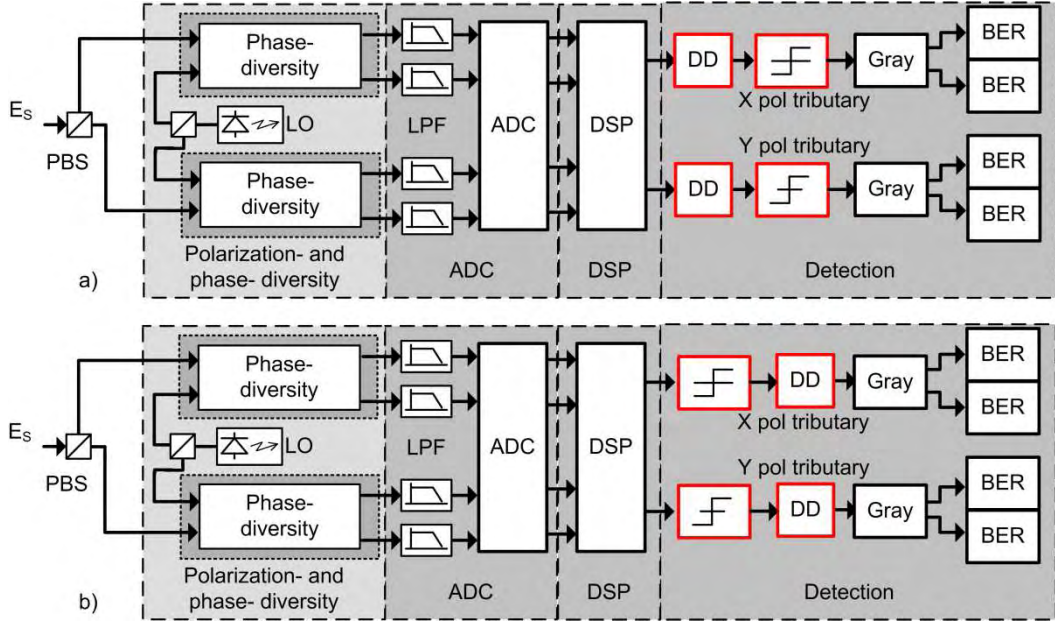
Fig. 16 Block diagram of a digital coherent receiver; a) Differential receiver; b) Synchronous receiver; (Abbreviations: PBS: Polarization beam splitter, LO: Local oscillator, LPF: Low-pass filter, ADC: Analog-to-digital converter, DSP: Digital signal processing unit, DD: Differential decoding, Gray: Gray decoding, BER: Bit-error-rate counting).

In an ideal SP-QPSK system with no transmission impairments, sampling the complex photocurrent at the output of each phase-diversity receiver, with symbol-spaced sampling, at the center of the symbol period, produces (Section IV.4, eq. (102))

$$\tilde{i}_{X,Y}[n] = IA_{X,Y}[n]e^{j\phi_k[n]}e^{j(2\pi f_{IF}nT_S + \Delta\phi_n[n])} + p_{X,Y}[n] \tag{105}$$

while the same operation for a PDM-QPSK system, produces (Section IV.4, eq. (104))

$$\tilde{i}_{X,Y}[n] = I\left\{a_{X,Y}[n]e^{j\phi_{X,k}[n]} + b_{X,Y}[n]e^{j\phi_{Y,k}[n]}\right\}e^{j(2\pi f_{IF}nT_S + \Delta\phi_n[n])} + p_{X,Y}[n] \tag{106}$$

where subscripts X, Y refer to the X and Y polarization phase-diversity receivers, respectively, n denotes the sampling instant, $I = R\sqrt{P_S P_{LO}/2}$ denotes the scaling factor due to optical signal power and photodetector responsivity, A, α, b are complex coefficients depending on the received SOP, and $p[n]$ is a complex Gaussian noise sequence due to additive noise. Each of the real and imaginary parts of $p[n]$ have variance σ_p^2. When the signal and local oscillator lasers have Lorentzian lineshape, the phase noise difference sequence $\Delta\phi_n[n]$ is a Wiener process that is a Gaussian random walk function [140],

$$\Delta\phi_n[n] = \Delta\phi_n[n-1] + w[n] \tag{107}$$

where $w[n]$ is a real Gaussian noise sequence of variance σ_w^2 and $\sigma_w^2 = 2\pi\Delta v/R_S$ and Δv, the combined linewidth, is the sum of the 3-dB laser linewidth of the signal and LO lasers [140]. The intermediate frequency offset f_{IF} will change in real systems due to laser frequency drift, but is relatively constant compared to other time-varying processes, and will be considered as constant in the context of this thesis.

From (105) and (106), it is thus obvious that, even a back-to-back system with noise sources and/or IF offset, needs DSP algorithms to perform demodulation and detection. Algorithms that ensure

polarization-insensitive detection, elimination of phase noise and intermediate frequency, and at the same time robust to ASE noise, are needed.

2. Ideal system eye and constellation diagrams

In this section, we present some typical eye and constellation diagrams (constellations)[5] at the output of the LPF filters of a phase-diversity receiver, in order to familiarize ourselves with the eye diagrams and constellations depicted throughout this and subsequent sections. In the absence of any noise source, or imperfection, the photocurrents at the output of phase-diversity receiver used in a SP-QPSK system, should have two distinct values. This can be easily seen from (102) and (105), where, ideally, the I (real-part) and Q (imaginary-part) photocurrents are the cosine and sine of the modulation phase, respectively. This is depicted in Fig. 17a and Fig. 17b by the dark eye diagram, and in Fig. 17c by the square constellation, composed of dark circles. In lightshade color, Fig. 17 also depicts the eye diagrams and the corresponding constellation, in the presence of a random, constant in time, polarization rotation. Introduction of the SOP dependent terms in (102), changes the phase of the in-phase and quadrature photocurrents, producing two distinct rails in the eye diagram, and rotating the constellation by a constant angle.

Similar color coding is used in Fig. 18 for the case of a PDM-QPSK system. The same rationale can be used for explaining the shape of the eye diagrams and the constellation. The increased number of rails in the eye diagrams and the increased number of points in the constellation, compared to the SP-QPSK case, are due to the fact that the I and Q photocurrents in (104), (106), contain the two modulation phases and the phase introduced by the cross-polarization interference terms, thus producing up to 16 distinct combinations.
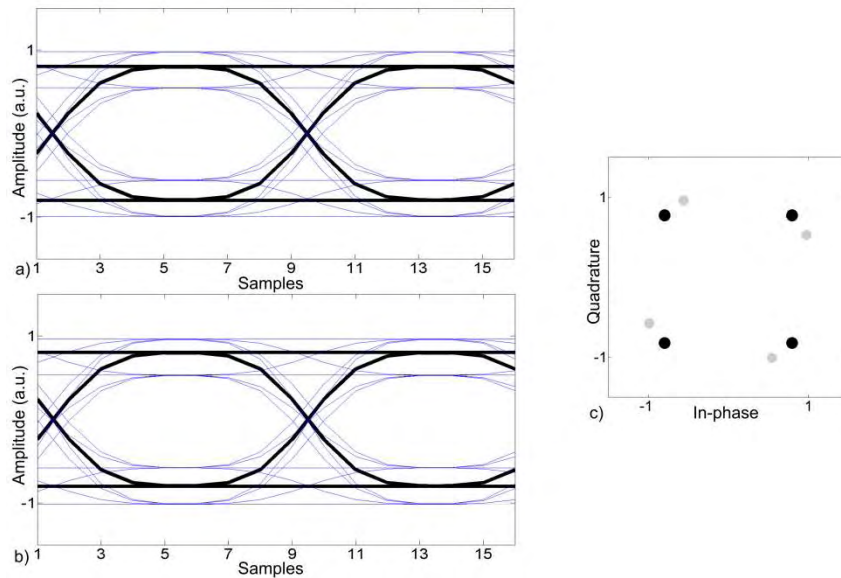
Fig. 17 SP-QPSK system with no noise sources and zero IF offset. (a), (b) Eye diagrams of the received photocurrents at the two outputs of a phase-diversity receiver (X polarization). Dark traces: Ideal eye diagrams; Lightshade traces: Eye diagrams with random polarization rotation c) Corresponding constellation diagrams (same color coding as in (a), (b)). Simulation parameters: Electrical filter: 4th-order Bessel filter with 0.8 R_S 3-dB bandwidth; Random polarization rotation: J_{11}=0.5994-j0.1683, J_{12}=0.1307-j0.7716, J_{21}=0.1307-j0.7716, J_{22}=0.5994+j0.1683.

---

[5] A constellation diagram is a graphical depiction of the signal space diagram for actual signals in a simulation or experimental scenario. Constellations should ideally look like signal space diagrams with arbitrary amplitude. In the presence of impairments or noise, the constellation diagram has a shape which is characteristic to the modulation format but might be much different compared to the corresponding signal space diagram. The constellation diagram is generated from the eye diagram by sampling the eye diagram and depicting the samples on an axis. For QPSK, the I and Q signal eye diagrams are sampled at the middle of the symbol period, and the these samples are depicted on the I and Q orthogonal axes, respectively.
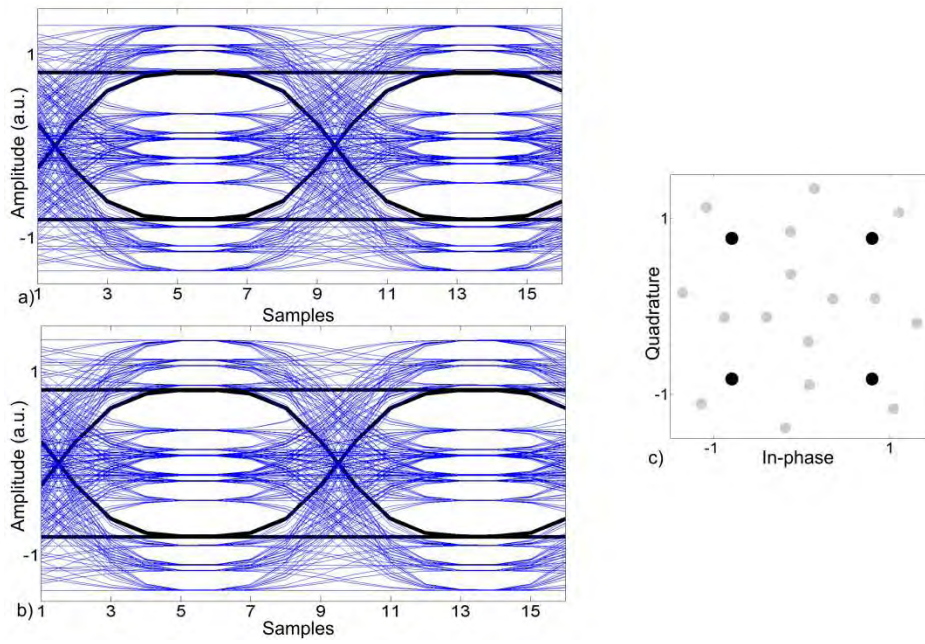
Fig. 18 PDM-QPSK system with no noise sources and zero IF offset. (a), (b) Eye diagrams of the received photocurrents at the two outputs of a phase-diversity receiver (X polarization). Dark traces: Ideal eye diagrams; Lightshade traces: Eye diagrams with random polarization rotation c) Corresponding constellation diagrams (same color coding as in (a), (b)). Simulation parameters: Electrical filter: 3rd -Bessel filter with 0.8 R_S 3-dB bandwidth; Random polarization rotation: J_{11} $J_{11}=0.5994-j0.1683$, $J_{12}=0.1307-j0.7716$, $J_{21}=0.1307-j0.7716$, $J_{22}=0.5994+j0.1683$.

3. Basic elements of equalization

Most signal transformations in linear optical communications systems can be mathematically represented by matrix operations [119]. Therefore, linear transmission impairments can in principle be eliminated by performing inverse matrix operations on the received photocurrent samples. The matrix elements can be scalars or vectors, their elements constant or time varying, updated according to a minimization criterion. In this section, we briefly outline the equalization schemes used in the context of this thesis. For more details see [141]–[143],

An equalizer essentially approximates a discrete inverse impulse response. In matrix form, an equalizer is written as

$$\mathbf{W} = [\mathbf{w}_{i,j}], i, j = 1, 2 \tag{108}$$

where $\mathbf{w}_{i,j}$ are in general vectors, comprised of k elements also called the filter tap weights, which can be written as

$$\mathbf{w}_{i,j} = \left(w_{i,j}^{(1)}, \dots, w_{i,j}^{(k)} \right)^T \tag{109}$$

We assume that the equalizer input is a vector $\mathbf{Y} = [\mathbf{y}_1, \mathbf{y}_2]^T$ whose elements are signal sample vectors containing k samples each, i.e.,

$$\mathbf{y}_i = \left(y_i[n], \dots, y_i[n-k+1] \right)^T, i, j = 1, 2 \tag{110}$$

The output of the equalizer is simply

$$\mathbf{Z} = \mathbf{W}^T \mathbf{Y} \tag{111}$$

where, $\mathbf{Z} = [z_1, z_2]^T$ and z_1, z_2 are, coplex in general, scalars.

The matrix operation described by (111) can be represented by four FIR filters in butterfly structure, as shown in Fig. 19. FIR impulse responses are represented as complex-weight vectors.
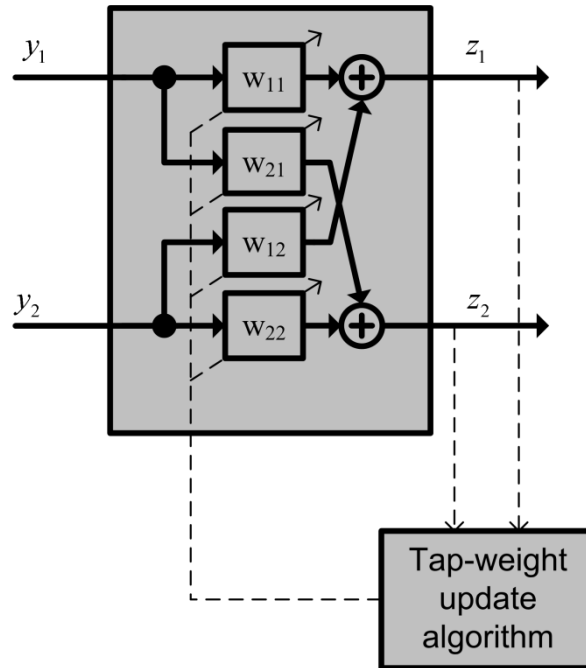
Fig. 19 General form of a butterfly structured filter; (Abbreviations: y_1, y_2: signal sample vectors containing k samples each; z_1, z_2 scalars; $w_{i,j}$: vectors comprised of k elements, also called the filter tap weights).

Matrix estimation can be performed adaptively, sample-by-sample, by minimizing a cost function. Various cost functions and adaptation schemes have been proposed in the literature, depending on the application under consideration. QPSK is a modulation format, which has complex symbols with constant magnitude. Therefore, the constant modulus algorithm (CMA) [141], [144], is well suited for adaptation, due to QPSK envelope constancy. It is widely studied in the optical communications literature, mainly because it is insensitive to phase noise and non-zero IF offsets. Using the stochastic gradient algorithm [141], the recursion for adapting the elements of $\mathbf{W}$, for the simple case of scalar elements, can be written as

$$\mathbf{W}\big[n+1\big] = \mathbf{W}\big[n\big] + \mu \mathbf{Y}^* \left[z_1\big[n\big]\Big\{R_2^{(1)} - \big|z_1\big[n\big]\big|^2\Big\} \quad z_2\big[n\big]\Big\{R_2^{(2)} - \big|z_2\big[n\big]\big|^2\Big\} \right] \tag{112}$$

where

$$R_2^{(i)} = \frac{E\Big\{\big|d_i\big[n\big]\big|^4\Big\}}{E\Big\{\big|d_i\big[n\big]\big|^2\Big\}}, \, i = 1, 2. \tag{113}$$

In the above, $d[n]$ is the transmitted complex symbol at time n, μ is the algorithm step size, affecting the algorithm convergence properties, and $E\{\}$ denotes expectation. For normalized QPSK complex symbols with unit amplitude, $R_2^{(i)} = 1$, $i=1,2$. Variations of recursion (112) were also used, but will be described in separate sections.

The CMA equalizer is the method of choice for performing POLDMUX, since its butterfly structure can emulate the inverse fiber matrix transfer function (100) apart from performing equalization. of ISI. Using the CMA (or its variants), two DSP schemes were implemented in the context of this thesis, shown in Fig. 20. The first, depicted in Fig. 20a, uses the CMA (or its variants) as a POLDMUX and equalizer, and is followed by other processing algorithms. The second, depicted in Fig. 20b, uses the CMA (or its variants) as a POLDMUX, and is followed by an additional equalizer (based on the CMA principle), operating on real valued sample vectors, the I and Q demultiplexed photocurrent samples. Details of the use of this structure will be provided in SectionVII.5. When using fractionally-spaced sampling, it should be noted that the equalizer described by (111) performs downsampling to one sample-per-symbol, since it produces scalar values at its output, regardless of the sample vector size at its input.
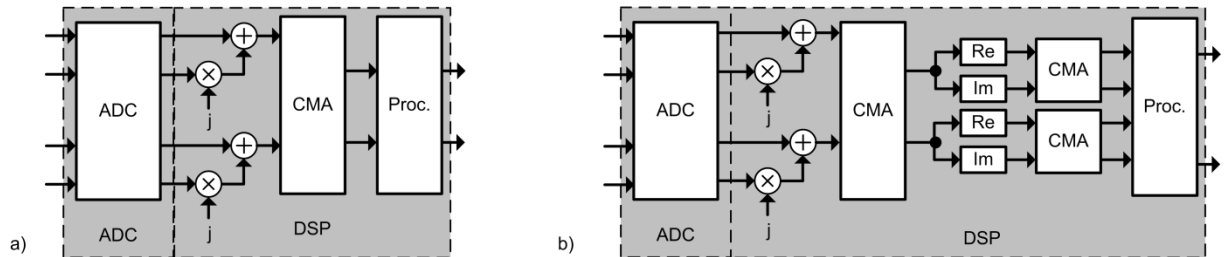
Fig. 20 Block diagram of the two DSP schemes implemented in the context of this thesis. a) The CMA or one of its variants is used for both equalization and POLDMUX; b) The CMA or one of its variants is used for both equalization and POLDMUX, followed by an extra equalization step, acting on the I and Q demulitplexed samples; (Abbreviations: ADC: Analog to digital converter; CMA: Constant Modulus Algorithm equalizer (or variant); Proc.: Processing; Re: Real part of a complex sample; Im: Imaginary part of a complex sample).

4. Polarization combining and polarization demultiplexing

Regardless if SP- or PDM-QPSK systems are used, the received SOP plays an important role on the relative magnitude and phase of the received photocurrent samples, as indicated by (105) and (106). To ensure polarization-insensitive reception for SP-QPSK, a polarization-diversity receiver followed by some sort of polarization combining is needed, in order to produce a single photocurrent, independent of the polarization rotation experienced in the channel. For PDM-QPSK, polarization combining is substituted by polarization demultiplexing, in order to separate the two polarization tributaries. We now describe the various polarization combining and polarization demultiplexing algorithms used in the context of this thesis.

Polarization rotations alter the transmitted SOP and create the need for polarization combining and polarization demultiplexing. They can be modeled as a matrix operation on the transmitted electrical field vectors. The analytic signal representation of the received electric field $\hat{\mathbf{E}}_R$ can be written as

$$\hat{\mathbf{E}}_R = \mathbf{J}\hat{\mathbf{E}}_S \tag{114}$$

where $\mathbf{J}$ is given by (100) or (101), and $\hat{\mathbf{E}}_S$ is given by (98) or (103), for SP-QPSK and PDM-QPSK systems, respectively. Since the complex photocurrents are proportional to the analytic signal of the received electric field, polarization combining and polarization demultiplexing can be performed by estimating the channel's complex conjugate transpose matrix, i.e.,

$$\mathbf{W} = \mathbf{J}^{\dagger} \tag{115}$$

where † denotes the complex conjugate transpose matrix, which equals the inverse of the matrix for unitary matrices. The received complex photocurrent vector $\tilde{\mathbf{I}}[n] = \begin{bmatrix} \tilde{i}_X[n] & \tilde{i}_Y[n] \end{bmatrix}^T$ is transformed into an output complex vector $\tilde{\mathbf{Z}}[n] = \begin{bmatrix} \tilde{z}_X[n] & \tilde{z}_Y[n] \end{bmatrix}^T$ by applying

$$\tilde{\mathbf{Z}}[n] = \hat{\mathbf{W}}[n]\tilde{\mathbf{I}}[n] \tag{116}$$

where $\hat{\mathbf{W}}[n]$ is an estimate of (115) for time sample n. Extending (116) for more samples, produces an equation similar to (111), and therefore polarization combining and polarization demultiplexing can be performed by equalizers.

Various methods have been proposed for estimating the complex filter taps of these equalizers [111], [148]–[156]. In this thesis, we have concentrated on three of them, namely, a decision-directed POLDMUX method [111], a POLDMUX algorithm imposing constraints on the acceptable values of the inverse fiber transfer matrix according to its physical properties, which uses the CMA criterion [156], and the conventional CMA equalizer structure, which imposes no constraints on the acceptable values of the inverse fiber transfer matrix [153]. In the following, we describe the three algorithms. The algorithm performance will be analyzed in Section VI.1.

i. Decision-directed polarization demultiplexer algorithm [111]

The decision-directed method, attempts to estimate the product $\mathbf{Q} = \mathbf{WJ}$, which should ideally produce $\mathbf{Q} = \mathbf{I}$, where $\mathbf{I}$ is the 2×2 unit matrix. It uses the iterative formula

$$\hat{\mathbf{W}}[n+1] = \mathbf{Q}^{-1}[n]\hat{\mathbf{W}}[n] \tag{117}$$

Using a small-signal approximation assuming that $\mathbf{Q} \approx \mathbf{I}$, we can write

$$\mathbf{Q}^{-1}[n] = (\mathbf{I} - (\mathbf{I} - \mathbf{Q}[n]))^{-1} = (\mathbf{I} + (\mathbf{I} - \mathbf{Q}[n])) \tag{118}$$

and use this to produce a new estimate $\hat{\mathbf{W}}[n+1]$, using the recursion

$$\hat{\mathbf{W}}[n+1] = (\mathbf{I} + \mu(\mathbf{I} - \mathbf{Q}[n]))\hat{\mathbf{W}}[n] \tag{119}$$

where μ is the algorithm step size parameter. Matrix $\mathbf{Q}$ is found by the soft and hard decisions of the received complex symbols (see [3,4]), as

$$\mathbf{Q}[n] = \frac{1}{2}\tilde{\mathbf{Z}}[n]\hat{\mathbf{Z}}^{T}[n] \tag{120}$$

where $\hat{\mathbf{Z}}[n]$ is the vector containing the hard decision of complex symbols $\tilde{\mathbf{Z}}[n]$, assuming that all other impairments have been removed (i.e., IF offset, phase noise etc). The factor ½ ensures that $\left|\det\left(\hat{\mathbf{W}}\mathbf{J}\right)\right| \to 1$. Improvement in performance was observed when monitoring $\left|\det\left(\hat{\mathbf{W}}[n+1]\right)\right|$ and preventing it from becoming large, where a value of two was found sufficient after a trial end error investigation. This algorithm is subsequently referred to as the decision directed POLDMUX.

ii. Constant modulus algorithm polarization demultiplexer

The CMA, described in Section V.3, can perform POLDMUX, when using single-tap weights. No constraints are imposed on the acceptable values of the elements of the transfer matrix. For the simple case of single-tap weights [143], the recursion can be written as

$$\hat{\mathbf{W}}[n+1] = \hat{\mathbf{W}}[n] + \mu \begin{bmatrix} \tilde{i}_{X}^{*}[n] \\ \tilde{i}_{Y}^{*}[n] \end{bmatrix} \left[\tilde{z}_{X}[n]\left\{1 - \left|\tilde{z}_{X}[n]\right|^{2}\right\} \quad \tilde{z}_{Y}[n]\left\{1 - \left|\tilde{z}_{Y}[n]\right|^{2}\right\} \right] \tag{121}$$

where μ is the algorithm step size and * denotes conjugation. This algorithm will be subsequently referred to as the CMA POLDMUX.

iii. Constrained constant modulus algorithm polarization demultiplexer [156]

Advantage can be taken from knowledge of the physical properties of the fiber rotation matrix, in order to reduce the number of independently adjustable parameters of the estimated matrix, which produces more accurate results and faster estimations in terms of symbols needed for convergence. The complex conjugate transpose of the fiber rotation matrix (101) can be written as

$$\mathbf{W}(\alpha,\varepsilon) = \begin{bmatrix} \cos\alpha\cos\varepsilon - j\sin\alpha\sin\varepsilon & \sin\alpha\cos\varepsilon - j\cos\alpha\sin\varepsilon \\ -\sin\alpha\cos\varepsilon - j\cos\alpha\sin\varepsilon & \cos\alpha\cos\varepsilon + j\sin\alpha\sin\varepsilon \end{bmatrix} \tag{122}$$

and thus, instead of four complex parameters, two real parameters need only be estimated. We have dropped the sample index n to avoid clutter. Estimates of α and ε, $\hat{\alpha}$ and $\hat{\varepsilon}$, respectively, are obtained in an iterative manner, using

$$\mathbf{D}[n+1] = \mathbf{D}[n] - \mu\nabla\xi[n] \tag{123}$$

where $\mathbf{D}[n]$ is the estimated parameter vector defined as $\mathbf{D}[n] = \begin{bmatrix} \hat{\alpha}[n] & \hat{\varepsilon}[n] \end{bmatrix}^{T}$, μ is the algorithm step size, and the gradient $\nabla\xi(n)$ is defined as

$$\nabla\xi[n] = \begin{bmatrix} \dfrac{\partial\xi[n]}{\partial\alpha} & \dfrac{\partial\xi[n]}{\partial\varepsilon} \end{bmatrix}^{\mathrm{T}} \tag{124}$$

In (123), (124) $\xi[n]$ is the instantaneous cost function defined as

$$\xi = \left(\left|z_{1}[n]\right|^{2} - R_{2}^{(1)}\right)^{2} + \left(\left|z_{2}[n]\right|^{2} - R_{2}^{(2)}\right)^{2} \tag{125}$$

This algorithm will be subsequently referred to as the constrained CMA (CCMA).

iv. Constant modulus algorithm and constrained constant modulus algorithm for polarization combining

Both the CMA and the CCMA POLDMUXs can be used in SP-QPSK systems, in which case, only one of the two outputs are fed to the remaining part of the DSP. A special case of the CCMA POLDMUX algorithm, applicable only to SP-QPSK systems, was also constructed and tested. The channel in this case can be represented by a vector, fully defined by two parameters [114], as,

$$\mathbf{J}(\theta, \chi) = \begin{bmatrix} \cos \chi & \sin \chi e^{j\theta} \end{bmatrix} \tag{126}$$

or a vector fully defined by three parameters

$$\mathbf{J}(\theta, \varphi, \chi) = \begin{bmatrix} \cos \chi e^{j\theta} & \sin \chi e^{j\varphi} \end{bmatrix} \tag{127}$$

A similar procedure compared to (123) and (124) is followed for updating the estimated parameters.

v. Maximal ratio combining for polarization combining

A simple method for POLCOMB, having no analogy in POLDMUX, was proposed in [145], [146], and is based on the theory of Maximal Ratio Combining [147]. It is assumed that the received state of polarization is constant over a period of time much larger than the symbol period.

The ratio of the samples is first calculated as

$$r[n] = \tilde{i}_X[n] / \tilde{i}_Y[n] = A_X / A_Y = A \tag{128}$$

and then their average over a large number of N symbols is found

$$\bar{r} = \frac{1}{2N} \sum_{j=1}^{N} r[j] \tag{129}$$

For the case where $|\bar{r}| < 0.5$, an amplitude and phase factor is calculated

$$b = \frac{|\bar{r}^2|}{1 + |\bar{r}^2|} \tag{130}$$

$$\eta = arg\{\bar{r}\}$$

and a single complex photocurrent, independent of the incoming SOP is formed as

$$\tilde{i}[n] = \frac{1}{\sqrt{b}} \left(i_X[n] + |\bar{r}| i_Y[n] e^{j\eta} \right) \tag{131}$$

When $|\bar{r}| \geq 0.5$, we simply use

$$b = \frac{1 + |\bar{r}^2|}{|\bar{r}^2|} \tag{132}$$

$$\eta = -arg\{\bar{r}\}$$

5. Laser phase noise

Phase noise is an unavoidable impairment in coherent optical communications, due to the fact that the lasers used at the transmitter and receiver side are non-ideal oscillators (Section IV.1). Depending on the laser sources used, the laser 3-dB linewidth can vary from a few hundred kHz (ECLs) to several MHz (DFBs).

Fig. 21 shows the evolution of the phase of a free running laser, exclusively due to the laser phase noise, over a period of 3.5 μs, for three different 3-dB laser linewidths, 500 kHz, 5 MHz, and 50 MHz, respectively.
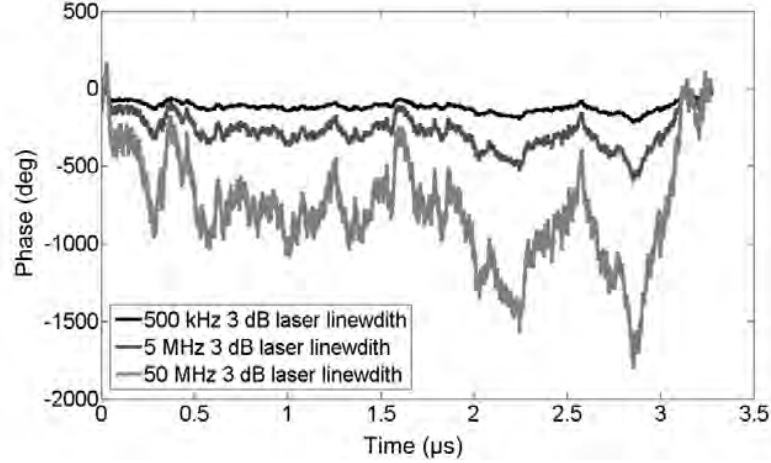
Fig. 21 Evolution of the phase of a free running laser vs time.

In coherent optical systems, the total laser-linewidth × symbol-period product is used as a measure of laser phase noise, denoted as $\Delta v T_S$ or, using the symbol rare, as the ratio $\Delta v/R_S$. Fig. 22 shows representative eye diagrams, and corresponding constellations, at the output of the phase-diversity receiver, for a SP-QPSK system, in the absence of ASE noise and with zero IF, for two cases, $\Delta v T_S = 5 \times 10^{-5}$ (corresponding to 500 kHz laser linewidth at 10 GBd – typical value for an ECL) and $\Delta v T_S = 5 \times 10^{-4}$ corresponding to 5 MHz laser linewidth at 10 GBd – typical value for a good quality DFB).
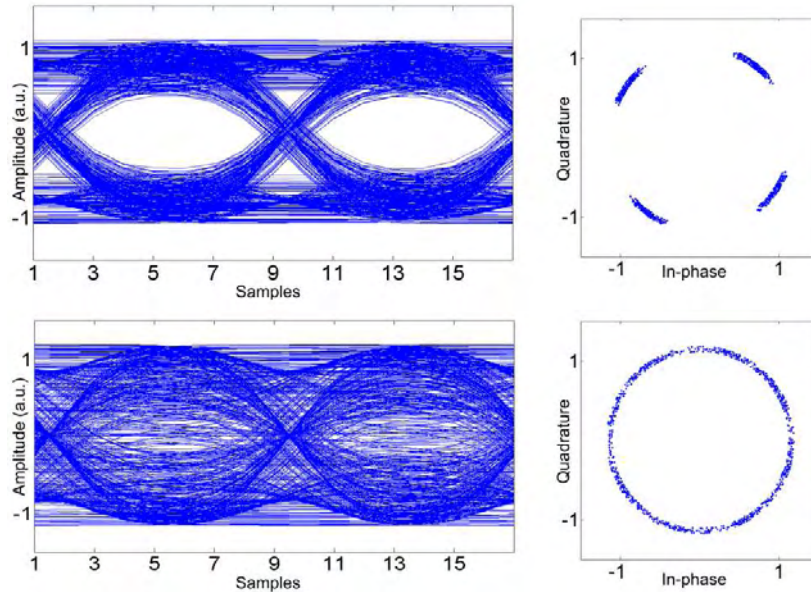
Fig. 22 Eye diagrams and constellation diagrams of the received photocurrents at one of the outputs of a phase-diversity receiver in the presence of phase noise, for a SP-QPSK system. No ASE noise is included and zero

intermediate frequency is assumed; (a), (b) $\Delta v T_S = 5\times10^{-5}$; (c), (d) $\Delta v T_S = 5\times10^{-4}$; (Conditions: NRZ pulses, Electrical filter: 4th-order Bessel with 0.8 3-dB bandwidth, 8 samples per symbol, 5000 symbols).

From the constellations of Fig. 22, it is clear that, if the lasers are free running, the constellation points will, sooner or later, wander into the neighboring quadrant, causing errors. Fig. 23 shows the OSNR penalty due to 3 dB laser linewidth at BER = 10^{-3} for a SP-QPSK system, for both receiver configurations of Fig. 16, the synchronous receiver (Fig. 23a), and the differential receiver (Fig. 23b). As a reference, the required OSNR for BER = 10^{-3} of the synchronous receiver is used, which is the smallest. The differential receiver exhibits a penalty of approximately 1.9 dB for a zero laser-linewidth $\times$ symbol-period product. However, it can support laser-linewidth $\times$ symbol-period products as large as 3×10^{-3} with a penalty smaller than 3 dB (corresponding to a 30 MHz 3-dB laser linewidth at 10 GBd). The synchronous receiver, though beneficial for zero laser-linewidth $\times$ symbol-period products, tolerates orders of magnitude less phase noise. The 3-dB penalty threshold is at a laser-linewidth $\times$ symbol-period product of approximately $1.5\times10^{-6}$ (corresponding to a 10 kHz 3-dB laser linewidth at 10 GBd, which is practically unobtainable). Thus, the differential receiver dramatically increases the phase noise tolerance of the system. However, phase noise estimation and compensation is still essential in phase modulated systems.
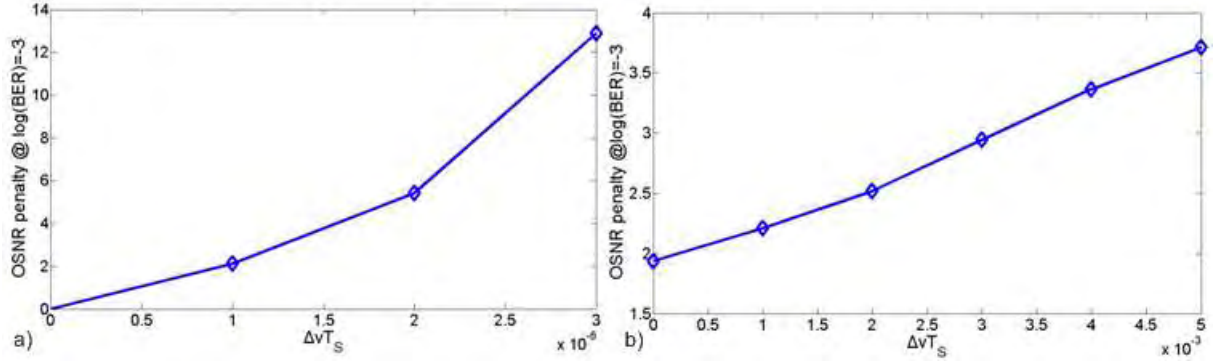
Fig. 23 OSNR penalty vs 3-dB laser-linewidth $\times$ symbol-period product for SP-QPSK systems using: a) Synchronous receiver; b) Differential receiver.

A number of phase noise estimation algorithms have been developed for optical coherent communications systems using digital receivers. A maximum *a posteriori* method for joint estimation of phase noise and transmitted symbols was used to evaluate optimal system performance [140], [157]. Due to the inapplicable nature of joint data- and phase-estimation in real-time systems, other methods have been proposed, estimating data and phase separately. The modulation data must first be removed, and then some form of additive noise reduction must be performed, while the varying phase noise is tracked and reduced. Data modulation can be removed using a decision-directed approach (decision feedback) [140], applying a nonlinearity to the received samples [158], or, recently, by using a multiplier-free, hardware-efficient algorithm [159]. The decision-directed approach has been used in [160]–[163]. The only nonlinearity used in the optical communications literature up to now is the *M*-th power law [111], [140], [157], [164], [165] (Appendix G). Only recently, the multiplier-free approach has been considered for hardware efficient designs [166]–[168]. In the remainder of this section, we describe in detail each algorithm implemented in the context of this thesis.

In the description of all algorithms, we will use as a starting point the same expression for the complex photocurrent samples, (105). In the absence of IF offset, the complex photocurrent at the output of each phase-diversity receiver in a SP-QPSK system, or at the output of the POLDMUX in a PDM-QPSK system, is

$$\tilde{i}_{X,Y}[n] = Ie^{j\phi_{k,X,Y}[n]}e^{j\Delta\phi_n} + p_{X,Y}[n] \tag{133}$$

i.   Decision-directed phase estimation

Decision-directed algorithms make decisions about the received modulation symbols, and by assuming that these decisions are correct, produce a feedback signal to remove the phase noise from the received

samples. There are two similar approaches to decision-directed phase estimation, both of which are depicted in Fig. 24. The main difference lies in the sequence of processing steps, as will be made clear immediately.

The first phase estimation circuit is illustrated in Fig. 24a ([160], [162]). Starting from the complex photocurrent sample given by (133), an estimate of the phase noise $\Delta\hat{\phi}_n[n-1]$ is subtracted from the incoming complex sample $\tilde{i}[n]$. For the first sample, an initial guess is needed (usually a complex symbol with zero phase). The resulting complex sample is

$$\hat{d}[n] = e^{j\phi_k[n]}e^{j\left(\Delta\phi_n[n]-\Delta\hat{\phi}_n[n-1]\right)} + p_1[n] \tag{134}$$

where $p_1[n]$ is a different complex Gaussian noise sequence from $p[n]$ having the same variance σ_p^2. Sample $\hat{d}[n] = \exp\left(j\hat{\phi}_k[n]\right)$ is a soft estimate[3] of complex symbol $d[n] = \exp\left(j\phi_k[n]\right)$. This soft estimate is fed into a complex symbol decision circuit, which produces a hard estimate[4] $\widehat{d}[n]$. The decision circuit has a decision function given analytically by

$$\Gamma(x) = \mathrm{sgn}\left(\mathrm{Re}\{x\}\right) + j\,\mathrm{sgn}\left(\mathrm{Im}\{x\}\right) \tag{135}$$

The complex conjugate of the hard estimate is multiplied by the soft estimate, to remove the data symbol

$$\hat{d}[n]\widehat{d}^*[n] = e^{j\left(\hat{\phi}_k[n]-\bar{\phi}_k[n]\right)}e^{j\left(\Delta\phi_n[n]-\Delta\hat{\phi}_n[n]\right)} + p_2[n] \tag{136}$$

where the asterisk denotes complex conjugation, and $p_2[n]$ is a complex Gaussian noise sequence, different from $p_1[n]$ and $p[n]$, with the same variance σ_p^2. Assuming that the hard estimate $\widehat{d}[n]$ is a correct approximation of the actual complex symbol $d[n]$, the quantity in (136) depends solely on the noise terms. Its argument is used to estimate the new phase noise sample, $\Delta\hat{\phi}_n[n]$, to be used with the next incoming complex sample $\tilde{i}[n]$. The phase noise sample is simply calculated as

$$\Delta\hat{\phi}_n[n] = \mu\,arg\left\{\hat{d}[n]\widehat{d}^*[n]\right\} \tag{137}$$

where μ is the algorithm step size ($0\leq\mu\leq1$). (This algorithm is subsequently referred to as Crivelli's algorithm, after [160]). In practice, the arg{ } function need not be computed, since, as depicted in Fig. 24a, it is immediately followed by the complex exponentiation function.
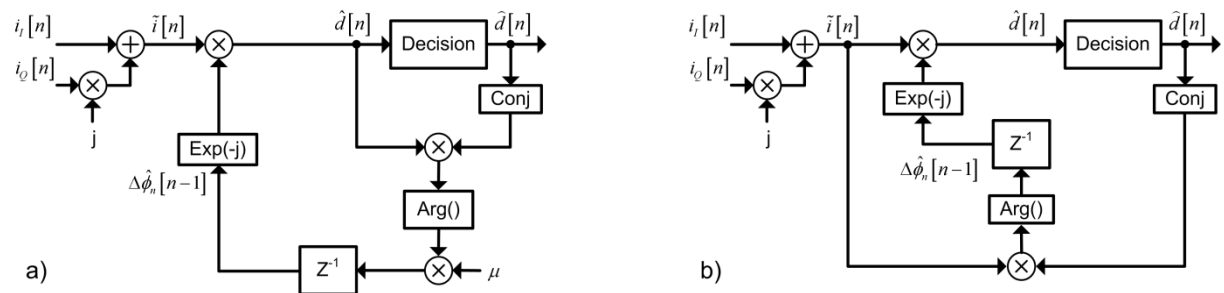
Fig. 24 Block diagrams of decision-directed algorithms for the estimation and compensation of phase noise. a) Crivelli's algorithm [160]; b) Taylors's algorithm [140]; (Abbreviations: exp(-j): Complex exponentiation; Z^{-1}: Single time unit delay; arg(): Complex number argument; Conj.: Complex conjugation; Decision: Complex symbol decision circuit; μ: algorithm step size).

The second approach for decision-directed phase estimation is depicted in Fig. 24b ([140], [161]). Again, an approximation of the phase noise $\Delta\hat{\phi}_n[n-1]$ is subtracted from the incoming complex

sample $\tilde{i}[n]$. The primary difference is that the complex conjugate of the hard estimate of the transmitted complex symbol is multiplied to the *received* complex sample and not the soft decision, i.e., the quantity formed is

$$\tilde{i}[n]\hat{d}^*[n] = e^{j(\phi_k[n]-\hat{\phi}_k[n])}e^{j\Delta\phi_n[n-1]} + p_3[n] \tag{138}$$

where $p_3[n]$ is a complex Gaussian noise sequence, different from $p[n]$, with the same variance σ_p^2. Assuming that the hard estimate is a correct approximation of the transmitted phase, the new phase estimate $\Delta\hat{\phi}_n[n]$ can be directly estimated using the recursion

$$\Delta\hat{\phi}_n[n] = \arg\{\tilde{i}[n]\hat{d}^*[n]\} \tag{139}$$

(This algorithm is subsequently referred to as Taylor's algorithm, after [140]). Again, in practice, the *arg*{} function need not be computed, since, as depicted in Fig. 24b, it is immediately followed by the complex exponentiation function.

Alternatively, a filtering process can be used in (139) to reduce the impact of additive noise, i.e.,

$$\Delta\hat{\phi}_n[n] = \arg\left\{\sum^N \tilde{i}[n]\hat{d}^*[n]\right\} \tag{140}$$

where filtering is performed using a rectangular sliding window of size N (This algorithm is subsequently referred to as Savory's algorithm, after [161][140]). Again, in practice, the *arg*{} function need not be computed since, as depicted in Fig. 24b, it is immediately preceded by the complex exponentiation function. Savory's algorithm is equivalent to Taylor's algorithm for N=1.

ii.   *M*-th power law phase estimation

The *M*-th power law methods for phase estimation rely on the inherent property of *M*-ary PSK modulation formats, that the modulation phase is eliminated if the signal samples are raised to the *M*-th power (Appendix G). If the samples in (133) are raised to the 4-th power, then an estimation of $\Delta\phi_n[n]$ can be obtained, as

$$\Delta\hat{\phi}_n[n] = \frac{1}{4}\arg\{\tilde{i}^4[n]\} = \Delta\phi_n[n] + m[n] \tag{141}$$

where $m[n]$ is a noise process whose statistics are described in Appendix G. However, the process of computing the *arg*{} of a complex number introduces *phase ambiguity* and the phase estimates require *unwrapping* (Appendix H). Thus, the phase sequence described by (141) will be replaced by a new, unwrapped one

$$\Delta\hat{\phi}_n^{unwrap}[n] = \Delta\hat{\phi}_n[n] + \frac{\pi}{2}p \tag{142}$$

where factor p is defined in Appendix H. Unfortunately, unwrapping is a highly non-linear procedure and in the low OSNR or large phase noise regions, is prone to cycle slipping, i.e., phase slips of magnitude $\pi/2$, also called phase jumps, which are undetectable in QPSK because constellation points differing by $\pi/2$ are stable operating points, and thus lead to errors. Two unwrapping procedures were implemented, a rudimentary and a complex one, in an attempt to reduce the number of cycle slips (Appendix H).

The first method implemented for phase estimation using the *M*-th power law, is the FIR filter method [140], [157], [164], [165]. Its block diagram is presented in Fig. 25. The incoming samples are raised to the 4-th power, and the argument is extracted and unwrapped. The unwrapped phases are passed through an FIR filter

$$\Delta\hat{\phi}_{n,filt}^{unwrap}[n] = \Delta\hat{\phi}_n^{unwrap}[n] \otimes w[n] \tag{143}$$

where $\otimes$ denotes convolution, and $w[n]$ is the filter transfer function. The filter has a finite delay Δ and thus the incoming samples are buffered for the same delay. The filtered samples are passed through a complex exponentiation module and multiplied to the corresponding input sample, thus removing the estimate of the phase noise. The FIR filter is a lowpass filter, which smoothes out the additive noise, while tracking the varying phase.
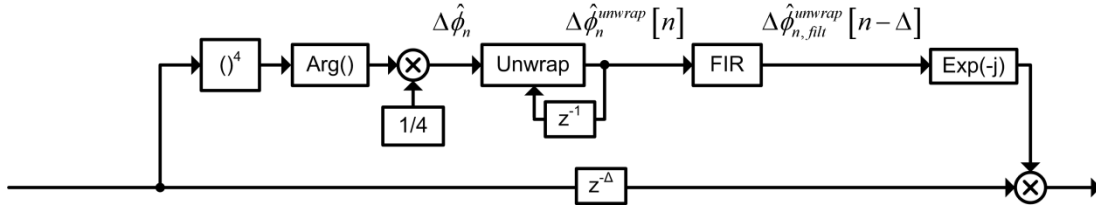

Fig. 25 Block diagram of the M-th power filter method; (Abbreviations: exp(-j): Complex exponentiation; $Z^{-\Delta}$: Δ time units delay; arg(): Complex number argument; Unwrap: Phase unwrapping; FIR: Finite impulse response filter).

The best linear estimate of $\Delta\hat{\phi}_n[n]$ that can be made is by applying a Wiener filter to $\Delta\hat{\phi}_n^{unwrap}[n]$ [157], [140]. There are two kinds of Wiener filters that can be considered, zero-lag (causal) filters, which make estimates for $\Delta\hat{\phi}_{n,filt}^{unwrap}[n]$ based on all $\Delta\hat{\phi}_n^{unwrap}[n]$ up to, and including, the *n-th* sample, and a finite-lag (non-causal) filters, which look up to the symbol $\Delta\hat{\phi}_n^{unwrap}[n+D]$ in the future, where D is a positive integer. Finite-lag filters are expected to give better results because they look forward in time by D symbols, as well as looking into the infinite past. It is trivial to cope with the non-causal nature of the finite lag filter in the digital domain, provided D is kept small, by buffering the unwrapped phases $\Delta\hat{\phi}_n^{unwrap}[n]$ for an extra D samples. Of course a practical filter can not use an infinite number of previous samples so the filter transfer fraction has to be truncated to N coefficients. The transfer function was found to be

$$w[n] = A\left(a^n u[-n-1] + b^n u[n]\right) \tag{144}$$

where $u[n]$ is the unit step function and A, α, b are coefficients defined by the following set of equations

$$
\begin{aligned}
A &= \frac{r}{a-b} \\
a &= \frac{1}{2}\left(2+r+\sqrt{r}\sqrt{r+4}\right) \\
b &= \frac{1}{2}\left(2+r-\sqrt{r}\sqrt{r+4}\right) \\
r &= \frac{\sigma_w^2}{\sigma_m^2}
\end{aligned}
\tag{145}
$$

and σ_m^2 is the variance of noise process $m[n]$ (Appendix G). Due to the unknown details of the statistics of $m[n]$ in the wide range of OSNRs and 3-dB laser linewidths studied in the context of the Monte Carlo simulations, values for parameter r were taken from a list of possible values and the value of the best result was kept. Fig. 26 shows the impulse response of the Wiener filter for a number of values r and in the case where N=15. Fig. 26(a) – (c) show the impulse response of a causal filter, for r=10, r=1, r=0.1, whereas Fig. 26(e) – (g) show the impulse response of a non-causal filter, for r=10, r=1, r=0.1. In all subsequent analysis, the non-causal filter impulse response was always used, since small delays were used. Various approximations of the Wiener solution were investigated. In [164], an approximation using coefficients corresponding to binary numbers was used (hardware efficient). In [111] an integrate and dump filter was used as an approximation. All approximations are compared in Section VI.3.
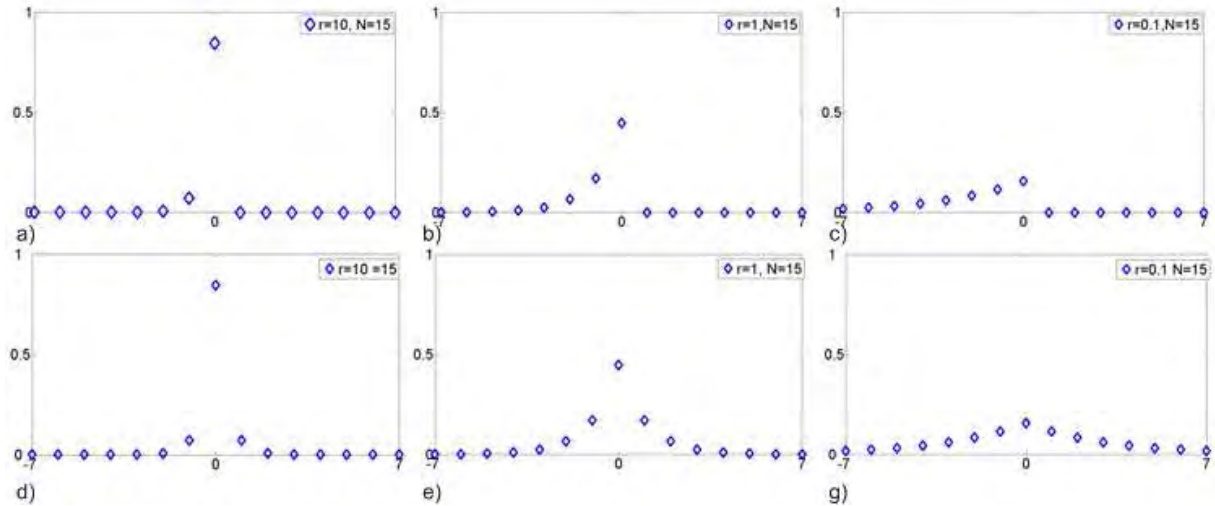
Fig. 26 Impulse response of the Wiener filter for N=15. a) causal filter with *r*=10; b) causal filter with *r*=1; a) causal filter with *r*=0.1; d) non-causal filter with *r*=10; e) non-causal filter with *r*=1; f) non-causal filter with *r*=0.1.

The second method for estimating the phase noise based on the *M*-th power law is a block phase estimation method. The phase noise in a block of samples is estimated and the same estimate is removed from all the samples in the block. The incoming samples are buffered into *K* blocks, each containing *N* samples, as shown in Fig. 27a. Each block of *N* samples is processed as shown in Fig. 27b, for the *k-th* block. The samples are raised to the fourth power to remove the modulating data. Then, the samples are summed, a form of filtering, and the argument of the result is extracted and quartered, in order to inverse the raising to the 4-th power operation, producing

$$\Delta\hat{\phi}_n^{k-th} = \frac{1}{4}\arg\left\{\sum_{n=(k-1)N+1}^{kN} \tilde{i}^4[n]\right\} \tag{146}$$

The phase estimate is an approximation of the average phase of all the samples in the block.

Unwrapping must be performed between the phase estimates of neighboring blocks, which is however less prone to errors compared to unwrapping the phases of all samples in the block. As shown in Appendix G, the raised to the 4-th power samples contain an additive noise portion apart from the phase noise. Intuitively, large block sizes are preferable in low OSNR and small phase noise regimes, when the additive noise is dominant, since the filter filters out the additive noise. In contrast, large phase noise requires small filter lengths, since the overall phase will vary substantially in the block length, rendering the phase estimate inaccurate.

A detailed analysis of the performance of all aforementioned algorithms is provided in Section VI.3.

Fig. 27 Block diagram of the block phase estimator; a) Block diagram of the MUX-DMUX unit; b) Detailed block diagram of the processing unit; (Abbreviations: exp(-j): Complex exponentiation; arg(): Complex number argument; Unwrap: Unwrapping process).
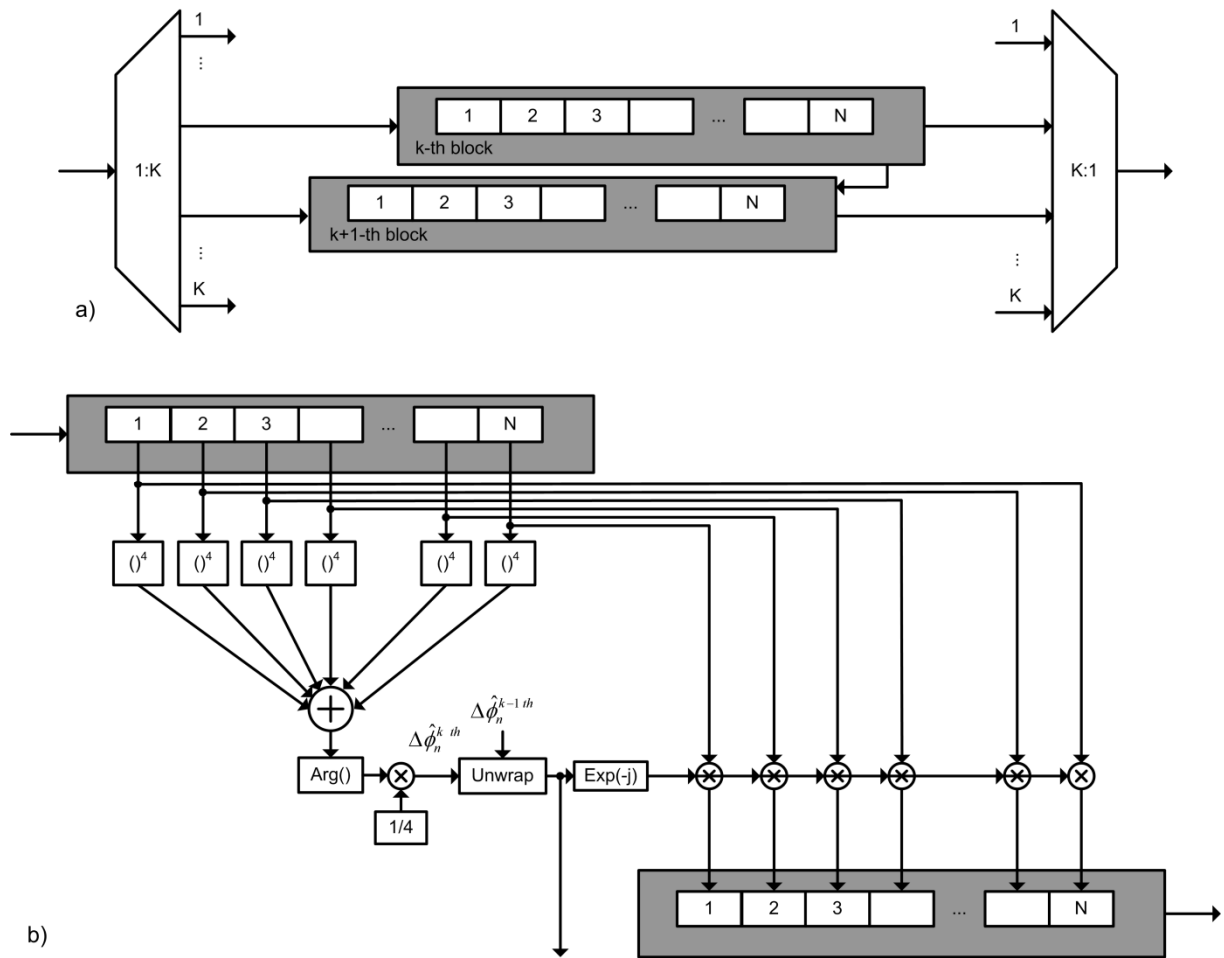
6. Intermediate frequency offset

Phase-diversity receivers are quadrature downconversion receivers [169]. They are the equivalent to multiplying the incoming signal with a complex exponential whose frequency is the frequency of the local oscillator. Multiplying a real signal with a complex exponential, and subsequent baseband filtering, results in downconverting only one side of the bilateral power spectral density (PSD) of the modulated signal, to baseband. The other side experiences infinite attenuation. In the time domain, the in-phase and quadrature components of the phase modulated signal are preserved in the generated photocurrents. This process is better illustrated in Fig. 28.
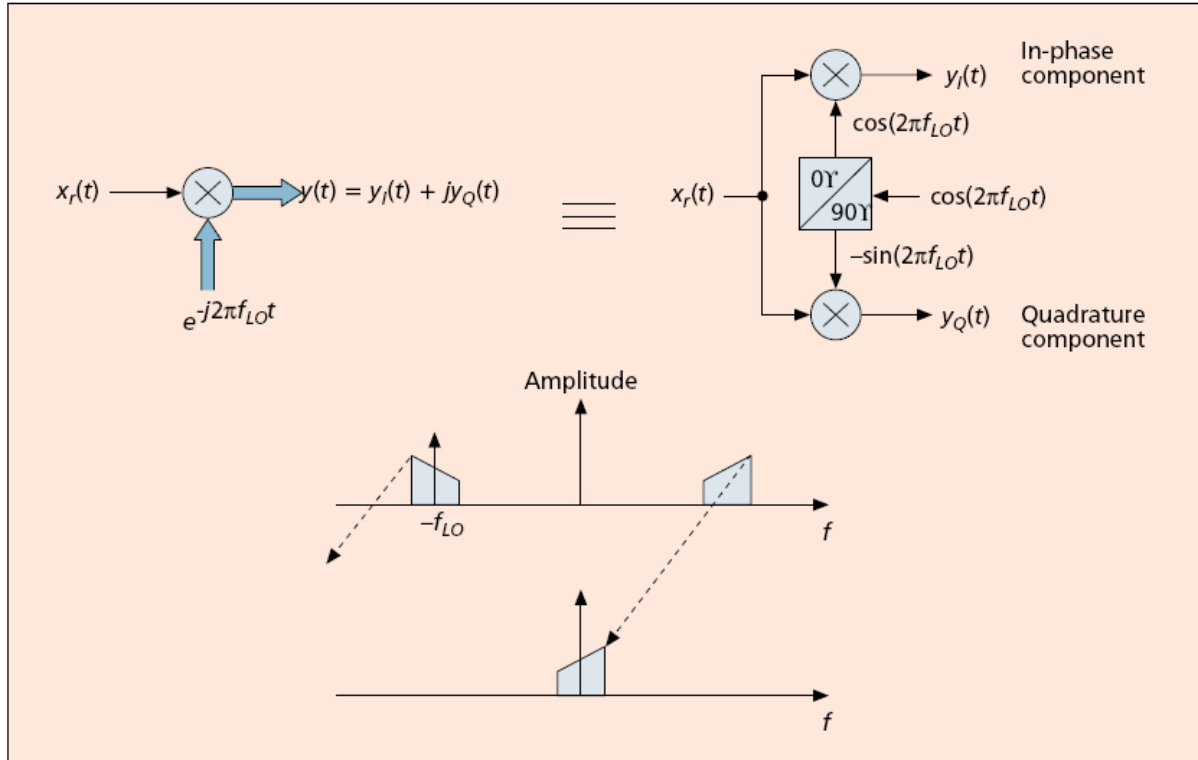
Fig. 28 The result of mixing a real signal with a complex exponential (Copied from [169].)

A non-zero carrier frequency difference between the received signal and the signal of the local oscillator results in translating the signal power spectral density to the intermediate frequency f_{IF}, rather than to baseband. In addition, an image spectral component from the unwanted side of the received bilateral PSD is translated to $-f_{IF}$. This distorts the total received PSD if $f_{IF} < R_S$, introducing penalty in system performance. In Fig. 29, the PSD of the received complex photocurrent at the output of a coherent phase-diversity receiver is shown, for a QPSK modulated signal. The signal has 1 GBd symbol rate. The light-colored (green) PSD corresponds to a zero IF offset, whereas the dark-colored (red) PSD at the background, corresponds to a 2.5 GHz IF offset ($f_{IF} = 2.5\ R_S$). The central lobe, residing around the baseband in the ideal case, is translated to $\pm f_{IF}$ in the latter case. The existence of an IF offset affects the electrical low pass filter optimal bandwidth characteristics. If the IF offset is larger than the symbol rate, then a bandpass filter, rather than a low pass filter, is needed.

For symmetric PSDs, and in the case where $f_{IF} << R_S$, as can be expected in practical systems which will have some form of frequency control, the impact on the signal spectrum is negligible. However, in QPSK, the IF offset also affects the instantaneous phase of the phasor reconstructed at the receiver, by introducing a constant phase offset per sample. This offset causes the absolute value of the phase of the phasor to increase or decrease monotonically, as a linear function of time. As a result the complex sample phasor rotates constantly upon the complex plane, with a rate proportional to the IF offset, leading vey fast to erroneous phase decisions at the demodulator. Fig. 30 shows a representative eye diagram, and the corresponding constellation, at the output of the phase-diversity receiver, for a SP-QPSK system, in the absence of any noise source, for the case of $f_{IF}=0.01\ R_s$. The constellation

93

diagram is circular. From the constellation in Fig. 30, it is clear that, as in the case of laser phase noise, sooner or later, the constellation points will fall into wrong quadrants, causing errors.
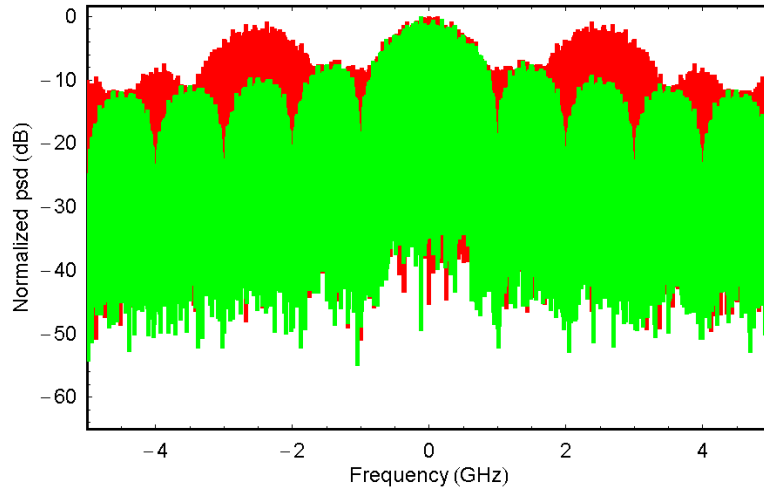

Fig. 29 Power Spectral Density (PSD) of the received complex photocurrent at the output of a coherent phase-diversity receiver is shown, for a QPSK modulated signal, for two different IF offsets. Light-colored (green) PSD: zero IF offset; Dark-colored (red) PSD: 2.5 GHz IF offset, corresponding to $f_{IF} = 2.5\ R_S$.
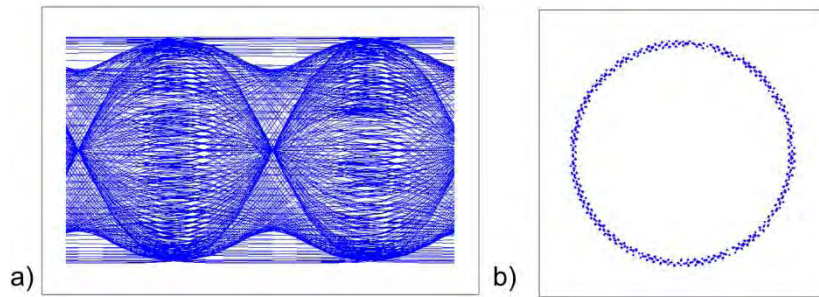
Fig. 30 Eye diagram and corresponding constellation diagram of the received photocurrent at one of the outputs of a phase-diversity receiver, in the presence of an IF offset equal to 0.01 R_S. No noise sources are included; (Conditions: NRZ pulses, Electrical filter: 4th-order Bessel with 0.8 3-dB bandwidth, 8 samples per symbol, 5000 symbols).

In coherent optical systems, the total IF offset $\times$ symbol-period product is used as a measure of the IF offset, denoted as $f_{IF}T_S$ or, using the symbol rare, as the ratio f_{IF}/R_S. Fig. 31 shows the OSNR penalty at BER = 10^{-3} for a SP-QPSK system, for both receiver configurations of Fig. 16, the synchronous receiver (left), and the differential receiver (right). As a reference, the required OSNR for BER = 10^{-3} of the synchronous receiver is used, which is the smallest. The differential receiver can support IF offset $\times$ symbol-period products as high as 0.02 with penalty smaller than 3 dB (corresponding to 200 MHz IF offset at 10 GBd). Using the synchronous receiver, though beneficial in the case of zero IF offset $\times$ symbol-period products, tolerates orders of magnitude less IF offset. The 3-dB penalty threshold is at an IF offset $\times$ symbol period product as small as 0.8×10^{-6} (corresponding to 8 kHz IF offset at 10 GBd). Thus, the differential receiver dramatically increases the IF offset tolerance of the system, although IF offset estimation and compensation is still essential in phase modulated systems.

Depending on the relative value of the IF offset with respect to the symbol rate, optical systems are classified into three categories: i) homodyne (f_{IF}=0) ii) heterodyne ($f_{IF} \geq R_S$), and iii) intradyne ($0<f_{IF}<R_S$). In the heterodyne case, the IF offset should be removed before channel synchronization, let aside any impairment mitigation and DSP [171]. Contemporary coherent optical QPSK systems are expected to have $f_{IF} \cong 0$ with the use of some sort of automatic frequency control (AFC), so any residual IF offset will be caused by non-ideal estimation operation of the loop control algorithm [172], [173]. Thus, these systems will be considered intradyne systems, and some sort of IF offset estimation

94

and compensation algorithm will be needed. Various algorithms for IF estimation and compensation exist in the digital communications literature [171], [174], and some of these have been adapted in the optical communications literature. More recently, new algorithms have been proposed, specifically for optical communications [175]–[179].
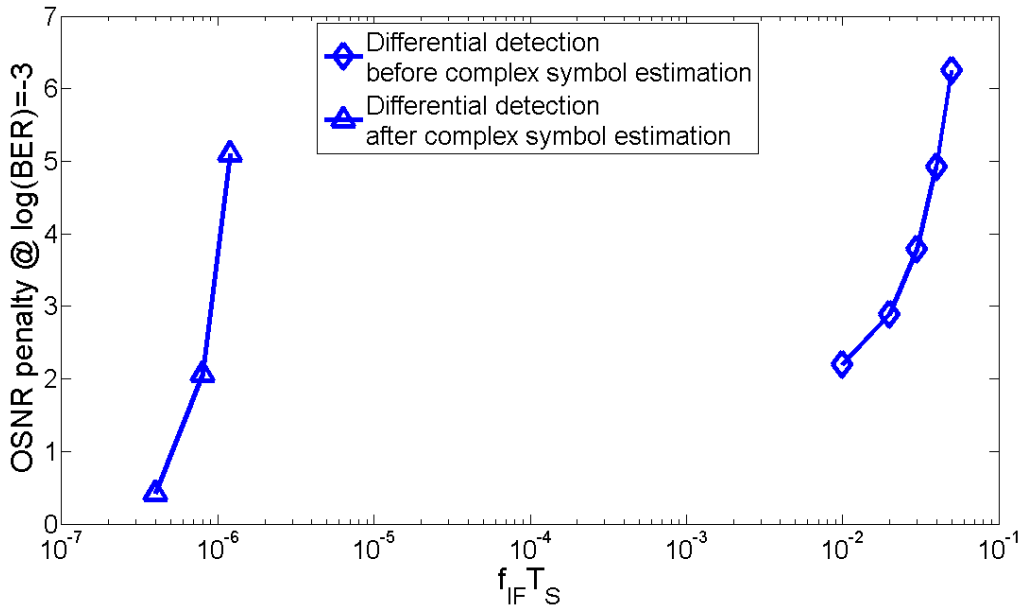
Fig. 31 OSNR penalty vs IF offset × symbol period product for SP-QPSK systems using the synchronous receiver (left) and the differential receiver (right).

In the context of this thesis, we have implemented three IF offset estimation and compensation algorithms, the phase increment algorithm [171], [175], as well as the Tretter and Key algorithms (see [174] and references therein). In the following, we describe in detail these algorithms.

In the description of all algorithms, we will use as a starting point the same expression for the complex photocurrent which was given in (105). The complex photocurrent at the output of each phase-diversity receiver for a SP-QPSK system, or at the output of the POLDMUX in a PDM-QPSK system, assuming non-zero IF offset, is

$$\tilde{i}_{X,Y}[n] = I e^{j\phi_{k,X,Y}[n]} e^{j\Delta\phi_n + j2\pi f_{IF} nT_S} + p_{X,Y}[n] \tag{147}$$

i. Phase Increment algorithm

The phase increment algorithm is based on the fact that the phase difference between two consecutive samples in (147), due exclusively to the IF offset, is constant. Neglecting additive noise, this phase difference is easily found by taking the argument of the product of one sample with the complex conjugate of the previous sample, raised to the fourth power

$$\frac{1}{4}\arg\left\{\left(\tilde{i}[n]\tilde{i}^*[n-1]\right)^4\right\} \cong 2\pi f_{IF} T_S + \Delta\phi_n[n] - \Delta\phi_n[n-1] \tag{148}$$

Since $\Delta\phi_n[n] - \Delta\phi_n[n-1]$ is a zero-mean Gaussian random variable (see (107)), averaging over a large number L of samples, largely eliminates phase noise, giving a direct estimate of f_{IF}, expressed as

$$\hat{f}_{IF} \cong \frac{1}{2\pi T_S} \frac{1}{4} \arg\left\{\sum_{n=0}^{L-1}\left(\tilde{i}[n]\tilde{i}^*[n-1]\right)^4\right\} \tag{149}$$

The larger the block size L, the better the estimate, provided that the intermediate frequency offset remains constant. The block diagram of the phase increment algorithm is shown in Fig. 32.
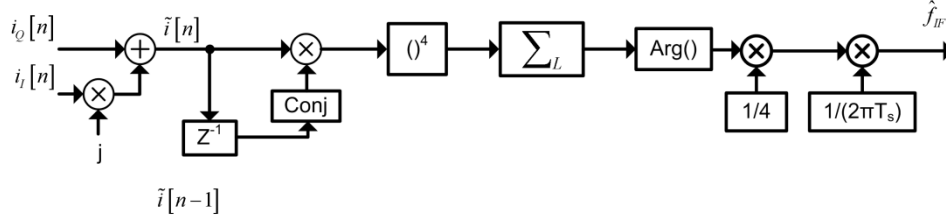
Fig. 32 Block diagram of the phase increment algorithm for estimating the IF offset; (Abbreviations: Z^{-1}: Single time unit delay; arg(): Complex number argument; Conj.: Complex conjugation).

ii. Tretter and Kay estimation algorithms

The estimation algorithms proposed by Tretter and Kay are least-squares estimators [174]. The concept behind Tretter's algorithm is to follow the ever growing trajectory of the signal phase, as a function of time, at the output of the fourth order nonlinearity, removing the modulation data, and estimating its slope, which is directly proportional to the IF offset. It holds that

$$\frac{1}{4}\arg\{\tilde{i}^4[n]\} \cong 2\pi f_{IF} n T_S + \Delta\phi_n[n] \tag{150}$$

This phase increases (or decreases) without bound (monotonically) over time. Thus (150) can be viewed as noisy samples of a linear function whose slope is $2\pi f_{IF} T_S$. Clearly, estimating the slope of this line amounts to estimating the IF offset, for the two quantities are proportional. The phase produced from (150) however, is a wrapped phase, and thus, phase unwrapping is needed before a correct estimation is made. In order to achieve a least-squares solution to the problem over a number of L samples, weight coefficients are used to estimate the slope. Tretter's algorithm is summarized in the following set of equations

$$\hat{f}_{IF} = \frac{1}{2\pi T_S} \frac{1}{4} \sum_{n=0}^{L-1} w_n^{(T)} \arg^{unwrap}\{\tilde{i}^4[n]\} \tag{151}$$

where

$$w_k^{(T)} = \frac{6(2k-L+1)}{L(L^2-1)}, 0 \le k \le L-1 \tag{152}$$

Kay's algorithm is, mathematically, equivalent to Tretter's algorithm [174], only it is much simpler, since it avoids unwrapping. Kay's algorithm is summarized in the following set of equations

$$\hat{f}_{IF} = \frac{1}{2\pi T_S} \frac{1}{4} \sum_{n=0}^{L-1} w_n^{(T)} \arg\{(\tilde{i}[n]\tilde{i}^*[n-1])^4\} \tag{153}$$

and

$$w_k^{(T)} = \frac{6k(L-k)}{L(L^2-1)}, 0 \le k \le L-1 \tag{154}$$

IF offset compensation is performed by multiplying the received sample sequence with a continuously rotating phasor whose frequency equals the estimated IF offset, i.e.,

$$\tilde{i}'[n] = e^{-i2\pi f_{IF} n T_S} \tag{155}$$

After IF offset compensation, the discrete time symbol sequence has the form

$$\tilde{i}_{X,Y}[n] = Ie^{j\phi_{k,X,Y}[n]}e^{j\Delta\phi_n + j2\pi f_d n T_S} + c_{X,Y}[n] \tag{156}$$

where $f_d = f_{IF} - \hat{f}_{IF}$ is the remaining intermediate frequency and $c[n]$ is a different complex Gaussian noise sequence from $p[n]$ having the same variance σ_p^2.

7. Quadrature Imbalance

The general form of the I and Q photocurrents for a SP-QPSK system, at the output of any phase diversity receiver, are given in (96). In the general case, they are of different magnitude, i.e., $I_{ip} \neq I_{qp}$, and have different phase deviations from the ideal, i.e., $\varepsilon \neq \delta \neq 0°$, i.e., the photocurrents are not in quadrature. These non-idealities are often called amplitude and phase mismatch respectively, and are also known in classical communications as quadrature imbalance (QI), or I/Q mismatch [169], [170], [180].

QI affects the downconverted signal spectrum at the output of the quadrature downconversion receiver. Fig. 33 illustrates the impact of QI on the received signal spectra (Appendix I). The mirror image of the unilateral spectrum, which would ideally experience infinite attenuation, now experiences finite attenuation (Fig. 33a), and is added to the desired unilateral spectrum, distorting the received PSD (Fig. 33b). For zero IF offset, and symmetrical spectra, QI has no impact on system performance. For non-zero IF offsets, or non-symmetric spectra, QI causes PSD aliasing, and affects system performance.
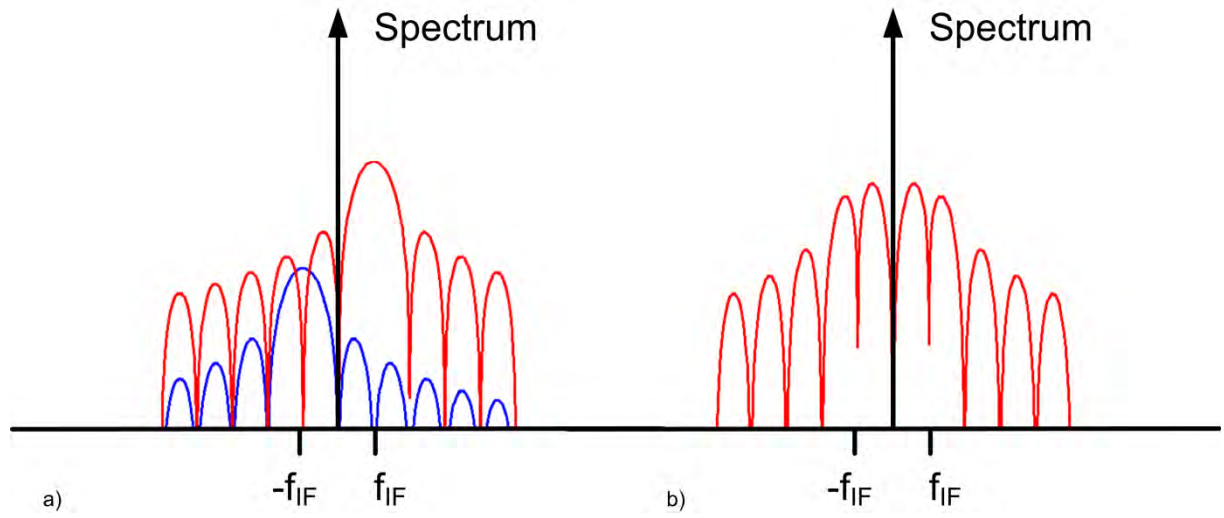
Fig. 33 Spectra of the received signal at the phase-diversity receiver output. a) Intermixing of the image signal (light shade, or blue) and the desired signal (dark shade, or red) results in a distorted spectrum; b) The resulting distorted signal.

For symmetric PSDs, and in the case where $f_{IF} \ll R_S$, the impact on the signal spectrum is negligible. However, in QPSK, QI affects the phasor reconstructed at the receiver, causing penalty in system performance. The photocurrents at the output of the phase diversity receiver can be written as

$$i_I(t) = I_I + I_{ip}\cos\left[\varphi(t) + \varepsilon\right]$$
$$i_Q(t) = I_Q + I_{qp}\sin\left[\varphi(t) - \delta\right]$$

(157)

where $\varphi(t)$ is the common phase term containing the modulation phase, the IF offset, and the phase noise. The complex signal formed at the input of the DSP can be expressed, after some effort (Appendix J), as

$$\tilde{i}(t) = (I_I + jI_Q) + I_{ip}\left[K_1\, e^{j\varphi(t)} + K_2\, e^{-j\varphi(t)}\right]$$

(158)

where

$$K_1 = \frac{1}{2}e^{j\varepsilon}\left[1 + \left(I_{qp}/I_{ip}\right)e^{-j(\varepsilon+\delta)}\right]$$
$$K_2 = \frac{1}{2}e^{-j\varepsilon}\left[1 - \left(I_{qp}/I_{ip}\right)e^{j(\varepsilon+\delta)}\right]$$

(159)

Fig. 34 shows typical eye diagrams and the corresponding constellation diagrams for the I and Q photocurrents at the output of the phase-diversity receiver of a SP-QPSK system, in the absence of noise and IF offset, in the ideal case (Fig. 34a), in the presence of amplitude mismatch (Fig. 34b), and in the presence of phase mismatch (Fig. 34c). The received constellation diagrams are distorted.
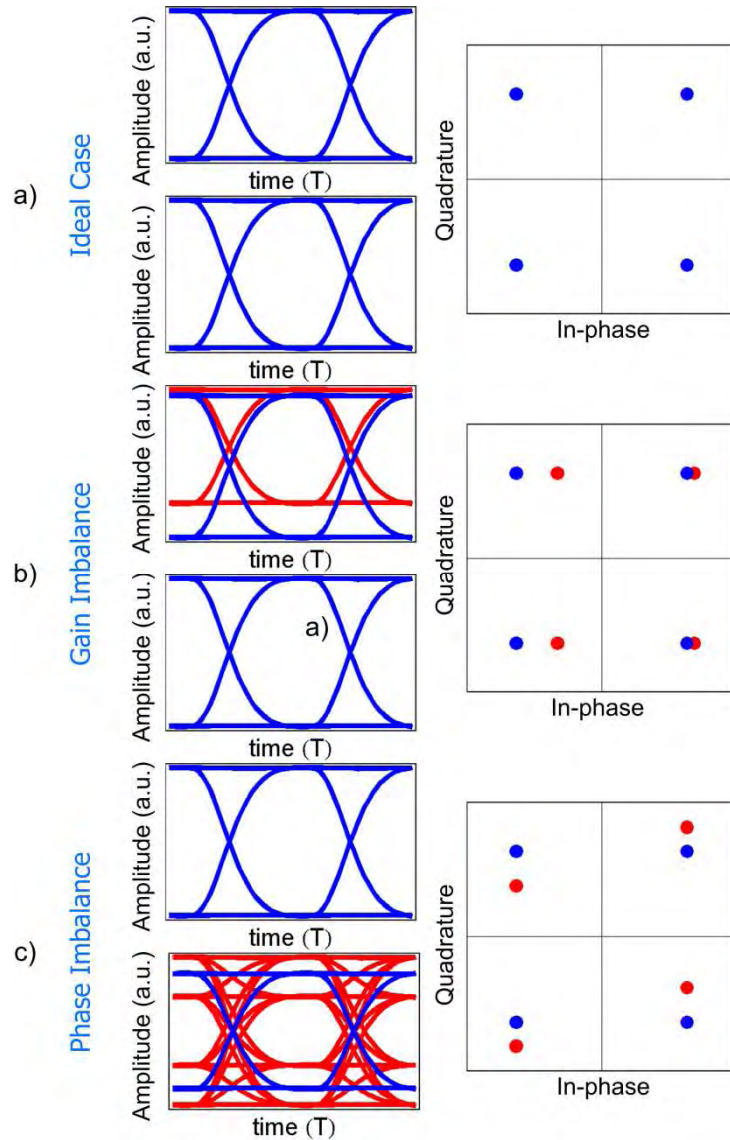
Fig. 34 Received eye diagrams and the corresponding constellation diagrams for various cases of QI, at the output of the phase diversity receiver of a SP-QPSK system. a) Ideal system; b) Amplitude mismatch (I_{ip}=0.8 I_{qp}); c) Phase mismatch (δ=20°, ε=0°).

In the presence of IF offset, the constellation points will rotate and will form an ellipse instead of the circular constellation, typical for QPSK systems (Fig. 30). Especially for PDM-QPSK systems, the received constellation, which ideally contains up to 16 points (Fig. 18), will form up to four concentric ellipses, as can be seen in Fig. 35.

QI affects the performance of all DSP algorithms and thus deteriorates system performance. Fig. 36 shows the impact on the form of the constellation diagrams at various stages of the digital coherent receiver, for a PDM-QPSK system with amplitude mismatch (I_{ip}=0.6 I_{qp}) and phase mismatch (δ=30°, ε=0°). Blue dots correspond to zero IF offset whereas gray lines correspond to the case where the IF offset is non-zero. Fig. 36a depicts the constellation at the output of the phase-diversity receiver, Fig. 36b depicts the constellation at the output of the POLDMUX, and Fig. 36c depicts the constellation at the output of the phase estimation and compensation module. System performance is degraded by the fact that all algorithms assume that the photocurrents are orthogonal.

99
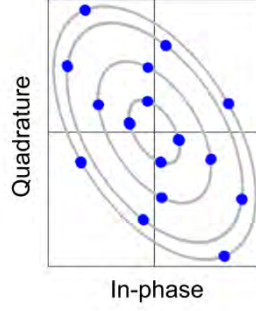
Fig. 35 Received constellation diagram at the output of a phase-diversity receiver for a PDM-QPSK system, in the presence of both amplitude mismatch (I_{ip}=0.6 I_{qp}) and phase mismatch (δ=30°, ε=0°). Dots: Constellation in the absence of IF offset; Solid lines: Constellation in the presence of IF offset.
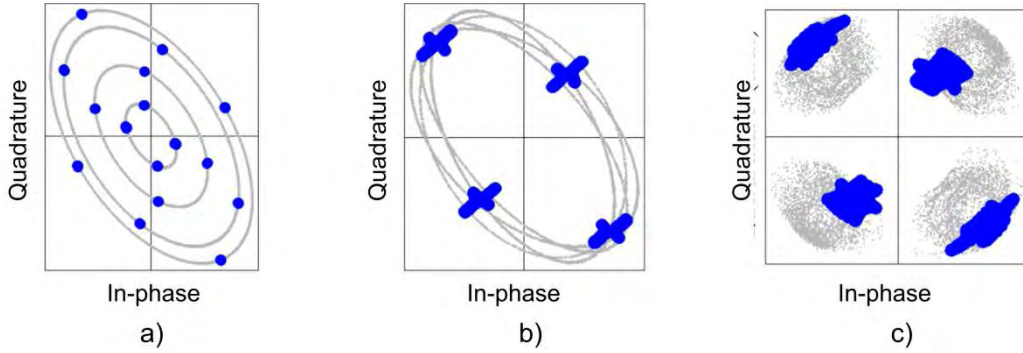
Fig. 36 Constellation diagrams at various stages of the digital coherent receiver, for a PDM-QPSK system with amplitude mismatch (I_{ip}=0.6 I_{qp}) and phase mismatch (δ=30°, ε=0°). Dark shapes correspond to the case where the IF offset is zero, whereas light-shade lines correspond to the case where the IF offset is non zero. a) the constellation at the output of the phase-diversity receiver; b) constellation at the output of the POLDMUX; c) constellation at the output of the phase estimation and compensation module.

In order to thoroughly investigate system performance when QI is left unattended, for a large number of combinations, we used the semi-analytical method for evaluating system performance (Appendix C), for a SP-QPSK system. The model of a 2×4 90° optical hybrid was used (Appendix E), and the explicit impact of each adjustable parameter of this hybrid was investigated in two cases. More precisely, the phase mismatch caused by non-ideal phase shifts ε and δ was examined, in the first case in conjunction with non-ideal 3-dB coupler coupling coefficients α_1, α_2, α_3, and α_4, and in a the second case in conjunction with non-equal responsivities R_1, R_2, R_3, and R_4. Fig. 37 shows the OSNR penalty at BER=10^{-9} for a number of cases. As seen in (159), the phase mismatch depends on the sum of ε and δ, thus a total phase mismatch is calculated as $\theta = \varepsilon + \delta$. For each value of θ, twenty combinations of ε and δ were used. Responsivity deviation was calculated as the ratio between the responsivities of a balanced photodetector, i.e., R_1 / R_2. The 3-dB coupler coupling coefficient was varied from its nominal value of 0.5. All 3-dB couplers at the input of the hybrid (signal splitting couplers) and output of the hybrid (signal combining couplers), were investigated separately. No noise source was included, and thus no compensating algorithms were used.

From Fig. 37, it can be seen that penalties can routinely exceed 3 dB, even for relatively small deviations from the nominal settings. Phase mismatch is the most influential impairment. Non-ideal signal combining couplers affect system performance less than non-ideal signal splitting couplers. Though amplitude mismatch can be effectively reduced by using an automatic gain control (AGC) at the output of the photodetectors, phase mismatch is a much more subtle imperfection for QPSK modulation, and needs dedicated compensation.

A number of QI compensation algorithms have been developed for optical communications systems using digital coherent receivers. A QI estimation and compensation method based on the geometric properties of the received constellation diagram was first proposed in [129], used in the analysis of

experimental results in [181], and described in more detail in [182]. In [183], a Gram-Schmidt orthogonalization procedure was proposed (adapted from [141]), to orthogonalize the non-orthogonal photocurrents due to QI. A simpler variant of this method, addressing only phase mismatch, was proposed in [184]. Finally, in [185], [186], a dedicated, blind, adaptive QI compensation scheme, based on the constant modulus algorithm (CMA) was proposed. We now describe these algorithms in more detail.
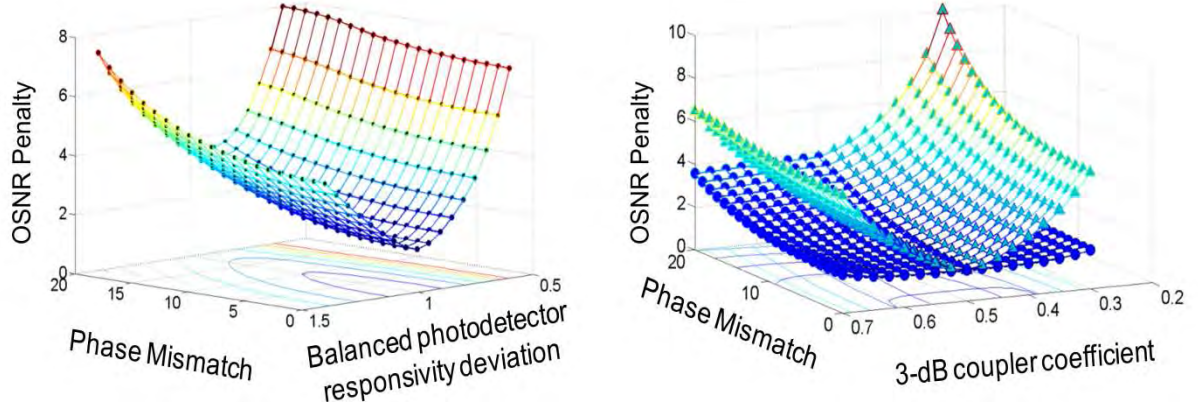
Fig. 37 OSNR penalty at $P_e=10^{-9}$ for various settings of the optical hybrid and BPDs. (a) Combination of phase mismatch and BPD responsivity ratio deviation; (b) Combination of phase mismatch and coupling coefficient values (Circles: Non-ideal output couplers, Triangles: Non-ideal input couplers).

i. Ellipse fitting estimation

The discrete counterpart of (157), when sampled once per symbol, at the center of the symbol period, can be re-written as

$$
\begin{aligned}
i_I[n] &= I_I + I_{ip}\cos\big(\omega[n]\big) \\
i_Q[n] &= I_Q + I_{qp}\sin\big(\omega[n]+\theta\big)
\end{aligned}
\tag{160}
$$

where $\omega[n]=\varphi[n]+\varepsilon$ and $\theta = \varepsilon+\delta$. The pair of parametric equations (160) generates an ellipse when plotted on a x-y diagram [187]. This is also true in the case of PDM-QPSK systems when sampled once per symbol, at the center of the symbol (Fig. 35).

The amplitude and phase mismatch are directly related to the ellipse quadratic equation parameters. In particular, the ellipse center is related to the DC offset, the ellipse maximal points are related to the amplitude mismatch, also denoted as $\lambda=I_{ip}/I_{qp}$, and the ellipse rotation angle is related to the phase mismatch θ. By fitting the ellipse to a quadratic equation, estimates of I_I, I_Q, λ and θ are produced, i.e., $\hat{I}_I$, $\hat{I}_Q$, $\hat{\lambda}$ and $\hat{\theta}$, respectively [188]–[191] (Appendix K).

Having obtained these estimates, QI compensation can be performed, using an orthogonalization procedure which transforms the ellipse back to a circle (Appendix L), [192]. Starting from the received photocurrent vector $\mathbf{I}[n]=\begin{bmatrix} i_I[n] & i_Q[n] \end{bmatrix}^T$, first, the DC offset is removed, producing a vector with no DC-offset, $\mathbf{I}_{DC-free}[n]$, as

$$
\mathbf{I}_{DC-free}[n]=\begin{bmatrix} i_I[n]-\hat{I}_I \\ i_Q[n]-\hat{I}_Q \end{bmatrix}
\tag{161}
$$

Subsequently, the DC-free photocurrent samples are scaled and rotated into a new vector $\mathbf{I}_Q[n]$, whose elements are orthogonal, using a 2×2 matrix, formulated as

$$\mathbf{I}_Q[n] = \begin{pmatrix} E & 0 \\ P & 1 \end{pmatrix} \cdot \mathbf{I}_{DC-free}[n] \tag{162}$$

where

$$\begin{aligned} E &= \hat{\lambda}^{-1} \cos(\hat{\theta}) \\ P &= -\hat{\lambda}^{-1} \sin(\hat{\theta}) \end{aligned} \tag{163}$$

This algorithm is subsequently referred to as the ellipse-fitting algorithm.

ii.   Constrained CMA

Removing the DC components from (157), e.g., by using a DC block module, enables us to rewrite (157) in matrix form, as follows:

$$\mathbf{I} = \mathbf{M}\mathbf{I}_\mathbf{Q} \tag{164}$$

where $\mathbf{I} = \begin{bmatrix} i_I(t) & i_Q(t) \end{bmatrix}^T$ is the received photocurrent vector, $\mathbf{I}_\mathbf{Q} = \begin{bmatrix} \cos\varphi(t) & \sin\varphi(t) \end{bmatrix}^T$ is the desired quadrature component vector, and $\mathbf{M}$ is a 2×2 real mixing matrix representing QI, given by

$$\mathbf{M} = \begin{pmatrix} I_{ip}\cos\varepsilon & -I_{ip}\sin\varepsilon \\ -I_{qp}\sin\delta & I_{qp}\cos\delta \end{pmatrix} \tag{165}$$

Thus, the effects of QI can be removed, by finding an estimate $\hat{\mathbf{M}}^{-1}$ of the inverse matrix

$$\mathbf{M}^{-1} = \sec\theta \begin{pmatrix} I_{ip}^{-1}\cos\delta & I_{qp}^{-1}\sin\varepsilon \\ I_{ip}^{-1}\sin\delta & I_{qp}^{-1}\cos\varepsilon \end{pmatrix} \tag{166}$$

Neglecting the multiplication factor $\sec(\theta)$ we set the expression of the equalizer matrix as

$$\mathbf{W}(I_{ip}, I_{qp}, \varepsilon, \delta) = \begin{pmatrix} I_{ip}^{-1}\cos\delta & I_{qp}^{-1}\sin\varepsilon \\ I_{ip}^{-1}\sin\delta & I_{qp}^{-1}\cos\varepsilon \end{pmatrix} \tag{167}$$

The CMA is used to estimate parameters I_{ip}, I_{qp}, ε, δ by minimizing the instantaneous cost function $\xi[n] = e^2[n]$, where $e[n] = \hat{\mathbf{I}}_\mathbf{Q}^\mathrm{T}[n] \cdot \hat{\mathbf{I}}_\mathbf{Q}[n] - R$ is the error function, R is the sum of the average optical signal and noise powers (usually normalized to unity), and $\hat{\mathbf{I}}_\mathbf{Q}[n]$ is the estimate of the desired quadrature component vector, found by

$$\hat{\mathbf{I}}_\mathbf{Q}[n] = \mathbf{W}(\hat{I}_{ip}[n], \hat{I}_{qp}[n], \hat{\varepsilon}[n], \hat{\delta}[n])\mathbf{I}[n] \tag{168}$$

In order to produce estimates $\hat{I}_{ip}[n], \hat{I}_{qp}[n], \hat{\varepsilon}[n], \hat{\delta}[n]$, we define the array of estimated parameters $\mathbf{Z}[n] = \begin{bmatrix} \hat{I}_{ip}[n] & \hat{I}_{qp}[n] & \hat{\varepsilon}[n] & \hat{\delta}[n] \end{bmatrix}^T$, and use the stochastic gradient algorithm for its update [141], i.e.,

$$\mathbf{Z}[n+1] = \mathbf{Z}[n] - \mu\nabla\xi[n] \tag{169}$$

where

$$\nabla\xi[n] = \begin{bmatrix} \dfrac{\partial\xi[n]}{\partial I_{ip}} & \dfrac{\partial\xi[n]}{\partial I_{qp}} & \dfrac{\partial\xi[n]}{\partial\varepsilon} & \dfrac{\partial\xi[n]}{\partial\delta} \end{bmatrix}^\mathrm{T} \tag{170}$$

and μ is the algorithm step size. The independently-adjustable parameters can be further reduced, e.g., by setting ε or $\delta = 0°$, or using λ instead of separately calculating I_{ip} and I_{qp}. However, these simplifications add a small penalty as will be seen in Section VI.5. This algorithm is subsequently referred to as the QI CCMA.

iii. Gram-Schmidt orthogonalization

In [183], a mixing-matrix approach is also used to compensate for QI. The difference is in the idea behind calculating the elements of the matrix. The in-phase component of the received photocurrent vector is first scaled to unit energy, forming a new vector

$$\mathbf{I}^{(0)}[n] = \begin{bmatrix} i_I[n]/\sqrt{P_I} \\ i_Q[n] \end{bmatrix} \tag{171}$$

where $P_I = E\{i_I^2[n]\}$. The projection of the normalized in-phase component is then subtracted from the quadrature component, by multiplying (171) with

$$\mathbf{W} = \begin{bmatrix} 1 & 0 \\ -\rho/\sqrt{P_I} & 1 \end{bmatrix} \tag{172}$$

producing an intermediate vector

$$\mathbf{I}^{(1)}[n] = \begin{bmatrix} i_I[n]/\sqrt{P_I} \\ i_Q[n] - i_I[n]/P_I \end{bmatrix} = \begin{bmatrix} i_I'[n] \\ i_Q'[n] \end{bmatrix} \tag{173}$$

where $\rho = E\{i_I[n]i_Q[n]\}$ is the correlation coefficient. Finally, the quadrature component $i_Q'[n]$ is normalized to unit energy, and the desired quadrature component vector is formed as

$$\mathbf{I}_Q[n] = \begin{bmatrix} i_I'[n] \\ i_Q'[n]/\sqrt{P_{Q'}} \end{bmatrix} \tag{174}$$

where $P_{Q'} = E\{i_Q'^2[n]\}$. This algorithm will subsequently be referred to as the Gram-Schmidt orthogonalization algorithm.

A similar approach is used in [184]. As in the previous case, it is assumed that the received in-phase signal exists solely on the in-phase axis, whereas the received quadrature signal is split into two components, one on the in-phase, and one on the quadrature axis. By using simple trigonometry, it can be shown that

$$\mathbf{I}[n] = \begin{bmatrix} 1 & 0 \\ \sin\theta & \cos\theta \end{bmatrix} \mathbf{I}_Q[n] \tag{175}$$

where θ is the quadrature error angle, as defined in Fig. 38.

It is straightforward to calculate θ, by using time-averaged operations, since it is easy to show that

$$\sin\theta = E\{i_I[n]i_Q[n]\}/E\{i_I^2[n]\} \tag{176}$$

Thus, $\mathbf{I}_Q$ can easily be found by finding the inverse of the matrix in (175), as

$$\mathbf{I}_Q[n] = \begin{bmatrix} 1 & 0 \\ \dfrac{-\sin\theta}{\cos\theta} & \dfrac{1}{\cos\theta} \end{bmatrix} \mathbf{I}[n] \tag{177}$$

This algorithm will not be used in the remains of this thesis, due to its similarity to the Gram-Schmidt orthogonalization.

It has been shown, that all aforementioned algorithms are also suitable for PDM-QPSK systems. However, not all are suitable for both kinds of sampling, i.e., both symbol-spaced and fractionally-spaced [186]. The ellipse fitting algorithm can estimate the ellipse parameters successfully in the case of PDM-QPSK and symbol-spaced sampling, since the constellation is the concatenation of ellipses

(Fig. 35). However, in the case of fractionally-spaced sampling, the received constellation does not have an ellipse-like shape and the algorithm fails. On the contrary, the effect of QI can still be described by a mixing matrix, since QI is a characteristic of each phase-diversity receiver and not of the received signal. Thus, the QI CCMA and the Gram Schmidt orthogonalization algorithms work perfectly both for PDM QPSK signals, and for fractionally spaced sampling.
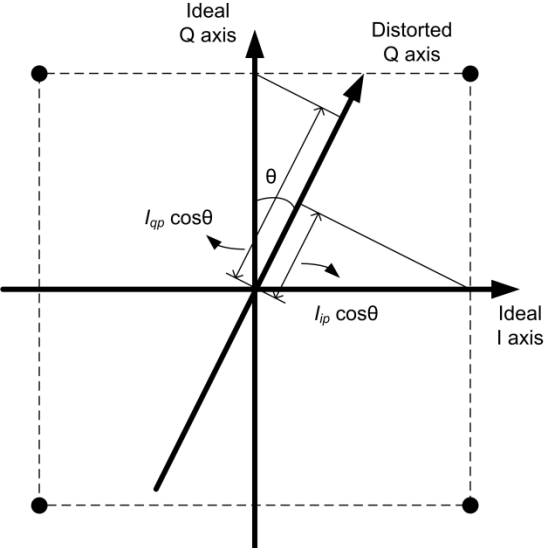

Fig. 38 A two-dimensional representation of two non-orthogonal signals at the output of the 90° optical hybrid. The in-phase signal exists solely on the in-phase axis, whereas the quadrature signal does not exist solely on the quadrature axis, but can be described as a function of signals existing on both axes and an angle θ. (Adapted from [184].)

8. Distortion due to low LO power

Optical 90° hybrids produce linear superpositions of the electrical fields of the received signal and the signal of the LO. They are followed by photodiodes, which produce the photocurrents that convey all phase and amplitude information of the modulated optical signal. The photocurrent amplitudes (see (94) for 2×4 90° optical hybrids, and (95) for 2×2 90° optical hybrids), depend on signal power, which, in general, is a function of time, since it depends on the transmitted pulse shape (see Fig. 10).When single-ended detection is employed, a time-dependent DC offset survives, ideally cancelled when balanced detection is incorporated. When balanced detection is not a choice, this distortion is mitigated by using a large LO-to-signal power ratio (LOSPR), which, is reportedly around 20 dB [44], [68].

Fig. 39 shows the impact of inefficient LO laser power on the received signal eye-diagrams and constellations, for the case of a PDM-QPSK system exhibiting random polarization rotation, and a non-zero IF offset. Fig. 39(a)-(c) correspond to LOSPR=20 dB, whereas Fig. 39(d)-(f) correspond to LOSPR=0 dB. Apart from the photocurrent amplitude being one order of magnitude smaller in the latter case, the constellation is severely distorted. The otherwise concentric constellations of Fig. 18, become eccentric circles.

Fig. 40 shows the OSNR penalty at BER = 10^{-3} vs the LOSPR for a PDM-QPSK system with ASE noise and a random polarization rotation. A CMA POLDMUX is employed with N=1 filter tap weights. It can be seen that the LOSPR must be larger than 16 dB for negligible system penalty.

In order to combat this distortion, the algorithm adopted in [92] is employed. Approximations of the signal-dependent DC offset and LO-dependent DC offset are obtained, denoted as $\overline{I}_S, \overline{I}_{LO}$, respectively, using averaging operations.

Initially, an estimate of the LOSPR=P_{LO}/P_S is needed. It is also assumed that $P_{LO}/P_S = \overline{I}_S / \overline{I}_{LO}$. The photocurrent samples are considered as the sum of a time-varying signal-dependent term and a constant LO-dependent term, as

$$i_I[n] = \overline{I}_{LO} + \overline{I}_S[n] + \tilde{i}_S[n] + I_{ip}\cos(\varphi[n])$$
$$i_Q[n] = \overline{I}_{LO} + \overline{I}_S[n] + \tilde{i}_S[n] + I_{qp}\sin(\varphi[n])$$

(178)

where $\tilde{i}_S[n]$ is the AC photocurrent component due to the received signal. It is then assumed that

$$i_I^2[n] + i_Q^2[n] \approx 4\tilde{i}[n]\overline{I}_L + 4\overline{I}_S\overline{I}_{LO}$$
$$\overline{i_I^2[n] + i_Q^2[n]} = 4\overline{I}_S\overline{I}_{LO}$$

(179)

An initial estimation for the LO-dependent DC offset is

$$\overline{I}_{LO}^{(1)} = \frac{1}{2}\sqrt{\frac{P_{LO}}{P_S}\overline{i_I^2[n] + i_Q^2[n]}}$$

(180)

This is used to obtain an initial estimation of the signal-dependent AC photocurrent

$$\tilde{i}_S^{(1)}[n] = \frac{i_I^2[n] + i_Q^2[n] - \overline{i_I^2[n] + i_Q^2[n]}}{4\overline{I}_L}$$

(181)

Despite of the simplicity of this algorithm, it has been successfully used in the analysis of experimental results (Section VII).

105
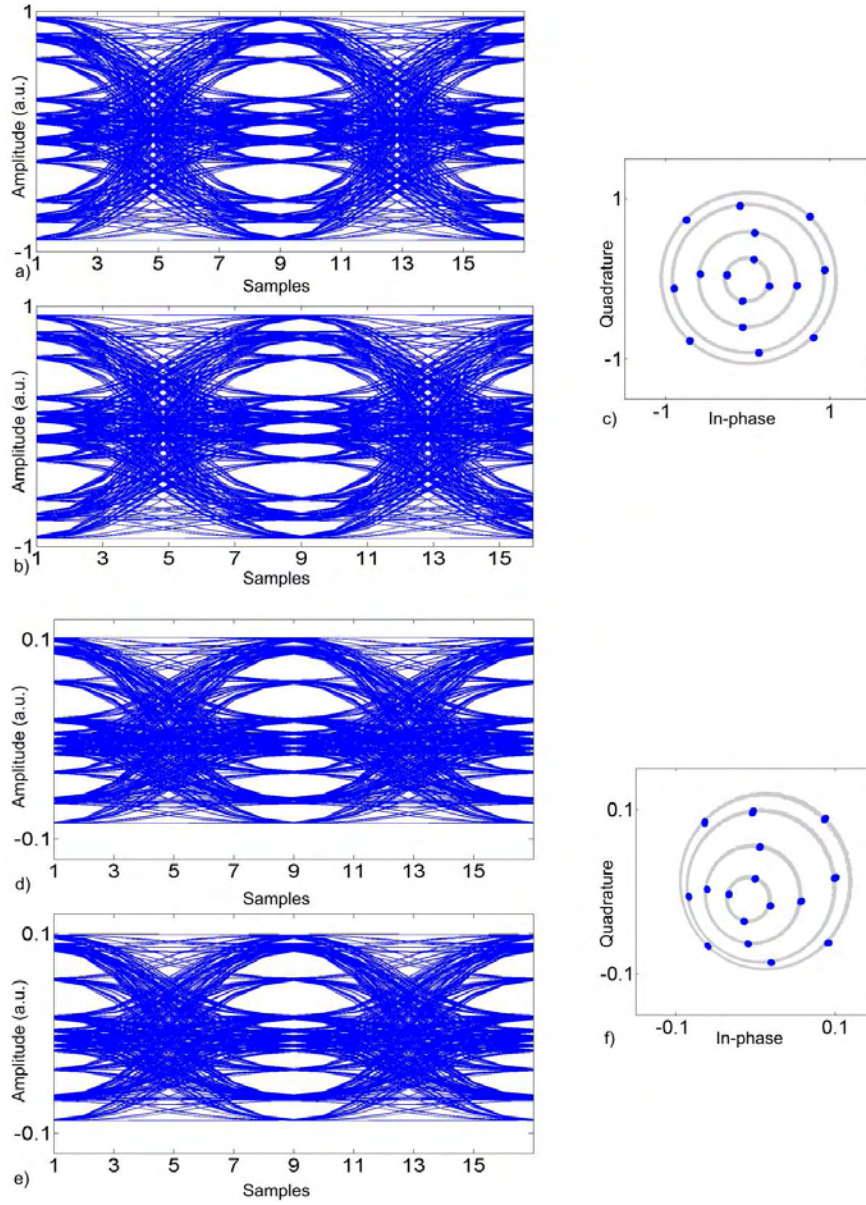
Fig. 39 PDM-QPSK system with no noise sources and zero IF offset. (a), (b): Eye diagrams of the received photocurrents at the two outputs of a phase-diversity receiver (X polarization) for LOSPR=20 dB; (c): Corresponding constellation. (d), (e): Eye diagrams of the received photocurrents at the two outputs of a phase-diversity receiver (X polarization) for LOSPR=0 dB; (f): Corresponding constellation. (Simulation parameters: Electrical filter: 4th-order Bessel filter with 0.8 R_S 3-dB bandwidth; Random polarization rotation: J_{11}=0.5994-j0.1683, J_{12}=0.1307-j0.7716, J_{21}=0.1307-j0.7716, J_{22}=0.5994+j0.1683).
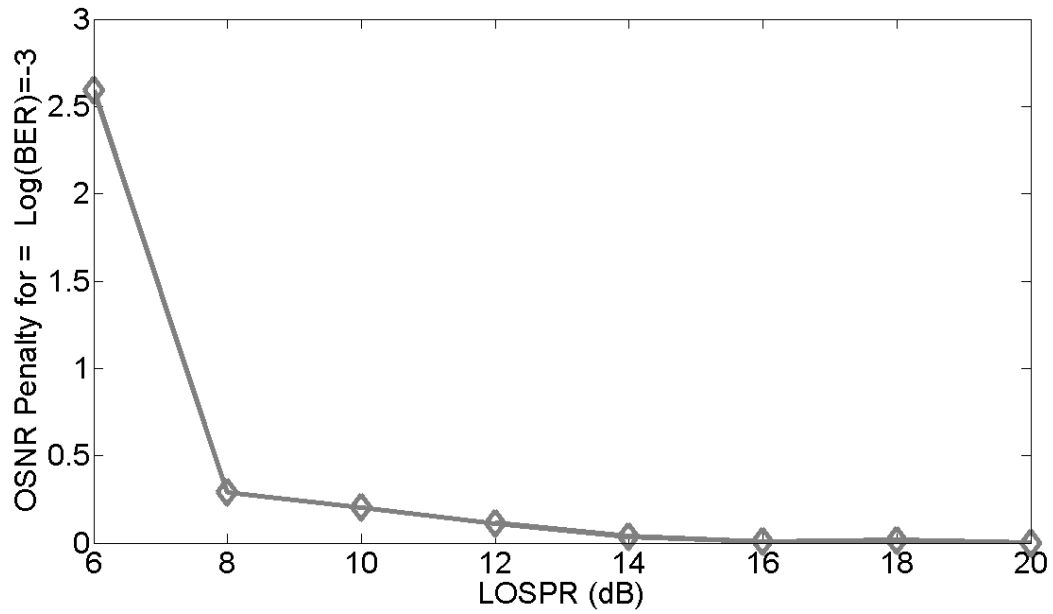
Fig. 40 the OSNR penalty at BER = 10^{-3} vs the LOSPR for a PDM-QPSK system with ASE noise and a random polarization rotation. A CMA POLDMUX is employed with N=1 filter tap weights. (Simulation parameters: Electrical filter: 4th-order Bessel filter with 0.8 R_S 3-dB bandwidth; Random polarization rotation: J_{11}=0.5994-j0.1683, J_{12}=0.1307-j0.7716, J_{21}=0.1307-j0.7716, J_{22}=0.5994+j0.1683).

VI.   Simulation results

In this section, we analyze various aspects of the performance of coherent optical communications systems using the simulation setup described in Section IV. 5, and the algorithms described in Section V.

1. Performance of polarization combining and polarization demultiplexing algorithms in the presence of ASE noise

In this section we compare the performance of various POLCOMB and POLDMUX algorithms, for SP-QPSK and PDM-QPSK systems, in the presence of ASE noise (Section V.4). The OSNR is measured at a 0.125 R_S resolution bandwidth (Appendix M).

Fig. 41a shows a representative eye diagram at the output of a phase-diversity receiver, for a SP-QPSK system, at 13 dB OSNR. Fig. 41b shows the corresponding constellation diagram. Additive noise uniformly increases the size of the constellation points, giving them a disk like shape. Extremely noisy points will lie well outside the main part of the disk, and if they cross the thresholds, will cause a symbol error. Differential detection and Gray decoding can reduce the overall bit error rate.
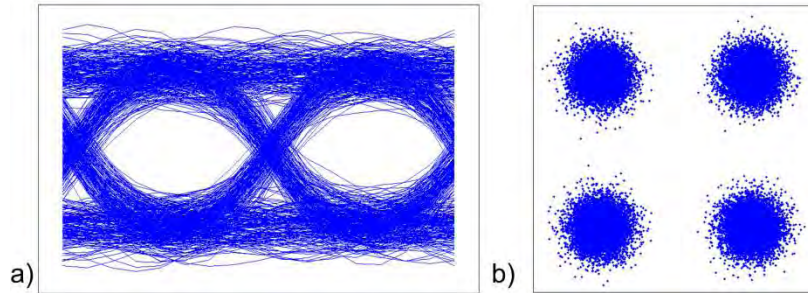

Fig. 41 a) Eye diagram at one of the outputs of the phase-diversity receiver, for a SP-QPSK system;. b) Corresponding constellation diagram. The OSNR is 13 dB. No phase noise is included and a zero IF offset is assumed.

Fig. 42 shows the BER vs SNR per bit, calculated using Monte Carlo simulation, in a SP-QPSK system, with solely ASE noise included, for the synchronous receiver (Fig. 16a) and the differential receiver (Fig. 16b). The electrical filter is a 4th-order Bessel filter with 3 dB bandwidth equal to 0.5 R_S. It can be seen that differential detection, though beneficial in terms of removing uncompensated phase noise (Section V.5) or IF offset (Section V.6), incurs a 2.3 dB penalty on system performance. This is due to the fact that subtracting the noisy samples, as done in the differential receiver prior to complex symbol detection, doubles the noise variance, thus deteriorating system performance. The theoretical BER vs SNR per bit curve calculated using the semi-analytical method for an ideal QPSK system (Appendix C), is also included for comparison. The 1 dB penalty between the performance calculated by the semi-analytical method and that counted by Monte-Carlo simulation is attributed to the simplifying assumptions in the former method, compared to the real-system models incorporated in the latter.

From this point, we will focus our attention on the differential receiver, unless otherwise stated, in order to investigate the possibility of gaining better performance compared to the 1.9 dB seen in Fig. 42. Fig. 43 shows the required OSNR for BER 10^{-3} vs the electrical filter 3-dB bandwidth, expressed as a fraction of R_S, for a SP-QPSK system, calculated using Monte-Carlo simulation, for a number of POLCOMB cases. The electrical filter used is a 4th-order Bessel filter. The optimal filter bandwidth for such a high BER is found to be approximately 0.5 R_S. An ideal SP-QPSK system is one with no polarization rotation, thus needing no POLCOMB. All other POLCOMB cases correspond to a constant polarization rotation over the simulation time window. We observe that the MRC achieves optimal SP-QPSK system performance for all filter bandwidths. The CCMA has a small penalty compared to the ideal, whereas the CCMA algorithms adapted for a SP-QPSK system achieve optimal

SP-QPSK performance only for the optimal filter bandwidth (SectionV.4.iv). It is important to note, that the CMA algorithm performs approximately 2.3 dB better than the ideal SP-QPSK case, achieving performance close to the same system when using synchronous detection. This is attributed the ability of the CMA to successfully remove the ASE noise term, common in both complex photocurrents, effectively mitigating the effect of differential detection before complex symbol estimation. Also important, is the fact that a CMA-based POLCOMB with more than one tap per FIR filter, can remove ISI due to tight LPF filtering, achieving good performance for electrical filter bandwidths as small as $0.3\,R_S$.
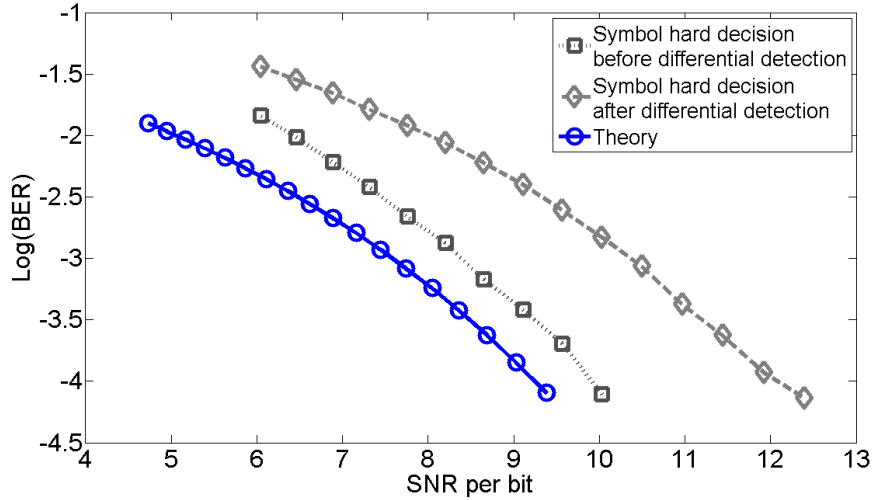
Fig. 42 BER vs SNR per bit, calculated using Monte Carlo simulation, in a SP-QPSK system, with ASE being the only noise source, for the two detection techniques shown in Fig. 16. (Symbols: Diamonds: Differential detection; Squares: Synchronous detection; circles: Ideal system performance calculated using a semi-analytical method).
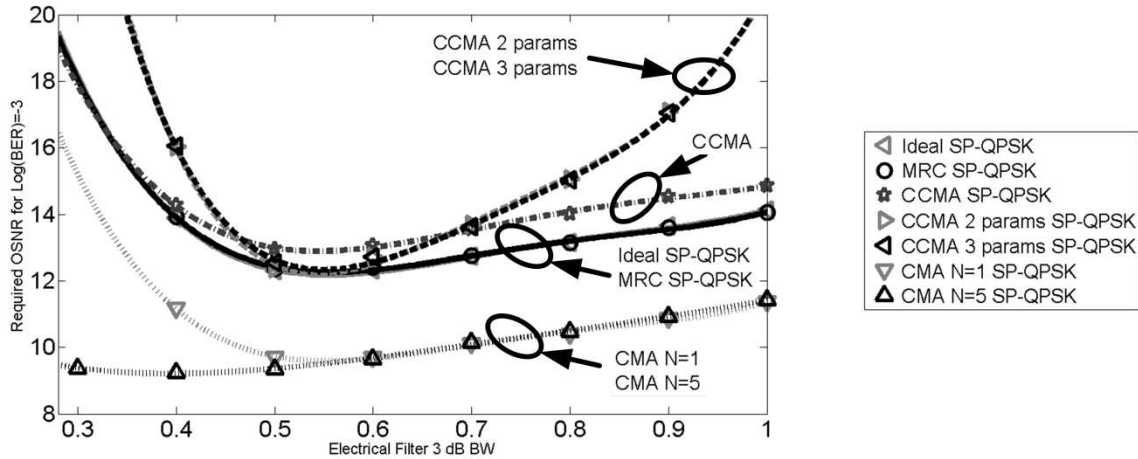
Fig. 43 Required OSNR for BER 10^{-3} vs electrical filter 3-dB bandwidth for a number of polarization combining cases, for a SP-QPSK system. (Simulation parameters: Electrical filter: 4th-order Bessel filter; Random polarization rotation: J_{11}=0.5994-j0.1683, J_{12}=0.1307-j0.7716, J_{21}=0.1307-j0.7716, J_{22}=0.5994+j0.1683).

Fig. 44 shows the required OSNR for BER 10^{-3} vs the electrical filter 3-dB bandwidth for a PDM-QPSK system, expressed as a fraction of R_S, calculated using Monte-Carlo simulation, for a number of POLDMUX cases. The electrical filter used is again a 4th-order Bessel filter. The optimal filter bandwidth for such a high BER is found again to be approximately $0.5\,R_S$. The CMA POLDMUX with more than one tap can remove the ISI incurred by tight LPF filtering, achieving good performance for electrical filter bandwidths as small as $0.3\,R_S$. The simple CMA and CCMA

algorithms have identical performance. Contrary to the SP-QPSK case, no algorithm achieves performance identical to that of the synchronous receiver.
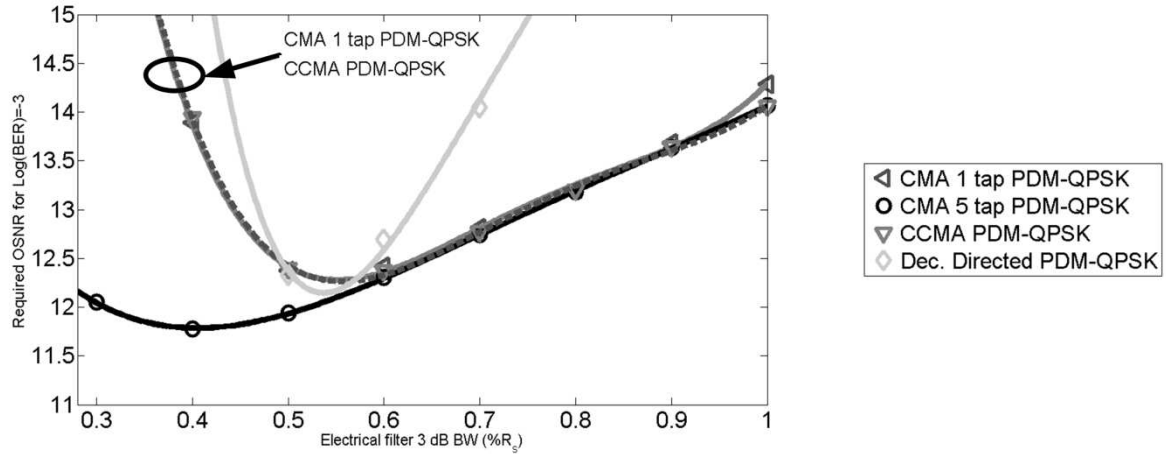
Fig. 44 Required OSNR for BER 10^{-3} vs electrical filter 3 dB bandwidth for a number of POLDMUX cases, for a PDM-QPSK system. (Simulation parameters: Electrical filter: 4th-order Bessel filter; Random polarization rotation: J_{11}=0.5994-j0.1683, J_{12}=0.1307-j0.7716, J_{21}=0.1307-j0.7716, J_{22}=0.5994+j0.1683).

Fig. 45 shows the BER vs SNR per bit waterfall curves calculated using Monte-Carlo simulation, for the optimum electrical filter bandwidth found above, i.e. 0.5 R_S, for both the SP- and the PDM-QPSK systems. These curves allow us to compare the performance of various SP- and PDM-QPSK systems. The theoretical BER vs SNR per bit curve calculated using the semi-analytical method, for an ideal SP-QPSK system, is also included, for comparison. The results reveal the identical performance of a SP-QPSK system using the differential receiver (no polarization rotation), and a PDM-QPSK system using a POLDMUX and the differential receiver. Both systems perform approximately 3 dB worse than the theoretical QPSK, and the SP-QPSK system with the synchronous receiver at BER=10^{-3}.
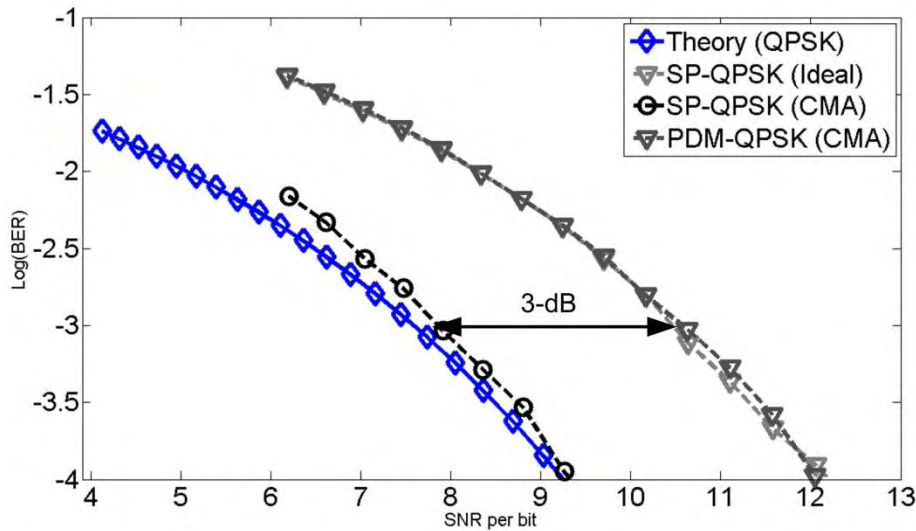
Fig. 45 BER vs SNR for the SP-QPSK and PDM-QPSK system used in this thesis, compared to the theoretical curve. Electrical filter: SP- and PDM-QPSK systems, 4th-order Bessel with 0.5 R_S 3-dB bandwidth. Theoretical performance, 1st-order Gaussian filter with 0.5 R_S 3-dB bandwidth. (Simulation parameters: Random polarization rotation: J_{11}=0.5994-j0.1683, J_{12}=0.1307-j0.7716, J_{21}=0.1307-j0.7716, J_{22}=0.5994+j0.1683).

2. Performance of polarization demultiplexing algorithms in the presence of ASE noise and time-varying polarization rotations

As a case study, we investigated the performance of the various POLDMUX algorithms in time-varying polarization rotation conditions. The motivation behind this study was the fact that, PDM-QPSK was also proposed for use in optical interconnects [193], in which arbitrary channel switching occurs frequently, abruptly changing channel parameters, forcing the POLDMUX algorithm to re-converge. In this context, BER is governed by the speed of convergence. The OSNR is measured at a $0.125\ R_S$ resolution bandwidth (Appendix M).

The channel model of (101) was used only in this case the azimuth and ellipticity, α and ε, respectively, were considered time-dependent. Two models of time-dependence were investigated. First, step changes were assumed, in order to evaluate the POLDMUX algorithm performance in the event of channel switching. An initial steady-state was assumed (α, $\varepsilon=0$) and the POLDMUX was left to converge. Then, α and ε were abruptly changed, and the BER was evaluated from that point onwards. Fig. 46a shows the initial SOP on the Poincaré sphere (red dot) and the final SOPs for 100 different measurements (blue dots). Parameters α and ε were assumed to be random variables following statistics which produce uniform SOPs on the Poincaré sphere [194]. Second, α and ε were assumed to perform a random walk on the Poincaré sphere, in order to evaluate the POLDMUX algorithm tracking capability, in fast changing conditions. Starting from an initial steady state (α, $\varepsilon=0$), it was assumed that random variables α and ε change on a per sample basis (simulation-time samples), according to the recursion $\alpha_{k+1}=\alpha_k+\delta\alpha$, and $\varepsilon_{k+1}=\varepsilon_k+\delta\varepsilon$, where k denotes the k-th simulation sample, and $\delta\alpha$, $\delta\varepsilon$ are normal random variables with zero mean and variance σ^2. The variance controls the average SOP rotation speed, which we estimate by summing the length of the differential arcs caused by $\delta\alpha$, $\delta\varepsilon$, and dividing the result by the simulation time-window. An example of such a random walk trajectory is shown in Fig. 46b.

Fig. 47 shows the BER performance vs OSNR, for the various POLDMUX algorithms described in Section V.4, using the step-change time-dependent model. The optimal electrical field 3-dB bandwidth found in Section VI.1 was used. Each point represents the average BER measurements over 100 trials. Ideal system performance is included as a reference. As the OSNR increases, a BER floor emerges, attributed to the fact the BER is dominated from the error bursts caused by the finite time needed by the equalizers to converge to a new stable condition rather than additive noise. The CCMA algorithm produces one order of magnitude better BER floor performance compared to the other algorithms, due to the fact that it converges much faster, owing to the constraints imposed on the values of the elements of the inverse channel matrix.

Fig. 48 shows the required OSNR for BER equal to 10^{-3} vs the SOP rotation speed, using the random walk time-dependent model. Each algorithm has a different threshold after which performance deteriorates exponentially. Again, the CCMA algorithm exhibits one order of magnitude better performance.
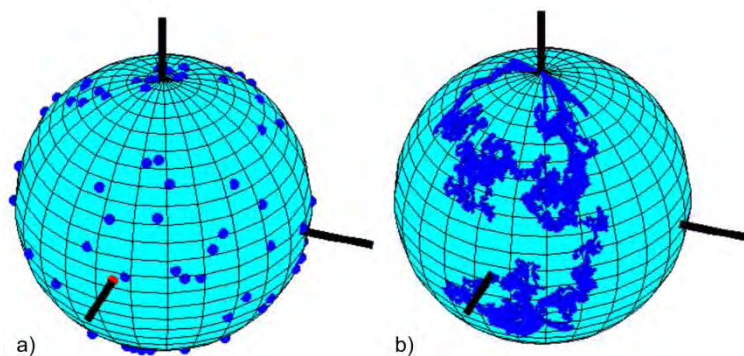
Fig. 46 SOP trajectory due to polarization rotation on the Poincaré sphere. a) Step changes in the SOP; red dot: initial SOP; blue dots: SOP after step change; b) Random walk changes in the SOP. Trajectory of time varying SOP.
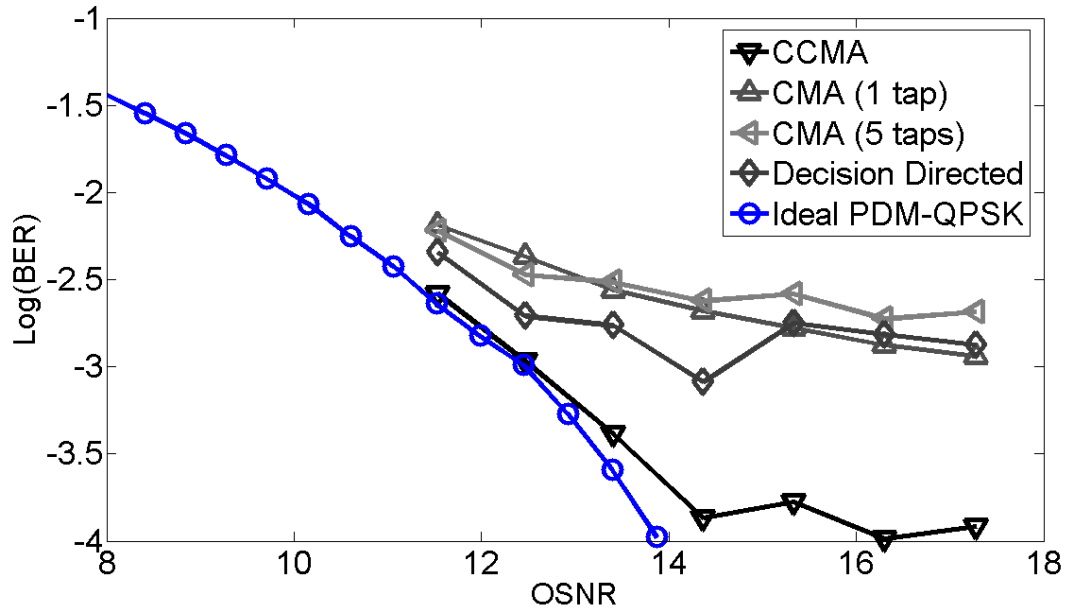
Fig. 47 BER vs OSNR for a number of POLDMUX algorithms, in a system with step SOP changes. Electrical filter: 4th-order Bessel with 0.5 R_S 3-dB bandwidth.
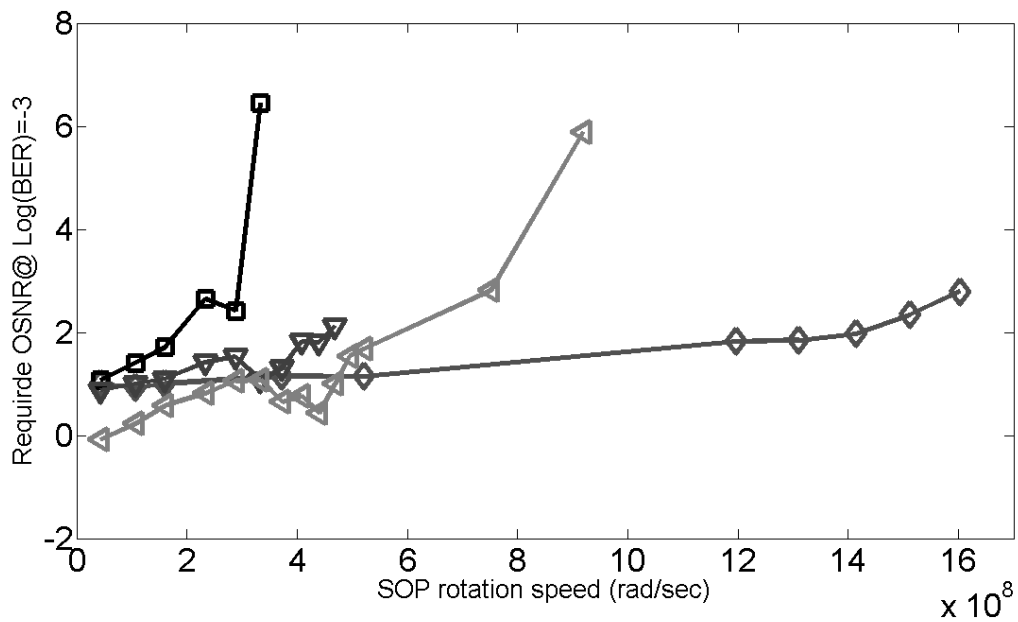
Fig. 48 Required OSNR for BER 10^{-3} vs SOP rotation speed for a system with time varying SOP emulated by a random walk. Electrical filter: 4th-order Bessel with 0.5 R_S 3-dB bandwidth.

3. Performance of phase noise estimation algorithms

In this section we investigate the performance of the various phase compensation algorithms described in Section V.5. We investigate their performance in a SP-QPSK system, in the presence of ASE noise. Both receiver configurations were investigated, the synchronous and differential receivers (see Fig. 16). The OSNR is measured at a 0.125 R_S resolution bandwidth (Appendix M).

Fig. 49 shows the OSNR penalty at BER=10^{-3}, for the best cases of the decision-directed algorithms described in Section V.5.i and the two receiver configurations. Fig. 49a, corresponds to the synchronous receiver, whereas Fig. 49b corresponds to the differential receiver. In both figures, the performance of the system using the differential receiver with no phase noise compensation is included as a comparison (Fig. 23b). From Fig. 49a it can be seen that decision-directed phase noise compensation can improve system performance dramatically (compare with Fig. 23a). Actually, the synchronous receiver can achieve the same performance as the ideal differential receiver with no phase noise compensation in the region of large laser-linewidth $\times$ symbol-period products, while Savory's algorithm performs better in the low laser-linewidth $\times$ symbol-period products. On the other hand, from Fig. 49b, it can be seen that decision-directed algorithms deteriorate the performance of differential receiver.
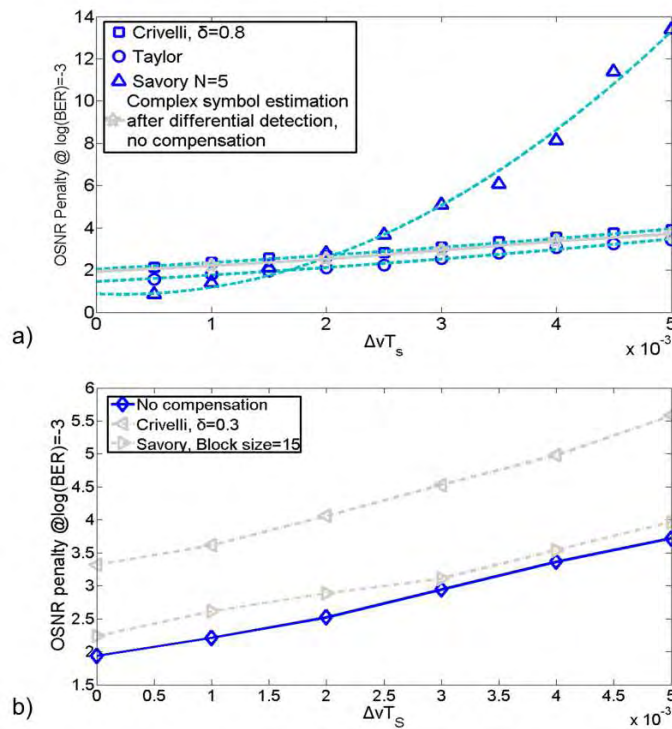
Fig. 49 OSNR penalty at BER=10^{-3} for various decision-directed phase noise compensation algorithms. a) Synchronous receiver; b) Differential receiver.

Fig. 50 shows the OSNR penalty at BER=10^{-3}, for M-th power law phase estimation method with a Wiener impulse response (Section V.5.ii), for the two receiver configurations. Fig. 50a corresponds to the synchronous receiver, whereas Fig. 50b corresponds to the differential receiver. In both figures, the performance of the system using the differential receiver with no phase noise compensation is included as a comparison (Fig. 23b). The Wiener solution improves the performance of both receivers. Using the enhanced unwrapping procedure (Appendix H) can offer system improvement of approximately 1 dB in the case of the synchronous receiver, and, in the large laser-linewidth $\times$ symbol-period product region, produces the best system performance. In all cases, the parameter r of (145) is optimized performing a sweep over a large number of values ranging from 10^{-5} to 100. The best result is always kept.
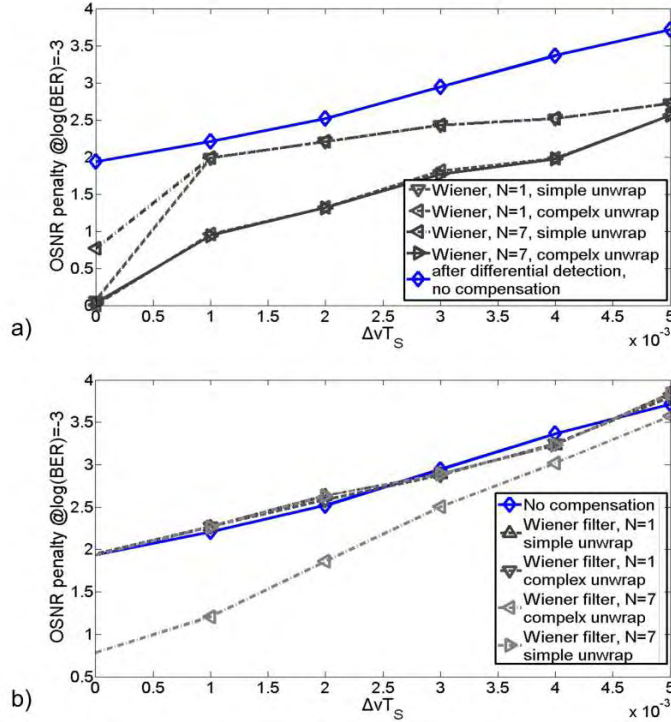
Fig. 50 OSNR penalty at BER=10^{-3} for various *M*-th power phase noise compensation algorithms using the Wiener solution. a) Synchronous receiver; b) Differential receiver.

Due to the difficulties in implementing the Wiener solution, the various approximations described in Section V.5.ii were tested. In Fig. 51, the two approximations are compared. Fig. 51a corresponds to the synchronous receiver, whereas Fig. 51b corresponds to the differential receiver. Whereas Noé's algorithm is suitable for laser linewidth × symbol period products up to approximately 3×10^{-3}, Hoffmann's algorithm offers good system performance for all laser linewidth × symbol period products up to 3×10^{-5}.

In Fig. 52 the performance of the block phase algorithm, commonly used in the first coherent QPSK systems studied experimentally [165], is examined, for both receiver configurations. Fig. 52a corresponds to the synchronous receiver, whereas Fig. 52b corresponds to the differential receiver. In Fig. 52a, the important role of the block size is illustrated. Large block sizes are favorable in the case of small laser-linewidth × symbol-period products, since the slowly varying phase noise can be tracked from block to block correctly. The larger the laser-linewidth × symbol-period product, the smaller the required block size. In contrast, Fig. 52b indicates that system performance for the differential receiver is not improved by the block phase estimation method.

Fig. 53 compares the OSNR penalty at BER=10^{-3}, for the best cases of the all algorithms, comparing both receiver configurations. The differences are small, but the best performance of all is obtained synchronous receiver, when the Wiener solution is used, with a filter size of seven taps, using the enhanced unwrapping method. The most hardware-efficient method is Hoffmann's algorithm, also with seven coefficients, for which both receiver configurations perform similarly, with a small penalty compared to the Wiener solution. Nonetheless, we safely conclude that the 3-dB laser linewidth is not the limiting impairment in coherent systems, since laser linewidth × symbol period products as high as 5×10^{-3} can be tolerated with a penalty smaller than 3 dB (corresponding to lasers with 50 MHz linewidth at 10 GBd).
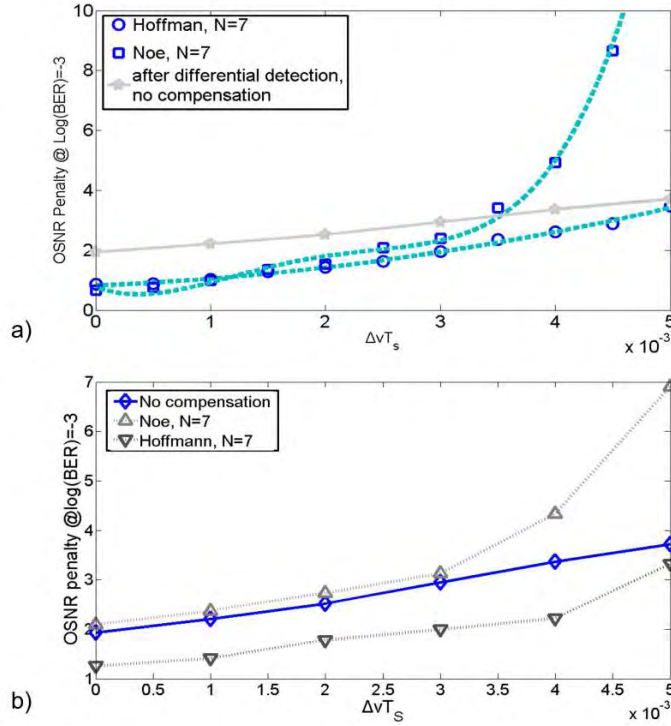
Fig. 51 OSNR penalty at BER=10^{-3} for various *M*-th power phase noise compensation algorithms using a Wiener solution approximation. Noé's algorithm: rectangular filter approximation; Hoffmann's algorithm: Binary coefficient filter approximation. a) synchronous receiver; b) Differential receiver.
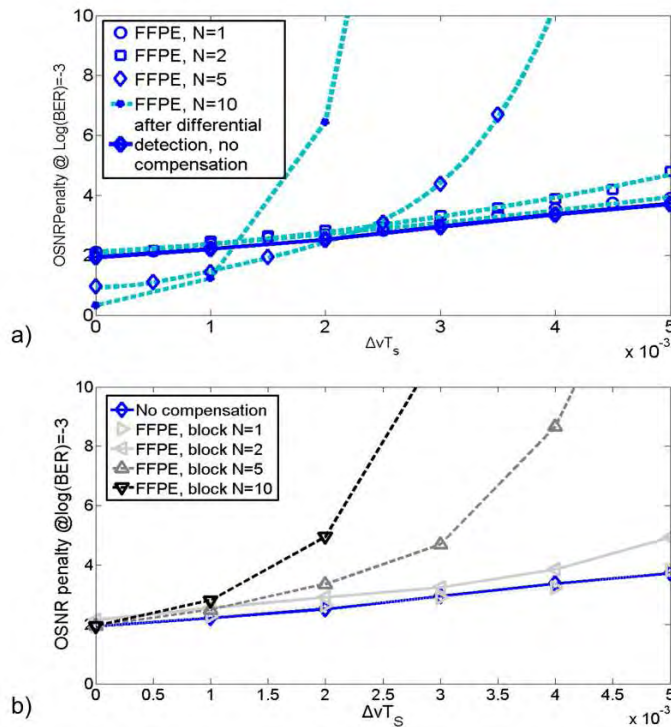
Fig. 52 OSNR penalty at BER=10^{-3} for various *M*-th power phase noise compensation algorithms using the block phase method. a) Receiver Synchronous receiver; b) Differential receiver.
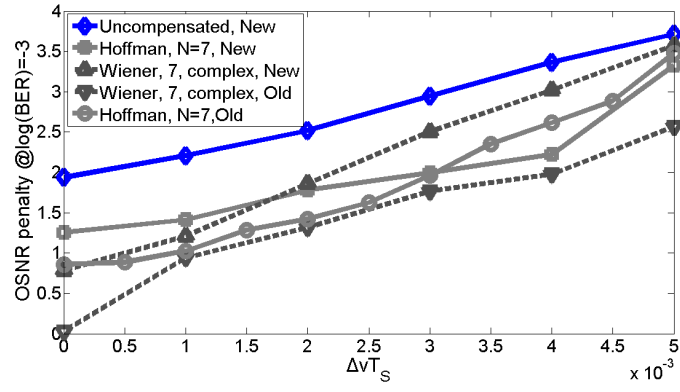
Fig. 53 Comparison of the OSNR penalty at BER=10^{-3} for the best cases of the algorithms described in this section, for both receiver configurations.

4. Performance of intermediate frequency offset compensation algorithms

In this section we compare the estimation error of the various IF offset compensation algorithms described in Section V.6, using the mean absolute estimation error as a criterion. IF offsets in the range between and 0.15 R_S are investigated.

Fig. 54 compares the performance of the three algorithms for three different laser-linewidth × symbol-period products, namely $\Delta v T_S = 0$, $\Delta v T_S = 5 \times 10^{-5}$ (500 kHz 3-dB laser linewidth at 10 GBd), and $\Delta v T_S = 2 \times 10^{-3}$ (20 MHz 3-dB laser linewidth at 10 GBd), for the phase increment algorithm (Fig. 54a), Tretter's algorithm (Fig. 54b), and Kay's algorithm (Fig. 54c). It can be seen that the laser linewidth does not affect the estimation capability of any of the algorithms, however, every one of the three algorithms have totally different performance. It is also worth noting that the phase increment algorithm produces the best estimation, which, especially for high OSNRs, is almost ideal. However, the algorithm fails to estimate correctly IF offsets larger than 0.125 R_S. In all cases, the estimation block length is equal to the simulation time window, i.e., 32768 symbols.
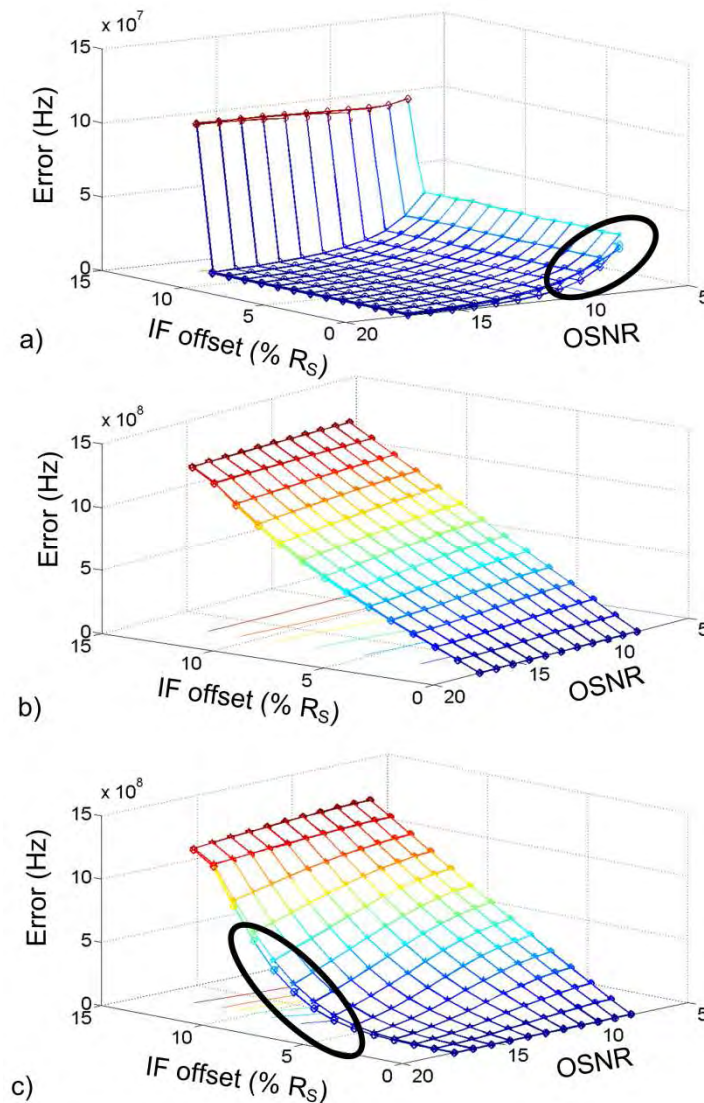
Fig. 54 Estimation capability of a) the phase increment algorithm; b) the Tretter algorithm; c) the Kay algorithm. In each figure three different laser-linewidth × symbol-period products are depicted , $\Delta v T_S = 0$, $\Delta v T_S = 5 \times 10^{-5}$, and $\Delta v T_S = 2 \times 10^{-3}$.

Fig. 55 compares the three algorithms for the case where $\Delta v T_S = 2 \times 10^{-3}$. It is obvious that the phase increment algorithm performs better with more than an order of magnitude, even for IF offsets

approaching 0.1 R_S. In the remainder of this thesis, we will use the phase increment algorithm for IF offset estimation and compensation, unless stated otherwise.
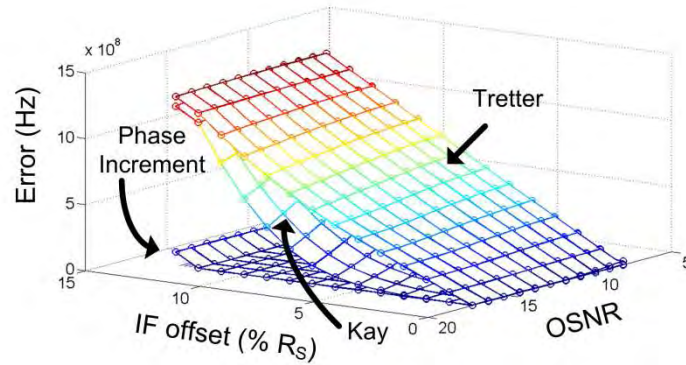
Fig. 55 Comparison of IF offset estimation algorithm performance. Laser linewidth $\times$ symbol period product $\Delta v T_S = 2 \times 10^{-3}$.

In any practical system, the block size over which the IF offset will be estimated will be much smaller than the simulation window size used above. In Fig. 56 we show the mean absolute estimation error for $\Delta v T_S = 0$ (Fig. 56a) and $\Delta v T_S = 2 \times 10^{-3}$ (Fig. 56b), for estimation block sizes equal to 32768, 1024, 512, 128 symbols. The smaller the block size the worse the estimation, especially for low OSNRs. Phase noise doesn't have much impact on estimation capability. We can see that in the low OSNR region, the estimation is much larger than the original IF offset, and thus, subtracting it from the complex samples will actually increase the IF offset, deteriorating the performance of the phase noise removing algorithms which follow.
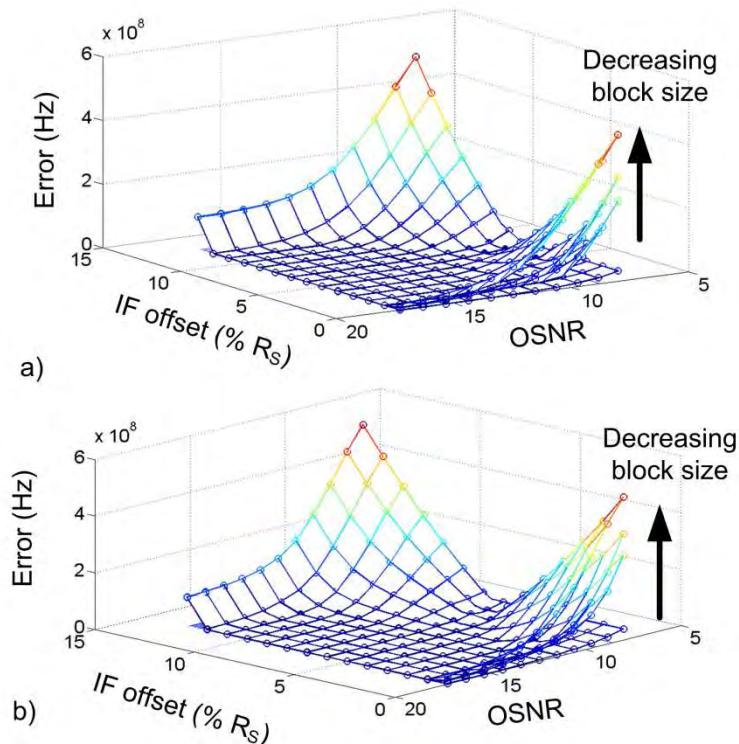
Fig. 56 Estimation capability of the phase increment algorithm for various estimation block sizes. a) $\Delta v T_S = 0$; b) $\Delta v T_S = 2 \times 10^{-3}$.

118

5. Performance of quadrature imbalance compensation algorithms

In this section, we investigate the performance of the QI compensation algorithms described in Section V.7. A PDM-QPSK system is used and both amplitude and phase mismatch are simulated. We study the BER performance vs OSNR in a realistic system which has both non-zero IF offset and phase noise. The IF offset is set to 500 MHz, a typical value for intradyne coherent systems, as exhibited in the analysis of the experimental results in Section VI. The 3-dB laser linewidth is assumed to be 5 MHz, typical for a good quality DFB laser. Since quadrature imbalance is an effect imposed by the phase-diversity receiver, QI compensation algorithms are inserted immediately after the sampling module and before the IF offset and phase noise compensating algorithms. Receivers operating with both symbol-spaced and fractionally-spaced sampling were investigated. The differential receiver is used, since IQ imbalance compensation algorithms often leave a residual rotation of the constellation at their output. For IF offset compensation, the phase increment algorithm is used (Section V.6.i), whereas for phase noise compensation, the block phase estimation algorithm is used, with a block size N=10 (Section V.5.ii).

An ideal receiver exhibiting no QI is considered as a reference, using a rudimentary CMA POLDMUX algorithm, with 1 tap and 2 taps, for symbol-spaced and fractionally-spaced sampling, respectively. QI is then introduced. A specific case of amplitude and phase mismatch is assumed, corresponding to a rather exaggerated, arbitrarily set case, in which $\varepsilon=0°$ and $\delta=30°$ / $\delta=-30°$ for each phase-diversity receiver, respectively, the coupling coefficients of the 3-dB couplers are set to +30% of their nominal value, and the balanced photodetector responsivity ratio deviation is +20%. Fig. 57 (a)-(e) show representative constellations at the input (a), the output of the POLDMUX ((b) (d)), and after phase tracking ((c) (e)), with, and without QI compensation, respectively, at 22 dB OSNR.
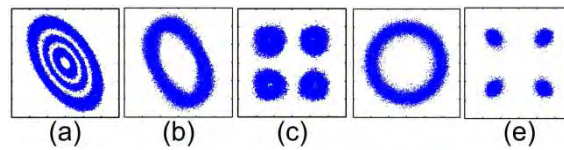
Fig. 57 Representative constellations: (a) input; (b), (d) at the output of the POLDMUX and (c), (e), after phase tracking, with, and without QI compensation, respectively, for a system with symbol-spaced sampling.

Fig. 58 and Fig. 59 show the BER vs. OSNR for a variety of QI compensation options, for the receivers with symbol-spaced and fractionally-spaced sampling, respectively. Dotted curves correspond to the case where no dedicated QI compensation is performed, rather the CMA POLDMUX is the only algorithm with equalizing capabilities. It is obvious that although multi tap butterfly equalizers are successful in mitigating ISI, they are inadequate for compensating large amounts of QI. It is also interesting to note that in the presence of QI, they also exhibit extremely slow convergence properties (not apparent in the figures), requiring as many as 20,000 symbols. This is attributed to the inability of the transverse filter in each butterfly branch to unravel the erroneous superposition of the two quadratures. For the ellipse fitting algorithm, only 1,000 samples were used for ellipse estimation, since the ellipse shape is formed by a small number of samples. In implementing the Gram-Schmidt orthogonalization algorithm, time averaging over realizable block sizes is performed and it was found that a minimum block size is required. As described in V.7.ii, the constrained QI CMA can be implemented using four independently adjustable parameters, or, alternatively, taking advantage of the form of the inverse transfer matrix (167), reducing their number to three (λ, ε, δ) or two (λ, δ). Decreasing the number of independently adjustable parameters produces a penalty, which is more significant in the case of fractionally-spaced sampling. It is interesting to note that all optimized algorithms exhibit almost identical, close to ideal performance, due to their similar operating principle, i.e., they are zero-forcing equalizers that differ only in the accuracy of the estimation of the parameters of the mixing matrix.
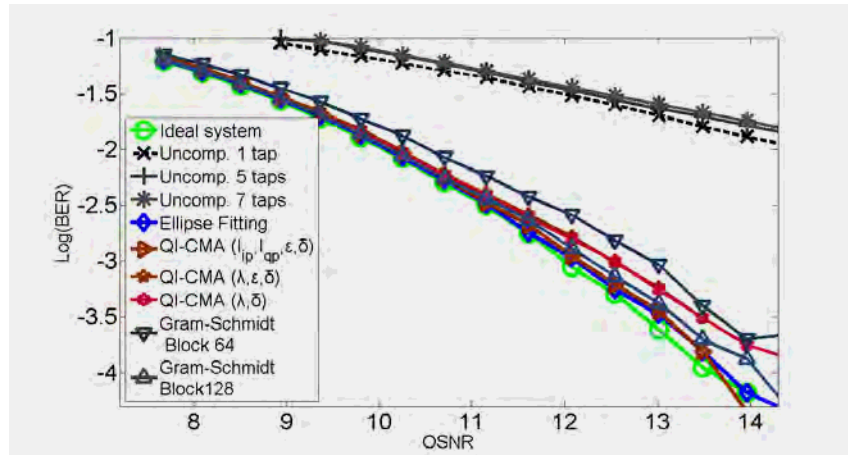
Fig. 58 BER vs OSNR for a system with symbol-spaced sampling for a number of QI compensation algorithms.
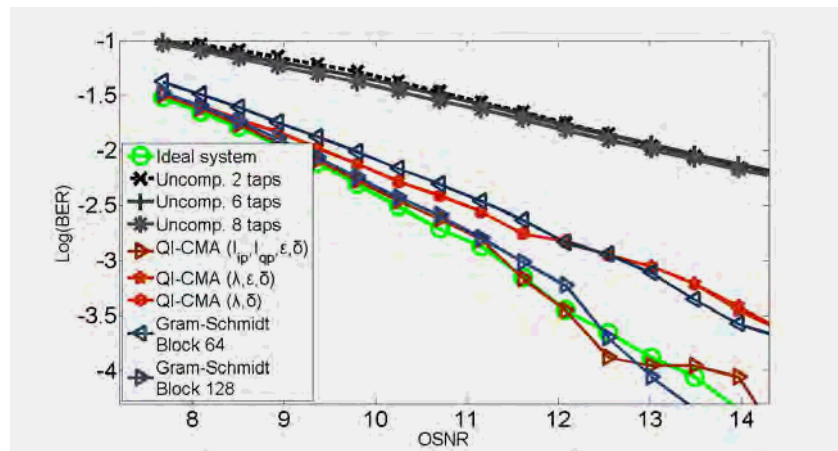
Fig. 59 BER vs OSNR for a system with fractionally-spaced sampling at twice the symbol rate for a number of QI compensation algorithms.

VII. Experimental results

In this section, we present the experimental setup used to evaluate the performance of the algorithms described in Section V and analyze the experimental results for a number of situations.

1. Experimental setup

The basic SP-QPSK polarization- and phase-diversity experimental setup is shown in Fig. 60. Light from an ECL laser, acting as an optical carrier, is QPSK phase modulated, using an integrated LiNbO$_3$ QM (Photline MPZ-LN). The QM was driven by a pair of bipolar binary NRZ waveforms, produced by a pulse pattern generator (PPG), which is driven by a PRBS with period 2^7-1. Bit rates in the range of 0.1–10.7 Gbps were used. The two binary waveforms are identical, time-shifted by a 36 bit periods for de-correlation.

The phase-modulated optical signal is transmitted over an optical channel, which varied depending on the experiment. A short span of SMF fiber was used in back-to-back experiments designed to provide proof-of-concept results. Fiber spans of 75 km SMF or 100 km Corning® LEAF® (subsequently referred to as LEAF) were used to emulate transmission over repeater-less distances. In all cases, a variable optical attenuator (VOA) and an EDFA were used at the receiver side to adjust the received OSNR. The light after the VOA was detected using a polarization- and phase-diversity coherent receiver. One of the two phase-diversity receivers was comprised of a bulk component 2×2 90° optical hybrid followed by two photodiodes with 10 GHz bandwidth, whereas the other was comprised of an integrated LiNbO$_3$ 2×4 90° optical hybrid (CeLight CL-QOH-90) and two balanced photodetectors with 40 GHz bandwidth. A tunable ECL was used as an LO. The signal from the LO was split in a polarization independent 3-dB coupler. The frequency of the LO was manually tuned within a signal bandwidth interval from the frequency of the optical carrier, resulting in a small but non-zero IF offset, thus categorizing the experiments as intradyne.
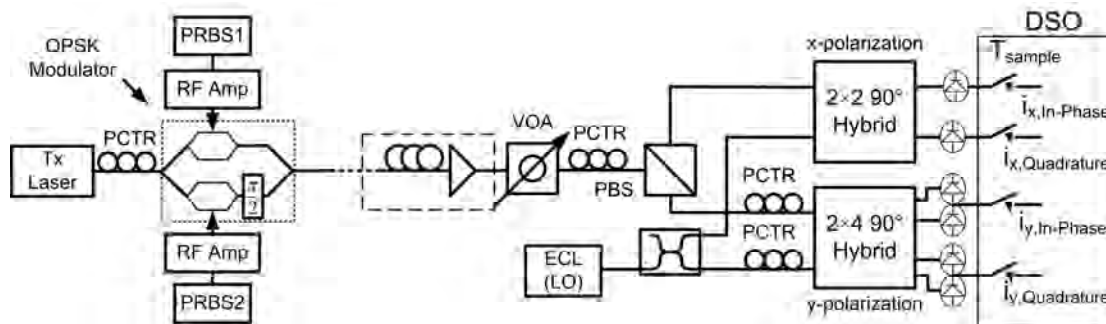
Fig. 60 Experimental setup for coherent a SP-QPSK system with polarization- and phase-diversity. (Abbreviations: Tx Laser: Transmitter laser, PCTR: Polarization controller, RF Amp: Radio frequency amplifier, PRBS: Pseudo random binary sequence, VOA: Variable optical attenuator, PBS: Polarization beam splitter, ECL: External cavity laser, DSO: Digital sampling oscilloscope, T$_{sample}$: Sampling period).

Each of the phase-diversity receivers produce two output photocurrents, one for the in-phase and one for the quadrature part of each of the polarization tributaries of the received optical signal. The four photocurrents were fed into a four-channel DSO (Agilent Infiniium 80804B), were sampled, and stored. The sampling capability of the DSO is 20 GSamples per second when all four channels are recorded, and 40 GSamples per second, when only two of the channels are recorded. Each measurement lasts 51.25 µs. The stored samples were processed off-line with a personal computer using Mathematica or MATLAB.

A variant of the basic QPSK experimental setup was used for producing PDM-QPSK signals, as shown in Fig. 61. The light at the output of the QM was split into two equal-amplitude components, using a symmetric, polarization independent 3-dB coupler. One of the two components was delayed using approximately 8 m of SMF optical fiber. The SOPs of the two signals were adjusted using two

PCs until the two signals became aligned with the principal axes of the PBC, and were combined forming a PDM-QPSK signal.
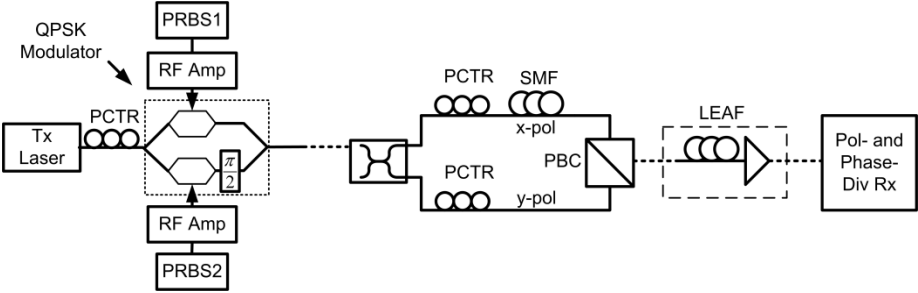
Fig. 61 Experimental setup for a coherent PDM QPSK system with polarization- and phase-diversity.

2. General processing

In this section we present the general processing steps used in the analysis of all the experimental results. We also present the basic non-idealities encountered, and refer to the algorithms used to mitigate them.

i. Channel synchronization

All algorithms described in Section V require one or two samples-per-symbol. Depending on the symbol rate of the experiment, the DSO can acquire 200 samples-per-symbol for the 0.1 GBd experiments, up to 2 samples-per-symbol for the 10 GBd experiments. In the case where the DSO has more samples-per-symbol than needed by the DSP algorithms, a downsampling operation must be performed, in which an initial sample from the measurement is chosen and, starting from this sample, samples at constant intervals are taken, at the desired rate. The initial sample to choose from for each of the four photocurrents is not a trivial task to find. Due to the non-standardized length of the optical fibers used at the receiver, the two polarization tributaries experience different delays from the polarization beam splitter to the input of the hybrids. Moreover, the optical hybrids are different and have different operating principles, thus imposing different delays upon the signals. Finally, there are unequal delays are due to the unequal signal paths between the photodiodes and the DSO. It is therefore not trivial to combine samples of the four photocurrents corresponding to same time instants, as required by the DSP algorithms. Some sort of channel synchronization is needed for every experiment and, as it was found, synchronization in many cases requires introducing relative delays which are tens of times larger than the symbol period.

Though channel synchronization is by no means a trivial process, we adopted a simple method to synchronize the channels, based on the shape of the received constellation, on the grounds that the delays pose a systematic error and once calculated, can be eliminated manually.

Fig. 62 shows the received constellation for two different initial sampling instances, for a 10 GBd experiment. In Fig. 62a, the first received sample of the in-phase photocurrent is combined with the first received sample of the quadrature photocurrent. Although the received constellation diagram is expected to be an ellipse (or ideally a circle), it has an irregular shape instead. In Fig. 62b, a differential delay of three samples is used between the initial samples used from the two sequences, giving the expected ellipse-like constellation.
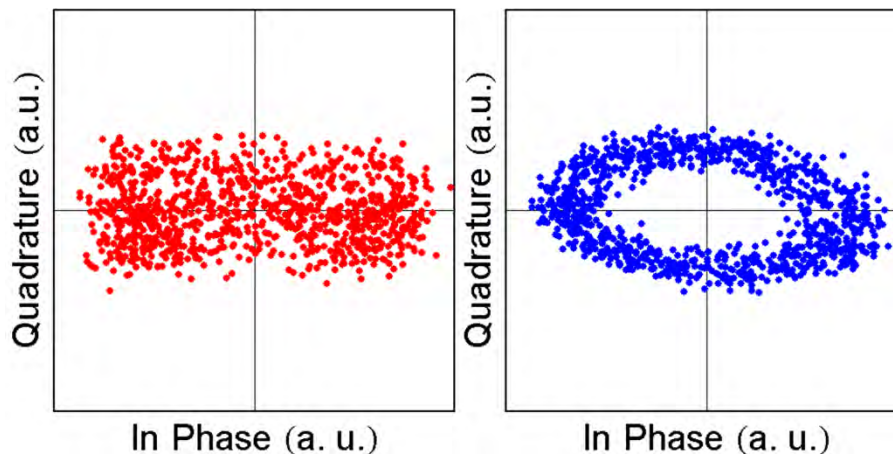
Fig. 62 Constellation diagrams for 1000 samples of a 10 GBd back-to-back experiment. Sampling is performed at the symbol rate. The constellation to the left corresponds to the case where wrong sampling instances are used for the in-phase and quadrature photocurrents used. The constellation to the right corresponds to the case where the correct sampling instances are used.

To calculate the delay, the received eye diagrams for the 1 and 5 GBd back-to-back experiments are plotted, because the high SNR and large number of samples-per-symbol produce clearly distinguishable eye diagrams. Then, two different synchronization processes are performed, targeting

123

the elimination of two different timing errors. The first, is to find the correct sampling instant producing samples at the center of the eye diagram. The second is to find how many symbol periods the two waveforms differ in order to become synchronized. An example of this procedure is shown in Fig. 63 for a 1 GBd back-to-back experiment. The outline of the eye diagrams of the received quadratures is clearly visible and the optimal sampling instants can be found visually by a trial and error procedure. The upper constellation corresponds to a wrong sampling instant combination, while the lower constellation to the correct sampling instant combination. When analyzing PDM-QPSK data, an additional differential timing error must be found, the timing error between the two polarization tributaries. This is determined by observing the output of the POLDMUX.
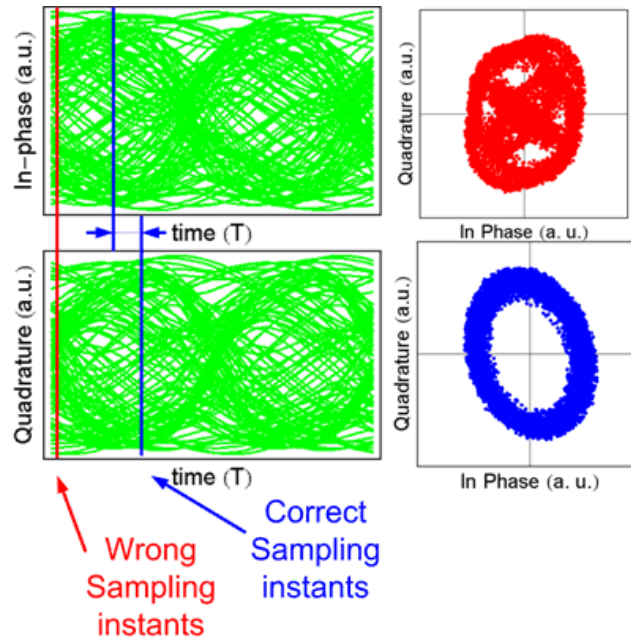
Fig. 63 Procedure for finding the differential delay between quadratures in a 1 GBd experiment. The outline of the eye diagrams of the received quadratures is clearly visible and the optimal sampling instants can be found visually by a trial and error procedure.

ii. Transmitter and receiver distortions and imperfections

Having addressed the issue of synchronizing the received photocurrents, the next task is to identify imperfections and distortions that might affect signal reception and deteriorate system performance, without being expected. Imperfect electrical and electronic equipment were identified as the main culprits behind unexpected distortions. More specifically, time-drifting and multi-level waveforms at the output of the PPG were found to cause significant distortions upon the received signal.

Fig. 64 shows the eye diagrams at one of the two outputs of the PPG, for a 10 GHz pulse rate, for two different time instances of the same measurement. The light-colored waveform corresponds to the beginning of the measurement, whereas the dark-colored waveform to the end of the measurement. The time drift is obvious and is approximately half a symbol period. This affects the optimal sampling instant at the receiver as the measurement evolves.

Fig. 65, left, shows the constellation diagrams at the output of the bulk component phase-diversity receiver, for three different symbol rates, namely 1 GBd, 5 GBd and 10 GBd, for a SP-QPSK system in back-to-back configuration. Constellations correspond to a sampling instant found by examining the first samples of the measurement. The measurements are composed of 50000, 250000, and 500000 symbols, for the 1 GBd, 5 GBd and 10 GBd cases, respectively, but only the first 250000 symbols are depicted in the constellations for the latter two cases. To the right of each constellation diagram is the plot of the absolute value of the complex photocurrent sample for the whole length of the measurement. It can be seen that, as time passes, especially for the case of the 10 GBd experiment, the absolute value becomes smaller, and eventually fades to zero. Keeping the original sampling instant

124

will cause reception to be lost in the 10 GBd case. This change in the complex sample absolute value, is caused by the time drift shown in Fig. 64, and is more severe in the 10 GBd case.
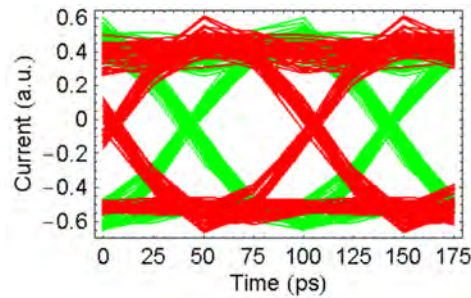
Fig. 64 Eye diagrams at one of the two outputs of the PPG, for a 10 GHz pulse rate, for two time instances of the same measurement. The light-colored waveform corresponds to the beginning of the measurement, whereas the dark-colored waveform to the end of the measurement.

Another subtle imperfection affecting the received constellation is multi-level waveforms at the output of the PPG. Fig. 66 shows the constellation diagram formed by the two outputs of the PPG for the 100 GBd experiment. It is clear that the voltage waveforms exhibit non-negligible ringing at their upper trace, more specifically, two distinct levels are obvious. These non-ideal pulses, which drive the QM, lead to erroneous phase variations at the QM output (see Fig. 10). This makes the received constellations thicker in one quadrant, as verified via simulation in a list of figures shown in Fig. 67. More specifically, Fig. 67a shows the ideal constellation diagram at the output of a phase-diversity receiver, in the case of a SP-QPSK system, in the absence of any form of noise, and with zero IF offset and QI. Fig. 67b shows the same constellation diagram when the pulses driving the QM exhibit a 20% ringing at their upper trace, equal to the measured ringing seen in the experimental results. Fig. 67c corresponds to the case where there is a non-zero IF offset and non-negligible QI. It can be seen that the upper right quadrant of the constellation is thicker than the rest of the constellation due to the multi-level waveforms at the transmitter. Fig. 67d depicts an experimental constellation diagram similar to Fig. 67c, verifying that multi-level waveforms at the transmitter-side affect the received signal constellation shape.

125
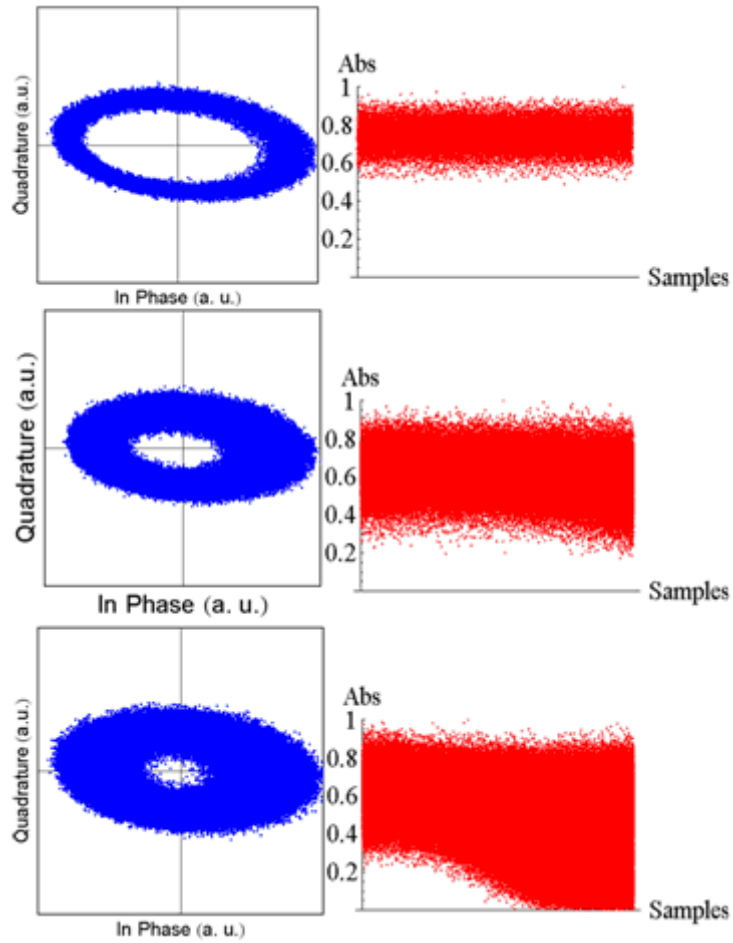
Fig. 65 Left: Constellation diagrams for three back-to-back experiments, with different symbol rates. Right: Magnitude of the corresponding phasors a) 1 GBd, b) 5 GBd, c) 10 GBd. The constellation for the 1 GBd cases is made of 50000 symbols, whereas for the 5 GBd and 10 GBd case 250000 symbols are shown. The plots corresponding to the magnitude of the phasors are made of the whole length of the measurement, which is 50000, 250000 and 500000 symbols for the 1 GBd, 5 GBd and 0 GBd cases, respectively.
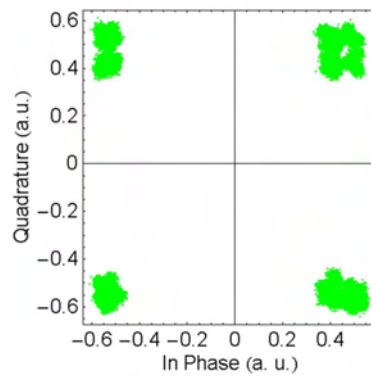
Fig. 66 Constellation diagram formed by the two outputs of the PPG for a 100 MHz pulse rate.
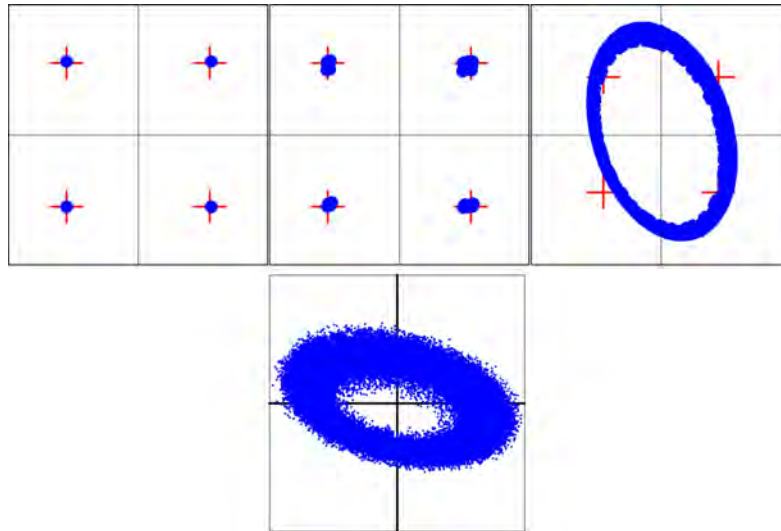
Fig. 67 a) Ideal constellation diagram at the output of a phase-diversity receiver, b) Constellation diagram when the pulses driving the QM exhibit a 20% ringing at the upper trace, c) Constellation diagram when the pulses driving the QM exhibit a 20% ringing at the upper trace and there is a non-zero IF offset and non-negligible QI, d) Experimental constellation.

iii.   Quadrature imbalance

The next step in analyzing the experimental results is to identify various impairments and imperfections defined mathematically in Section V, in order to asses which algorithms should be used. Fig. 68a shows the downconverted complex PSD for a 0.1 GBd back-to-back experiment. The main lobe of the modulated signal resides at the IF offset, which is estimated visually to be approximately -250 MHz. An attenuated image of the central lobe can be seen at $-f_{IF}$, caused by QI. For larger symbol rates and assuming that the IF offset is within the range ± 400MHz, the impact of QI will not be so severe on the shape of the PSD but, as shown in Section V.7, will cause a non-negligible penalty, and therefore, it will have to be compensated. Fig. 68b shows the same PSD after QI compensation. QI compensation greatly reduces the unwanted image spectral component from the received PSD. The central lobe of the image spectrum is attenuated by more than 10 dB compared to Fig. 68a.
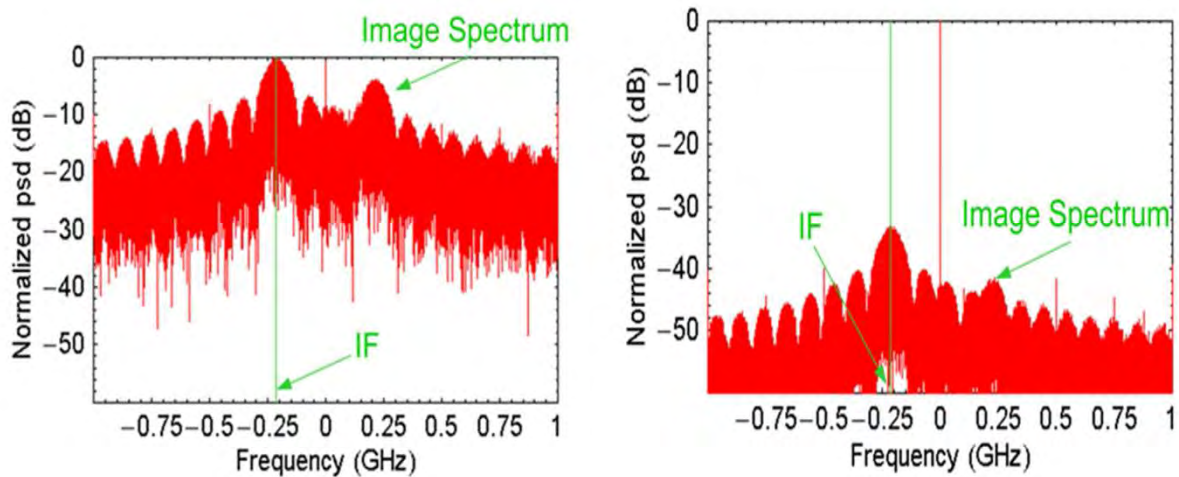
Fig. 68 a) Received signal single-sided PSD, for a 0.1 GBd back-to-back experiment. QI causes an attenuated image of the central lobe to reside at –IF; b) Two-sided PSD for a 0.1 GBd back-to-back experiment, after QI compensation.

After QI compensation, using any of the QI compensation algorithms analyzed in Section V.7, the constellation diagram resembles a circle, as shown in Fig. 69, in comparison to the initial constellation diagram.
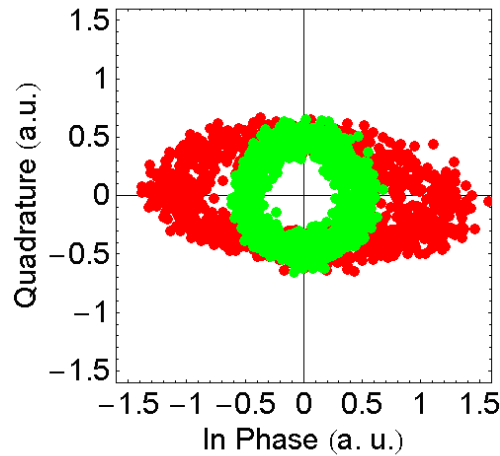
Fig. 69 Constellation diagrams for 1000 received symbols of a 10 GBd back-to-back experiment, before (red points) and after QI compensation (green points). DC offset has been removed with DC block.

iv.   IF offset compensation

The impact of a non-zero IF-offset is also evident on the received signal PSD, as shown already in Fig. 68, where the central lobe of the received signal PSD resides at the IF offset, rather than at baseband. After compensating for the IF offset, the spectrum of the received signal is transferred to the baseband. This is better shown in Fig. 70 for the same 0.1 GBd back-to-back experiment as in depicted Fig. 68, where the initial spectrum with QI and IF offset are also shown for comparison.
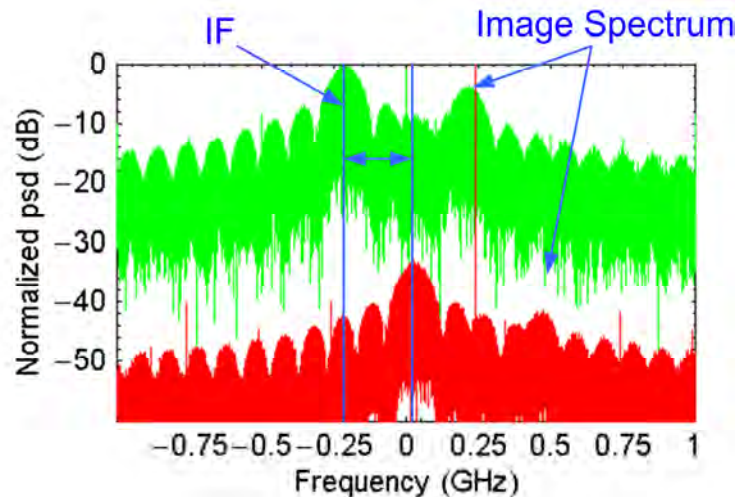
Fig. 70 Two-sided PSD for a 0.1 GBd back-to-back experiment, after QI compensation and IF compensation (below). The initial spectrum is shown for comparison (above).

In Fig. 71, we can see the unwrapped phases for 1000 data-free phasor samples , from a 10 GBd back-to-back experiment, before IF estimation (red) and after compensation (other colors), for all three estimation algorithms described in Section V.6. Each algorithm produces a different estimation, and thus produces a different unwrapped phase sequence at its output. It is clear that the phase increment algorithm produces the best estimate, since the slope of the unwrapped phases after IF offset removal is smaller than the other two. Kay's estimator produces the worst estimate, as predicted in Section VI.4.
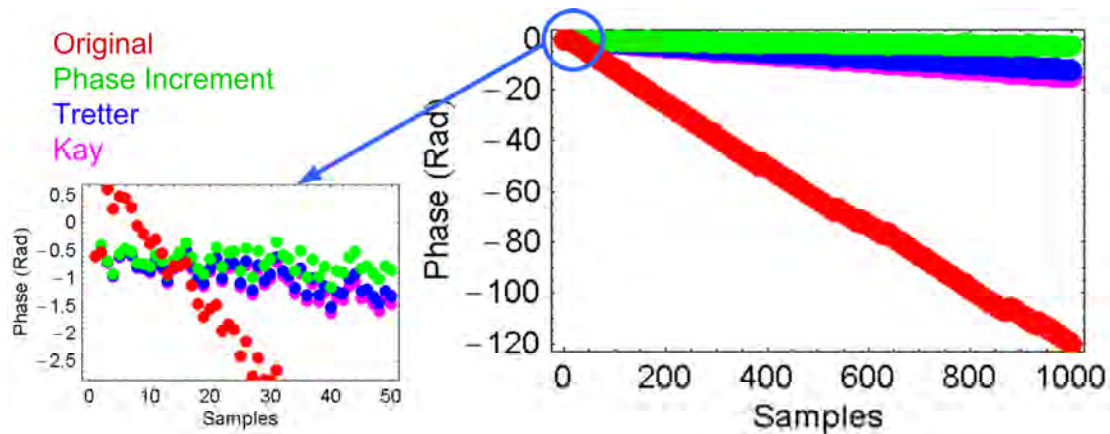
Fig. 71 Unwrapped phases before IF offset estimation and removal (red) and after IF offset estimation and removal, a) Green: Phase increment algorithm (f_{IF}: -206.32 MHz), b) Tretter's algorithm (f_{IF}: -191.76 MHz), c) Kay's algorithm (f_{IF}: -187.16 MHz).

In the analysis of the experimental results, it was found that compensation of the IF offset eliminates only the bulk intermediate frequency but doesn't turn it exactly zero. This is partly due to the fact that noise in the samples contaminates the estimate of the IF offset, and partly due to the fact that the frequency of any practical laser always varies slightly with time. In some cases it was found beneficial to perform a second IF offset estimation and compensation before performing phase noise compensation, even though most phase noise compensation algorithms can tolerate small IF offsets. In Fig. 72, the unwrapped phases for the same 1000 data-free phasor samples as in Fig. 71 are shown, after a second IF removal step. For the bulk IF removal, the phase increment algorithm was chosen, since from Fig. 71, we found that it produced the best estimation. Tretter's algorithm seems to produce the best fine-resolution estimation in the second IF removal step, producing a nearly zero-slope phase trajectory at its output. A second estimation with the phase increment algorithm makes no difference on the result. Kay's algorithm produces again the worst estimate.
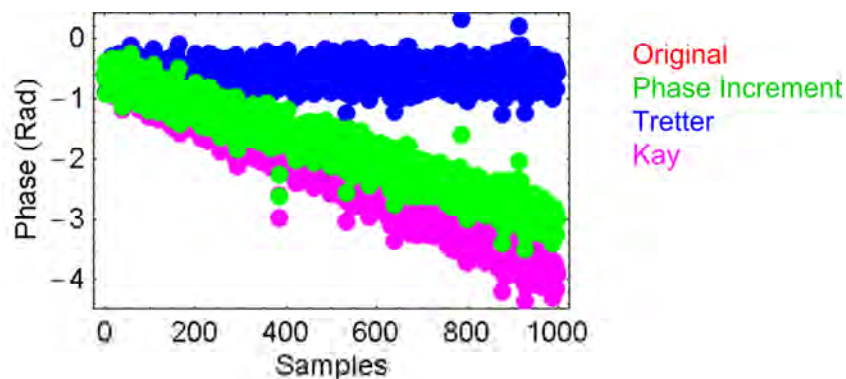
Fig. 72 Unwrapped phase trajectories before second IF estimation and removal (red – not seen because it coincides with the green trace) and after second IF estimation and removal, a) Green: Phase increment algorithm (second estimate: 97.42 kHz), b) Tretter's algorithm (second estimate: -3.88 kHz), c) Kay's algorithm (second estimate: 1.45 kHz).

v.   Phase noise

In practice, any of the algorithms described in Section V.5 can be used for phase noise compensation. However, unwrapping should be avoided, since, in a highly noisy environment, unwrapping exhibits cycle slips. Errors can be reduced by using the enhanced phase unwrapping technique described in Appendix H, but cycle slips are not eliminated completely. Fig. 73 shows the constellation diagrams after phase noise correction for the two different unwrapping functions, for a 10 GBd back-to-back experiment, when the Wiener filter solution is used. Next to the constellation diagrams, are the unwrapped phases before (red) and after filtering (green). The upper set corresponds to the

129

rudimentary unwrapping algorithm, whereas the lower set corresponds to the enhanced unwrapping algorithm. In the first case phase jumps and therefore symbol errors occur frequently. In the second case the results are better for this part of the measurement, however, errors still occur since the random nature of the phase noise, in conjunction with the remaining IF, produce all kinds of confusing combinations. On the other hand, for the same measurement, any algorithm not using unwrapping, produces zero errors.
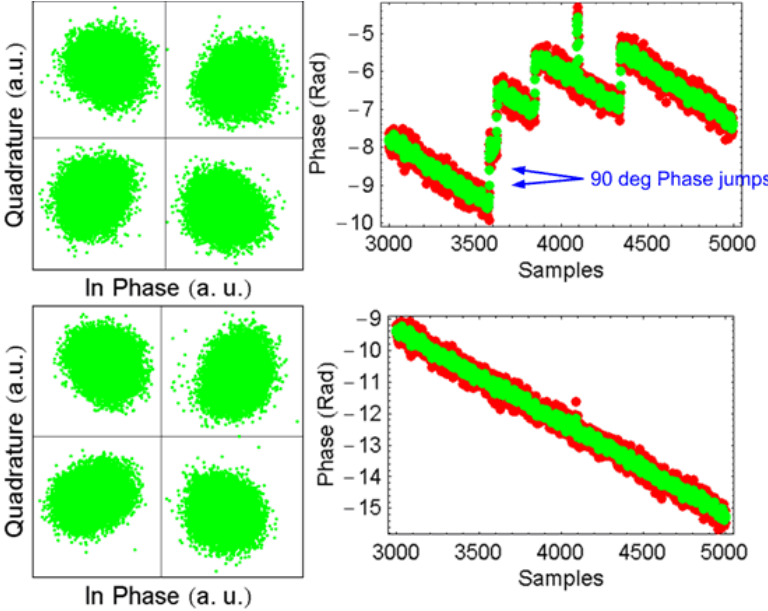
Fig. 73 Constellation diagrams after phase noise correction and unwrapped phase trajectories before (red), and after phase filtering (green), for a 10 GBd back-to-back experiment, with Wiener filtering phase noise compensation. The upper graphs correspond to the rudimentary unwrap algorithm, whereas the lower graphs correspond to the enhanced unwrap algorithm. The unwrapped phases indicate that a small IF still exists. Filtering reduces the variance of the phase, and using the enhanced phase unwrap algorithm reduces the number of phase jumps by 77% in this particular measurement.

3. Analysis of 0.1 GBd experimental data

In this section we present the results obtained by analyzing the experimental data from a 0.1 GBd PDM-QPSK experiment, over 100 km of LEAF optical fiber. The experimental setup used is shown in Fig. 61. The sequence of steps followed to analyze the experimental data are shown in Fig. 74, starting from the output of the DSO.
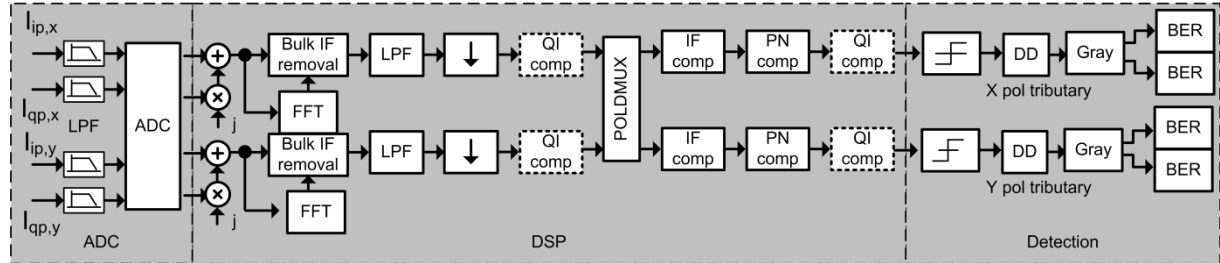
Fig. 74 The sequence of steps involved in analyzing the experimental data obtained from a single-channel 0.1 GBd PDM QPSK experimental set-up. (Symbols: LPF: Low-pass filter; ADC: Analog-to-digital converter; FFT: Fast Fourier transform; QI comp.: Quadrature imbalance compensation; POLDMUX: polarization demultiplexer; IF comp.: IF offset compensation; PN comp.: Phase noise compensation; DD: Differential detection.)

The four photocurrents at the output of the coherent polarization- and phase-diversity receiver are sampled by the DSO, which also acts as a low-pass filter with an approximate 3-dB bandwidth of 4 GHz. The photocurrents are sampled at a rate of 20 GHz, which for the 0.1 GBd signal corresponds to 200 samples per symbol. The measurement is approximately 5,000 symbols long. The frequency of the LO laser is controlled manually, and so the IF offset is substantial compared to the symbol rate. From a range of experiments, it was always found to be larger than 100 MHz, so the 0.1 GBd experiment is categorized as a heterodyne experiment. Therefore, the bulk IF offset must first be removed in order to obtain signal around baseband [171]. The IF offset is found using an FFT method, and the estimated IF offset is removed by multiplying a complex rotating phasor from the received samples, whose frequency is the opposite of the frequency produced by the FFT. After bringing the signal close to baseband, low-pass filtering is performed to remove out-of-band noise. After filtering, a resampling process is performed at a constant sampling rate. Depending on the algorithms to be used, sampling is performed at the symbol rate, or at twice the symbol rate, corresponding to one or two samples-per-symbol, respectively. At the same time, the channel synchronization procedure described in Section VII.2.i is performed, by starting the sampling process from different instances of the four signal vectors, and combining the samples with relative delays from the beginning of the measurement. After resampling, a number of DSP algorithms described in Section V and various combinations of those are used, amongst them, QI compensation algorithms (Section V.7), POLDMUX algorithms (Section V.4), IF offset estimation and compensation algorithms (Section V.6), and phase noise compensation algorithms (Section V.5). Algorithms whose necessity is debatable, as explained further down, are illustrated in dotted lines in Fig. 74. Finally, error counting is performed, by comparing the received symbol sequences with the transmitted sequences, derived from the PRBSs. In what follows, we illustrate the performance of the various DSP algorithms or the penalty for not using them.

Fig. 75 shows the PSD of the X-polarization tributary of the received signal, corresponding to the 2×4 90° optical hybrid, before bulk IF offset removal (Fig. 75a) and after bulk IF offset removal and low-pass filtering (Fig. 75b). Observing Fig. 75a, it can be seen that the central lobe of the received signal PSD is around 350 MHz, i.e., the IF offset is approximately 350 MHz ($f_{IF} = 3.5\ R_S$). It can also be seen that an attenuated image of the central lobe resides at approximately -350 MHz, a phenomenon caused by QI (see Section V.7). Due to the noisy PSD, the FFT estimation of the IF offset is not absolutely

accurate, and a trial and error testing revealed that the optimal frequency for the rotating phasor to perform bulk IF compensation is -371.6 MHz. After IF offset removal, the central lobe is translated to the baseband and, despite additional low-pass filtering, the side lobes are still visible, though attenuated.
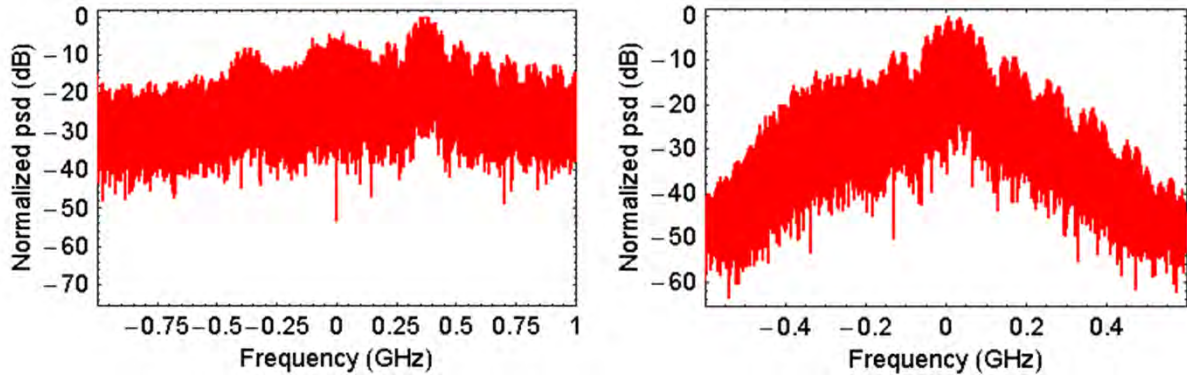
Fig. 75 PSD of the received complex signal at the out put of the 2×4 90° optical hybrid. a) Before bulk IF offset removal, b) After bulk IF offset removal and low-pass filtering. The IF offset is approximately 350 MHz.

Fig. 76 shows the eye diagrams at the output of the LPF after bulk IF removal. The transitions of the eye diagram can clearly be distinguished, facilitating the manual channel synchronization process. An interesting fact is that, within the symbol period, there seem to be two smaller eye diagrams of different durations. Simulations revealed that this discrepancy is due to the fact that the delay introduced by the fiber when constructing the PDM-QPSK signal at the transmitter side, is not an integer multiple of the symbol period. It is expected that the larger the symbol rate, the smaller this phenomenon will be, as is verified in subsequent sections. Fig. 76 also shows the sampling points used for the two polarization tributaries. The sampling instances are phenomenally the same, except that the two polarization tributaries must be combined with a difference of one symbol period, i.e., 200 samples.
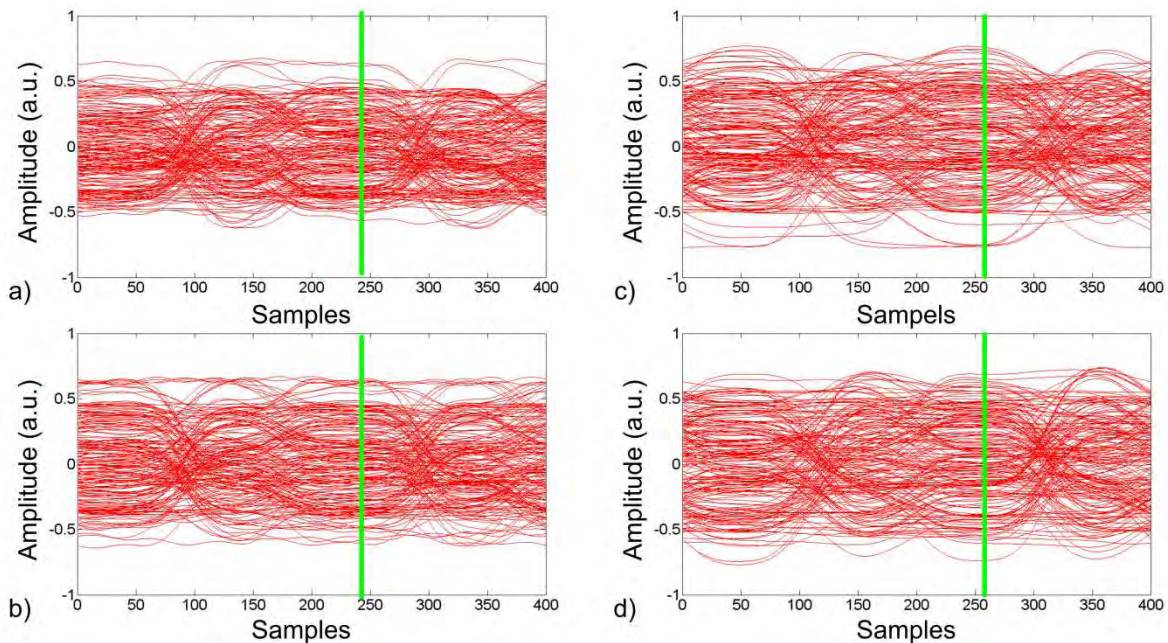
Fig. 76 Eye diagrams for the received photocurrents, after bulk IF removal and low-pass filtering. a) I_{ipx}; b) I_{qpx}; c) I_{ipy}; d) I_{qpy}.

Fig. 77 shows the constellations produced when symbol-spaced sampling is performed at the sampling instants denoted in Fig. 76, for the X polarization (Fig. 77a) and Y polarization (Fig. 77b) tributaries, respectively. The constellations in Fig. 77 are composed of concentric circles with unequal radii. These, are a tell-tale sign of cross-polarization interference between the two PDM-QPSK signals, in the presence of a non-zero IF offset [156]. Although the spectrum in Fig. 75a indicates that substantial QI is present, the constellations are circle-like, indicating that no QI exists. This however is due to the large distance of the unwanted side lobe from base band, due to the large IF offset, and the tight filtering which reduces its effect, as seen in Fig. 75b.
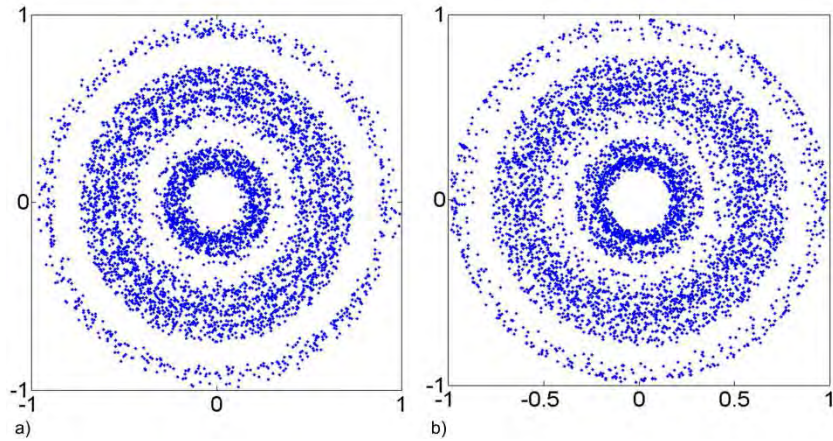
Fig. 77 Received constellation for the a) X-polarization tributary; b) Y polarization tributary.

Assuming that no QI exists based on the form of the constellations of Fig. 77, the sampled photocurrents are immediately fed into the polarization demultiplexer, without performing QI compensation. For symbol spaced sampling, both the CMA POLDMUX algorithm, and the CCMA POLDMUX algorithm can be used (Section V.4.iii). After polarization demultiplexing, the phase increment algorithm is used to perform IF offset estimation and compensation (Section V.6.i), and the FFPE algorithm to perform phase noise compensation (Section V.5.ii), using averaging over 14 samples.

Fig. 78 shows the final constellations at the end of the processing chain, before differential detection, for various POLDMUX cases. Fig. 78(a),(b), correspond to the CCMA POLDMUX whereas Fig. 78c corresponds to the CMA POLDMUX algorithm. Each of the two distinct colors represent one of the two transmitted polarization tributaries. Permutation of the outputs of the polarization demultiplexer is common for both algorithms [156], and therefore the BER is the only criterion in deciding which output corresponds to which transmitted polarization.

Fig. 78a corresponds to the case where parameters $R_2^{(1)}, R_2^{(2)}$ of the CCMA assume values $R_2^{(1)} = R_2^{(2)} = 1$, as should be expected in the case of QPSK (see (113) and (125)). It turns out that these are not the correct values in this case. Trial and error analysis revealed that the optimal values for parameters $R_2^{(1)}, R_2^{(2)}$ are $R_2^{(1)} = 2R_2^{(2)} = 2$, which are the values which produce the constellations in Fig. 78b. The final constellations have different average radii. Simulation analysis revealed that the asymmetry in the radii is connected with the relative values of $R_2^{(1)}, R_2^{(2)}$ and originates from the non-ideal polarization multiplexing process at the transmitter. More specifically, it was found that, due to maladjustment of the PCs or due to the non-ideal power splitting of the 3-dB coupler when forming the PDM signal, the two polarization tributaries that are combined at the PBC have unequal average powers, leading to different final constellation radii [156]. Fig. 78c corresponds to the CMA

POLDMUX algorithm with single-tap filter tap weights (Fig. 19). Using more filter tap weights does not alter the shape of the final constellation.

Though the constellations in Fig. 78(b),(c) are clear, obviously some phenomenon has not been compensated for, since the final constellations are rhomb like. Comparing the constellations with those of Fig. 34, intuitively QI comes in mind. In Section V.7 it was argued that QI is a phenomenon introduced by the phase-diversity receiver. Naturally, the QI compensation algorithm should be placed immediately after sampling the received photocurrents, as indicated in Fig. 74, in order to eliminate the impact of the phenomenon, before applying any other algorithm targeting transmission phenomena or noise. Fig. 79 shows the final constellations when the Gram-Schmidt orthogonalization of QI is applied (Section V.7.iii). Averaging is performed over the whole length of the received complex symbols. Fig. 79a corresponds to the case where the CCMA POLDMUX algorithm is used (with $R_2^{(1)} = 2R_2^{(2)} = 2$) whereas Fig. 79b corresponds to the case where the CMA POLDMUX algorithm is used (using single-tap filter tap weights). Comparing to Fig. 78b and Fig. 78c, it is seen that little improvement is achieved.
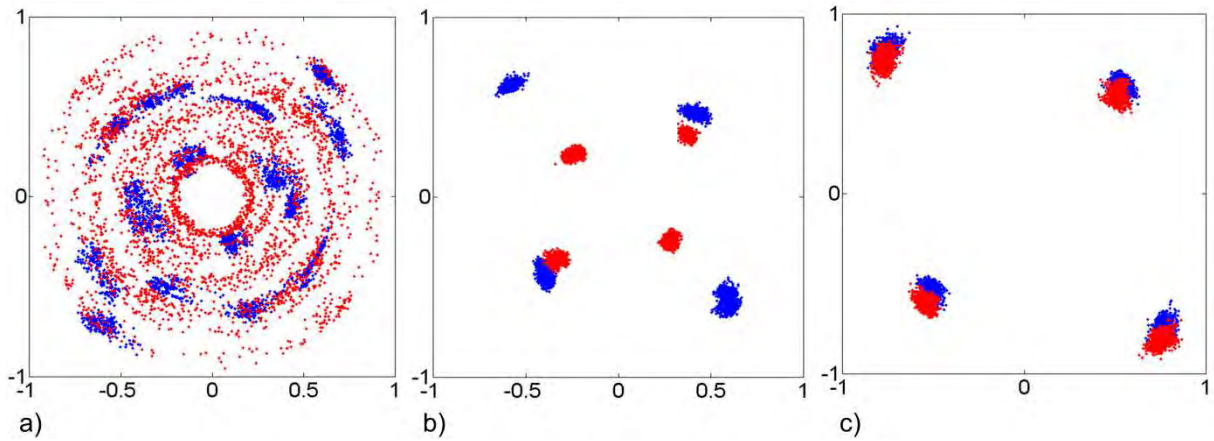
Fig. 78 Final constellations for various POLDMUX scenarios. a) CCMA POLDMUX with equal $R^{(i)}$ parameters ($R^{(1)}$= $R^{(2)}$=1); b) CCMA POLDMUX with unequal $R^{(i)}$ parameters ($R^{(1)}$= 2$R^{(2)}$=2); c) CMA POLDMUX with single-tap filter tap weights.
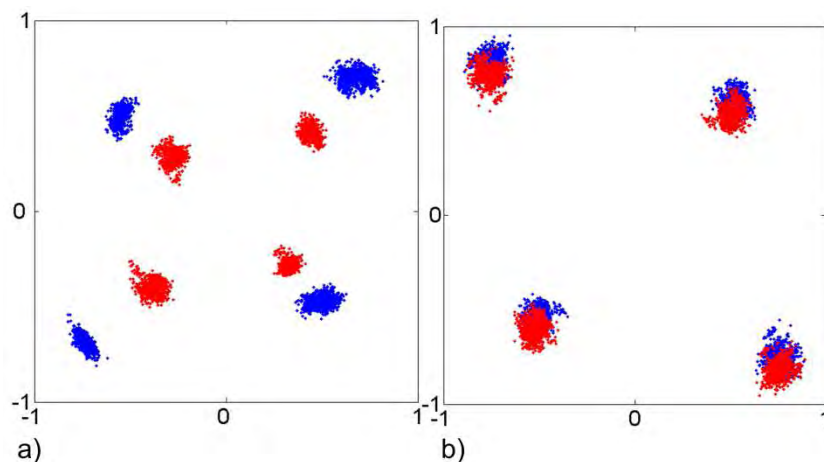
Fig. 79 Final constellations for various POLDMUX scenarios when Gram-Schmidt orthogonalization of QI is performed before POLDMUX a) CCMA POLDMUX with unequal $R^{(i)}$ parameters ($R^{(1)}$= 2$R^{(2)}$=2); b) CMA POLDMUX with single-tap filter tap weights.

A recent article addressing quadrature imbalance in OFDM coherent systems [195], indicates that QI can also be caused by a non-ideal transmitter (transmitter QI). Transmitter QI should be compensated

after IF offset estimation and compensation, as explained in [195]. Applying the Gram-Schmidt orthogonalization algorithm to the complex symbols after IF offset _and_ phase noise compensation produces the constellations depicted in Fig. 80. Fig. 80a corresponds to the case where the CCMA POLDMUX algorithm is used whereas Fig. 80b corresponds to the case where the CMA POLDMUX algorithm is used. Constellations for both polarizations have regained their ideal form, suggesting either that there also exists transmitter QI in the experimental setup, or non-ideal polarization multiplexing at the transmitter is essentially a quadrature imbalance problem, solved algorithmically with the aforementioned way. Even better results are obtained when using the QI CMA algorithm for QI compensation (Section V.7.ii), both at the beginning, and at the end of the processing chain, as indicated by the constellations in Fig. 81. Fig. 81a corresponds to the case where the CCMA POLDMUX algorithm is used whereas Fig. 81b corresponds to the case where the CMA POLDMUX algorithm is used.
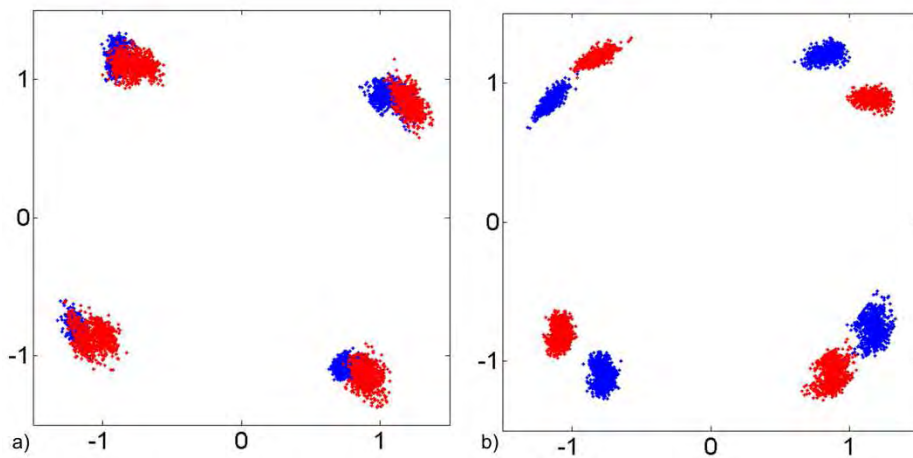
Fig. 80 Final constellations for various POLDMUX scenarios when Gram-Schmidt orthogonalization QI compensation is performed before POLDMUX and after IF offset and phase noise estimation and compensation. a) CCMA POLDMUX with unequal $R^{(i)}$ parameters ($R^{(1)}= 2R^{(2)}=2$); b) CMA POLDMUX with single-tap filter tap weights.
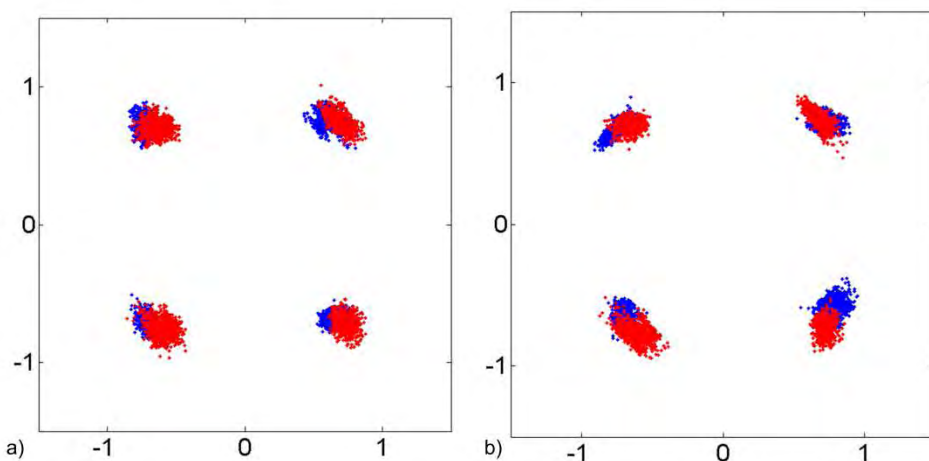
Fig. 81 Final constellations for various POLDMUX scenarios when QI CMA QI compensation is performed before POLDMUX and after IF offset and phase noise estimation and compensation. a) CCMA POLDMUX with unequal $R^{(i)}$ parameters ($R^{(1)}= 2R^{(2)}=2$); b) CMA POLDMUX with single-tap filter tap weights.

To conclude, the optimal DSP algorithm sequence for the 0.1 GBd PDM QPSK experiment is as follows: First remove the bulk IF offset, then perform QI compensation to remove receiver QI, then

perform POLDMUX to remove random polarization rotations in the fiber, then remove the residual IF offset, then filter the phase noise, and finally perform QI compensation to remove transmitter QI. Analysis revealed that the QI-CMA algorithm for QI compensation produces slightly better results than the Gram-Schmidt orthogonalization algorithm. When using the CMA for polarization demultiplexing, single tap filter tap weights are sufficient, and more taps bring no improvement in performance. Applying fractionally-spaced sampling at twice the symbol rate was investigated, but was not found necessary, since it made no improvement in performance.

4. Analysis of 1 GBd experimental data

In this section we analyze the experimental data obtained from a 1 GBd PDM-QPSK experiment over 100 km of LEAF optical fiber, based on the experimental setup shown in Fig. 61. The sequence of DSP algorithms used to analyze the 1 GBd experimental data is shown in Fig. 82, starting from the output of the DSO.
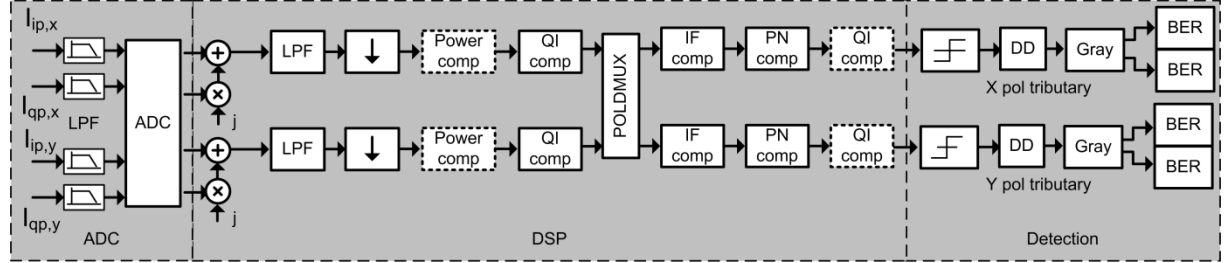
Fig. 82 The sequence of steps involved in analyzing the experimental data obtained from a single-channel 1 GBd PDM QPSK experimental set-up. (Symbols: LPF: Low-pass filter; ADC: Analog-to-digital converter; Power comp.: Low LO-to-signal power ratio compensation; QI comp.: Quadrature imbalance compensation; POLDMUX: polarization demultiplexer; IF comp. IF offset compensation; PN comp.: Phase noise compensation; DD: Differential detection.)

The four photocurrents at the output of the coherent polarization- and phase-diversity receiver are sampled by the DSO, which also acts as a low-pass filter with an approximate 3-dB bandwidth of 4 GHz. The photocurrents are sampled at a rate of 20 GHz, which for the 1 GBd signal corresponds to 20 samples-per-symbol. The measurement is approximately 50000 symbols long. The frequency of the LO laser is controlled manually, and is typically between 100 and 500 MHz. Thus the 1 GBd experiment is categorized as an intradyne experiment, and therefore bulk IF offset need not be removed prior to other DSP algorithms [171]. Low-pass filtering is performed to remove out-of-band noise. After filtering, a resampling process is performed with a constant sampling rate. Depending on the algorithms to be used, sampling is performed at the symbol rate, or at twice the symbol rate, corresponding to one or two samples-per-symbol, respectively. At the same time, the channel synchronization procedure described in Section VII.2.i is performed, by starting the sampling process from different instances of the four signal vectors, and combining the samples with relative delays from the beginning of the measurement. After this resampling process, a number of DSP algorithms described in Section V and various combinations of those where used, amongst them, compensation of low LO-to-signal power ratio (Section V.8), QI compensation algorithms (Section V.7), POLDMUX algorithms (Section V.4), IF offset estimation and compensation algorithms (Section V.6), and phase noise compensation algorithms (Section V.5). Algorithms whose necessity is debatable, are illustrated in dotted lines in Fig. 82. Finally, error counting is performed, by comparing the received symbol sequences with the expected sequences, derived from the PRBS sequences used at the transmitter. In what follows, we illustrate the performance of the various DSP algorithms, or the penalty for not using them.

Fig. 83 shows the PSD of the received signal at the output of the 2×4 90° optical hybrid, before (Fig. 83a) and after low-pass filtering (Fig. 75b). From Fig. 83a, it is seen that the central lobe of the received signal PSD is around 350 MHz, i.e., the IF offset is approximately 350 MHz ($f_{IF} = 0.35\ R_S$). Though this IF offset is far from the estimation capability of the best IF offset estimation algorithm found by simulation (i.e. the phase increment algorithm whose estimation range up to 0.125 R_S – see Fig. 55), as we will see, the residual IF offset is small enough for the phase noise estimation algorithm to clear the constellation without the use of a second stage of IF compensation.

Fig. 84 shows the eye diagrams at the output of the LPF. The transitions of the eye diagram can clearly be distinguished, facilitating the manual channel synchronization process. The relative delays between the quadratures per polarization, and between the polarization tributaries, are close to those found by analyzing the 0.1 GBd experiment (Section VII.3), since they pose a systematic error. Fig. 84 also shows the sampling points used for the two polarization tributaries. The sampling point of the two quadratures corresponding to the Y-polarization tributary (Fig. 84c, d) differs by one symbol, i.e. 20 samples, and the sampling points corresponding to the X and Y polarization tributaries differ by 200 samples i.e. 10 symbols. This is the same differential delay between the two polarization tributaries as in the 0.1 GBd case.
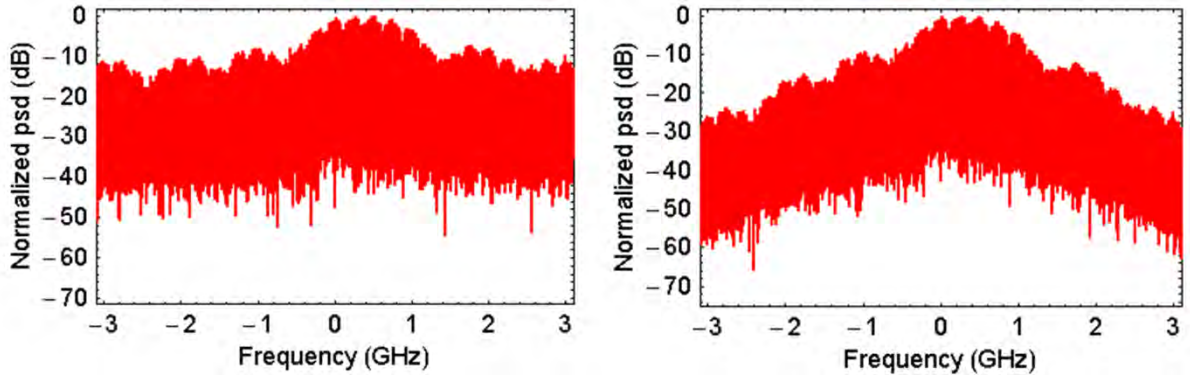
Fig. 83 Power spectral density of the received complex signal at the output of the 2×4 90° optical hybrid. a) Before low-pass filtering, b) After low-pass filtering. The IF offset is seen to be approximately 350 MHz.
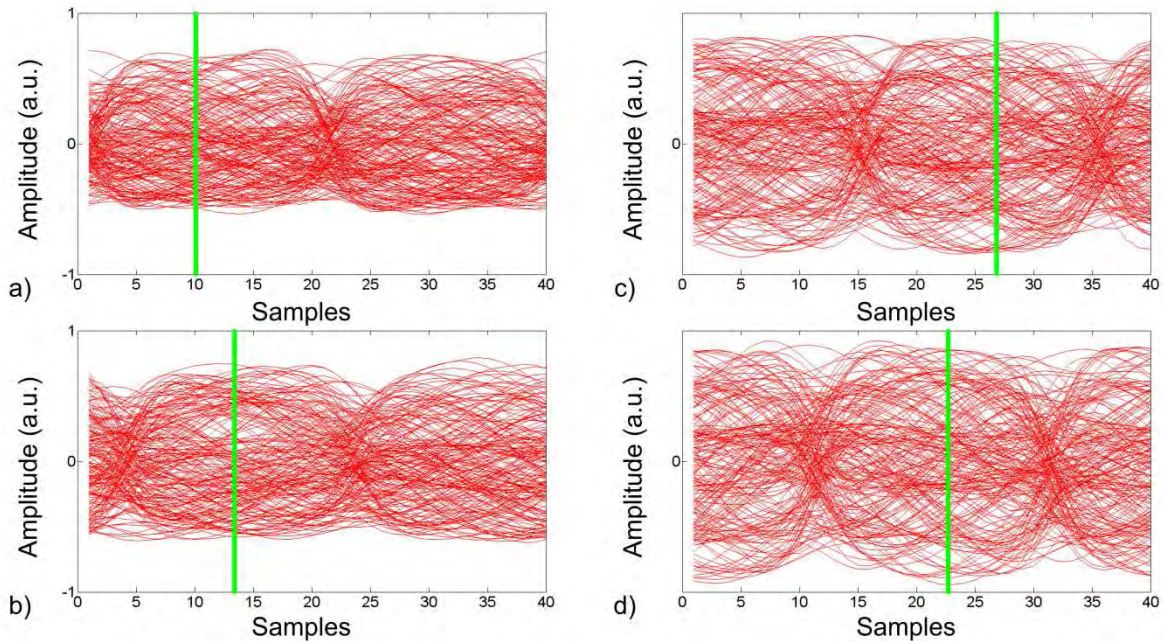
Fig. 84 Eye diagrams for the received photocurrents, after low-pass filtering. a) I_{ipx}; b) I_{qpx}; c) I_{ipy}; d) I_{qpy}.

Fig. 85 shows the constellations produced when symbol-spaced sampling at the sampling instants denoted in Fig. 84 is performed, for the X-polarization (Fig. 85a) and Y-polarization (Fig. 85b) tributaries, respectively. The constellation in Fig. 85a, corresponding to the 2×2 90° hybrid, is composed of eccentric ellipses with unequal radii, owing to a mixture of low LO-to-signal power ratio at the receiver, QI, and cross-polarization interference between the two PDM QPSK signals, in the presence of a non-zero IF offset (Fig. 35). The constellation in Fig. 85b, corresponding to the 2×4 90°

138

hybrid which uses balanced detection, and is composed of concentric ellipses with unequal radii, a tell-tale sign of QI and cross-polarization interference between the two PDM-QPSK signals, in the presence of a non-zero IF offset (Fig. 35).

Based on the shape of the received constellations, we easily conjecture that the effects of both QI and low LO-to-signal power ratio (for the 2×2 90° optical hybrid) have to be combated prior to polarization demultiplexing. For symbol spaced sampling, both the CMA POLDMUX algorithm (Section V.4.ii) and the CCMA POLDMUX algorithm (Section V.4.iii) can be used. After polarization demultiplexing, the phase increment algorithm is used to perform IF offset estimation and compensation (Section V.6.i), and the FFPE algorithm to perform phase noise filtering (Section V.5.ii) averaging over 14 samples. Finally, QI compensation is performed at the end of the processing chain when needed. The Gram-Schmidt orthogonalization algorithm is used, performing averaging over all the symbols. We first use the CMA POLDMUX algorithm with a small number of filter tap weights, so that compensation can be performed in case of some unidentified distortion, and then investigate whether single-tap filter tap weights can be used, in order to use the CCMA POLDMUX algorithm.
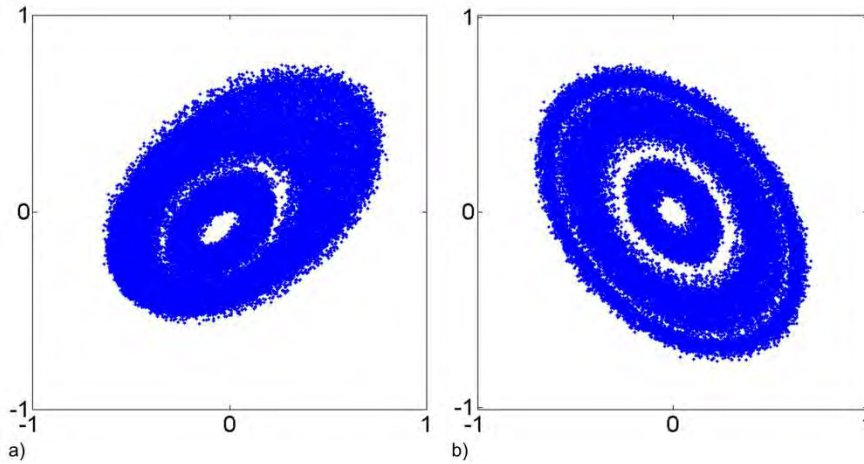
Fig. 85 Received constellation for the a) X-polarization tributary; b) Y-polarization tributary.

Fig. 86a shows the final constellation when all algorithms depicted in Fig. 82 are used, and the CMA POLDMUX algorithm uses 13-tap filter tap weights.
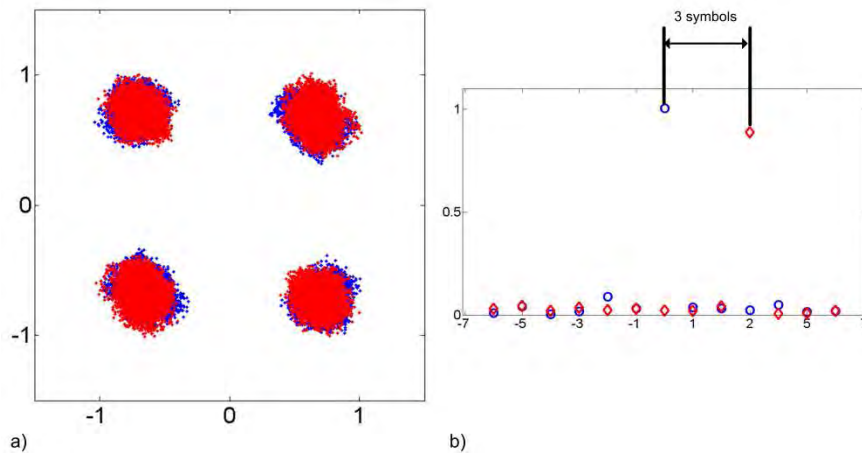
Fig. 86 a) Final constellation when using a 13-tap filter tap weights CMA POLDMUX algorithm. The two polarization tributaries are purposefully shifted by 3 symbols compared to the ideal. b) Magnitude of the $\mathbf{w}_{11}$ (circles) and $\mathbf{w}_{21}$ (rhombs) filter tap weights.

139

The following parameters were used in the analysis. For combating low LO-to-signal power ratio we use LOSPR$_{Xpol}$ = 12 dB and LOSPR$_{Ypol}$ = 20 dB. The first 13000 symbols after the CMA POLDMUX are discarded, in order to remove the transient phenomena in the equalizer. The phase increment algorithm produces an IF offset estimation of approximately 108 MHz, for both polarization tributaries.

The differential sampling instant between the X and Y polarization tributaries was purposefully set to 13 symbols compared to the ideal value of 10 symbols, to illustrate an alternative method as to how the two polarization tributaries can be synchronized. Fig. 86b depicts the magnitude of the coefficients of the final equalizer filter tap weights for the butterfly structure depicted in Fig. 19. Circles correspond to $\mathbf{w}_{11}$, whereas rhombs correspond to $\mathbf{w}_{21}$. The difference between the maximum values corresponds to the differential error in combining the two tributaries at the input. A single-tap equalizer structure would be unable to correctly combine the two polarization tributaries, because it would not be able to perform the necessary relative shifting. For what follows, we use the ideal differential sampling of 10 symbols, and remove the final QI compensation stage which doesn't play an important role in the case of the CMA POLDMUX algorithm.

Using the correct differential sampling instant between the X- and Y-polarization tributaries introduces a very subtle effect, that of singularity [196], [197]. Both equalizer outputs converge to the same symbol sequence, which is mathematically manifested as the (generalized) determinant of matrix (108) becoming zero. The final constellation diagrams for the two polarization tributaries, in the case where single-tap filter tap weights are used, are shown in separate figures in Fig. 87. The constellations are perfectly the same, having only a relative rotation of 90°. Fig. 88 shows the magnitude of the two complex outputs for the period the algorithm converges. It can be seen that after approximately 4800 symbols, the outputs become identical in magnitude. Using more filter tap weights doesn't alter the result.
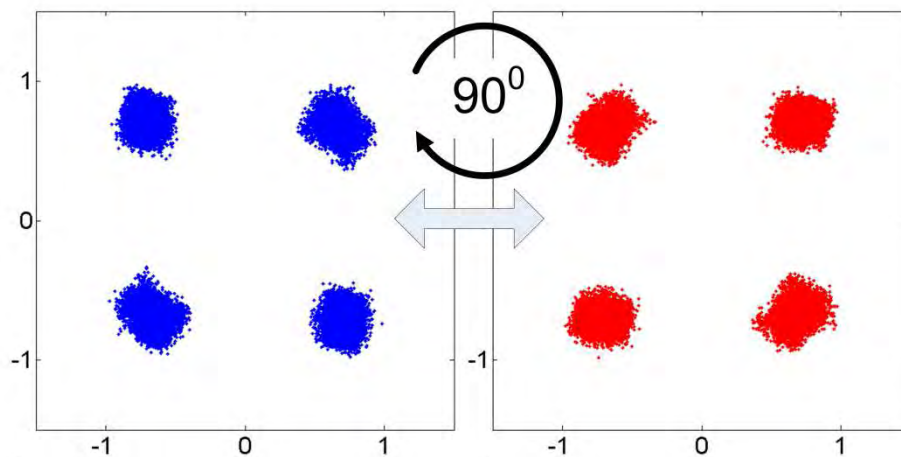
Fig. 87 Final constellations when using a 13-tap CMA POLDMUX algorithm. The two polarization tributaries have no purposeful shifting compared to the ideal. The two constellations are exactly the same, rotated by 90°.

It was found that no combination of DSP algorithms can prevent this outcome for the CMA POLDMUX when the ideal relative delay between the polarization tributaries is used at the input. This is due to the fact that one of the two polarization tributaries at the input has stronger average power and the equalizer converges to this polarization tributary at both of its outputs. In order to work around this problem, two ways were used. The one is to use the multi-user CMA (MU-CMA) algorithm proposed in [197], and the other is to use the CCMA algorithm, both of which avoid singularity.
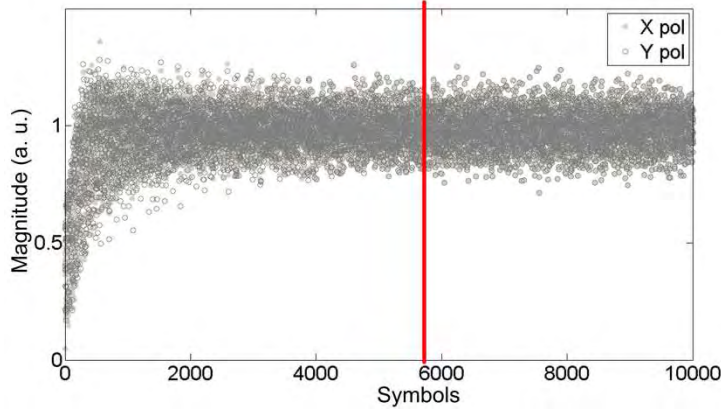
Fig. 88 Magnitude of the X and Y polarization tributaries at the output of the CMA POLDMUX. After a short conversion period, the magnitudes are identical.

We first show the results obtained by using the CCMA algorithm. Fig. 89 corresponds to various scenarios in which the CCMA POLDMUX algorithm is used. Fig. 89a shows the final constellation when all algorithms depicted in Fig. 82 are used. The following parameters were used in the analysis. The low LO-to-signal power ratio compensating algorithm uses parameters $LOSPR_{Xpol}$ = 12 dB and $LOSPR_{Ypol}$ = 20 dB. The first 13000 symbols after the CCMA POLDMUX are discarded, in order to remove the transient phenomena in the equalizer. The CCMA uses $R_2^{(1)} = R_2^{(2)} = 1$, as should be expected in the case of QPSK (see (113) and (125)). As in the 0.1 GBd case, it turns out that this are not the suitable values. Using $R_2^{(1)} = 2R_2^{(2)} = 2$ produces the constellations in Fig. 89b which are error-free. Fig. 89c corresponds to the case where QI compensation at the end of the processing chain is omitted. It can be seen that transmitter quadrature imbalance or non-ideal polarization multiplexing process at the transmitter is effectively solved by using a QI compensation technique at the end of the processing chain, as described in [195]. Fig. 89d shows the final constellation when the algorithm for low LO-to-signal power ratio is omitted. Clearly, a small system performance penalty exists.

Subsequently, we investigate system performance using the MU-CMA POLDMUX algorithm proposed in [197]. Fig. 90 shows the final constellation diagrams for a variety of cases, when using the MU-CMA POLDMUX, and various combinations of algorithms depicted in Fig. 82. Both polarization tributaries are successfully retrieved at the end. The following parameters are used in the analysis. The low LO-to-signal power ratio compensating algorithm uses parameters $LOSPR_{Xpol}$ = 12 dB and $LOSPR_{Ypol}$ = 20 dB. The first 20000 symbols after the MU-CMA POLDMUX are discarded, in order to remove the transient phenomena in the equalizer. The phase increment algorithm produces an IF offset estimation of approximately 108 MHz, for both polarization tributaries. The Gram-Schmidt orthogonalization algorithm is used, performing averaging over all the symbols. The MU-CMA was found to be extremely sensitive to its parameters. The best results are obtained when using 4-tap filter tap weights or more, δ_{max}=2, and a step size μ in the range of 5×10^{-3} (Fig. 90a).
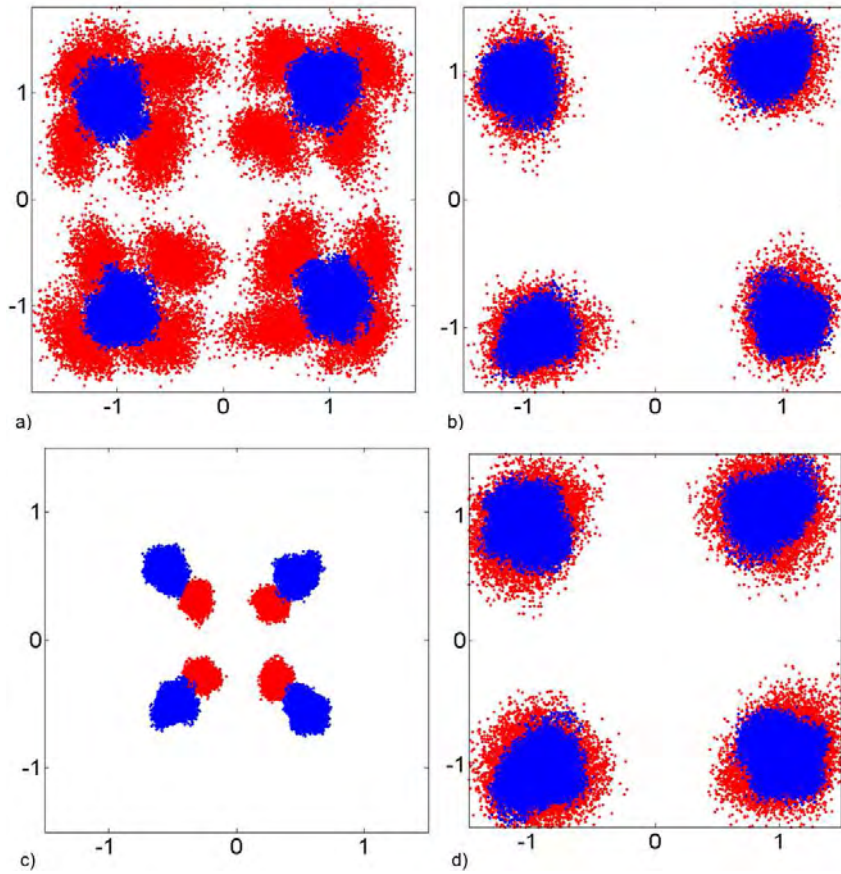
Fig. 89 Final constellations for various scenarios, when using the CCMA POLDMUX algorithm. a) Compensation of low LO-to-signal power ratio and QI compensation using Gram-Schmidt orthogonalization, CCMA POLDMUX with equal $R^{(i)}$ parameters ($R^{(1)}= R^{(2)}=1$), transmitter QI compensation using the Gram-Schmidt orthogonalization; b) Compensation of low LO-to-signal power ratio power and QI compensation using Gram-Schmidt orthogonalization, CCMA POLDMUX with equal $R^{(i)}$ parameters ($R^{(1)}= 2R^{(2)}=2$), transmitter QI compensation using the Gram-Schmidt orthogonalization; c) As in b), without the final stage of transmitter QI compensation; d) As in b), without low LO-to-signal power ratio compensation.
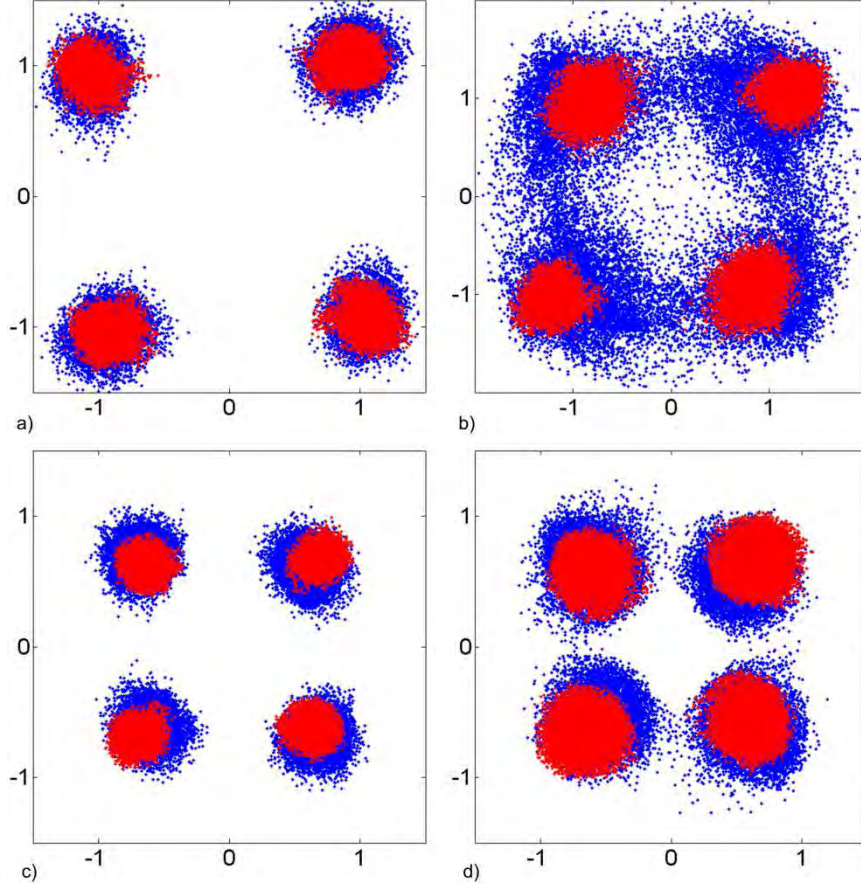
Fig. 90 Final constellations for various scenarios, when using the MUCMA POLDMUX algorithm. a) Compensation of low LO-to-signal power ratio, QI compensation using Gram-Schmidt orthogonalization, MUCMA POLDMUX with 4-tap filter tap weights, δ_{max}=2, and transmitter QI compensation using Gram-Schmidt orthogonalization; b) Compensation of low LO-to-signal power ratio, QI compensation using Gram-Schmidt orthogonalization algorithm, MUCMA POLDMUX with 7-tap filter tap weights, δ_{max}=8, and transmitter QI compensation using Gram-Schmidt orthogonalization; c) As in a), without the final stage of transmitter QI compensation or the low LO-to-signal power ratio; d) As in a), without the low LO-to-signal power ratio compensation algorithm, or any QI compensation.

To illustrate the sensitivity of the algorithm, a wide range of values for δ_{max} were investigated, in conjunction with various numbers of filter tap weights. It was found that a very limited number of combinations produce the two polarization tributaries correctly demultiplexed at the output. In the majority of cases, the equalizer falls into singularity, or does not converge for one, or none of the outputs. For example, using less than 4-tap filter tap weights, causes singularity regardless of the value of δ_{max}. Using more taps (in the range between four and eight) produces good results, when δ_{max} is kept smaller than 6. Using a larger value for δ_{max} prevents the equalizer from converging correctly at one of the two outputs, as in Fig. 90b , where the equalizer uses 7-tap filter tap weights and δ_{max}=8. Using correct parameters for the equalizer (as in Fig. 90a) but omitting the low LO-to-signal power ratio compensation algorithm at the beginning, and the final QI compensation at the end, produces good results, as seen in Fig. 90c. Omitting the QI compensation stage before the POLDMUX, causes large system performance deterioration (Fig. 90d).

We now turn our attention to the IF offset estimation issue. From Fig. 83 we see that the IF offset is approximately 350 MHz, i.e., 0.35 R_S, and is therefore outside the estimation range of the phase increment algorithm. We investigate if the true IF offset can accurately be found by observation of the

received PSD or whether this method is inaccurate for PDM-QPSK systems in the case where $f_{IF} < R_S$, as in this case.

Fig. 91 shows the unwrapped phase trajectories for the two polarization tributaries at the output of the CCMA POLDMUX, for the best case, corresponding to Fig. 89b. The slope of the phase trajectory for each polarization tributary is different, indicating that each polarization has a different IF offset. This is counterintuitive, since the IF offset is common for both polarization tributaries. However, thermal noise for each photodiode in each phase diversity receiver is different. But, more importantly, due to the relative shifts imposed during the synchronization procedure, the instantaneous IF offset and phase noise values per sample in the POLDMUX are different, since they correspond to different time instances. This is the main reason for the different slopes in the unwrapped phases.

Indeed, the phase increment algorithm produces different IF offset values, for the X- and Y-polarization tributaries, i.e., 108 MHz, and 107 MHz, respectively. In Fig. 91 the unwrapped phase trajectory of an ideal complex rotating phasor is also shown. The ideal complex rotating phasor has a frequency of 54 MHz. Given the estimates of the IF offset, it is seen that due to the nature of the random-walk process introduced by phase noise, and the random fluctuations due to thermal noise, the unwrapped phase trajectories are equivalent to an ideal trajectory corresponding to a smaller frequency. In the inset of Fig. 91 a detail of the unwrapped phases is shown where the random fluctuations of the phase are evident.
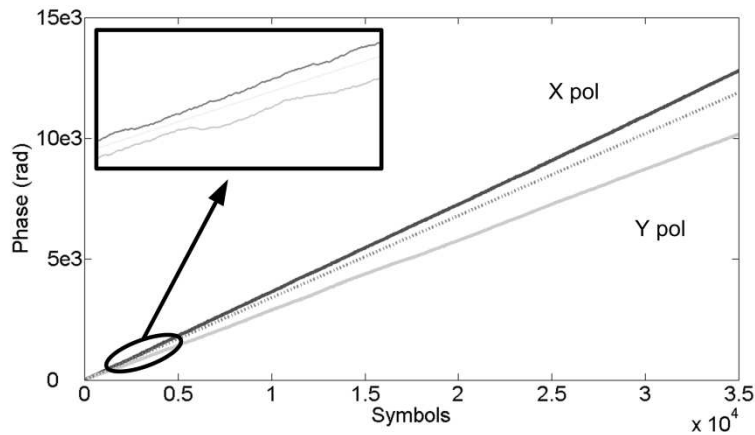
Fig. 91 Unwrapped phase trajectories for the two polarization tributaries at the output of the CCMA POLDMUX. Different slopes correspond to different IF offsets.

Fig. 92 shows the unwrapped phase for the two polarization tributaries after the phase increment algorithm. It can be seen that the phase trajectory of the X-polarization tributary is much closer to having a zero slope. This indicates that the X-polarization estimation value (108.8 MHz) is a better estimate than the Y polarization estimation value (107.7 MHz). The wavy trajectory resembles the unwrapped phase trajectory attributed to laser phase noise (see Fig. 21) and definitely means that the remaining IF offset is negligible. Therefore the IF offset is approximately 108 MHz, by far smaller than what the location of the central lobe of the received signal PSD shows in Fig. 83.

From Fig. 92, it can also be seen that after IF offset estimation and compensation, the two polarization tributaries contain different amounts of residual IF offset. Especially, one of the two polarization tributaries has a much larger residual IF offset compared to the other. Since a large residual IF offset might affect the performance of the phase noise estimation algorithms, more than one IF offset estimation stages were used to find if system performance will be improved. Applying the same algorithm to the same set of data does not alter the estimation, so different estimation algorithms are applied to the data in order to improve the IF offset estimate. The best sequence of estimation

144

algorithms is to apply Kay's algorithm after the phase increment algorithm and subsequently Tretter's algorithm. The results are summarized in Fig. 93. The final constellation after three IF offset estimation stages is practically un-altered compared to the case where only the phase increment is used. This shows that, in this case, the phase noise compensation algorithm is capable of removing small residual IF offset values.
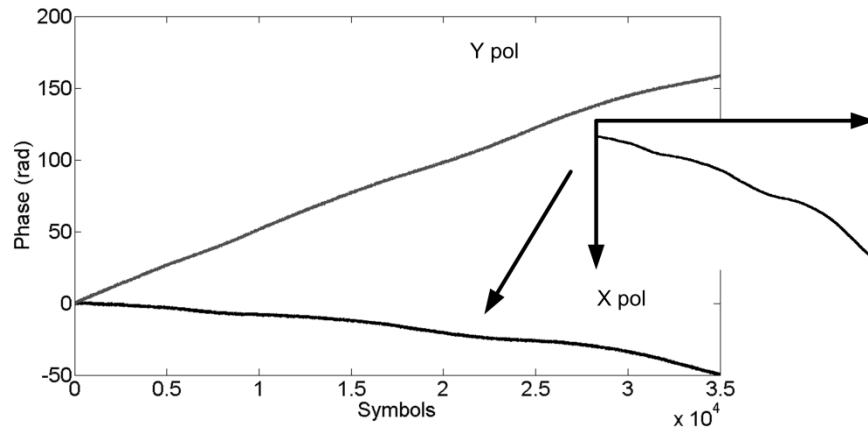
Fig. 92 Unwrapped phase trajectories for the two polarization tributaries at the output of the phase increment algorithm.
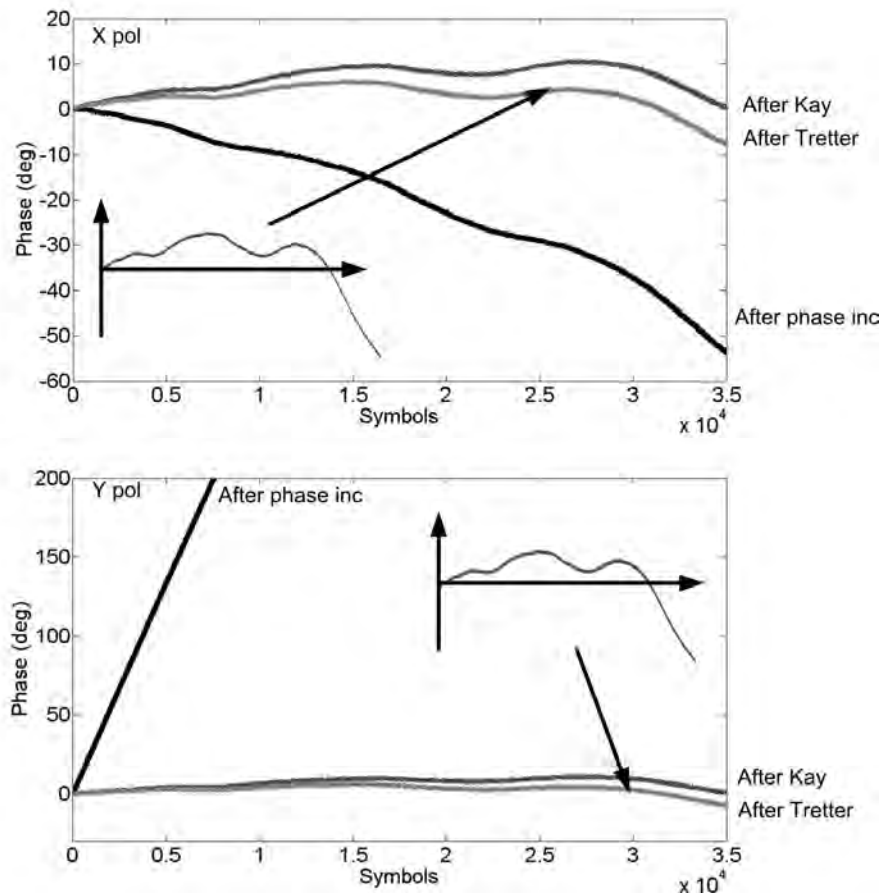
Fig. 93 Unwrapped phase trajectories for the two polarization tributaries at the output of successive IF offset estimation and compensation stages. a) X-polarization tributary; b) Y-polarization tributary.

145

To conclude, the optimal DSP algorithm sequence for the 1 GBd PDM QPSK experiment is as follows. For the CCMA POLDMUX, the effects of low LO-to-signal power ratio on the received signal corresponding to the 2×2 90° hybrid has to be removed first, followed by QI compensation. At the end of the processing chain transmitter-QI compensation has to be removed. The CMA POLDMUX fails to demultiplex the PDM-QPSK signal, falling into singularity, regardless of the sequence of other DSP algorithms used, or the number of taps. In order to perform both polarization demultiplexing and equalization, the MU-CMA must be used. However, the MU-CMA POLDMUX algorithm needs a fine tuning of its parameters to avoid singularity, but has the advantage that it does not need compensation of the low LO-to-signal power ratio, or transmitter-QI compensation at the end of the processing chain. Applying fractionally-spaced sampling at twice the symbol rate was investigated, but is not necessary, since it makes no improvement in performance. Use of more than one IF compensation stages, offers no performance improvement in this case.

5. Analysis of 5 GBd experimental data

In this section we analyze the experimental data obtained from a 5 GBd PDM-QPSK experiment over 100 km of LEAF optical fiber, based on the experimental setup shown in Fig. 61. The sequence of DSP algorithms used to analyze the 5 GBd experimental data are shown in Fig. 94, starting from the output of the DSO.
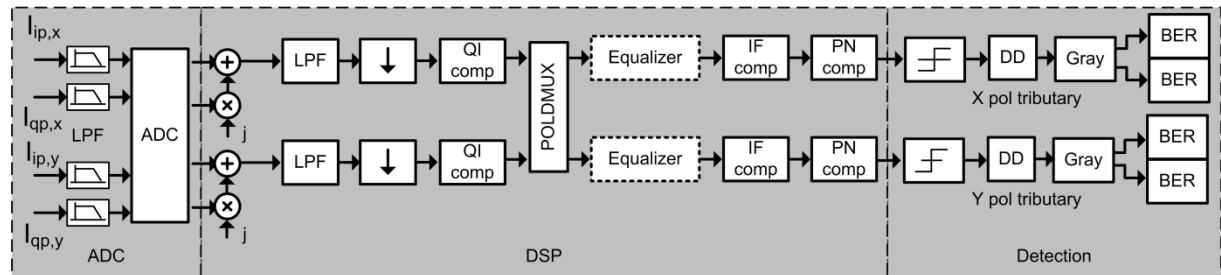
Fig. 94 The sequence of steps involved in analyzing the experimental data obtained from a single-channel 5 GBd PDM QPSK experimental set-up (Symbols: LPF: Low-pass filter; ADC: Analog-to-digital converter; QI comp.: Quadrature imbalance compensation; POLDMUX: polarization demultiplexer; IF comp. IF offset compensation; PN comp.: Phase noise compensation; DD: Differential detection.).

The four photocurrents at the output of the coherent polarization- and phase-diversity receiver are sampled by the DSO, which also acts as a low-pass filter with an approximate 3-dB bandwidth of 4 GHz. The photocurrents are sampled at a rate of 20 GHz, which for the 5 GBd signal corresponds to 4 samples-per-symbol. The measurement is approximately 250000 symbols long. The frequency of the LO laser is controlled manually, and is typically between 100 and 500 MHz. Thus the 5 GBd experiment is categorized as an intradyne experiment, and therefore bulk IF offset need not be removed prior to other DSP algorithms [171]. Low-pass filtering is performed to remove out-of-band noise. After filtering, a resampling process is performed with a constant sampling rate. Depending on the algorithms to be used, sampling is performed at the symbol rate, or at twice the symbol rate, corresponding to one or two samples-per-symbol, respectively. At the same time, the channel synchronization procedure described in Section VII.2.i is performed, by starting the sampling process from different instances of the four signal vectors, and combining the samples with relative delays from the beginning of the measurement. After this resampling process, a number of DSP algorithms described in Section V and various combinations of those are used, amongst them, QI compensation algorithms (Section V.7), POLDMUX algorithms (Section V.4), IF offset estimation and compensation algorithms (Section V.6), and phase noise compensation algorithms (Section V.5). The possibility of using an additional equalizing step after the POLDMUX algorithm is also investigated (Fig. 20), especially for the case of the CCMA which has no equalization capabilities. Finally, error counting is performed, by comparing the received symbol sequences with the expected sequences, derived from the PRBS sequences used at the transmitter. In what follows, we illustrate the performance of the various DSP algorithms, or the penalty for not using them.

Fig. 95 shows the eye diagrams at the output of the LPF. The transitions of the eye diagram can still be distinguished, facilitating the manual channel synchronization process. However, the small number of samples-per-symbol compared to the 0.1 GBd and 1 GBd experiments makes the synchronization difficult if no knowledge of the relative delays between the quadratures per polarization and between the polarization tributaries is known. Fig. 84 shows the sampling points used for the two polarization tributaries. The sampling point of the two quadratures corresponding to the Y-polarization tributary (Fig. 84c, d) differs by six symbols, i.e. 24 samples, which is approximately the same compared to the

20 samples found for the 1 GBd experiment. The sampling points corresponding to the X- and Y-polarization tributaries differ by 208 samples, approximately the same as the 200 samples in the 1 GBd experiment, only in this case they correspond to 52 symbols.

Fig. 96 shows the constellations produced when symbol-spaced sampling at the sampling instants denoted in Fig. 95 is performed, for the X-polarization (Fig. 96a) and Y-polarization (Fig. 96b) tributaries, respectively. The constellation in Fig. 96a, corresponding to the 2×2 90° hybrid, is composed of eccentric ellipses with unequal radii, owing to a mixture of inadequate LO-to-signal power ratio at the receiver (Section 8V.), QI, and cross-polarization interference between the two PDM QPSK signals, in the presence of a non-zero IF offset (Fig. 35), although the low OSNR does not enable the visual verification of all the phenomena. The constellation in Fig. 96b, corresponding to the 2×4 90° hybrid which uses balanced detection, is composed of concentric ellipses with unequal radii, a tell-tale sign of QI and cross-polarization interference between the two PDM QPSK signals, in the presence of a non-zero IF offset (Fig. 35), also not directly visible.
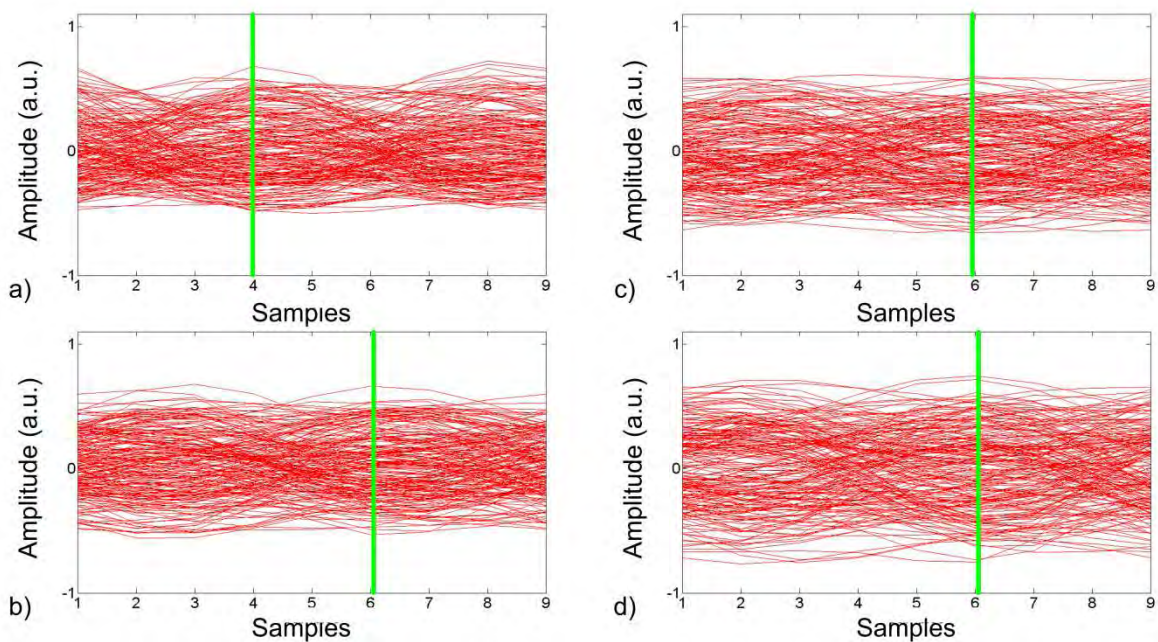
Fig. 95 Eye diagrams for the received photocurrents, after low-pass filtering. a) I_{ipx}; b) I_{qpx}; c) I_{ipy}; d) I_{qpy}.
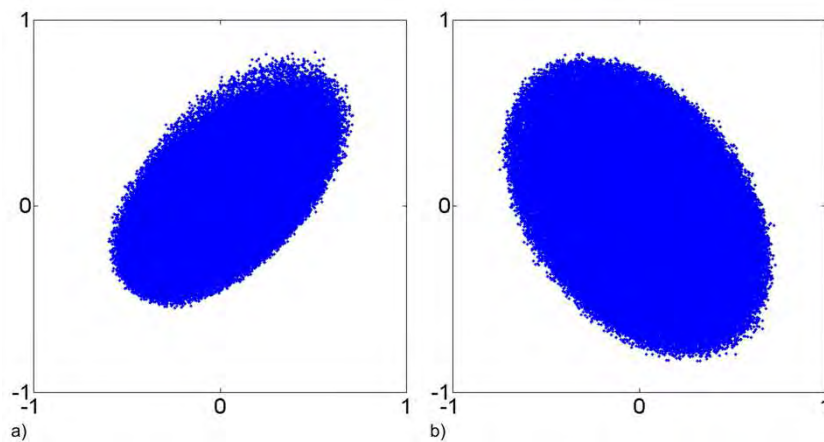
Fig. 96 Received constellation for the a) X-polarization tributary; b) Y-polarization tributary.

Based on the shape of the received constellations and previous experience from the 0.1 GBd and 1 GBd experiments, it is easy to conjecture that QI exists and must be compensated for. When using the CMA and MUCMA POLDMUX algorithms, experience gathered from the 1 GBd experiment indicates that low LO-to-signal power ratio effects and transmitter QI are successfully combated by the equalizer itself, and thus these algorithms are not used, a result also verified in the analysis but not shown here. After polarization demultiplexing, the phase increment algorithm is used to perform IF offset estimation and compensation (Section V.6.i), and the FFPE algorithm to perform phase noise filtering (Section V.5.ii), averaging over 14 samples. For QI, the Gram-Schmidt orthogonalization QI compensation algorithm is used, performing averaging over all the symbols. Both symbol-spaced and fractionally-spaced sampling at twice the symbol rate is used.

First, we use the CMA POLDMUX algorithm with a small number of taps, so that compensation can be performed in case of some unidentified distortion, and then investigate whether single-tap filter tap weights can be used, in order to use the CCMA POLDMUX algorithm. We use the ideal differential delay between the two signals. Initially, we use symbol-spaced sampling. Fig. 97a corresponds to the case where single-tap filter tap weights are used. The constellation is completely closed. Fig. 97b corresponds to the case where 5-tap filter tap weights are used. The constellation is relatively open but will not be error-free.

Next, we investigate the effect of using an additional equalizing step per complex symbol sequence, after the POLDMUX. The rationale behind this is that at 5 GBd, transmitter and receiver distortions become more important (Section VII.2.ii). Transmitter distortions are imposed on the signal prior to polarization multiplexing, and before polarization rotation which mixes the polarization tributaries causing cross-polarization interference. Therefore, this type of distortion could be best removed when the signals are already polarization demultiplexed. Fig. 97c corresponds to the case where the CMA POLDMUX uses single-tap filter tap weights, followed by CMA equalizers with 7-tap filter tap weights. Comparing to Fig. 97a, the result is much better. Fig. 97d corresponds to the case where the CMA POLDMUX uses 5-tap filter tap weights, followed by CMA equalizers with 7-tap filter tap weights. Though the results seem to be very similar, an important detail is that the constellation points have a disk-like shape, compared, e.g., with Fig. 97b where the constellation points are amorphous. This indicates that noise is the only impairment left to distort the signal in Fig. 97d.

Next, we continue to investigate the benefits of fractionally-spaced sampling at twice the symbol rate. Fig. 98 shows various scenarios for the case of fractionally-spaced sampling. Fig. 98a corresponds to the case where rudimentary 2-tap filter weights are used. Unlike the rudimentary single-tap case for the symbol-spaced sampling case, the constellations are completely open. Even better results are obtained when using 6-tap filter tap weights, as shown in Fig. 98b. Using the additional equalizing step per complex symbol sequence after the POLDMUX, the constellation opening is further improved. Fig. 98c corresponds to the case where the CMA POLDMUX uses 2-tap filter tap weights, followed by CMA equalizers with 7-tap filter tap weights, whereas Fig. 98d corresponds to the case where the CMA POLDMUX uses 6-tap filter tap weights, followed by CMA equalizers with 7-tap filter tap weights. Results are similar, so the use of the extra equalizing step isn't justified.

In all cases depicted in Fig. 97 and Fig. 98 the equalizer converges to a singularity, meaning that both outputs are the same apart from a constant rotation. Thus, either the CCMA, or MU-CMA POLDMUX algorithms must be used.

The MUCMA was first used in order to successfully recover both polarization tributaries with clear constellations. In all cases, the MUCMA uses $\delta_{max}=2$, and a step size μ in the range of 5×10^{-3} which were found to produce the best results. Fig. 99a corresponds to symbol-spaced sampling and 5-tap

filter tap weights. One of the two polarization tributaries is not recovered. Fig. 99b corresponds to the same case as Fig. 99a, followed by CMA equalizers with 11-tap filter tap weights. Fig. 99c corresponds to using fractionally-spaced sampling at twice the symbol rate and 6-tap filter tap weights. Both constellations are perfectly retrieved, producing a zero BER after differential detection. Fig. 99d corresponds to the same case as Fig. 99b, followed by CMA equalizers with 11-tap filter tap weights.

Finally, we use the CCMA POLDMUX to retrieve the data. Fig. 100a shows the final constellations when using symbol-spaced sampling. We use $R_2^{(1)} = 2R_2^{(2)} = 2$. The final constellations are totally closed. Fig. 100b shows the final constellations when using symbol-spaced sampling and the CCMA is followed by CMA equalizers with twenty single-tap filter tap weights. The constellation for one of the two polarization tributaries is open, indicating that the POLDMUX works correctly. However, the other polarization tributary is not recovered error-free. Fig. 100c shows the final constellation when fractionally-spaced sampling is performed. The CCMA POLDMUX has single-tap filter tap weights which means that every sampling instant it processes the current samples and not previous time-instant samples. This does not prohibit it from performing polarization demultiplexing on samples corresponding to the same symbol. However, since a downsampling procedure must be performed to keep one sample per symbol, CMA equalizers *must* be used after polarization demultiplexing. CMA equalizers with 20-tap filter tap weights are used. The result is somewhat better than that shown in Fig. 100b, but again not both polarization tributaries are retrieved error-free.
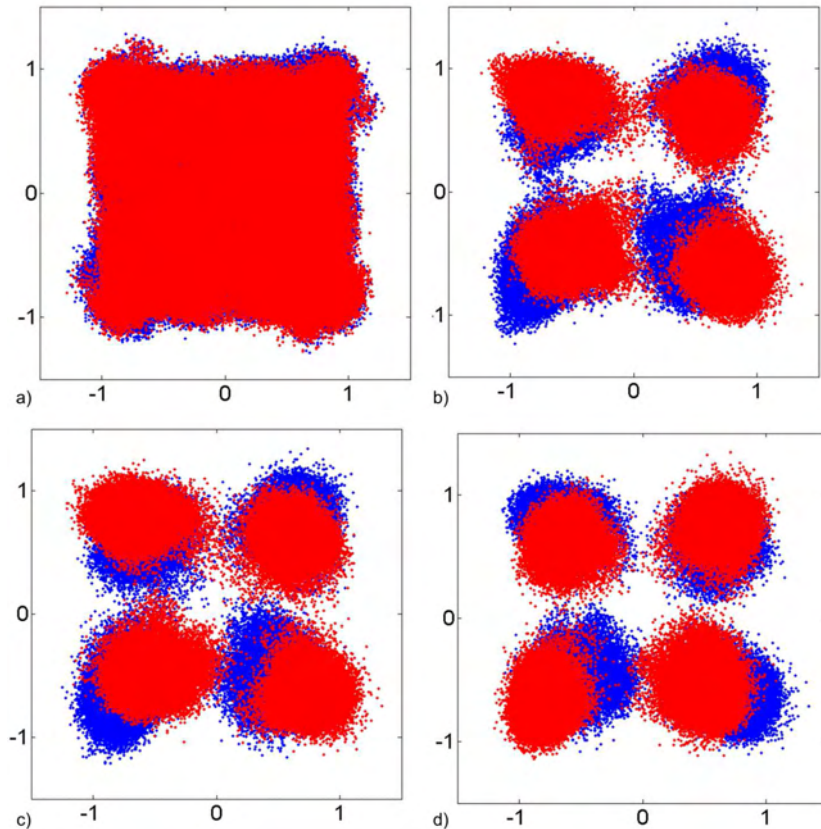
Fig. 97 Final constellations for various scenarios, when using the CMA POLDMUX algorithm with symbol-spaced sampling. QI compensation is performed using the Gram-Schmidt orthogonalization algorithm. In (c), (d), the outputs of the POLDMUX are fed into an additional equalizer for distortion mitigation. a) single-tap filter tap weights; b) 5-tap filter tap weights, c) single-tap filter tap weights, followed by 7-tap filter tap weights; d) 5-tap filter tap weights followed by 7-tap filter tap weights.
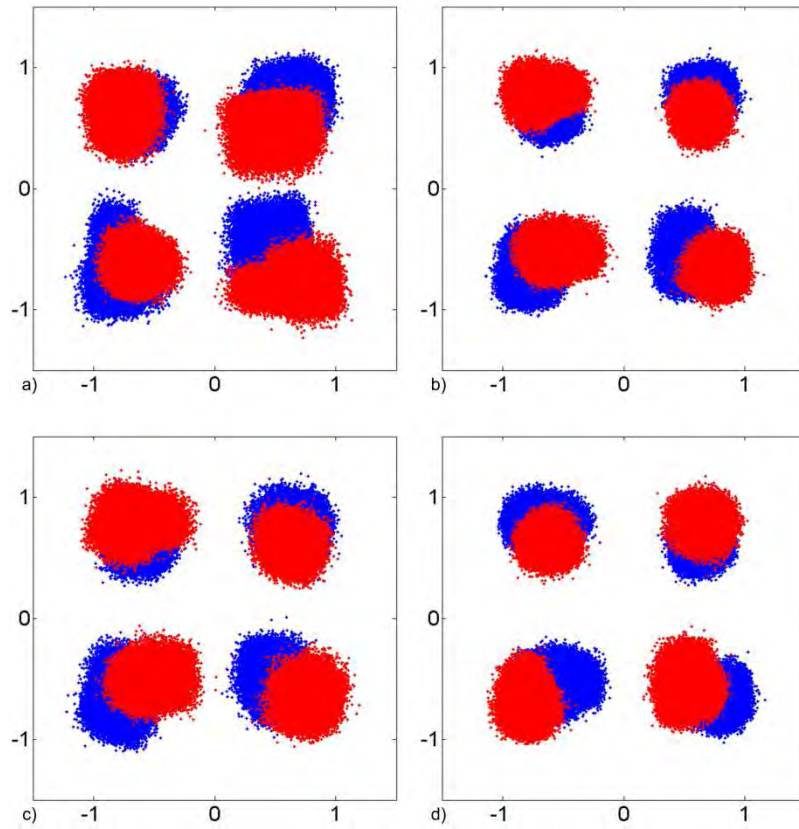
Fig. 98 Final constellations for various scenarios, when using the CMA POLDMUX algorithm with fractionally-spaced sampling at twice the symbol rate. QI compensation is performed using the Gram-Schmidt orthogonalization algorithm. In (c), (d), the outputs of the POLDMUX are fed into an additional equalizer for distortion mitigation. a) 2-tap filter tap weights; b) 6-tap filter tap weights, c) 2-tap filter tap weights, followed by 7-tap filter tap weights; d) 6-tap filter tap weights followed by 7-tap filter tap weights.

151
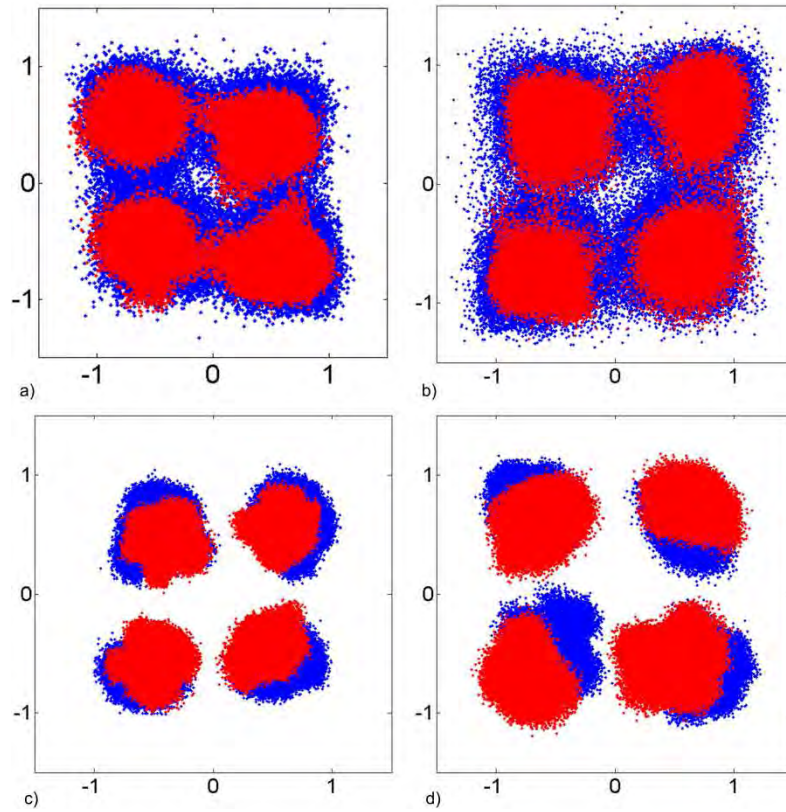
Fig. 99 Final constellations for various scenarios, when using the MUCMA POLDMUX algorithm. (a), (b): Symbol-spaced sampling. (c), (d), Fractionally-spaced sampling at twice the symbol rate. a) 5-tap filter tap weights; b) 5-tap filter tap weights followed by CMA equalizers with 11-tap filter tap weights; c) 6-tap filter tap weights; d) 6-tap filter tap weights followed by CMA equalizers with 11-tap filter tap weights.
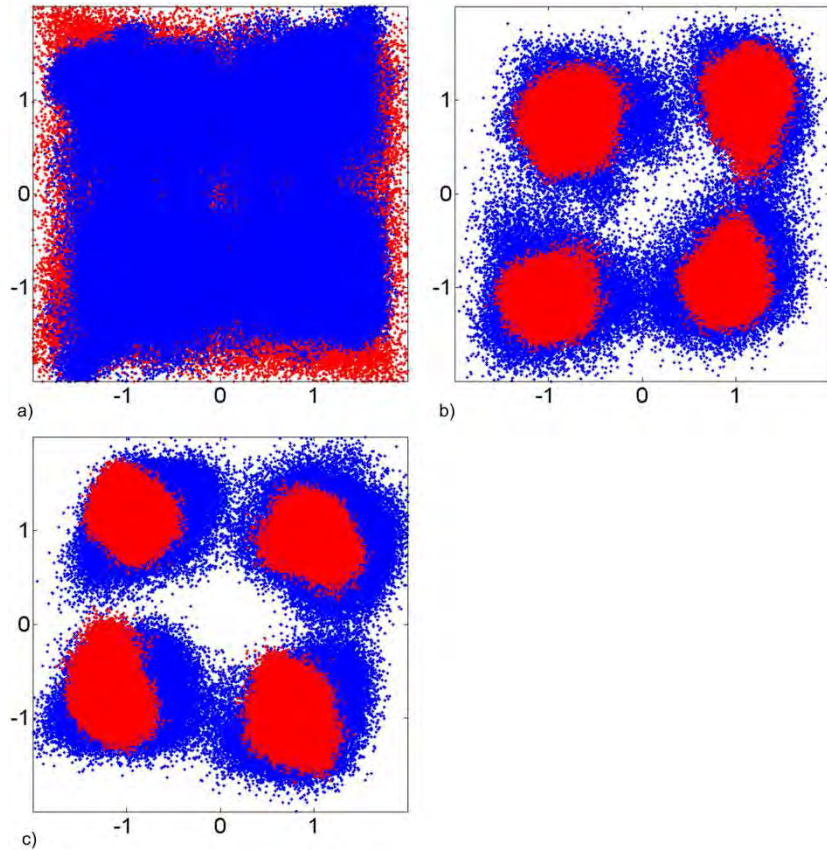
Fig. 100 Final constellations for various scenarios, when using the CCMA POLDMUX algorithm. (a), (b): Symbol-spaced sampling. (c): Fractionally-spaced sampling at twice the symbol rate. a) Single-tap filter tap weights; b) Single-tap filter tap weights for the POLDMUX, followed by CMA equalizers with 21-tap filter tap weights; c) Single-tap filter tap weights for the POLDMUX, followed by CMA equalizers with 21-tap filter tap weights.

To conclude, the 5 GBd PDM QPSK experimental data pose a challenge for successfully retrieving both polarization tributaries in the experimental set-up used in the context of this dissertation. Though the CMA POLDMUX seemingly performs polarization demultiplexing correctly, it falls into singularity, producing the same polarization tributary at both its outputs. The CCMA POLDMUX cannot retrieve both polarization tributaries error-free, even though it is shown that it can function well with fractionally-spaced sampling, followed by CMA equalizers for downsampling to one sample per symbol. The MU-CMA is the only polarization demultiplexing algorithm which successfully retrieved both polarization tributaries error-free. Though it is more time-consuming for simulations and will be more difficult for hardware implementation, it is the only choice under the circumstances investigated.

VIII.   Conclusions and recommendations for future research

The aim of this dissertation was to model an optical polarization-division-multiplexed (PDM) quadrature phase-shift keying (QPSK) system with a digital coherent receiver, and investigate its performance under realistic operating conditions. For this purpose, various digital signal processing (DSP) algorithms were implemented and tested both using simulation and upon experimental data.

Initially, an abstract model of a QPSK system was designed, using differential encoding and decoding, as well as Gray mapping and de-mapping. First, we designed a novel precoder for use in QPSK systems with quadrature modulators, incorporating differential encoding and Gray mapping. With this precoder, pseudo-random quaternary sequences were generated and the corresponding binary sequences at the input of the quadrature modulator were calculated. A semi-analytical method for the estimation of the system error probability was implemented and used to calculate the system performance theoretically.

Subsequently, we simulated a back-to-back coherent optical PDM QPSK system using a commercially available simulation software package [113]. Theoretical models of components used in optical PDM QPSK systems were implemented in the aforementioned software environment. More specifically, we implemented an optical quadrature modulator and a coherent polarization – and phase-diversity receiver. Two different optical 90° hybrids were implemented and analyzed.

The main DSP functionalities of the digital coherent receiver were then implemented using MATLAB, i.e., IF offset estimation and compensation and phase noise compensation. Using these algorithms, proof-of-concept SP-QPSK experimental results were analyzed, with symbol rates ranging from 0.1 GBd to 10 GBd. Analyzing these experimental results, several transmitter and receiver imperfections turned out to affect system performance substantially. These were namely, transmitter imperfections due to non-ideal quadrature modulation, time-drifting of modulation sequences, and quadrature imbalance due to non-ideal coherent receivers [182]. Special attention was given to quadrature imbalance [202], which was found to be the most important impairment for back-to-back operation, and a key phenomenon in transmission experiments. A number of quadrature imbalance algorithms were implemented using MATLAB, one of them designed by our team, and their performance was investigated, both via simulation, and using experimental data [185], [186].

After concluding the study of the basic functionalities of the digital coherent receiver, i.e., quadrature imbalance compensation, IF offset estimation and compensation and phase noise compensation, our focus shifted to transmission phenomena. Drift of the received state-of-polarization, though not evident in the short duration of the experimental results, was identified as a key transmission impairment to be mitigated. For this purpose, polarization combining algorithms for SP-QPSK systems were implemented and analyzed using MATLAB. For PDM QPSK systems, where random polarization rotations cause a mixing of the transmitted polarization tributaries at the receiver, polarization demultiplexing algorithms were adopted from [143], and used to analyze experimental data [156]. In the process of analyzing the experimental data, we concluded that the coefficients of conventional polarization demultiplexers can fall in to singularity, i.e., the two outputs of the polarization demultiplexer converge to the same polarization tributary. This situation was remedied by robust algorithms developed by our team [156], [197]. The latter algorithm, [197], was successfully used on experimental results [203].

Simultaneously, the results developed in the context of this dissertation were disseminated and used by other members of our team. A testbench has been implemented for simulation of all-order polarization mode dispersion using a Multi-canonical Monte Carlo simulation [204]. The same algorithms

developed in the context of this dissertation are being used in wavelength-space permutation switches for supercomputer optical interconnects [193].

Throughout this dissertation, it was demonstrated that optical PDM-QPSK systems with digital coherent receivers have certain very attractive practical attributes, apart from their superior theoretical performance. The algorithms in the digital coherent receiver can compensate for a large number of practical imperfections and transmission effects. More specifically, polarization demultiplexers compensate for random, fiber-induced, time-varying polarization rotations (Section V.4); phase noise compensation algorithms can compensate linewidth × symbol period products as large as 5×10^{-3} with OSNR penalties smaller than 3 dB (Section V.5); IF offset estimation and compensation algorithms can estimate IF offsets as large as 0.125 times the symbol rate with an error smaller than 1% (Section V.6); and finally quadrature imbalance compensation algorithms can alleviate non-ideal receiver imperfections, restoring system performance to the ideal (Section V. 7).

The tolerances to imperfections and non-idealities offered by the algorithms in the digital receiver make PDM-QPSK easy to implement even with off-the-shelf components. Cheap bulk-component 90° optical hybrids can be used, and their non-ideal, time-varying operation can be compensated for, by using quadrature imbalance algorithms. Off-the-shelf DFB lasers with large 3-dB linewidths can be used owing to the large tolerance to phase noise offered by the phase noise compensation algorithms. No feedback control of the LO laser is needed, since IF offset estimation and compensation algorithms can eliminate relatively large, time-varying, IF offsets.

PDM-QPSK systems at 40 Gb/s and 100 Gb/s are already becoming commercially available, which means that crucial decisions upon the algorithms to be implemented been taken by the industry. However it is not obvious that the optimality of these algorithms has been fully investigated. For future research, four topics should be of interest. 1) Investigate fundamental theoretical limits due to transmission effects, using semi-analytical or Multi-canonical Monte Carlo simulation methods. For example, fiber non-linearities such as SPM and XPM in WDM systems will govern the performance of ultra-long haul systems using PDM-QPSK. 2) Investigate implementation aspects of the algorithms proposed for the aforementioned transmission effects in the digital coherent receiver. Most algorithms proposed in the context of this thesis and in the literature, have been used in off-line signal processing. Hardware limitations due to complexity may introduce unforeseen penalties. 3) Explore various FEC schemes. Efficient and powerful FEC schemes are expected to be used. Designing good codes for various transmission phenomena is a major challenge. 4) Extend the digital coherent receiver algorithms and design to even more advanced modulation formats and other fiber types. Multi-QAM modulation formats, in conjunction with cheap multi-mode fibers will provide unprecedented information bandwidth to the end-user.

APPENIDIX

Appendix A   Signal representation nomenclature [2]

In this dissertation, an equivalent low-pass representation of narrowband signals is used. For completeness, in this appendix we present the formulation used in all Sections.

Suppose that a real-valued signal $x(t)$ has a frequency content concentrated within a narrow band of frequencies of bandwidth B, around a frequency f_c, as depicted in Fig. 101a. This is the case for optical signals which are centered around the laser emission frequency, which in this dissertation, is always 193.1 THz. In order to sample this signal and use it in a simulation, sampling should be performed at a rate $f_S \geq 2f_c+B$. Since this is an enormous sampling rate, it is of interest to find an equivalent low-pass representation of the signal. We first construct a signal that contains only the positive frequencies in $x(t)$ the *analytic signal* $x_+(t)$ [2],[4], as

$$
\begin{aligned}
X_+(f) &= 2u(f)X(f) \\
x_+(t) &= F^{-1}\{X_+(f)\}
\end{aligned}
\tag{182}
$$

where $u(f)$ is the unit step function in frequency, $X(f)$ is the spectrum of the narrowband signal $x(t)$, and $F^{-1}\{\}$ denotes the inverse Fourier transform. Fig. 101b shows the spectrum of the step function $2u(f)$. Fig. 101c shows the spectrum of the analytic signal. The analytic signal can be written as

$$
x_+(t) = x(t) + j\hat{x}(t)
\tag{183}
$$

where $\hat{x}(t)$ is the Hilbert transform of $x(t)$ defined as

$$
\hat{x}(t) = \frac{1}{\pi t} \otimes x(t)
\tag{184}
$$

and $\otimes$ denotes convolution. The analytic signal is a complex signal, since it has a one-sided spectrum. It is then shifted to baseband, by multiplying it with a complex phasor of frequency $-f_c$, forming the *complex envelope, $\tilde{x}(t)$*

$$
\begin{aligned}
\tilde{X}(f) &= X_+(f+f_c) \\
\tilde{x}(t) &= x_+(t)e^{-j2\pi f_c t}
\end{aligned}
\tag{185}
$$

By solving the time-domain equation (185) for the analytic signal and inserting it into the right hand side of (183), we get

$$
x(t) = \operatorname{Re}\{\tilde{x}(t)e^{j2\pi f_c}\}
\tag{186}
$$

Therefore, the narrowband signal $x(t)$ with bandwidth B can be represented by a complex band-pass signal $\tilde{x}(t)$ with bandwidth $B/2$, which can be sampled at a frequency $f_S \geq B$, a frequency which is realizable in simulations.
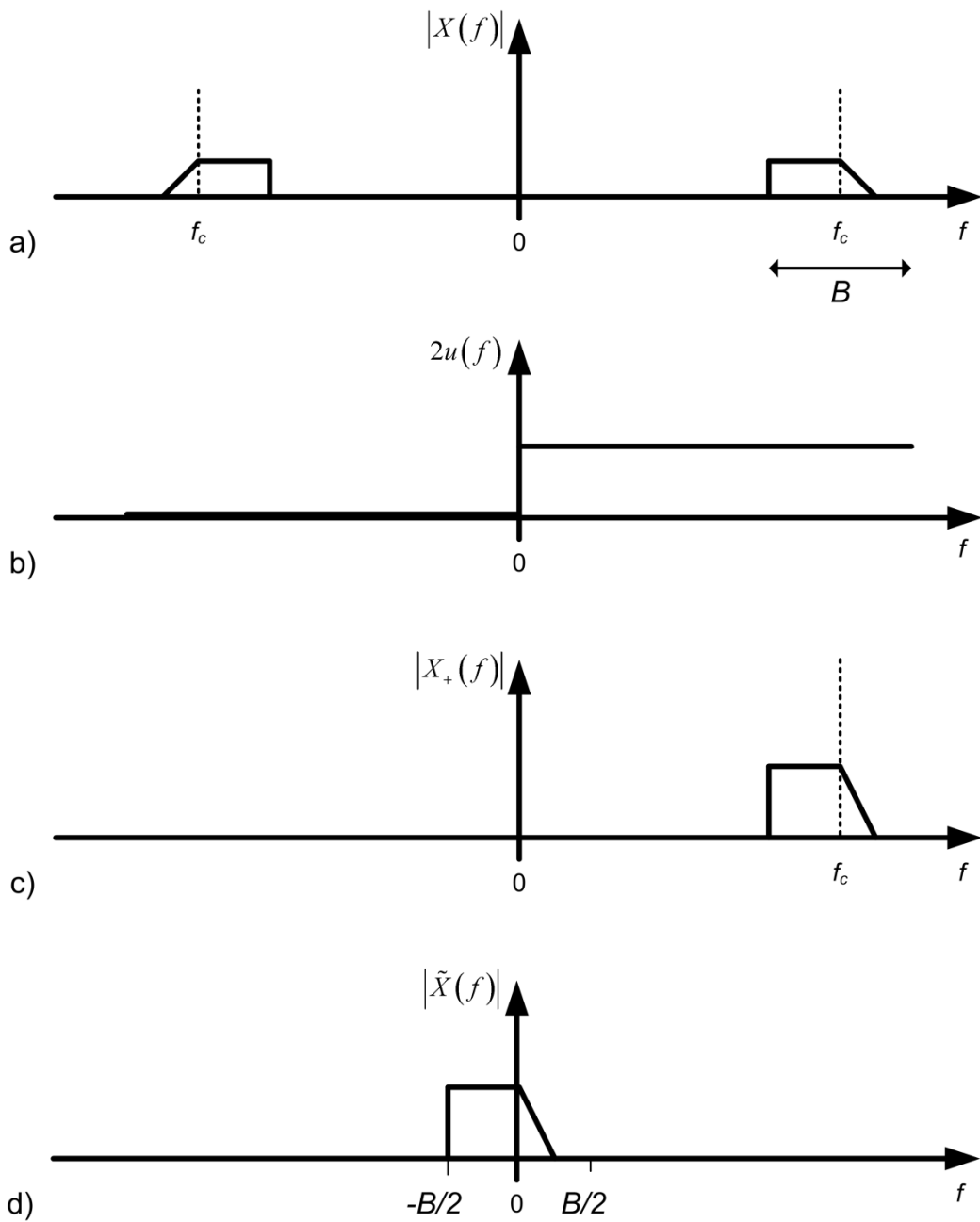
Fig. 101 Spectrum of various signals involved in the definition of the complex envelope representation of a narrowband signal. a) Spectrum of the narrowband signal. b) Spectrum of the frequency-domain unit step function. c) Spectrum of the analytic signal. d) Spectrum of the complex envelope representation.

Appendix B   QPSK Gray and differential encoding precoder

In order to derive the Boolean expressions implemented in the precoder used in the QPSK quadrature modulator, we construct the truth table describing its operation. We employ the following conventions in doing so.

Bit sequences $b_{1,k}$, $b_{2,k}$, belonging to an alphabet $\{b_i\}=\{0,1\}$, $i=0,1$ are transformed into bit sequences $e_{1,k}$, $e_{2,k}$, belonging to an alphabet $\{e_i\}=\{0,1\}$, $i=0,1$, using the precoder.

Bit sequences $e_{1,k}$, $e_{2,k}$, are mapped into real symbols $a_{1,k}$, $a_{2,k}$, belonging to an alphabet $\{a_i\}=\{-1,1\}$, $i=0,1$ following convention

$$
\begin{aligned}
e_k = 0 &\rightarrow a_k = -1 \\
e_k = 1 &\rightarrow a_k = 1
\end{aligned}
\tag{187}
$$

Differentially and Gray encoded complex symbols d_k belonging to an alphabet $\{d_n\}=\{1+j,-1+j,-1-j,1-j\}$, $n=0,1,2,3$ are formed as $a_{1,k}+ja_{2,k}$.

For clarity, we represent differentially and Gray-encoded complex symbol sequence d_k by the corresponding index sequence n_k. Thus, differential decoding, represented by symbol recursion $c_k=d_k d^*_{k-1}$ can also be represented as $n_{g,k}=<n_k-n_{k-1}>_{mod4}$, where $n_{g,k}$ is a sequence of Gray-coded integers. The Gray-encoded sequence $n_{g,k}$ is decoded into the two original bit sequences $b_{1,k}$, $b_{2,k}$, following mapping

$$
\begin{aligned}
n_g = 0 &\rightarrow b_1 b_2 = 00 \\
n_g = 1 &\rightarrow b_1 b_2 = 01 \\
n_g = 2 &\rightarrow b_1 b_2 = 11 \\
n_g = 3 &\rightarrow b_1 b_2 = 10
\end{aligned}
\tag{188}
$$

Owing to the memory introduced by differential encoding, present state $n_{g,k}$ is dictated by both n_k and n_{k-1} and so are bit sequence values $b_{1,k}$, $b_{2,k}$. All possible symbol combinations n_k and n_{k-1} in the channel are given in Table 2.

Table 2 All possible combinations of symbol pairs transmitted in the channel, the corresponding Gray-encoded complex symbol, and the corresponding pair of bits at the receiver output.

n_{k-1}	n_k	$n_{g,k}$	$b_{1,k}$	$b_{2,k}$
0	0	0	0	0
0	1	1	0	1
0	2	2	1	1
0	3	3	1	0
1	0	3	1	0
1	1	0	0	0
1	2	1	0	1
1	3	2	1	1
2	0	2	1	1
2	1	3	1	0
2	2	0	0	0
2	3	1	0	1
3	0	1	0	1
3	1	2	1	1
3	2	3	1	0
3	3	0	0	0

Given the mapping between e_k and n_k described above, Table 3 gives all combinations of $e_{1,k}$, $e_{2,k}$, which produce all the possible combinations n_k, n_{k-1} and therefore bit sequence values $b_{1,k}$, $b_{2,k}$.

Table 3 All possible combinations of precoder output bit pairs and the corresponding combinations of symbol pairs transmitted in the channel, the corresponding Gray encoded complex symbols, and the corresponding pair of bits at the output.

$e_{1,k-1}$	$e_{2,k-1}$	$e_{1,k}$	$e_{2,k}$	n_{k-1}	n_k	$n_{g,k}$	$b_{1,k}$	$b_{2,k}$
1	1	1	1	0	0	0	0	0
1	1	0	1	0	1	1	0	1
1	1	0	0	0	2	2	1	1
1	1	1	0	0	3	3	1	0
0	1	1	1	1	0	3	1	0
0	1	0	1	1	1	0	0	0
0	1	0	0	1	2	1	0	1
0	1	1	0	1	3	2	1	1
0	0	1	1	2	0	2	1	1
0	0	0	1	2	1	3	1	0
0	0	0	0	2	2	0	0	0
0	0	1	0	2	3	1	0	1
1	0	1	1	3	0	1	0	1
1	0	0	1	3	1	2	1	1
1	0	0	0	3	2	3	1	0
1	0	1	0	3	3	0	0	0

From Table 2 and Table 3, the truth table for the precoder is easily derived, and given in Table 4, assuming inputs $b_{1,k}$, $b_{2,k}$, $e_{1,k-1}$, $e_{2,k-1}$, and outputs $e_{1,k}$, $e_{2,k}$. Karnaugh tables for output variables $e_{1,k}$, $e_{2,k}$. not shown here, produce the Boolean expressions of (81).

Table 4 Truth table for the precoder used in a QPSK system with differential detection and Gray encoding

$b_{1,k}$	$b_{2,k}$	$e_{1,k-1}$	$e_{2,k-1}$	$e_{1,k}$	$e_{2,k}$
0	0	1	1	1	1
0	1	1	1	0	1
1	1	1	1	0	0
1	0	1	1	1	0
1	0	0	1	1	1
0	0	0	1	0	1
0	1	0	1	0	0
1	1	0	1	1	0
1	1	0	0	1	1
1	0	0	0	0	1
0	0	0	0	0	0
0	1	0	0	1	0
0	1	1	0	1	1
1	1	1	0	0	1
1	0	1	0	0	0
0	0	1	0	1	0

Appendix C   Semi-analytical method for the estimation of error probability

System performance can be evaluated in a number of ways via simulation, the most accurate being the counting of the bit-error-rate (BER), under actual system conditions. Since this is difficult to perform, especially for low target BERs, due to the overhead caused by simulation time, other reliable techniques for estimating the BER performance of a system are needed, such as the probability of error, or error probability P_e [4]. For the theoretical evaluation of the performance of coherent M-PSK systems, it is necessary to use the error probability, P_e, as a criterion. Different expressions for the error probability of these systems in the exclusive presence of additive white Gaussian noise are presented in several digital communications textbooks, e.g., [198], [199], with various degrees of accuracy. Adaptation of these formulae in the case of optical communications systems employing binary PSK (BPSK) and QPSK modulation and an optically-preamplified, synchronous homodyne receiver was done by [200].

All aforementioned analytical expressions for the error probability contain simplifying assumptions for mathematical tractability, so they are valid only in idealized cases, e.g., for perfectly rectangular, non-return-to-zero (NRZ) pulses, in the absence of distortion. As a result, they are inadequate for capturing the impact of fiber transmission impairments and electronic DSP functionalities of the synchronous homodyne receiver on the system performance. Therefore, it is necessary to develop a quasi-analytical method for the accurate evaluation of the error probability [201]. According to this technique, the distortion of the signal due to transmission impairments and electronic DSP functionalities is computed by simulation in the absence of noise, the noise statistics at the input of the decision circuit are calculated analytically, and the average bit error probability is estimated using an analytical formula.

The expression for the received photocurrent samples at the output of the ADC circuit, for a SP-QPSK system, when symbol-spaced sampling is performed, is given by (105). In the absence of any form of noise source, or IF offset, the photocurrent sample for the n–th symbol is given by

$$\tilde{i}[n] = IA[n]e^{j\phi_k[n]} \tag{189}$$

where $I = R\sqrt{P_S P_{LO}/2}$ is the photocurrent amplitude due to photodetection, and $A[n]$ is the time varying amplitude due to ISI. Ideally, $A[n]=1$. Neglecting the scaling factor I, or normalizing to a unit symbol power, the expression for the symbol error probability is

$$P_{e|s} = erfc(\rho_b) \tag{190}$$

where ρ_b is the equivalent per-bit OSNR

$$\rho_b = A^2/2\sigma_b^2 \tag{191}$$

The per-bit error probability for Gray mapping is approximately

$$P_{e|b} \cong \frac{1}{2}P_{e|s} = \frac{1}{2}erfc(\rho_b) \tag{192}$$

In the presence of distortion, the error probability varies between symbols. We evaluate the average symbol error probability using the arithmetic mean over all the simulated symbols

$$\overline{P}_{e|s} = \frac{1}{N_{symbols}} \sum_{n=1}^{N_{symbols}} P_{e|s_k} \tag{193}$$

where $N_{symbols}$ denotes the number of simulated symbols and $P_{e|s_k}$ is the conditional error probability for the k–th symbol. In order to take into account the intersymbol interference (ISI) due to m adjacent symbols on each side of a symbol, we select $N_{symbols}$ so as to contain all possible combinations of $2m+1$ symbols. The most efficient way to do so is to use de Bruijn symbol sequences. Since each QPSK symbol takes four possible values, one needs to simulate $N_{symbols} = 4^{2m+1}$. A sequence of length 4^{2m+1} containing all possible patterns of m bits within a period 4^{2m+1} exactly once is called a de Bruijn sequence of length $2m+1$.

The notion of symbol error probability can be easily explained visually. Fig. 102 shows the series of conceptual steps for the calculation of the per-symbol error probability. Fig. 102 shows the ideal QPSK constellation diagram in 3-D form, where the third dimension corresponds to the probability density function (pdf) of the amplitude of the four possible symbols to be received. At each time instant, only one of the four possible symbols are received, and ideally, the pdf is a Dirac delta function of unit amplitude. The effect of additive noise is to transform the received pdf. Since the in-phase and quadrature components of the total receiver noise are independent, identically distributed (i.i.d.) Gaussian random variables with zero mean and variance σ^2, their joint probability density function (pdf) is written as

$$p_{n_1,n_2}(n_1,n_2) = \frac{1}{2\pi\sigma^2} e^{-\frac{n_1^2+n_2^2}{2\sigma^2}}$$

(194)

In this case, the received symbol pdf becomes as shown in Fig. 102b. Performing symbol hard-decision corresponds to setting the thresholds depicted in Fig. 102c. The probability of error for the in-phase component of the received complex symbol is the integral of the pdf at the sampling point, below the threshold (Fig. 102d red circle). The same holds for the probability of error for the quadrature component of the received complex symbol (not shown). The symbol error probability is simply the mean of the error probabilities per quadrature.
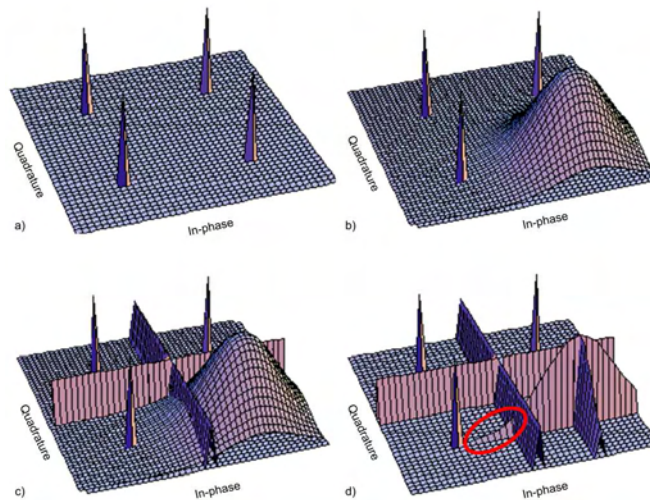
Fig. 102 Graphical representation of the calculation of symbol error probability in QPSK. a) probability density functions of the four possible complex symbols; b) One complex symbol has additive Gaussian noise superimposed; c) graphical depiction of the thresholds used; d) part of the probability density function used to calculate the error probability (red circle).

Throughout this dissertation, the threshold was always assumed to be fixed at zero for both the in-phase and quadrature symbol components.

Appendix D   Optical quadrature modulator

In this section, we derive the input/output characteristic of the optical quadrature modulator. As a starting point, we derive the transfer function of a LiNbO$_3$ Mach-Zehnder modulator in terms of scattering matrices. A scattering matrix defines the relationship between the input and output analytic electric fields of a device [119], [120].

A LiNbO$_3$ Mach-Zehnder modulator is comprised of an input directional 3-dB coupler, two parallel branches connected to each of the output ports of the directional 3-dB coupler, two phase shifters causing voltage-dependent phase shifts on the optical signal of each of the branches, and an output directional 3-dB coupler, whose inputs are the two phase shifted optical signals. Only one of the input ports of the directional 3-dB coupler is active and only one of the outputs of the output directional 3-dB coupler is used for further transmission of the electrical field.

The scattering matrix of a lossless, polarization-independent, directional coupler is written [119]

$$\mathbf{S} = \frac{1}{\sqrt{2}}\begin{pmatrix} 1 & j \\ j & 1 \end{pmatrix}. \tag{195}$$

The scattering matrix of the two parallel branches of a push-pull Mach-Zehnder modulator, with the phase shifters, is written

$$\mathbf{D} = \begin{pmatrix} e^{\frac{j\phi}{2}} & 0 \\ 0 & e^{-\frac{j\phi}{2}} \end{pmatrix} \tag{196}$$

where ϕ is the sum of a phase shift due to the propagation φ_0 and a phase shift due to the voltage-dependent refractive index (Pockels effect) [120]

$$\phi = \varphi_0 - \pi \frac{V}{V_\pi} \tag{197}$$

where

$$\varphi_0 = \frac{2\pi}{\lambda_0} nL$$

$$V_\pi = \frac{\lambda_0 d}{r n^3 L} \tag{198}$$

and λ_0 is the free-space wavelength of the input optical beam, L is the length of the phase-shifters, d is the distance between the electrodes, n is the refractive index in the absence of voltage, r is the Pockels electro-optic coefficient, V_π is the half-wave voltage, and V is the applied drive voltage. The birefringence of LiNbO$_3$ is neglected.

Assuming that only one of the input ports of the input directional 3-dB coupler is used, with an input analytic electrical field denoted $\hat{\mathbf{E}}_{i,1}(t)$, the analytic electric fields at the output ports of the output directional 3-dB coupler are

$$\begin{pmatrix} \hat{\mathbf{E}}_{o,1} \\ \hat{\mathbf{E}}_{o,2} \end{pmatrix} = \mathbf{SDS}\begin{pmatrix} \hat{\mathbf{E}}_{i,1} \\ 0 \end{pmatrix}. \tag{199}$$

Discarding one of the outputs, it can be shown that the input/output relationship for a Mach-Zehnder modulator is

167

$$\hat{\mathbf{E}}_{o,1} = j\sin\frac{\phi}{2}\hat{\mathbf{E}}_{i,1} \tag{200}$$

For the modeling of the quadrature modulator, which is a Mach-Zehnder modulator super structure, composed of a Mach-Zehnder modulator in each branch and an additional phase shifter, we define the scattering matrix for the nested Mach-Zehnder modulators as

$$\mathbf{M} = \begin{pmatrix} j\sin\dfrac{\phi_1}{2} & 0 \\ 0 & j\sin\dfrac{\phi_2}{2} \end{pmatrix} \tag{201}$$

and the phase shifter as

$$\mathbf{\Phi} = \begin{pmatrix} e^{\frac{j\phi_3}{2}} & 0 \\ 0 & e^{-\frac{j\phi_3}{2}} \end{pmatrix} \tag{202}$$

We have assumed that phase shifting is equally split between the two branches. The analytic electric fields at the output ports of the directional 3-dB coupler at the output of the quadrature modulator are

$$\begin{pmatrix} \hat{\mathbf{E}}_{o,1} \\ \hat{\mathbf{E}}_{o,2} \end{pmatrix} = \mathbf{S}\mathbf{\Phi}\mathbf{M}\mathbf{S}\begin{pmatrix} \hat{\mathbf{E}}_{i,1} \\ 0 \end{pmatrix}. \tag{203}$$

Discarding one of the outputs, it can be shown that the input/output relationship for the quadrature modulator is

$$\hat{\mathbf{E}}_{o,1} = \frac{j}{2}e^{-j\frac{\pi V_3}{2V_{\pi 3}}}\left\{\sin\left[\frac{\pi V_1(t)}{2V_{\pi_1}}\right] - e^{-j\frac{\pi V_3}{V_{\pi 3}}}\sin\left[\frac{\pi V_2(t)}{2V_{\pi_2}}\right]\right\}\hat{\mathbf{E}}_{i,1} \tag{204}$$

In the ideal case, $V_3 = V_{\pi 3}$, $V_1(t) = a_1 V_{\pi 1} g_1(t)$, $V_2(t) = a_2 V_{\pi 2} g_2(t)$, and $g_1(t) = g_2(t) = g(t)$ is the pulse shape of the modulating voltage waveforms at the two Mach-Zehnder modulators and $a_1, a_2 = \pm 1$ correspond to the input binary bits in polar form. Then we can write

$$\hat{\mathbf{E}}_{o,1} = \frac{1}{2}(a_1 + ja_2)\sin\left[\frac{\pi}{2}g(t)\right]\hat{\mathbf{E}}_{i,1} \tag{205}$$

Since it is assumed, for simplicity, that the polarization of the optical signals is preserved, we can write

$$\tilde{E}_{out} = \frac{1}{2}\sum_{k=0}^{\infty}d_k\sin\left[\frac{\pi}{2}g(t - kT_S)\right]\tilde{E}_{in} \tag{206}$$

or

$$\hat{\mathbf{E}}_{out} = \frac{1}{2}\sum_{k=0}^{\infty}d_k\sin\left[\frac{\pi}{2}g(t - kT_S)\right]\hat{\mathbf{E}}_{in} \tag{207}$$

where $d = a_1 + ja_2$ is the complex modulation symbol and k corresponds to the k–th modulation symbol.

Appendix E   2×4 optical 90° hybrid

In this section, we derive the input/output characteristic of the integrated 2×4 90° optical hybrid and give the photocurrent expressions at the output of the corresponding phase-diversity receiver. The block diagram of the optical hybrid is shown in Fig. 103. It is comprised of four polarization independent directional couplers, DCPL1-DCPL4, with splitting ratios α_1-α_4, respectively, and two polarization independent phase shifters, PS1 and PS2, with phase shift values, ε and $90°+\delta$ respectively. All couplers and phase shifters are externally controlled using bias voltages.

Assume that the analytic signal of the electric field of the received optical waveform is

$$\hat{\mathbf{E}}_S = \sqrt{2P_S} \exp\left[j\left(2\pi f_S t + \phi_{n,S} + \phi_k \right)\right]\left|e_S\right\rangle \tag{208}$$

and that the analytic signal of the electric field of the LO is

$$\hat{\mathbf{E}}_{LO} = \sqrt{2P_{LO}} \exp\left[j\left(2\pi f_{LO} t + \phi_{n,LO} \right)\right]\left|e_{LO}\right\rangle \tag{209}$$

where P_S, P_{LO} are the average optical powers, f_S, f_{LO} are the carrier frequencies, $\phi_{n,S}, \phi_{n,LO}$ are the laser phase noises, and $\left|e_S\right\rangle,\left|e_{LO}\right\rangle$ are the normalized Jones vectors, for the received and LO signals, respectively. In addition, ϕ_k denotes the modulation phase corresponding to the k–th symbol interval.

The scattering matrix of a lossless, polarization-independent directional coupler with splitting ratio α is [119]

$$\mathbf{S} = \frac{1}{\sqrt{2}}\begin{pmatrix} \sqrt{1-a} & j\sqrt{a} \\ j\sqrt{a} & \sqrt{1-a} \end{pmatrix}. \tag{210}$$

The phase shifters simply introduce a phase shift $e^{j\varepsilon}$ and $je^{j\delta}$. At the input, only two of the four coupler input ports are used, and so $\hat{\mathbf{E}}_A = \hat{\mathbf{E}}_S$, $\hat{\mathbf{E}}_B = \hat{\mathbf{E}}_C = 0$ and $\hat{\mathbf{E}}_D = \hat{\mathbf{E}}_{LO}$. At the output of the hybrid, all four coupler output ports are used, each illuminating a photodetector. The four photodetectors, with responsivities R_1-R_4 are connected in pairs (1-2 and 3-4) forming two balanced photodetectors.
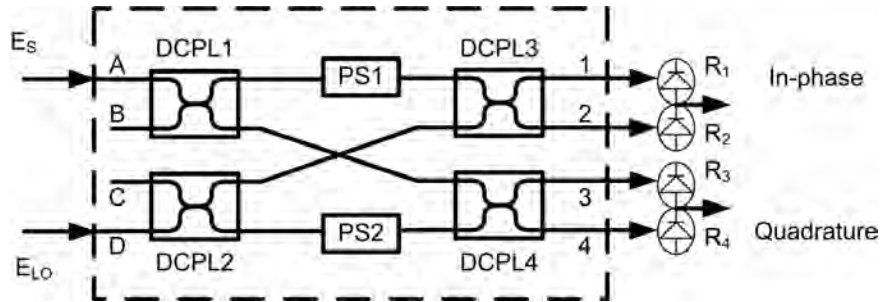
Fig. 103 Block diagram of the 2×4 90° optical hybrid. (Abbreviations: DCPL: Directional coupler, PS: Phase shifter, R_1-R_4: Responsivity).

With some elementary algebra, the scattering matrix of the optical hybrid is

$$\begin{pmatrix} \exp(j\varepsilon)\sqrt{a_3 a_1} & -\sqrt{(1-a_3)(1-a_2)} \\ j\exp(j\varepsilon)\sqrt{(1-a_3)a_1} & j\sqrt{(1-a_2)a_3} \\ j\sqrt{(1-a_1)a_4} & -\exp(j\delta)\sqrt{(1-a_4)a_2} \\ -\sqrt{(1-a_4)(1-a_1)} & j\exp(j\delta)\sqrt{a_4 a_2} \end{pmatrix} \tag{211}$$

Assuming constant polarization, we can drop polarization notation from the analytical signals of the electric fields. Then, the hybrid input/output characteristic becomes

$$
\begin{pmatrix} \hat{E}_1 \\ \hat{E}_2 \\ \hat{E}_3 \\ \hat{E}_4 \end{pmatrix} = \begin{pmatrix} \exp(j\varepsilon)\sqrt{a_3 a_1} & -\sqrt{(1-a_3)(1-a_2)} \\ j\exp(j\varepsilon)\sqrt{(1-a_3)a_1} & j\sqrt{(1-a_2)a_3} \\ j\sqrt{(1-a_1)a_4} & -\exp(j\delta)\sqrt{(1-a_4)a_2} \\ -\sqrt{(1-a_4)(1-a_1)} & j\exp(j\delta)\sqrt{a_4 a_2} \end{pmatrix} \begin{pmatrix} \hat{E}_S \\ \hat{E}_{LO} \end{pmatrix}.
\tag{212}
$$

The output photocurrent at each photodetector is

$$
i_i = \frac{1}{2} R_i \left\langle \hat{E}_i(t)\hat{E}_i^\dagger(t) \right\rangle, i = 1,2,3,4
\tag{213}
$$

where the angle brackets denote time averaging over an interval proportional to the response time of the photodiode and † denotes complex conjugation. The analytic expressions of the four photocurrents are

$$
\begin{aligned}
i_1 &= R_1 \left\{ a_3 a_1 P_s + (1-a_3)(1-a_2)P_{lo} - 2\sqrt{a_3 a_1(1-a_3)(1-a_2)}\sqrt{P_s P_{lo}}\cos\left(2\pi f_{IF} t + \Delta\phi_n + \phi_k + \varepsilon\right) \right\} \\
i_2 &= R_2 \left\{ (1-a_3)a_1 P_s + (1-a_2)a_3 P_{lo} + 2\sqrt{a_3 a_1(1-a_3)(1-a_2)}\sqrt{P_s P_{lo}}\cos\left(2\pi f_{IF} t + \Delta\phi_n + \phi_k + \varepsilon\right) \right\} \\
i_3 &= R_3 \left\{ (1-a_1)a_4 P_s + (1-a_4)a_2 P_{lo} + 2\sqrt{a_2 a_4(1-a_1)(1-a_4)}\sqrt{P_s P_{lo}}\sin\left(2\pi f_{IF} t + \Delta\phi_n + \phi_k - \delta\right) \right\} \\
i_4 &= R_4 \left\{ (1-a_4)(1-a_1)P_s + a_4 a_2 P_{lo} - 2\sqrt{a_2 a_4(1-a_1)(1-a_4)}\sqrt{P_s P_{lo}}\sin\left(2\pi f_{IF} t + \Delta\phi_n + \phi_k - \delta\right) \right\}
\end{aligned}
\tag{214}
$$

The two quadrature photocurrents i_I and i_Q are formed as $i_I = i_2 - i_1$ and $i_Q = i_3 - i_4$

$$
\begin{aligned}
i_I &= \left[R_2 a_1(1-a_3) - R_1 a_1 a_3 \right] P_s + \left[R_2 a_3(1-a_2) - R_1(1-a_3)(1-a_2) \right] P_{lo} \\
&\quad + 2\left[R_1 + R_2 \right]\sqrt{P_s P_{lo}}\sqrt{a_1 a_3(1-a_3)(1-a_2)}\cos\left(2\pi f_{IF} t + \Delta\phi_n + \phi_k + \varepsilon\right) \\
i_Q &= \left[R_3 a_4(1-a_1) - R_4(1-a_4)(1-a_1) \right] P_s + \left[R_3 a_2(1-a_4) - R_3 a_4 a_2 \right] P_{lo} + \\
&\quad + 2\left[R_3 + R_4 \right]\sqrt{P_s P_{lo}}\sqrt{a_4 a_2(1-a_1)(1-a_4)}\sin\left(2\pi f_{IF} t + \Delta\phi_n + \phi_k - \delta\right)
\end{aligned}
\tag{215}
$$

Assuming ideal directional couplers ($\alpha_1 = \alpha_2 = \alpha_3 = \alpha_4 = 0.5$), ideal phase shifting ($\varepsilon = \delta = 0°$), and perfectly balanced photodetectors ($R_1 = R_2 = R_3 = R_4 = 1$) the hybrid input/output characteristic becomes

$$
\begin{pmatrix} \hat{E}_1 \\ \hat{E}_2 \\ \hat{E}_3 \\ \hat{E}_4 \end{pmatrix} = \frac{1}{2} \begin{pmatrix} 1 & -1 \\ j & j \\ j & -1 \\ -1 & j \end{pmatrix} \begin{pmatrix} \hat{E}_S \\ \hat{E}_{LO} \end{pmatrix}
\tag{216}
$$

From (215), the corresponding photocurrents are

$$
\begin{aligned}
i_I &= R\sqrt{P_s P_{lo}}\cos\left(2\pi f_{IF} t + \Delta\phi_n + \phi_k\right) \\
i_Q &= R\sqrt{P_s P_{lo}}\sin\left(2\pi f_{IF} t + \Delta\phi_n + \phi_k\right)
\end{aligned}
\tag{217}
$$

Balanced detection thus removes any DC components.

Appendix F   2×2 optical 90° hybrid

In this section, we derive the input/output characteristic of the 2×2 90° optical hybrid proposed in [125], and give the photocurrent expressions at the output of the phase-diversity receiver. The block diagram of the hybrid is shown in Fig. 104. It is comprised of four polarization controllers (PCTR1-PCTR4), a directional coupler, and two fiber polarizers (Pol1 and Pol2). All controllers and polarizers are manually controlled. The polarizers are followed by single photodetectors, with responsivities R_1 and R_2, respectively.
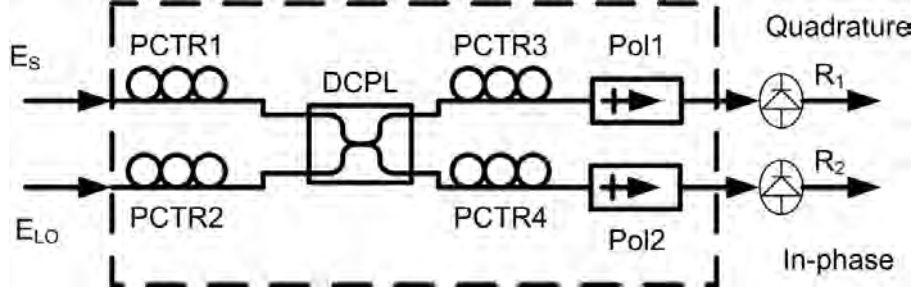
Fig. 104 Block diagram of the 2×2 90° optical hybrid. (Abbreviations: DCPL: Directional coupler, PCTR: Polarization controller, Pol: Linear fiber polarizer, R: Responsivity).

Assume that the analytic signal of the electric field of the received optical waveform is

$$\hat{\mathbf{E}}_S = \sqrt{2P_S}\,\exp\left[\,j\left(2\pi f_S t + \phi_{n,S} + \phi_k\right)\right]\big|e_S\big\rangle \tag{218}$$

and that the analytic signal of the electric field of the LO is

$$\hat{\mathbf{E}}_{LO} = \sqrt{2P_{LO}}\,\exp\left[\,j\left(2\pi f_{LO} t + \phi_{n,LO}\right)\right]\big|e_{LO}\big\rangle \tag{219}$$

where P_S, P_{LO} are the average optical powers, f_S, f_{LO} are the carrier frequencies, $\phi_{n,S}, \phi_{n,LO}$ are the laser phase noises, and $\big|e_S\big\rangle, \big|e_{LO}\big\rangle$ are the normalized Jones vectors, for the received and LO signals, respectively. In addition ϕ_k denotes the modulation phase corresponding to the k–th symbol interval.

We assume that the directional coupler is a lossless, polarization-independent device, with a scattering matrix given by (195). Because the SOPs of the received and LO signals are important, we cannot drop polarization notation. The analytic electrical field vectors at the input of the hybrid can be written as

$$\hat{\mathbf{E}}_1(t) = \hat{E}_S(t)\big|e_S\big\rangle$$
$$\hat{\mathbf{E}}_2(t) = \hat{E}_{LO}(t)\big|e_{LO}\big\rangle \tag{220}$$

After the polarization controllers, these electric field vectors become

$$\hat{\mathbf{E}}_3(t) = \hat{E}_S(t)\big|e_S{}'\big\rangle$$
$$\hat{\mathbf{E}}_4(t) = \hat{E}_{LO}(t)\big|e_{LO}{}'\big\rangle \tag{221}$$

After the polarization-independent ideal directional coupler

$$\hat{\mathbf{E}}_5(t) = \frac{1}{\sqrt{2}}\left[\hat{\mathbf{E}}_3(t) + j\hat{\mathbf{E}}_4(t)\right] = \frac{1}{2}\left[\hat{E}_S(t)\left|e_S'\right\rangle + j\hat{E}_{LO}(t)\left|e_{LO}'\right\rangle\right]$$

$$\hat{\mathbf{E}}_6(t) = \frac{1}{\sqrt{2}}\left[j\hat{\mathbf{E}}_3(t) + \hat{\mathbf{E}}_4(t)\right] = \frac{1}{2}\left[j\hat{E}_S(t)\left|e_S'\right\rangle + \hat{E}_{lo}(t)\left|e_{LO}'\right\rangle\right]$$

(222)

Assuming that polarization controllers PCTR3, PCTR4 produce SOPs $\left|p_1\right\rangle$ and $\left|p_2\right\rangle$ respectively and that fiber polarizers Pol1 and Pol2 have principle axes along polarization directions $\left|p_1\right\rangle$ and $\left|p_2\right\rangle$ respectively,

$$\hat{\mathbf{E}}_7(t) = \frac{1}{2}\left[\hat{E}_S(t)\left\langle p_1\middle|e_S'\right\rangle + j\hat{E}_{LO}(t)\left\langle p_1\middle|e_{LO}'\right\rangle\right]\left|p_1\right\rangle$$

$$\hat{\mathbf{E}}_8(t) = \frac{1}{2}\left[j\hat{E}_S(t)\left\langle p_2\middle|e_S'\right\rangle + \hat{E}_{LO}(t)\left\langle p_2\middle|e_{LO}'\right\rangle\right]\left|p_2\right\rangle$$

(223)

we define

$$\left\langle p_1\middle|e_S'\right\rangle = \alpha_1 e^{i\zeta_1}$$

$$\left\langle p_1\middle|e_{LO}'\right\rangle = \beta_1 e^{i\xi_1}$$

$$\left\langle p_2\middle|e_S'\right\rangle = \alpha_2 e^{i\zeta_2}$$

$$\left\langle p_2\middle|e_{LO}'\right\rangle = \beta_2 e^{i\xi_2}$$

(224)

After the photodiodes

$$i_1 = \frac{R_1}{4}\left\{\alpha_1^2 P_S + \beta_1^2 P_{LO} + 2\alpha_1\beta_1\sqrt{P_S P_{LO}}\sin\left[2\pi f_{IF}t + \Delta\phi_n + \phi_k + \zeta_1 - \xi_1\right]\right\}$$

$$i_2 = \frac{R_2}{4}\left\{\alpha_2^2 P_S + \beta_2^2 P_{LO} - 2\alpha_2\beta_2\sqrt{P_S P_{LO}}\sin\left[2\pi f_{IF}t + \Delta\phi_n + \phi_k + \zeta_2 - \xi_2\right]\right\}$$

(225)

For ideal hybrid operation

$$(\zeta_2 - \xi_2) - (\zeta_1 - \xi_1) = (2k+1)\frac{\pi}{2}$$

(226)

The simplest arrangement of input polarizations to achieve orthogonality between the two photocurrents is to have 45° linear and right-hand circular polarization, for the received and LO signals, respectively

$$\left|e_S'\right\rangle = \frac{\left|x\right\rangle + \left|y\right\rangle}{\sqrt{2}}$$

$$\left|e_{LO}'\right\rangle = \frac{\left|x\right\rangle + j\left|y\right\rangle}{\sqrt{2}}$$

(227)

Then, we can write

$$\hat{\mathbf{E}}_5(t) = \frac{1}{\sqrt{2}}\left[\hat{\mathbf{E}}_3(t) + j\hat{\mathbf{E}}_4(t)\right] = \frac{1}{2}\left\{\left[\hat{E}_S(t) + j\hat{E}_{LO}(t)\right]\left|x\right\rangle + \left[\hat{E}_S(t) - \hat{E}_{LO}(t)\right]\left|y\right\rangle\right\}$$

$$\hat{\mathbf{E}}_6(t) = \frac{1}{\sqrt{2}}\left[j\hat{\mathbf{E}}_3(t) + \hat{\mathbf{E}}_4(t)\right] = \frac{1}{2}\left\{\left[j\hat{E}_S(t) + \hat{E}_{LO}(t)\right]\left|x\right\rangle + j\left[\hat{E}_S(t) + \hat{E}_{LO}(t)\right]\left|y\right\rangle\right\}$$

(228)

After the polarization independent ideal directional coupler

$$\hat{\mathbf{E}}_5(t) = \frac{1}{\sqrt{2}}\left[\hat{\mathbf{E}}_3(t) + j\hat{\mathbf{E}}_4(t)\right] = \frac{1}{2}\left\{\left[\hat{E}_S(t) + j\hat{E}_{LO}(t)\right]|x\rangle + \left[\hat{E}_S(t) - \hat{E}_{LO}(t)\right]|y\rangle\right\}$$

$$\hat{\mathbf{E}}_6(t) = \frac{1}{\sqrt{2}}\left[j\hat{\mathbf{E}}_3(t) + \hat{\mathbf{E}}_4(t)\right] = \frac{1}{2}\left\{\left[j\hat{E}_S(t) + \hat{E}_{LO}(t)\right]|x\rangle + j\left[\hat{E}_S(t) + \hat{E}_{LO}(t)\right]|y\rangle\right\}$$

(229)

Assuming the fiber polarizers have principle axes along polarization directions $|p_1\rangle = |x\rangle$ and $|p_2\rangle = |y\rangle$, the electrical field vectors at the output of the hybrid are

$$\hat{\mathbf{E}}_7(t) = \frac{1}{2}\left[\hat{E}_S(t) + j\hat{E}_{LO}(t)\right]|x\rangle$$

$$\hat{\mathbf{E}}_8(t) = \frac{j}{2}\left[\hat{E}_S(t) + \hat{E}_{LO}(t)\right]|y\rangle$$

(230)

and the resulting photocurrents are

$$i_1 = \frac{R_1}{4}\left\{P_S + P_{LO} + 2\sqrt{P_S P_{LO}}\,\sin\left[2\pi f_{IF}t + \Delta\phi_n + \phi_k\right]\right\}$$

$$i_2 = \frac{R_2}{4}\left\{P_S + P_{LO} + 2\sqrt{P_S P_{LO}}\,\cos\left[2\pi f_{IF}t + \Delta\phi_n + \phi_k\right]\right\}$$

(231)

It is clear that $i_1 = i_Q$ and $i_2 = i_I$. It is also clear that single-ended detection produces DC terms, depending on both the received signal and the LO signal power.

Appendix G   M-th power law removal of information symbols

Though this process is generic to all *M*-ary PSK formats, the case of QPSK is explicitly analyzed. The complex photocurrent at the output of each phase-diversity receiver in a SP-QPSK system, is

$$\tilde{i}[n] = \exp\left(j\phi_k[n]\right)\exp\left\{j\left(2\pi f_{IF} nT_S + \Delta\phi_n[n]\right)\right\} + p[n] \tag{232}$$

where ϕ_k, for QPSK, belongs to an alphabet $\phi_k = \{\pi/4, 3\pi/4, 5\pi/4, 7\pi/4\}$, and we have dropped amplitude *I* for simplicity. Raising (232) to the 4th-power, produces

$$\tilde{i}^4[n] = \exp\left(j4\phi_k[n]\right)\exp\left\{j4\left(2\pi f_{IF} nT_S + \Delta\phi_n[n]\right)\right\} + q[n] \tag{233}$$

where *q*[*n*] is a sum of unwanted cross terms between the signal and the additive noise process. The quantity $4\phi_k$ belongs to an alphabet $4\phi_k = \{4\pi/4, 12\pi/4, 20\pi/4, 28\pi/4\} = \{\pi, 3\pi, 5\pi, 9\pi\}$ and in all cases produces $\exp\left(j4\phi_k\right) = -1$, thus removing phase modulation. Quantity *q*[*n*] is given by

$$q[n] = 4\exp\left(j3\phi_k[n]\right)\exp\left\{j3\left(2\pi f_{IF} nT_S + \Delta\phi_n[n]\right)\right\} p[n] + O\left[p^2[n]\right] \tag{234}$$

The quantity $3\phi_k$ belongs to an alphabet $3\phi_k = \{3\pi/4, 9\pi/4, 15\pi/4, 21\pi/4\} = \{3\pi/4, \pi/4, 3\pi/4, 5\pi/4\}$ thus producing the complex conjugate of the transmitted modulation symbol. Though *q*[*n*] is essentially a random process, it is no longer Gaussian. It can be approximated as a Gaussian noise process with variance σ_q^2, given as [140]

$$\sigma_q^2 = 16\sigma_p^2 144 + \sigma_p^4 + 384\sigma_p^6 + 192\sigma_p^8 \tag{235}$$

It is clear that, in the absence of IF offset, an estimate of $\Delta\phi_n[n]$ can be obtained from the argument of $\tilde{i}^4[n]$ simply by using

$$\Delta\hat{\phi}_n[n] = \frac{1}{4} arg\left\{\tilde{i}^4[n]\right\} = \Delta\phi_n[n] + m[n] \tag{236}$$

where 4*m*[*n*] is the angular projection of *p*[*n*] corrupting the estimate of $\Delta\phi_n[n]$ [157]. Assuming that the additive noise *q*[*n*] is small, a small angle approximation can be adopted, in which

$$4\Delta\hat{\phi}_n[n] = arg\left\{\tilde{i}^4[n]\right\} = 4\Delta\phi_n[n] + q_1[n] \tag{237}$$

where q_1[*n*] is a real Gaussian noise sequence with variance σ_q^2.

Appendix H Phase unwrapping

The phase noise estimates for the received complex samples are be given by (236), which we show again at this point for easiness of reference

$$\Delta \hat{\phi}_n [n] = \frac{1}{4} arg \left\{ \tilde{i}^4 [n] \right\} = \Delta \phi_n [n] + m[n] \tag{238}$$

The arg{} function however cannot distinguish between phases that differ by 2π, and produces results within the $(-\pi,\pi]$ interval, i. e., the resulting phase estimate $\Delta \hat{\phi}_n [n]$ lies in the interval $(-\pi/4,\pi/4]$ and it is a *wrapped* phase [171]. To reinstate linearity over time, special techniques have to be used to *unwrap* the phases [157], [140], [171].

The unwrapping process used in the context of this thesis, is based on the idea of adding (or subtracting) an integer multiple of $\pi/2$ to (from) $\Delta \hat{\phi}_n [n]$, depending on the values of the previous estimates, in order to ensure that the magnitude of the phase difference between adjacent symbols is always less than $\pi/4$. Two approaches were followed in the context of this thesis. The rudimentary approach uses the difference between the previous unwrapped estimate and the current wrapped estimate for estimating whether a jump occurs. It is best formulated as [157],

$$\Delta \hat{\phi}_n^{unwrap} [n] = \Delta \hat{\phi}_n [n] + \frac{\pi}{2} p \tag{239}$$

where

$$p = \left\lfloor 0.5 + \frac{\pi}{2} \left(\Delta \hat{\phi}_n^{unwrap} [n-1] - \Delta \hat{\phi}_n [n] \right) \right\rfloor \tag{240}$$

and $\lfloor \quad \rfloor$ denotes the floor function.

At low SNR or large phase noise, the fluctuations due to noise are large, and the rudimentary unwrapping technique may produce erroneous phase jumps, or else, cycle slips. Phase jumps occur when the real phase makes a jump larger than $\pi/4$ in its trajectory. The wrap property of the 0.25arg{} function will produce a wrapped phase value which will "confuse" the unwrap process. A wrong value of p will be computed, and a phase jump will occur. Phase jumps are initially $\pi/4$ but eventually the unwrapped phases will settle at a $\pi/2$ mean phase difference compared to before the jump. Phase jumps are thus undetectable in QPSK and produce symbol errors, because constellation points differing by $\pi/2$ are stable operating points.

A more sophisticated method for unwrapping should be used in such cases. The problem of phase jumps can be avoided if several previous phases are used to compute p and for this purpose, a second, enhanced method of phase unwrapping was used. This method uses three previous phases, equally weighted, to compute p. The formula used for updating (240) is hereby

$$p = \left\lfloor 0.5 + \frac{2}{\pi} \left[\left(\frac{\Delta \hat{\phi}_n^{unwrap} [n-1] + \Delta \hat{\phi}_n^{unwrap} [n-2] + \Delta \hat{\phi}_n^{unwrap} [n-3]}{3} \right) - \Delta \hat{\phi}_n [n] \right] \right\rfloor \tag{241}$$

This method can easily be extended to accommodate even more previous estimates.

To illustrate the issue of phase jumps, an unwrapped phase produced by (239) is depicted in Fig. 105, for the two cases of unwrapping described previously. Phase jumps occur when using the rudimentary unwrap procedure, but are avoided when using the sophisticated method
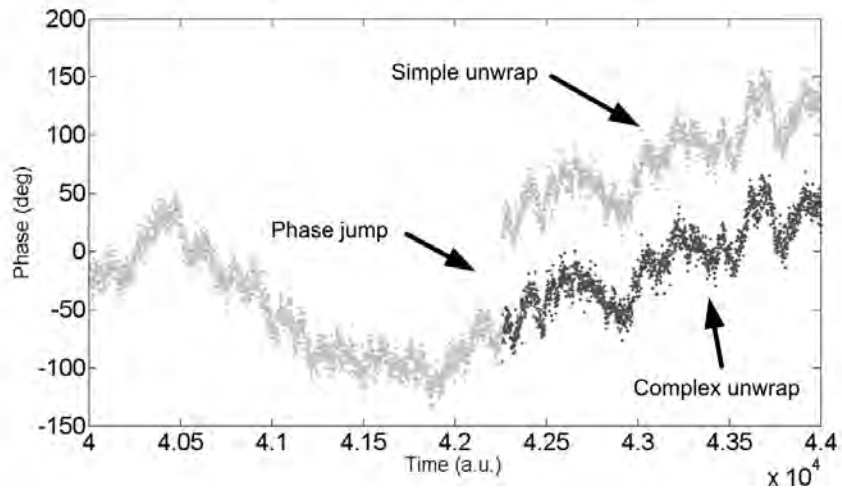
Fig. 105 Unwrapped phase using the rudimentary and sophisticated unwrapping procedure. A phase jump is avoided using the latter.

Appendix I   Spectrum distortion due to quadrature imbalance and non-zero IF offset

In this section we provide mathematical proof of the distortion on the received signal spectrum caused by quadrature imbalance and non-zero IF offsets. We calculate the spectrum of the mirror image of the unilateral spectrum, which would ideally experience infinite attenuation and give an expression for the total spectrum.

Neglecting DC offsets, phase noise, and modulation, the outputs of the phase diversity receiver (157), are written as

$$i_I(t) = A(1+\varepsilon)g(t)\cos(2\pi f_{IF} t + \theta)$$
$$i_Q(t) = A(1-\varepsilon)g(t)\sin(2\pi f_{IF} t - \theta)$$

$$(242)$$

where A is the received pulse amplitude, $g(t)$ is the received pulse shape, ε is a small distortion of the amplitude, θ is a small distortion of the phase, and $\varphi(t)$ is the common phase term containing the modulation phase, the IF offset, and the phase noise. The complex received signal is

$$\tilde{i}(t) = i_I(t) + j i_Q(t)$$

$$(243)$$

Using Euler's formulae for representing the cosine and sine function

$$\cos(x) = \frac{1}{2}\left(e^{jx} + e^{-jx}\right)$$

$$\sin(x) = \frac{1}{2j}\left(e^{jx} - e^{-jx}\right)$$

$$(244)$$

the complex signal in (243) is written as

$$\tilde{i}(t) = Ag(t)(\cos\theta + j\varepsilon\sin\theta)e^{j2\pi f_{IF} t} + Ag(t)(\cos\theta - j\varepsilon\sin\theta)e^{-j2\pi f_{IF} t} =$$
$$= r_1 Ag(t)e^{j2\pi f_{IF} t + j\varphi_1} + r_2 Ag(t)e^{-j2\pi f_{IF} t - j\varphi_2}$$

$$(245)$$

where we have defined

$$r_1 = \sqrt{\cos^2\theta + \varepsilon^2\sin^2\theta}$$
$$r_2 = \sqrt{\varepsilon^2\cos^2\theta + \sin^2\theta}$$
$$\varphi_1 = \tan^{-1}\left(\varepsilon\tan\theta\right)$$
$$\varphi_2 = \tan^{-1}\left(\frac{\tan\theta}{\varepsilon}\right)$$

$$(246)$$

The signal spectrum of (245) is [2],

$$\tilde{I}(f) = r_1 e^{j\varphi_1} AG(f - f_{IF}) + r_2 e^{-j\varphi_2} AG(f + f_{IF})$$

$$(247)$$

Given that $g(t)$ is a real valued signal, it holds that $G^*(-f)=G(f)$, and (247) can be re-written as

$$\tilde{I}(f) = r_1\left\{e^{j\varphi_1} G(f - f_{IF}) + r_2 e^{-j\varphi_2} G^*(-f - f_{IF})\right\}$$

$$(248)$$

Assuming $\varepsilon \to 0$, and $\theta \to 0$, it follows that $r_1 \to 1$ and $r_2 \to 0$ and the spectrum of the mirror image of the unilateral spectrum approaches zero.

Appendix J Effect of quadrature imbalance on the received complex sample sequence

The general expressions of photocurrents at the output of the phase diversity receiver (157) can be formulated into a complex signal, as

$$\tilde{i}(t) = i_I(t) + ji_Q(t) = (I_I + jI_Q) + I_{ip}\left\{\cos\left[\varphi(t) + \varepsilon\right] + j\sin\left[\varphi(t) - \delta\right]\right\} \tag{249}$$

Using (244), we can re-write (249) as

$$\tilde{i}(t) = (I_I + jI_Q) + I_{ip}\frac{1}{2}\left[e^{j\varphi(t)}e^{j\varepsilon} + e^{-j\varphi(t)}e^{-j\varepsilon} + \frac{I_{qp}}{I_{ip}}e^{j\varphi(t)}e^{-j\delta} - \frac{I_{qp}}{I_{ip}}e^{-j\varphi(t)}e^{j\delta}\right] \tag{250}$$

and after proper factorization

$$\tilde{i}(t) = (I_I + jI_Q) + I_{ip}\left\{\frac{1}{2}e^{j\varepsilon}\left[1 + \frac{I_{qp}}{I_{ip}}e^{-j(\varepsilon+\delta)}\right]e^{j\varphi(t)} + \frac{1}{2}e^{-j\varepsilon}\left[1 - \frac{I_{qp}}{I_{ip}}e^{j(\varepsilon+\delta)}\right]e^{-j\varphi(t)}\right\} =$$

$$= (I_I + jI_Q) + I_{ip}\left[K_1 e^{j\varphi(t)} + K_2 e^{-j\varphi(t)}\right] \tag{251}$$

179

Appendix K   Estimation of ellipse parameters by least squares fitting

In this section we derive estimates of the phase and amplitude mismatch of the received photocurrents, caused by non-ideal 90° optical hybrids. The discrete counterparts of (160), repeated here for convenience, are written as

$$i_I[n] = I_I + I_{ip} \cos\left(\psi[n]\right)$$
$$i_Q[n] = I_Q + I_{qp} \sin\left(\psi[n] - \theta\right)$$

(252)

These equations generate an ellipse when plotted on a x-y diagram.

An ellipse is described by a quadratic curve [188], [189], as

$$F(x,y) = ax^2 + bxy + cy^2 + dx + ey + f = 0$$

(253)

under the constraint b^2-$4ac$<1, and we define the ellipse parameter vector **a**, as **a**=$[a, b, c, d, e, f]^T$. Since m **a** represents the same quadratic curve as **a** does ($m \neq 0$), and assuming appropriate scaling, the constraint can be changed into an equality $4ac$-b^2=1. Under this assumption, the ellipse-fitting problem can be approached as a least-squares minimization problem of a predefined cost function, corresponding to the total distance between the data points and the ellipse quadratic curve [190], [191]. The minimization procedure is formulated as $\min_{\mathbf{a}} \|\mathbf{Da}\|^2$ subject to the constraint $\mathbf{a}^T\mathbf{Ca}$=1, where **D** is the design matrix constructed from a large number of N sample pairs, given by $\left(i_I[n], i_Q[n]\right)$, as

$$\mathbf{D} = \begin{pmatrix} i_I^2[1] & i_I[1]i_Q[1] & i_Q^2[1] & i_I[1] & i_Q[1] & 1 \\ i_I^2[2] & i_I[2]i_Q[2] & i_Q^2[2] & i_I[2] & i_Q[2] & 1 \\ \vdots & \vdots & \vdots & \vdots & \vdots & \vdots \\ i_I^2[N] & i_I[N]i_Q[N] & i_Q^2[N] & i_I[N] & i_Q[N] & 1 \end{pmatrix}$$

(254)

and **C** is the constraint matrix, given by

$$\mathbf{C} = \begin{pmatrix} 0 & 0 & 2 & 0 & 0 & 0 \\ 0 & -1 & 0 & 0 & 0 & 0 \\ 2 & 0 & 0 & 0 & 0 & 0 \\ 0 & 0 & 0 & 0 & 0 & 0 \\ 0 & 0 & 0 & 0 & 0 & 0 \\ 0 & 0 & 0 & 0 & 0 & 0 \end{pmatrix}$$

(255)

The estimation procedure can be applied to a limited number of symbols instead of the whole data sequence, since quadrature imbalance varies slowly with time.

Having obtained parameter vector **a**, a modified parameter vector **A** is computed, defined as

$$\mathbf{A} = [A, B, C, D, E, F] = \left[a, \frac{b}{2}, c, \frac{d}{2}, \frac{e}{2}, f\right]^T$$

(256)

corresponding to the quadratic curve

$$F(x,y) = Ax^2 + 2Bxy + Cy^2 + 2Dx + 2Ey + F = 0$$

(257)

Fig. 106 shows the ellipse quantities to be found, namely, the ellipse center (x_0, y_0), the ellipse maximal points (x_{max}, y_{max}), and the ellipse rotation angle ξ.

The ellipse center (x_0, y_0) is found as [189]

$$x_0 = \frac{CD - BE}{B^2 - AC}$$
$$y_0 = \frac{AE - BD}{B^2 - AC}$$

(258)

From the ellipse center, an estimate of the DC offset can be obtained as

$$\hat{I}_I = x_0$$
$$\hat{I}_Q = y_0$$

(259)

The ellipse maximal points (x_{max}, y_{max}) on the (x, y)−plane, are found by solving $F(x, y) = 0$ for two cases. x_{max} is the solution of $F(x, y_d) = 0$ where y_d is solution of $\dfrac{\partial F(x, y)}{\partial y} = 0$. Similarly, y_{max} is the solution of $F(x_d, y) = 0$ where x_d is solution of $\dfrac{\partial F(x, y)}{\partial x} = 0$. The two solutions per independent variable are

$$x_{max} = \frac{-CD + BF \pm \sqrt{C^2 D^2 - 2BCDE + B^2 CF - AC^2 F}}{-B^2 + AC}$$
$$y_{max} = \frac{BD - AE \pm \sqrt{ACD^2 - ABDE + A^2 E^2 + AB^2 F - A^2 CF}}{-B^2 + AC}$$

(260)

We keep the solution giving the largest numerical value.

From the ellipse center and maximal points, an estimate of the amplitude mismatch can be obtained as

$$\hat{\lambda} = (x_{max} - x_0) / (y_{max} - y_0)$$

(261)

The ellipse rotation angle a, is found as

$$\xi = \begin{cases} 0.5 \cot^{-1}\left(\dfrac{C - A}{2B}\right) & \text{for } b \neq 0 \text{ and } a < c \\[2mm] \dfrac{\pi}{2} + 0.5 \cot^{-1}\left(\dfrac{C - A}{2B}\right) & \text{for } b \neq 0 \text{ and } a > c \end{cases}$$

(262)

From the ellipse rotation angle, an estimate of the phase mismatch can be obtained as [187]

$$\hat{\theta} = \frac{\pi}{2} - \cos^{-1}\left\{ \tan(2\xi) \frac{(x_{max} - x_0)^2 - (y_{max} - y_0)^2}{2(x_{max} - x_0)(y_{max} - y_0)} \right\}$$

(263)
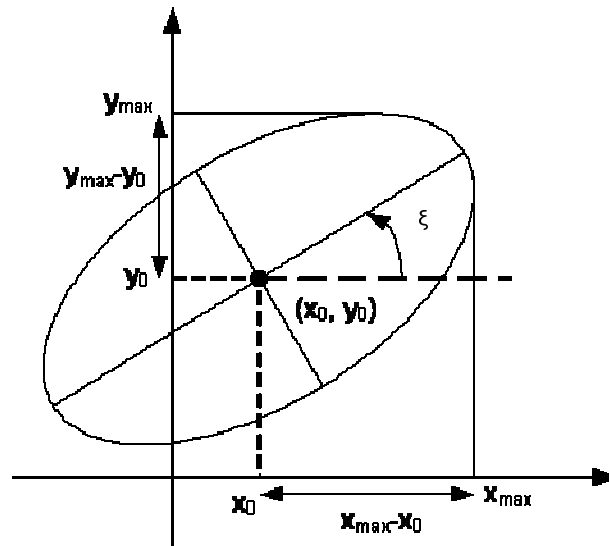
Fig. 106 Ellipse schematic defining all the quantities needed for estimating amplitude and phase mismatch.

Appendix L   Quadrature imbalance orthogonalization

In this section, we prove the orthogonalization procedure described in [192]. We adopt the formalism used in [115] for representing complex signals. Assume the outputs of the phase diversity receiver, (157), are written as

$$i_I(t) = A(1+\varepsilon)g(t)\cos(2\pi f_{IF}t)$$
$$i_Q(t) = Ag(t)\sin(2\pi f_{IF}t + \varphi) \tag{264}$$

The analytic signal representation of these signals is

$$\hat{i}_I(t) = A(1+\varepsilon)g(t)e^{j2\pi f_{IF}t}$$
$$\hat{i}_Q(t) = Ag(t)e^{j(2\pi f_{IF}t + \varphi - \pi/2)} \tag{265}$$

The vector representation of these signals, is

$$|i_I\rangle = A(1+\varepsilon)g(t)\left[\cos(2\pi f_{IF}t)\quad \sin(2\pi f_{IF}t)\right]^T$$
$$|i_Q\rangle = Ag(t)\left[\sin(2\pi f_{IF}t + \varphi)\quad -\cos(2\pi f_{IF}t + \varphi)\right]^T \tag{266}$$

These signals are depicted on the complex plane $x_1 - x_2$ in Fig. 107. We define a new complex plane, denoted as $x_1' - x_2'$, rotated with respect to the original plane $x_1 - x_2$ by $2\pi f_{IF}t$, such that signal $|i_I\rangle$ coincides with axis x_1'. The unit vectors of this plane are denoted as

$$|u_1\rangle = \left[\cos 2\pi f_{IF}t \quad \sin 2\pi f_{IF}t\right]^T$$
$$|u_2\rangle = \left[-\sin 2\pi f_{IF}t \quad \cos 2\pi f_{IF}t\right]^T \tag{267}$$

We can thus write

$$|i_I\rangle = A(1+\varepsilon)g(t)|u_1\rangle$$
$$|i_Q\rangle = Ag(t)\left(\sin\varphi|u_1\rangle - \cos\varphi|u_2\rangle\right) \tag{268}$$

The projection of $|i_Q\rangle$ on $|u_2\rangle$ is

$$\left|i_Q'\right\rangle = -A\cos\varphi|u_2\rangle = |i_Q\rangle - \sin\varphi|u_1\rangle = |i_Q\rangle - \frac{\sin\varphi}{1+\varepsilon}|i_I\rangle \tag{269}$$

We choose a new vector $\left|i_I'\right\rangle$, collinear with $|i_I\rangle$, having the same magnitude as $\left|i_Q'\right\rangle$

$$\left|i_I'\right\rangle = \frac{\cos\varphi}{1+\varepsilon}|u_1\rangle \tag{270}$$

We can thus transform signals $|i_I\rangle$ and $|i_Q\rangle$, into two new orthogonal signals $\left|i_I'\right\rangle$ and $\left|i_Q'\right\rangle$, using a transformation matrix, as

$$\begin{pmatrix} |i'_I\rangle \\ |i'_Q\rangle \end{pmatrix} = \begin{pmatrix} \dfrac{\cos\varphi}{1+\varepsilon} & 0 \\ -\dfrac{\sin\varphi}{1+\varepsilon} & 1 \end{pmatrix} \begin{pmatrix} |i_I\rangle \\ |i_Q\rangle \end{pmatrix}$$

(271)
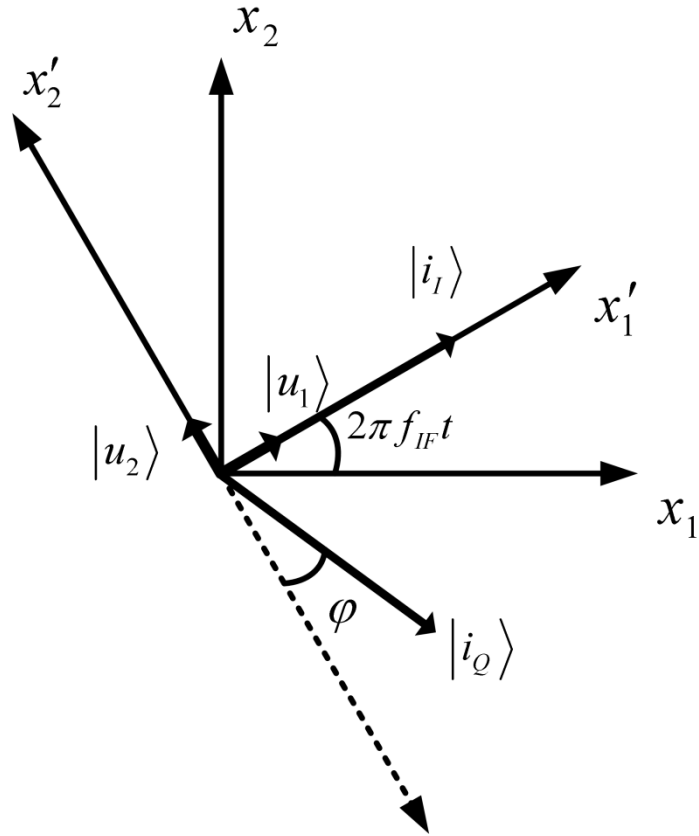
Fig. 107 Vector representation of the complex outputs of the phase diversity receiver on the complex plane.

Appendix M   Measurement of the optical signal-to-noise ratio

In the context of this dissertation, the only source of noise considered is ASE noise generated by an EDFA model [113]. The block diagram of section of the simulation block diagram (see Fig. 15) controlling the OSNR is shown Fig. 108. An ideal attenuator attenuates the incoming optical signal by A dB. It is followed by an EDFA that has a constant gain of A dB, equal to the attenuation of the attenuator. Therefore the signal power does not change but the signal is contaminated by ASE noise.
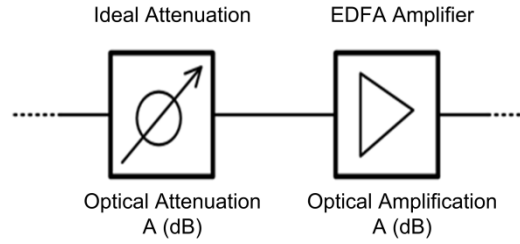
Fig. 108 The block diagram of section of the simulation block diagram controlling the OSNR.

The OSNR is measured in a bandwidth of 12.5 GHz for 10 GBd signals [78]–[80], using the block diagram shown in Fig. 109. The optical signal is centered around f_c = 193.1 THz. We assume that all signal power is concentrated in a 3-dB bandwidth equal to 5 R_S around the carrier. Assuming that the signal psd is negligible at frequencies larger than 2.5 R_S away from the carrier, we center an optical band-pass filter with a 50 GHz 3-dB bandwidth and infinite attenuation around f_c. The optical power at the output of this filter (P_1) contains the power of both the signal and the noise in the specified bandwidth. An identical optical band-pass filter with infinite attenuation and a 50 GHz 3-dB bandwidth is centered around an offset frequency Δf > 5 R_S. The optical power at the output of this filter (P_2) contains the power of the noise in the specified bandwidth. The signal power is then calculated as P_S=P_1-P_2. Subsequently, an identical optical band-pass filter with a 12.5 GHz 3-dB bandwidth and infinite is centered around an offset frequency Δf > 5 R_S. The optical power at the output of this filter (P_3) contains the power of the noise in the specified bandwidth (P_N=P_3). The OSNR is simply calculated as OSNR= P_S/P_N. Fig. 110 shows the output of an optical spectrum analyzer and depicts the offsets and 3-dB bandwidths described previously.
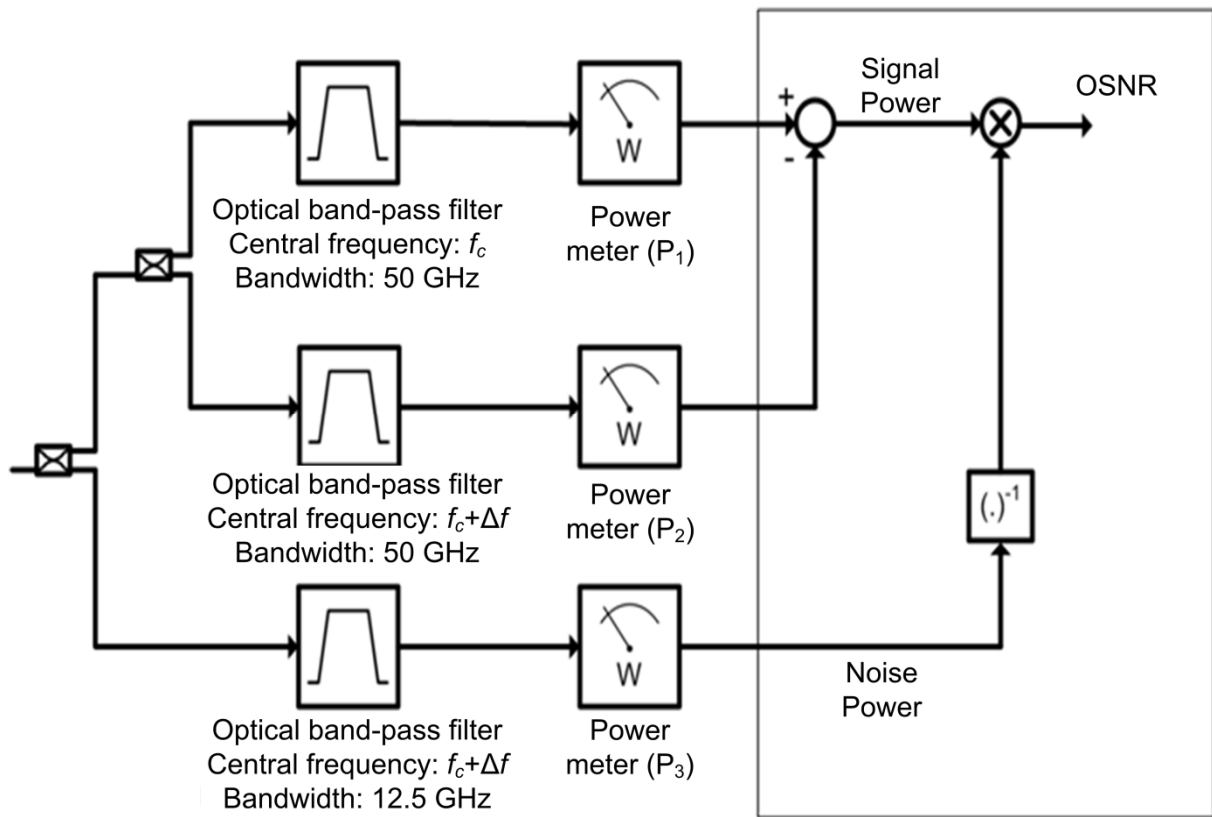
Fig. 109 Block diagram of the OSNR measurement module. OSNR is measured in a 12.5 GHz bandwidth.
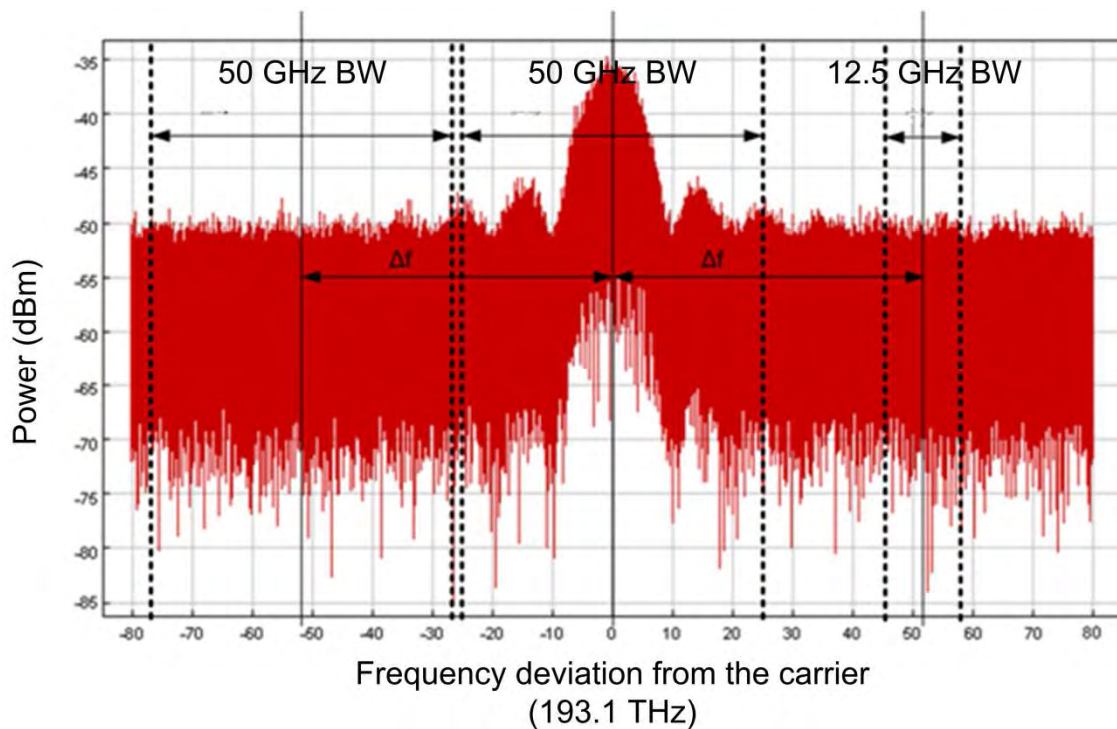
Fig. 110 Optical spectrum analyzer output for a 10 GBd PDM-QPSK signal contaminated with ASE noise. All bandwidths used for the measurement of the OSNR are depicted.

References

[1] P. J. Winzer and R.-J. Essiambre, "Advanced optical modulation formats," *in Proc. IEEE*, vol. 94, no. 5, pp. 952–985, May. 2006.

[2] J. Proakis, *Digital communications.* 4th Ed. New York: McGraw-Hill, 2000, ch. 4.

[3] Y. Okunev, *Phase and phase-difference modulation in digital communications.* Boston: Artech House, 1997.

[4] M. C. Jeruchim, P. Balaban, and K. S. Shanmugan, *Simulation of communication systems.* New York: Plenum Press, 1992.

[5] F. J. MacWilliams and N.J.A. Sloan, "Pseudo-random sequences and arrays," *in Proc. IEEE*, vol. 64, no.12, pp. 1715–1729, Dec. 1976.

[6] D. van den Borne, E. Gottwald, G.D. Khoe, and H. de Waardt, "Bit pattern dependence in optical DQPSK modulation," *Electron. Lett.*, vol. 43, no. 22, pp. 1223–1225, Oct. 2007.

[7] J. M. Kahn and K.-P. Ho, "Spectral efficiency limits and modulation/detection techniques for DWDM systems," *IEEE J. Sel. Top. Quantum Electron.*, vol. 10, no. 2, pp. 259–272, March/April 2004.

[8] J. Renaudier, G. Charlet, M. Salsi, O. B. Padro, H. Mardoyan, P. Tran, and S. Bigo, "Linear fiber impairments mitigation of 40-Gbit/s Polarization-Multiplexed QPSK by digital processing in a coherent receiver," *IEEE J. Lightw. Technol.*, vol. 26, no. 1, pp. 36–42, Jan. 2008.

[9] L. Kazovsky, G. Kalogerakis, and W.-T. Shaw, "Homodyne phase-shift-keying systems: Past challenges and future opportunities," *IEEE J. Lightw. Technol.*, vol. 24, no. 12, pp. 4876–4884, Dec. 2006.

[10] F. Derr, "Coherent optical QPSK intradyne system: Concept and digital receiver realization," *IEEE J. Lightw. Technol.*, vol. 10, no. 9, pp. 1290–1296, Sep. 1992.

[11] H. Sun, K.-T. Wu, and K. Roberts, "Real-time measurements of a 40 Gb/s coherent system," *Optics Express*, vol. 16, no. 2, pp. 873–879, Jan. 2008.

[12] R. Linke and A. Gnauk, "High-capacity coherent lightwave systems," *IEEE J. Lightw. Technol.*, vol. 6, no. 11, pp. 1750–1769, Nov. 1988.

[13] D. Smith, "Techniques for multigigabit coherent optical transmission," *IEEE J. Lightw. Technol.*, vol. LT-5, no. 10, pp. 1466–1478, Oct. 1987.

[14] L. Kazovsky, "Multichannel coherent optical communications systems," *IEEE J. Lightw. Technol.*, vol. LT-5, no. 8, pp. 1095–1102, Aug. 1987.

[15] T. Kimura, "Coherent optical fiber transmission," *IEEE J. Lightw. Technol.*, vol. LT-5, no. 4, pp. 414–428, Apr. 1987.

[16] T. Okoshi, "Recent advances in coherent optical fiber communication systems," *IEEE J. Lightw. Technol.*, vol. 5, no. 1, pp. 44–52, Jan. 1987.

[17] T. Okoshi and K. Kikuchi, *Coherent optical fiber communications.* Boston: Kluwer Academic, 1988.

[18] P. Henry and S. Personick, *Coherent lightwave communications.* New Jersey: IEEE Press, 1990.

[19]   S. Betti, G. de Marchis, and E. Iannone, *Coherent optical communications systems.* New York: Wiley, 1995.

[20]   S. Ryu, *Coherent lightwave communications systems*. Boston: Artec House, 1995.

[21]   I. Garrett and G. Jacobsen, "The effect of laser linewidth on coherent optical receivers with nonsynchronous modulation," *IEEE J. Lightw. Technol*., vol. LT-5, no. 4, pp. 551–560, Apr. 1987.

[22]   L. Kazovsky, "Performance analysis and laser linewidth requirements for optical PSK heterodyne communications systems," *IEEE J. Lightw. Technol*., vol. LT-4, no. 4, pp. 415–425, Apr. 1986.

[23]   T. Okoshi, "Polarization-state control schemes for heterodyne and homodyne optical fiber communications," *IEEE J. Lightw. Technol*., vol. LT-3, no. 6, pp. 1232–1237, Dec. 1985.

[24]   B. Glance, "Polarization independent coherent optical receiver," *IEEE J. Lightw. Technol*., vol. LT-5, no. 2, pp. 274–276, Feb. 1987.

[25]   L. Kazovsky, "Phase- and polarization-diversity coherent optical techniques," *IEEE J. Lightw. Technol*., vol. 7, no. 2, pp. 279–292, Feb. 1989.

[26]   L. Kazovsky, R Welter, A. Elrefaie, and W. Sessa, "Wide-linewidth phase diversity homodyne receivers," *IEEE J. Lightw. Technol*., vol. 6, no. 10, pp. 1527–1536, Oct. 1988.

[27]   A. Davis, M. Pettitt, J. King, and S. Wright, "Phase diversity techniques for coherent optical receivers," *IEEE J. Lightw. Technol*., vol. LT-5, no. 4, pp. 561–571, Apr. 1987.

[28]   T. Okoshi and Y. -H. Cheng, "Four-port homodyne receiver for optical fibre communications comprising phase and polarisation diversities," *Electron. Lett.*, vol. 23, no. 8, pp. 377–378, Apr. 1987.

[29]   Y. -H. Cheng, T. Okoshi, and O. Ishida, "Performance analysis and experiment of a homodyne receiver insensitive to both polarization and phase fluctuations," *IEEE J. Lightw. Technol*., vol. 7, no. 2, pp. 368–374, Feb. 1989.

[30]   R. Langenhorst, W. Pieper, H.G. Weber, H. Knupke, M. Flüge, and G. Wenke, "Balanced phase diversity receiver in 565 Mbit/s DPSK transmission system," *Electron. Lett.*, vol. 25, no. 19, pp. 1286–1288, Sept. 1989.

[31]   R.T.B. James, K. Iizuka, and Y. Imai, "Phase noise cancelled polarisation diversity scheme for DPSK optical communication," *Electron. Lett.*, vol. 25, no. 20, pp. 1394–1396, Sept. 1989.

[32]   S. Yamazaki and K. Emura, "Feasibility study on QPSK optical-heterodyne system," *IEEE J. Lightw. Technol*., vol. 8, no. 11, pp. 1646–1653, Nov. 1990.

[33]   J. R. Barry and J. M. Kahn, "Carrier synchronization for homodyne and heterodyne detection of optical quadriphase-shift keying," *IEEE J. Lightw. Technol*., vol. 10, no. 12, pp. 1939–1951, Dec. 1992.

[34]   R. Noé, E. Meissner, B. Borchert, and H. Rodler, "Direct modulation 565 Mbps PSK experiment with solitary SL-QW-DFB lasers and novel suppression of the phase transition periods in the carrier recovery," *Eur. Conf. Optical Communication (ECOC)*, post deadline paper ThPD I.5, 1992.

[35]   K. Iwashita and N. Takachio, "Chromatic dispersion compensation in coherent optical communications," *IEEE J. Lightw. Technol*., vol. 8, no. 3, pp. 367–375, Mar. 1990

[36]   J. H. Winters, "Equalization in coherent lightwave systems using a fractionally spaced equalizer," *IEEE J. Lightw. Technol.*, vol. 8, no. 10, pp. 1487–1491, Oct. 1990.

[37]   S. L. Woodward, S. -Y. Huang, M. D. Feuer, and M. Boroditsky, "Demonstration of an electronic dispersion compensator in a 100 km 10 Gbps ring network," *IEEE Photon. Technol. Lett.*, vol. 15, no. 6, pp. 867–869, Jun 2003.

[38]   C. R. S. Fludger, J. E. A. Whiteaway, and P.J. Anslow, "Electronic equalization for low-cost 10 Gbps directly modulated systems," *Optical Fiber Communication Conference (OFC)*, paper WM7, Los Angeles, CA, Feb. 2004.

[39]   A, Färbert, S. Lagenbach, N. Stojanovic, C. Dorschky, T. Kupfer, C. Schulien, J. -P. Elbers, H.Wernz, H. Griesser, and C. Glingener, "Performance of a 10.7 Gbps receiver with a digital equalizer using Maximum Likelihood Sequence Estimation," *Eur. Conf. Optical Communication (ECOC)*, paper Th4.1.5, Stockholm, Sweeden, Sept. 2004.

[40]   J. Sitch, "Implementation aspects of high-speed DSP for transmitter and receiver signal processing," *Conference on Lasers and Electro Optics Systems (LEOS) summer topical*, paper MA.4.3, 2007.

[41]   K. Roberts, "Electronic dispersion compensation beyond 10 Gbps," *Conference on Lasers and Electro Optics Systems (LEOS) summer topical*, paper MA.2.3, 2007.

[42]   S. J. Savory, "Digital signal processing options in long haul transmission," *Optical Fiber Communication Conference (OFC)*, paper OTuO3, San Diego, CA, Feb. 2008.

[43]   K. Roberts and I. Roberts, "DSP: A disruptive technology for optical transceivers," *Eur. Conf. Optical Communication (ECOC)*, paper 4.4.2, Vienna, Austria, Sept. 2009.

[44]   M. G. Taylor, "Coherent detection method using DSP to demodulate signal and subsequent equalization of propagation impairments," *Eur. Conf. Optical Communication (ECOC)*, paper We4.P.111, Rimini, Italy, Sept. 2003.

[45]   M. G. Taylor, "Coherent detection method using DSP for demodulation of signal and subsequent equalization of propagation impairments," *IEEE Photon. Technol. Lett.*, vol. 16, no. 2, pp. 674–677, Feb. 2004.

[46]   M. G. Taylor, "Measurement of phase diagrams of optical communication signals using sampled coherent detection," *NIST Tech. Dig.: Symp. Optical Fiber Measurement*, Boulder, CO, vol. 1024, pp. 163–166, Sept. 2004.

[47]   D.-S. Ly-Gagnon, K. Katoh, and K. Kikuchi, "Unrepeated optical transmission of 20 Gbps quadrature phase-shift keying signals over 210 km using homodyne phase-diversity and digital signal processing," *Electron. Lett.*, vol. 41, no. 4, pp. 206–207, Feb. 2005.

[48]   D.-S. Ly-Gagnon, K. Katoh, and K. Kikuchi, "Unrepeated 210-km transmission with coherent detection and digital signal processing," *Optical Fiber Communication Conference (OFC)*, paper OThL4, Anaheim, CA, Mar. 2005.

[49]   S. Tsukamoto, D.-S. Ly-Gagnon, K. Kikuchi, and K. Katoh, "Coherent demodulation of 40-Gbit/s Polarization-Multiplexed QPSK signals with 16-GHz spacing after 200-km transmission," *Optical Fiber Communication Conference (OFC)*, post deadline paper PDP29, Anaheim, CA, Mar. 2005.

[50]   S. Tsukamoto, D.-S. Ly-Gagnon, K. Katoh, and K. Kikuchi, "Demodulation of co-polarized 20 Gbps QPSK signals with 16-GHz spacing after 200 km transmission using coherent detection

and digital signal processing," *Conference on Lasers and Electro-Optics (LEOS)*, paper CWO3, Baltimore, MA, May 2005.

[51]   S. Tsukamoto, K. Katoh, and K. Kikuchi, "Unrepeated 20 Gbps QPSK transmission over 200 km SSMF using homodyne detection and digital signal processing," *Optical Fiber Communication Conference (OFC)*, paper OWB4, Anaheim, CA, Mar.2006.

[52]   K. Kikuchi, "Coherent detection of phase-shift keying signals using digital carrier-phase estimation," *Optical Fiber Communication Conference (OFC)*, paper OTuI4, Anaheim, CA, Mar. 2006.

[53]   S. Tsukamoto, K. Katoh, and K. Kikuchi, "Unrepeated transmission of 20 Gbps optical quadrature phase-shift-keying signal over 200 km standard single-mode fiber based on digital processing of homodyne-detected signal for group-velocity dispersion compensation," *IEEE Photon. Technol. Lett.*, vol. 18, no. 9, pp. 1016–1018, May 2006.

[54]   S. Tsukamoto, K. Katoh, and K. Kikuchi, "Coherent demodulation of optical multilevel phase-shift-keying signals using homodyne detection and digital signal processing," *IEEE Photon. Technol. Lett.*, vol. 18, no. 10, pp. 1131–1133, May 2006.

[55]   M. Nakazawa, M. Yoshida, K. Kasai, and J. Honqou, "20 Msymbol/s 64 and 128 QAM coherent optical transmission over 525 km using heterodyne detection with frequency-stabilized laser," *Electron. Lett.*, vol. 42, no. 12, pp. 710–712, Jun. 2006.

[56]   T. Pfau, S. Hoffmann, R. Peveling, S. Bhandare, S. W. Ibrahim, O. Adamczyk, M. Porrmann, and R. Noé, "Real time synchronous QPSK transmission with standard DFB lasers and digital I&Q receiver," *Conference on Coherent Optical Techniques and Applications (COTA)*, paper CThC5, Whistler, BC, Canada, June 2006.

[57]   T. Pfau, S. Hoffmann, R. Peveling, S. Bhandare, O. Adamczyk, M. Porrmann, R. Noé, and Y. Achiam, "1.6 Gbps real time synchronous QPSK transmission with standard DFB lasers," *Eur. Conf. Optical Communication (ECOC)*, paper Mo4.2.6, Cannes, France, Sept. 2006.

[58]   S. Savory, A. D. Stewart. S. Wood. G. Gavioli, M. G. Taylor, R. I. Killey, and P. Bayvel, "Digital equalization of 40 Gbps per wavelength transmission over 2480 km of standard fibre without optical dispersion compensation," *Eur. Conf. Optical Communication (ECOC)*, paper Th.2.5.5, Cannes, France, Sept. 2006.

[59]   C. S. Fludger, T. Duthel, T. Wuth, and C. Schulien, "Uncompensated transmission of 86 Gbps polarization multiplexed RZ-QPSK over 100 km of NDSF employing coherent equalization," *Eur. Conf. Optical Communication (ECOC)*, paper Th4.3.3, Cannes, France, Sept. 2006.

[60]   G. Charlet, N. Maaref, J. Renaudier, H. Mardoyan, P. Tran, and S. Bigo, "Transmission of 40 Gb/s QPSK with coherent detection over ultra-long distance improved by nonlinearity mitigation," *Eur. Conf. Optical Communication (ECOC)*, post deadline paper Th4.3.4, Cannes, France, Sept. 2006.

[61]   T. Pfau, S. Hoffmann, R. Peveling, S. Ibrahim, O. Adamczyk, M. Porrmann, S. Bhandare, R. Noé, and Y. Achiam, "Synchronous QPSK transmission at 1.6 Gbps with standard DFB lasers and real-time digital receiver," *Electron. Lett.*, vol. 42, no. 20, pp. 1175–1176, Sept. 2006.

[62]   T. Pfau, S. Hoffmann, R. Peveling, S. Bhandare, S. Ibrahim, O. Adamczyk, M. Porrmann, R. Noé, and Y. Achiam, "First real-time data recovery for synchronous QPSK transmission with standard DFB lasers," *IEEE Photon. Technol. Lett.*, vol. 18, no. 18, pp. 1907–1909, Sep. 2006.

[63]   A. Leven, N. Kaneda, A. Klein, U.-V. Koc, and Y.-K. Chen, "Real time implementation of 4.4 Gbps QPSK intradyne receiver using field programmable gate array," *Electron. Lett.*, vol. 42, no. 24, pp. 1421–1422, Nov. 2006.

[64]   S. J. Savory, G. Gavioli, R. I. Killey, and P. Bayvel, "Transmission of 42.8 Gbit/s Polarization Multiplexed NRZ-QPSK over 6400 km of standard fiber with no optical dispersion compensation," *Optical Fiber Communication Conference (OFC)*, paper OTuA1, Anaheim, CA, Mar. 2007.

[65]   S. -Y. Kim and K. Kikuchi, "1000 km transmission of 20 Gbps QPSK-NRZ co-polarized DWDM signals with spectral efficiency of 1 bit/s/Hz using coherent detection," *Optical Fiber Communication Conference (OFC)*, paper OThS4, Anaheim, CA, March 2007.

[66]   C. Laperle, B. Villeneuve, Z. Zhang, D. McGhan, H. Sun, and M. O'Sullivan, "Wavelength division multiplexing (WDM) and polarization mode dispersion (PMD) performance of a coherent 40 Gbps dual-polarization quadrature phase shift keying (DP-QPSK) transceiver," *Optical Fiber Communication Conference (OFC)*, post deadline paper PDP16, Anaheim, CA, March 2007.

[67]   G. Charlet, J. Renaudier, M. Salsi, H. Mardoyan, P. Tran, and S. Bigo, "Efficient mitigation of fiber impairments in a ultra-long haul transmission of 40 Gbit/s polarization-multiplexed data, by digital signal processing in a coherent receiver," *Optical Fiber Communication Conference (OFC)*, post deadline paper PDP17, Anaheim, CA, March 2007.

[68]   C. Fludger, T. Duthel, D. van den Borne, C. Schulien, E.-D. Schmidt, T. Wuth, E. de Man, G. D. Khoe, and H. de Waardt, "10×111 Gbit/s, 50 GHz spaced, POLMUX-RZ-DQPSK transmission over 2375 km employing coherent equalization," *Optical Fiber Communication Conference (OFC)*, post deadline paper PDP22, Anaheim, CA, Feb. 2007.

[69]   M. Nakazawa, J. Hongo, K. Kasai, and M. Yoshida, "Polarization-multiplexed 1 GSymbol/s 64 QAM (12 Gbps) coherent optical transmission over 150 km with an optical bandwidth of 2 GHz," *Optical Fiber Communication Conference (OFC)*, post deadline paper PDP26, Anaheim, CA, Feb. 2007.

[70]   T. Pfau, R. Peveling, S. Hoffmann, S. Bhandare, S. Ibrahim, D. Sandel, O. Adamczyk, M. Porrmann, R. Noé, Y. Achiam, D. Schlieder, A. Kozlovsky, Y. Benarush, J. Hauden, N. Grossard, and H. Porte, "PDL-tolerant real-time polarization-multiplexed QPSK transmission with digital coherent polarization diversity receiver," *Conference on Lasers and Electro Optics Systems (LEOS) summer topical*, paper MA.2.3, 2007.

[71]   S. Y. Kim and K. Kikuchi, "1000 km polarization-interleaved WDM transmission of 20 Gbps QPSK signals on the frequency grid with 12.5 GHz channel spacing using digital coherent receiver," *European Conference on Optical Communications (ECOC)*, paper 08.3.2, Berlin, Germany, Sept. 2007.

[72]   T. Pfau, R. Peveling, F. Samson, J. Romoth, S. Hoffmann, S. Bhandare, S. Ibrahim, D. Sandel, O. Adamczyk, M. Porrmann, R. Noé, J. Hauden, N. Grossard, A. Kozlovsky, Y. Benarush, and Y. Achiam, "Polarization-multiplexed 2.8 Gbps synchronous QPSK transmission with real time digital polarization tracking," *Eur. Conf. Optical Communication (ECOC)*, paper 08.3.3, Berlin, Germany, Sept. 2007.

[73]   S. J. Savory, V. Mikhailov, R. I. Killey, and P. Bayvel, "Digital coherent receivers for uncompensated 42.8 Gb/s transmission over high PMD fiber," *Eur. Conf. Optical Communication (ECOC)*, paper 10.4.1, Berlin, Germany, Sept. 2007.

[74]   G. Charlet, J. Renaudier, H. Mardoyan, O. B. Pardo, F. Cérou, P. Tran, and S. Bigo, "12.8 Tbit/s transmission of 160 PDM-QPSK (160×2×40 Gbit/s) channels with coherent detection over 2550 km," *Eur. Conf. Optical Communication (ECOC)*, post deadline paper 1.6, Berlin, Germany, Sept. 2007.

[75]   T. Sakamoto, A. Chiba, and T. Kawanishi, "50 Gbps 16 QAM by a quad-parallel Mach-Zehnder modulator," *Eur. Conf. Optical Communication (ECOC)*, post deadline paper 2.8, Berlin, Germany, Sept. 2007.

[76]   N. Kaneda, A. Leven, and Y.-K. Chen, "Block length effect on 5 Gbps real time QPSK intradyne receivers with standard DFB laser," *Electron. Lett.*, vol. 43, no. 20, pp. 1106–1107, Sept. 2007.

[77]   T. Pfau, R. Pevelin, J. Hauden, N. Grossard, H. Porte, Y. Achiam, S. Hoffmann, S. K. Ibrahim, O. Adamczyk, S. Bhandare, D. Sandel, M. Porrmann, and R. Noé, "Coherent digital polarization diversity receiver for real-time polarization-multiplexed QPSK transmission at 2.8 Gb/s," *IEEE Photon. Technol. Lett.*, vol. 19, no. 24, pp. 1988–1990, Dec. 2007.

[78]   J. Renaudier, G. Charlet, M. Salsi, O. B. Pardo, H. Mardoyan, P. Tran, and S. Bigo, "Linear fiber impairments mitigation of 40 Gbps polarization-multiplexed QPSK by digital processing in a coherent receiver," *IEEE J. Lightw. Technol.*, vol. 26, no.1, pp. 36–42, Jan. 2008.

[79]   C. Fludger, T. Duthel, D. van den Borne, C. Schulien, E.-D. Schmidt, T. Wurth, J. Geyer, E. D. Man, G.D. Khoe, and H. de Waardt, "Coherent equalization and POLMUX-RZ-DQPSK for robust 100-GE transmission," *IEEE J. Lightw. Technol.*, vol. 26, no.1, pp. 64–72, Jan. 2008.

[80]   C. Laperle, B. Villeneuve, Z. Zhan, D. McGhan, H. Sun and, M. O' Sullivan, "WDM performance and PMD tolerance of a coherent 40 Gbit/s Dual-Polarization QPSK Transceiver," *IEEE J. Lightw. Technol.*, vol. 26, no.1, pp. 168–175, Jan. 2008.

[81]   M. Yoshida, H. Goto, K. Kasai, and M. Nakazawa, "64 and 128 coherent QAM optical transmission over 150 km using frequency-stabilized laser and heterodyne PLL detection," *Optics Express*, vol. 16, no. 2, pp. 829–840, Jan. 2008.

[82]   T. Pfau, S. Hoffmann, O. Adamczyk, R. Peveling, V. Herath, M. Porrmann, and R. Noé, "Coherent optical communication: towards real-time systems at 40 Gbps and beyond," *Optics Express*, vol. 16, no. 2, pp. 866–872, Jan. 2008.

[83]   H. Goto, K. Kasai, M. Yoshida, and M. Nakazawa, "Polarization-multiplexed 1 Gsymbol/s 128 QAM (14 Gbps) coherent optical transmission over 160 km using a 1.4 GHz Nyquist filter ," *Optical Fiber Communication Conference (OFC)*, paper JThA45, San Diego, CA, Feb. 2008.

[84]   R. Freund, D. -D. Groß, M. Seimetz, L. Molle, and C. Caspar, "30 Gbps RZ-8PSK transmission over 2800 km standard single mode fiber without inline dispersion compensation," *Optical Fiber Communication Conference (OFC)*, paper OMI5, San Diego, CA, Feb. 2008.

[85]   X. Zhou, J. Yu, D. Qian, T. Wang, G. Zhang, and P. D. Magill, "8×114 Gbps, 25 GHz spaced, PolMux-RZ-8PSK transmission over 640 km of SSMF employing digital coherent detection and EDFA-only amplification," *Optical Fiber Communication Conference (OFC)*, post deadline paper PDP1, San Diego, CA, Feb. 2008.

[86]   G. Charlet, J. Renaudier, H. Mardoyan, P. Tran, O. B. Pardo, F. Verluise, M. Achouche, A. Boutin, F. Blache, J.-Y. Dupuy, and S. Bigo, "Transmission of 16.4 Tbit/s capacity over 2550 km PDM QPSK modulation format and coherent receiver," *Optical Fiber Communication Conference (OFC)*, post deadline paper PDP3, San Diego, CA, Feb. 2008.

[87]   L. E. Nelson, S. L. Woodward, M. D. Feuer, X. Zhou, P. D. Magill, S. Foo, D. Hanson, D. McGhan, H, Sun, M. Moyer, and M. O'Sallivan, "Performance of a 46-Gbps dual polarization QPSK transceiver in a high PMD fiber transmission experiment," *Optical Fiber Communication Conference (OFC)*, post deadline paper PDP9, San Diego, CA, Feb. 2008

[88]   M. S. Alfiad, D. van den Borne, T. Wuth, M. Kuschnerov, B. Lankl, C. Weiske, E. de Man, A. Napoli, and H. de Waardt, "111 Gbps POLMUX-RZ-DQPSK transmission over 1140 km SSMF with 10.7 Gbps NRZ OOK neighbours," *Eur. Conf. Optical Communication (ECOC)*, paper Mo4.E.2, Brussels, Belgium, Sept. 2008.

[89]   Y. Mori, C. Zhang, K. Igarashi, K. Katoh, and K. Kikuchi, "Transmission of 40 Gbps 16 QAM signal over 100 km standard single-mode fiber using digital coherent optical receiver," *Eur. Conf. Optical Communication (ECOC)*, paper Tu1.E.4, Brussels, Belgium, Sept. 2008.

[90]   J. Yu, X. Zhou, D. Qian, M. Huang, P. N. Ji, and G. Chang, "20×112 Gbps, 50 GHz spaced, PolMux-RZ-QPSK straight line transmission over 1540 of SSMF employing digital coherent detection and pure EDFA amplification," *Eur. Conf. Optical Communication (ECOC)*, paper Th2.A.2, Brussels, Belgium, Sept. 2008.

[91]   J. Renaudier, G. Charlet, O. B. Pardo, H. Mardoyan, P. Tran, M. Salsi, and S. Bigo, "Experimental analysis of 100 Gbps coherent PDM-QPSK long-haul transmission under constraints of typical terrestrial networks," *Eur. Conf. Optical Communication (ECOC)*, paper Th2.A.3, Brussels, Belgium, Sept. 2008.

[92]   X. Zhou, J. Yu, D. Qian, T. Wang, G. Zhang, and P. D. Magill, "High-spectral-efficiency 114 Gbps transmission using PolMux-RZ-8PSK modulation format and single-ended digital coherent detection technique," *IEEE J. Lightw. Technol.*, vol. 27, no.3, pp. 153–157, Feb. 2009.

[93]   G. Charlet, J. Renaudier, H. Mardoyan, P. Tran, O. B. Pardo, F. Verluise, M. Achouche, A. Boutin, F. Blache, J.-Y. Dupuy, and S. Bigo, "Transmission of 16.4 Tbit/s capacity over 2550 km using PDM QPSK modulation format and coherent receiver," *IEEE J. Lightw. Technol.*, vol. 27, no.3, pp. 153–157, Feb. 2009.

[94]   L. E. Nelson, S. L. Woodward, S. Foo, X. Zhou, M. D. Feuer, D. Hanson, D. McGhan, H, Sun, M. Moyer, M. O'Sallivan, and P. D. Magill,, "Performance of a 46 Gbps dual-polarization QPSK transceiver with real-time coherent equalization over high PMD fiber," *IEEE J. Lightw. Technol.*, vol. 27, no.3, pp. 158–167, Feb. 2009.

[95]   Y. Mori, C. Zhang, K. Igarashi, K. Katoh, and K. Kikuchi, "Unrepeated 200 km transmission of 40 Gbps 16 QAM signals using digital coherent receiver," *Optics Express*, vol. 17, no. 3, pp. 1435–1441, Feb. 2009.

[96]   C. Zhang, Y. Mori, K. Igarashi, K. Katoh, and K. Kikuchi, "Demodulation of 1.28 Tbps polarization-multiplexed 16-QAM signals on a single carrier with digital coherent receiver," *Optical Fiber Communication Conference (OFC)*, paper OTuG3, San Diego, CA, Mar. 2009.

[97]   J. Yu, X. Zhou, M. -F. Huang, D. Qian, L. Xu, and P. N. Ji, "Transmission of hybrid 112 and 44 Gbps PolMux-QPSK in 25 GHz channel spacing over 1600 km SSMF employing digital coherent detection and EDFA-only amplification," *Optical Fiber Communication Conference (OFC)*, paper OThR3, San Diego, CA, Mar. 2009.

[98]   M. S. Alfiad, D. van den Borne, S. L. Jansen, T. Wuth, M. Kuschnerov, G. Grosso, A. Napoli, and H. de Waardt, "111 Gbps POLMUX-RZ-DQPSK transmission over LEAF: optical versus

electrical dispersion compensation," *Optical Fiber Communication Conference (OFC)*, paper OThR4, San Diego, CA, Mar. 2009.

[99]   S. Oda, T. Tanimura, T. Hoshida, C. Ohshima, H. Nakashima, Z. Tao, and J. Rasmussen, "112 Gbps DP-QPSK transmission using a novel nonlinear compensator in digital coherent receiver," *Optical Fiber Communication Conference (OFC)*, paper OThR6, San Diego, CA, Mar. 2009.

[100]   J. Renaudier, G. Charlet, O. B. Pardo, H. Mardoyan, P. Tran, M. Salsi, and S. Bigo, "Transmission of 100 Gbps coherent PDM-QPSK over 16×100 km of standard fiber with all-erbium amplifiers," *Optics Express*, vol. 17, no. 7, pp. 5112–5117, Mar. 2009.

[101]   M. S. Alfiad, M. Kuschnerov, T. Wuth, T. J. Xia, G. Wellbrock, E. -D. Schmidt, D. van den Borne, B. Spinnler, C. J. Weiske, E. de Man, A. Napoli, M. Finkenzeller, S. Spaelter, M. Rehman, J. Behel, M. Chbat, J. Stachowiak, D. Peterson, W. Lee, M. Pollock, B. Bash, D. Chen, M. Freiberger, B. Lankl, and H. de Waardt, "111 Gbps transmission over 1040 km field-deployed fiber with 10G/40G neighbors," *IEEE Photon. Technol. Lett.*, vol. 21, no. 10, pp. 615–617, May 2009.

[102]   M. S. Alfiad, D. van den Borne, S. L. Jansen, T. Wuth, M. Kuschnerov, G. Grosso, A. Napoli, and H. de Waardt, "A comparison of electrical and optical dispersion compensation for 111 Gbps POLMUX-RZ-DQPSK," *IEEE J. Lightw. Technol.*, vol. 27, no. 16, pp. 3590–3598, Aug. 2009.

[103]   A. Sano, T. Kobayashi, K. Ishihara, H. Masuda, S. Yamamoto, K. Mori, E. Yamazaki, E. Yoshida, Y. Miyamoto, Y. Yamada, and H. Yamazaki, "240-Gb/s polarization-multiplexed 64 QAM modulation and blind detection using PLC-LN hybrid integrated modulator and digital coherent receiver," *Eur. Conf. Optical Communication (ECOC)*, post deadline paper PD2.2, Vienna, Austria, Sept. 2009.

[104]   M. Salsi, H. Mardoyan, P. Tran, C. Koebele, E. Dutisseuil, G. Charlet, and S. Bigo, "155×100 Gb/s coherent PDM QPSK transmission over 7200 km," *Eur. Conf. Optical Communication (ECOC)*, post deadline paper PD2.5, Vienna, Austria, Sept. 2009.

[105]   P. J. Winzer, Aa. H. Gnauk, G. Raybon, M. Schnecker, and P. J. Pupalaikis, "56 GBaud PDM-QPSK: Coherent detection and 2500 km transmission," *European Conference on Optical Communications*, post deadline paper PD2.7, Vienna, Austria, Sept. 2009.

[106]   D. Mongardien, P. Bousselet, O. B-. Pardo, P. Tran, and H. Bissessur, "2.6 Tb/s (26×100 Gb/s) unrepeatered transmission over 401 km using PDM-QPSK with coherent receiver," *Eur. Conf. Optical Communication (ECOC)*, paper 6.4.3, Vienna, Austria, Sept. 2009.

[107]   A. Gnauk and P. Winzer, "10×112 Gb/s 16 QAM transmission over 1022 km of SSMF with a spectral efficiency of 4.1 b/s/Hz and no optical filtering," *Eur. Conf. Optical Communication (ECOC)*, paper 8.4.2, Vienna, Austria, Sept. 2009.

[108]   L. Molle, M. Seimetz, D-. D. Gross, R. Freund, and M. Rohde, "Polarization multiplexed 20 GBd square 16 QAM long haul transmission over 1120 km using EDFA amplification," *Eur. Conf. Optical Communication (ECOC)*, paper 8.4.2, Vienna, Austria, Sept. 2009.

[109]   Y. Mori, C. Zhang, M. Usui, K. Igarashi, K. Katoh, and K. Kikuchi, "200 km transmission of 100 Gbps 32 QAM dual-polarization signals using a digital coherent receiver," *Eur. Conf. Optical Communication (ECOC)*, paper 8.4.6, Vienna, Austria, Sept. 2009.

[110]   J. Yu, X. Zhou, and M-. F. Huang, "8×114 Gb/s, 25 GH-spaced PolMux-RZ-8 QAM straight-line transmission over 800 km of SSMF," *Eur. Conf. Optical Communication (ECOC)*, paper P4.02, Vienna, Austria, Sept. 2009.

[111]   R. Noé, "Phase noise-tolerant synchronous QPSK/BPSK baseband-type intradyne receiver concept with feedforward carrier recovery," *IEEE Photon. Technol. Lett.*, vol. 17, no. 4, pp. 887–889, Apr 2005.

[112]   M. G. Taylor, "Accurate digital phase estimation process for coherent detection using a parallel digital processor," *Eur. Conf. Optical Communication (ECOC)*, paper Tu4.2.6, Glasgow, Scotland, Sept. 2005.

[113]   http://www.vpiphotonics.com/

[114]   S. Huard, *Polarization of light*. New York, NY: Wiley, 1997.

[115]   J. P. Gordon and H. Kogelnik, "PMD fundamentals: Polarization mode dispersion in optical fibers," *in Proc. of the National Academy of Sciences (PNAS)*, vol. 97, No. 9, pp. 4541–4550, Apr. 2000.

[116]   E. Alpman, "Estimation of oscillator phase noise for MPSK-based communication systems over AWGN channels," M. S. thesis, Chalmers University of Technology, Gothenburg, Sweden, 2004.

[117]   A. Kaplan, K. Achiam, A. Greenblatt, G. Harston, and P. S. Cho,"LiNbO integrated optical QPSK modulator and coherent receiver,"in *Proc. European Conference on Integrated Optics (ECIO)*, Prague, Czech Republic, Apr. 2–4, 2003, Paper WeA3.2, pp. 79–82.

[118]   R. Noé, U. Rückert, Y. Achiam, F. -J. Tegude, and H. Porte, "European synQPSK project: Towards synchronous optical quadrature phase shift keying with DFB lasers," *Conference on Coherent Optical Techniques and Applications (COTA)*, paper CThC4, Whistler, BC, Canada, June 2006.

[119]   P. E. Green, *Fiber optic networks*. Englewood Cliffs, NJ: Prentice-Hall, 1993.

[120]   B. E. A. Saleh and M. C. Teich, *Fundamentals of photonics*. New York: Wiley, 1991, ch. 7.

[121]   A. H. Gnauk and P. J. Winzer, "Optical phase-shift-keyed transmission," *IEEE J. Lightw. Technol.*, vol. 23, no. 1, pp. 115–130, Jan. 2005.

[122]   M. Seimetz and C. -M. Weinert, "Options, feasibility, and availability of 2×4 90° hybrids for coherent optical systems," *IEEE J. Lightw. Technol.*, vol. 24, no. 3, pp. 1317–1322, Mar. 2006.

[123]   D. Hoffmann, H. Heidrich, G. Wenke, R. Langenhorst, and E. Dietrich, "Integrated optics eight-port 90° hybrid on LiNbO$_3$," *IEEE J. Lightw. Technol.*, vol. 7, no. 5, pp. 794–798, May. 1989.

[124]   P. S. Cho, G. Harston, A. Greenblatt, A. Kaplan, Y. Achiam, R. M. Bertenberg, A. Brennermann, B. Adoram, P. Goldgeier, and A. Hershkovits, "Integrated optical coherent balanced receiver," *Conference on Coherent Optical Techniques and Applications (COTA)*, paper CThB2, Whistler, BC, Canada, June 2006.

[125]   L. G. Kazovsky, L. Curtis, W. C. Young, and N. K. Cheung, "All-fiber 90° optical hybrid for coherent communications," *Appl. Optics*, vol. 26, no. 3, pp. 437–439, Feb. 1987.

[126]   R. Epworth, J. Whiteaway, and S. J. Savory, "3 Fibre I & Q Coupler," U.S. patent 6859586, 2005.

[127]   S. J. Savory, G. Gavioli, R. I. Killey, and P. Bayvel, "Electronic compensation of chromatic dispersion using a digital coherent receiver," *Optics Express*, vol. 15, no. 5, pp. 2120–2126, Mar. 2007.

[128]   P. J. Anslow, C. R. S. Fludger, S. Savory, I. Hardcastel, and J. Fells "Frequency selective coherent receiver for agile networks," *Eur. Conf. Optical Communication (ECOC)*, paper Mo4.2.4, Cannes, France, Sept. 2006.

[129]   U. Koc, A. Leven, Y. Chen, and N. Kaneda, "Digital coherent quadrature phase shift keying (QPSK)," *Optical Fiber Communication Conference (OFC)*, paper OThI1, Anaheim, CA, Mar.2006.

[130]   K. Kikuchi, "Phase-diversity homodyne receiver for coherent optical communications," *Conference on Coherent Optical Techniques and Applications (COTA)*, paper CThB3, Whistler, BC, Canada, June 2006.

[131]   K. Kikuchi, "Phase-diversity homodyne detection of multilevel optical modulation with digital carrier phase estimation," *IEEE J. Select. Top. Quant Comm.*, vol. 12, no. 4, pp. 563–570, Jul./Aug. 2006.

[132]   A. Leven, N. Kaneda U. Koc, and Y. Chen, "Coherent receivers for practical optical communications systems," *Optical Fiber Communication Conference (OFC)*, paper OThK4, Anaheim, CA, Mar. 2007.

[133]   E. Ip, A. P. T. Lau, D. F. J. Barros, and J. M. Kang, "Coherent detection in optical fiber systems," *Optics Express*, vol. 16, no. 2, pp. 753–791, Jan. 2008.

[134]   K. Kikuchi, "Coherent transmission systems," *European Conference on Optical Communications*, paper Th2.A.1, Brussels, Belgium, Sept. 2008.

[135]   J. M. Kahn and E. Ip, "Principles of digital coherent receivers," *Optical Fiber Communication Conference (OFC)*, paper OTuG5, San Diego, CA, Mar. 2009.

[136]   G. Li, "Recent advances in coherent optical communication," *Advances in optics and photonics*, vol. 1, pp. 279–307, Feb. 2009.

[137]   J. Yu and X. Zhou, "Multilevel Modulations and Digital Coherent Detection", *Optical Fiber Technology*, vol. 15, no 3, pp 197-208, Feb. 2009.

[138]   G. P. Agrawal, *Fiber-optic communication systems*, 3nd ed. New York: Wiley, 1992, ch. 10.

[139]   E. Ip and J. Kahn, "Digital equalization of chromatic dispersion and polarization mode dispersion," *IEEE J. Lightw. Technol.*, vol. 25, no. 8, pp. 2033–2043, Aug. 2007.

[140]   M. Taylor, "Phase estimation methods for optical coherent detection using digital signal processing," *IEEE J. Lightw. Technol.*, vol. 27, no. 7, pp. 901–914, Apr. 2009.

[141]   S. Haykin, *Adaptive filter theory*, 3rd ed. Englewood Cliffs, NJ: Prentice-Hall, 1996.

[142]   A. H. Sayed, *Fundamentals of adaptive filtering*. Wiley-IEEE Press, 2003.

[143]   A. Vgenis, *Χρήση αυτορυθμιζόμενων ηλεκτρονικών εξισωτών σε οπτικά τηλεπικοινωνιακά συστήματα και δίκτυα με πυκνή πολυπλεξία μήκους κύματος και ρυθμό σηματοδοσίας 10 Gb/s ανά οπτικό κανάλι*, PhD dissertation (in Greek), University of Patras, June 2010.

[144]   D. Godard, "Self-recovering equalization and carrier tracking in two dimensional data communication systems," *IEEE Trans. Comm.*, vol. 28, no. 11, pp. 1867–1875, Nov. 1980.

[145]   S. Tsukamoto, Y. Ishikawa, and K. Kikuchi, "Optical homodyne receiver comprising phase and polarization diversities with digital signal processing," *Eur. Conf. Optical Communication (ECOC)*, paper Mo4.2.1, Cannes, France, Sept. 2006.

[146] K. Kikuchi, "Optical homodyne receiver comprising phase and polarization diversities with digital signal processing," *Conference on Lasers and Electro Optics Systems (LEOS) summer topical*, paper TuA.4.5, 2007.

[147] J. R. Barry, D. G. Messerschmitt, and E. A. Lee, *Digital communications*. MA: Kluwer Academic, 2004.

[148] M. Tseytlin, O. Ritterbush, and A. Salamon, "Digital, endless polarization control for polarization multiplexed fiber-optic communications," *Optical Fiber Communication Conference (OFC)*, paper MF8.3, San Diego, CA, Mar. 2003.

[149] S. Calabro, T. Dullweber, E. Gottwald, N. Hecker-Denschlag, E. Mullner, B. Opitz, G. Sebald, E. Schmidt, B. Spinnler, C. Weiske, and H. Zech, "An electrical polarization-state controller and demultiplexer for polarization multiplexed optical signals," *Eur. Conf. Optical Communication (ECOC)*, vol. 4, pp. 950–951, Rimini, Italy, Sep. 2003.

[150] R. Noé, "PLL-free synchronous QPSK polarization multiplex/diversity receiver concept with digital I&Q baseband processing," *IEEE J. Lightw. Technol.*, vol. 23, no. 2, pp. 802–808, Feb. 2005.

[151] Y. Han and G. Li, "Coherent optical communication using polarization multiple-input-multiple-output," *Opt. Express*, vol. 13, no. 19, pp. 7527–7534, Sept. 2005.

[152] M. T. Core, "Cross polarization interference cancellation for fiber optic systems," *IEEE J. Lightw. Technol.*, vol. 24, no. 1, pp. 305–312, Jan. 2006.

[153] A. Leven, N. Kaneda, and Y.-K. Chen, "A real-time CMA-based 10 Gb/s polarization demultiplexing coherent receiver implemented in an FPGA," in *Proc. Optical Fiber Communication Conference (OFC)*, Anaheim, CA, paper OTuO2, Feb. 2008.

[154] K. Kikuchi, "Polarization-demultiplexing algorithm in the digital coherent receiver," *Conference on Lasers and Electro Optics Systems (LEOS) summer topicals*, paper MC2.2, Acapulco, Mexico, Jul. 2008.

[155] H. Zhang, Z. Tao, L. Liu, S. Oda, T. Hoshida, and J. C. Rasmussen, "Polarization demultiplexing based on independent component analysis in optical coherent receivers," *Eur. Conf. Optical Communication (ECOC)*, paper Mo.3.D.5, Brussels, Belgium, Sept. 2008.

[156] I. Roudas, A. Vgenis, C. S. Petrou, D. Toumpakaris, J. Hurley, M. Sauer, J. Downie, Y. Mauro, and S. Raghavan, "Optimal polarization demultiplexing for coherent optical communications systems," *IEEE J. Lightw. Technol.*, vol. 28, no. 7, pp. 1121–1134, Apr. 2010.

[157] E. Ip and J. Kahn, "Feedforward carrier recovery for coherent optical communications," *IEEE J. Lightw. Technol.*, vol. 25, no. 9, pp. 2675–2692, Sep. 2007.

[158] A. Viterbi and A. Viterbi, "Nonlinear estimation of PSK-modulated carrier phase with application to burst digital transmission," *IEEE Trans. on Inform. Theory*, vol. IT-29, no. 4, July 1983.

[159] M. L. Boucheret, I. Mortensen, H. Favaro, and E. Belis, "A new algorithm for nonlinear estimation of PSK-modulated carrier phase," *in Proc. European Conference on Satellite Communications (ECSC)*, pp. 155–159, Nov. 1993.

[160] D. E. Crivelli, H. S. Carter, and M. R. Hueda, "Adaptive digital equalization in the presence of chromatic dispersion, PMD, and phase noise in coherent fiber optic systems," in *Proc. IEEE Global Telecommun. Conf.* (GLOBECOM), vol. 4, pp. 2545–2551, Dallas, TX, Nov. 2004.

[161]   S. J. Savory, G. Gavioli, R. I. Killey, and P. Bayvel, "Electronic compensation of chromatic dispersion using a digital coherent receiver," *Optics Express*, vol. 18, no. 5, pp. 2120–2126, Mar. 2007.

[162]   A. Vgenis, C. S. Petrou, I. Roudas, I. Chochliouros, G. Agapiou and T. Doukoglou, Adaptive electronic equalization for non-ideal optical coherent receivers, in *Proc. IEEE Communications Systems, Networks and Digital Signal Processing (CSNDSP)*, Graz, Austria, pp. 349-353, July 2008.

[163]   Y. Mori, C. Zhang, K. Igarashi, K. Katoh, and K. Kikuchi, "Unrepeated 200-km transmission of 40-Gbit/s 16-QAM signals using digital coherent receivers,"*Optics Express*, vol. 17, no. 3, pp. 1435–1441, Feb. 2008.

[164]   S. Hofmann, S. Bhandare, T. Pfau, O. Adamczyk, C. Wördehoff, R. Peveling, M. Porrmann, and R. Noé, "Frequency and Phase estimation for coherent QPSK transmission with unlocked DFB lasers," *IEEE Photon. Technol. Lett.*, vol. 20, no. 18, pp. 1569–1571, Sep 2008.

[165]   D.-S. Ly-Gagnon, S. Tsukamoto, K. Katoh, and K. Kikuchi, "Coherent detection of optical quadrature phase-shift keying with carrier phase estimation, " *IEEE J. Lightw. Technol.*, vol. 24, no. 1, pp. 12–21, Jan. 2006.

[166]   Z. Tao, L. Li, A. Isomura, T. Hoshida, and J. C. Rasmussen, "Multiplier-free phase recovery for optical coherent receivers," *Optical Fiber Communication Conference (OFC)*, paper OWT2, San Diego, CA, Feb. 2008.

[167]   S. Hofmann, R. Peveling, T. Pfau, O. Adamczyk, R. Eickhoff, and R. Noé, "Multiplier-free real-time phase tracking for coherent QPSK receivers," *IEEE Photon. Technol. Lett.*, vol. 21, no. 3, pp. 137–139, Feb 2009.

[168]   S. Hoffmann, M. El-Daraway, T. Pfau, C. Wördehoff, R. Peveling, U. Rückert, and R. Noé, "Realtime phase tracking with multiplier-free barycenter approximation in digital synchronous QPSK receiver with coherent detection," *Conference on Lasers and Electro Optics (CLEO)*, paper ThE2, Belek-Antalya, Turkey, Oct. 2009.

[169]   S. Mirabbasi and K. Martin, "Classical and modern receiver architectures," *IEEE Com. Magazine*, pp. 132–139, Nov. 2000.

[170]   B. Razavi, "Design considerations for direct-conversion receivers," *IEEE Trans Circuits Syst. II*, Vol. 44, no. 6, pp. 428–435, June 1997.

[171]   H. Meyr, M. Moeneclaey, and S. Fechtel, *Digital communication receivers.* Channel Estimation and Signal Processing, New York, John Wiley & Sons, 1998, ch. 8.

[172]   Z. Tao, H. Zhang, A. Isomura, T. Hoshida, and J. Rasmussen, "Simple, robust, and wide-range frequency offset monitor for automatic frequency control in digital coherent receivers," *Eur. Conf. Optical Communication (ECOC)*, paper Tu3.5.4, Brussels, Belgium, Sept. 2008.

[173]   K. Piyawanno, M. Kushnerov, B. Spinnler, and B. Lankl, "Fast and accurate automatic frequency control for coherent receivers," *Eur. Conf. Optical Communication (ECOC)*, paper 7.3.1, Vienna, Austria, Sept. 2009.

[174]   M. Morelli and U. Mengali, "Feedforward frequency estimation for PSK: a tutorial review," *European Trans. on Telecommun.*, Vol. 2, pp. 103-116, March/April 1998.

[175]   A. Leven, N. Kaneda, U.-V. Koc, and Y.-K. Chen, "Frequency estimation in intradyne reception," *IEEE Photon. Technol. Lett.*, vol. 19, no. 6, pp. 366–368, Mar. 2007.

[176]   L. Li, Z. Tao, S. Oda, T. Hoshida, and J. Rasmussen, "Wide-range, accurate and simple digital frequency offset compensator for optical coherent receivers," *Optical Fiber Communication Conference (OFC)*, paper OWT4, San Diego, CA, Feb. 2008.

[177]   S. Hoffmann, S. Bhandare, T. Pfau, O. Adamczyk, C. Wördehoff, R. Peveling, M. Porrmann, and R. Noé, "Frequency and phase-estimation for coherent QPSK transmission with unlocked DFB lasers," *IEEE Photon. Technol. Lett.*, vol. 20, no. 18, pp. 1569–1571, Sept. 2008.

[178]   H. Nakashima, T. Tanimura, T. Hoshida, S. Oda, J. Rasmussen, L. Li, Z. Tao, Y. Ishii, K. Shiota, K. Sugitani, and H. Adachi, "Novel wide-range frequency offset compensator demonstrated with real-time digital coherent receiver," *Eur. Conf. Optical Communication (ECOC)*, paper Mo3.D.4, Brussels, Belgium, Sept. 2008.

[179]   K. Piyawanno, M. Kushnerov, F. Hauske, B. Spinnler, E.-D. Schmidt, and B. Lankl, "Correlation-based carrier phase estimation for WDM DP-QPSK transmission," *IEEE Photon. Technol. Lett.*, vol. 20, no. 24, pp. 2090–2092, Dec. 2008.

[180]   M. Valkama, M. Renfors, and V. Koivunen, "Advanced methods for I/Q imbalance compensation in communication receivers," *IEEE Trans. Signal Proc.*, vol. 49, no. 10, pp. 2335–2344, Oct. 2001.

[181]   I. Roudas, M. Sauer, J. Hurley, Y. Mauro, and S. Raghavan, "Compensation of coherent DQPSK receiver imperfections," *Conference on Lasers and Electro Optics (LEOS) summer topicals*, paper MA3.4, Portland, OR, Jul. 2007.

[182]   C. S. Petrou, A. Vgenis, A. Kiourti, I. Roudas, J. Hurley, M. Sauer, J. Downie, Y. Mauro, and S. Raghavan, "Impact of transmitter and receiver imperfections on the performance of coherent optical QPSK communication systems," *Conference on Lasers and Electro Optics (LEOS)*, paper ThFF3, Newport Beach, CA, Nov. 2008.

[183]   I. Fatadin, S. J. Savory, and D. Ives, "Compensation of quadrature imbalance in an optical QPSK coherent receiver," *IEEE Photon. Technol. Lett.*, vol. 20, no. 20, pp. 1733–1735, Oct. 2008.

[184]   H. Sun and K.-T. Wu, "Method for quadrature phase angle correction in a coherent receiver of a dual-polarization optical transport system," U.S. Patent 6 917 031, July 12, 2005.

[185]   C. S. Petrou, A. Vgenis, I. Roudas, and L. Raptis, "Quadrature imbalance compensation for PDM QPSK coherent optical systems," in *Proc. IEEE LEOS*, paper ThE3, Belek-Antalya, Turkey, Oct. 2009.

[186]   C. S. Petrou, A. Vgenis, I. Roudas, and L. Raptis, "Quadrature imbalance compensation for PDM QPSK coherent optical systems", *IEEE Photon. Technol. Lett.*, vol. 21, no. 24, pp. 1876–1888, Dec. 2009.

[187]   E. Hecht, *Optics.* 4th ed., Addison–Wesley, 2002.

[188]   Weisstein, Eric W. "Quadratic Curve." From MathWorld-A Wolfram Web Resource. http://mathworld.wolfram.com/QuadraticCurve.html.

[189]   Weisstein, Eric W. "Ellipse." From MathWorld-A Wolfram Web Resource. http://mathworld.wolfram.com/Ellipse.html.

[190]   A. Fitzgibbon, M. Pilu and R. Fisher, "Direct least square fitting of ellipses," *Trans. Pattern Analysis and Machine Intelligence.*, vol. 21, no. 5, pp. 476–480, May 1999.

[191] R. Halíř and J. Flusser, "Numerically stable direct least squares fitting of ellipses," *in Skala, V (ed.) Proc. Int. Conf. in Central Europe on Computer Graphics, Visualization and Interactive Digital Media*, pp. 125–132, 1998.

[192] F. E. Churchill, G. W. Ogar, and B. J. Thompson, "The correction of I and Q errors in a coherent processor," *IEEE Trans. Aerospace and Electronics*, vol. AES-17, no. 1, pp. 131–137, Jan. 1981.

[193] F. Karinou, K. Vlachos, I. Roudas, B. R. Hemenway, C. S. Petrou, and A. Vgenis, "Wavelength-space permutation switch with coherent PDM QPSK transmission for supercomputer optical interconnects," *Optical Fiber Communication Conference (OFC)*, paper JWA62, San Diego, CA, Mar. 2010.

[194] A. Vannucci and A. Bononi, "Statistical characterization of the Jones matrix of long fibers affected by polarization mode dispersion (PMD)," *IEEE J. Lightw. Technol.*, vol. 20, no. 5, pp. 811–821, May 2002.

[195] H. S. Chung, S. H. Chang, and K. Kim, "Effect of QI compensation in an optical coherent OFDM receiver," *IEEE Photon. Technol. Lett.*, vol. 22, no. 5, pp. 308–310, Mar. 2010.

[196] S. Savory, "Digital filters for coherent optical receivers," *Optics Express*, vol. 16, no. 2, pp. 804–817, Jan. 2008.

[197] A. Vgenis, C. S. Petrou, C. B. Papadias, I. Roudas, and L. Raptis, "Nonsingular constant modulus equalizer for PDM-QPSK coherent optical receivers," *IEEE Photon. Technol. Lett.*, vol. 22, no. 1, pp. 45–47, Jan. 2010.

[198] J. Proakis, *Digital Communications*. New York: McGraw-Hill, 4th Ed., 2000, ch. 5.

[199] S. Benedetto, E. Biglieri, and V. Castellani, *Digital Transmission Theory*. Englewood Cliffs, NJ: Prentice-Hall, 1987, pp. 213–220.

[200] K.-P. Ho, Phase-Modulated Optical Communication Systems. New York: Springer, 2005.

[201] M. C. Jeruchim, "Techniques for estimating the bit error rate in the simulation of digital communications systems," *IEEE J. Select. Areas Commun.*, vol. SAC-2, pp. 153–170, Jan. 1984.

[202] C. Petrou, I. Roudas, and L. Raptis, "Impact of receiver imperfections on the performance of coherent intradyne DQPSK receivers," *Conference on Lasers and Electro-Optics (LEOS)*, paper CThJJ1, San Jose, CA, May 2008.

[203] A. Vgenis, C. Petrou, I. Roudas, and C. Papadias, "Robust PMD equalizer for coherent PDM-QPSK systems," submitted at *Eur. Conf. Optical Communication (ECOC)*, Milan, Italy, Sept. 2010.

[204] N. Mantzoukis, C. S. Petrou, A. Vgenis, T. Kamalakis, I. Roudas, and L. Raptis, "Outage probability due to PMD in coherent PDM QPSK systems with electronic equalization," *IEEE Photon. Technol. Lett.*, accepted for publication.